Research and Development of a Reconfigurable Robotic End-Effector for Machining and Part Handling

Submitted By:

Clydene Emmanual Reddy (BScEng, UKZN) - 212502866

Supervisor:

Dr Jared Padayachee

Co-Supervisor:

Professor Glen Bright

January 2020

Submitted in fulfilment of the academic requirements for the degree of:
Master of Science in Engineering (Mechanical Engineering),
College of Agriculture, Engineering and Science, University of KwaZulu-Natal.

Examiners Copy

COLLEGE OF AGRICULTURE, ENGINEERING AND SCIENCE

DECLARATION - SUBMISSION AND ORIGINALITY

Supervisor

As the Candidate's Supervisor, I agree to the submission of this dissertation.

Signed: ……..…..…… Date: ……..…….……

Dr Jared Padayachee

Co-Supervisor

As the Candidate's Co-Supervisor, I agree to the submission of this dissertation.

Signed: ……..……...… Date: ……...…….……

Professor Glen Bright

Student

I declare this dissertation has not previously been submitted for any degree in this, or any other University, and is the student's (MSc Eng. Candidate Clydene Emmanual Reddy's) own original work.

Signed: ……..…..…… Date: ……..……...

Mr Clydene Emmanual Reddy

COLLEGE OF AGRICULTURE, ENGINEERING AND SCIENCE

DECLARATION 1 - PLAGIARISM

I, Clydene Emmanual Reddy, declare that

1. The research reported in this thesis, except where otherwise indicated, is my original research.
2. This thesis has not been submitted for any degree or examination at any other university.
3. This thesis does not contain other persons' data, pictures, graphs or other information, unless specifically acknowledged as being sourced from other persons.
4. This thesis does not contain other persons' writing, unless specifically acknowledged as being sourced from other researchers. Where other written sources have been quoted, then:
    a. Their words have been re-written but the general information attributed to them has been referenced
    b. Where their exact words have been used, then their writing has been placed in italics and inside quotation marks, and referenced.
5. This thesis does not contain text, graphics or tables copied and pasted from the Internet, unless specifically acknowledged, and the source being detailed in the thesis and in the References sections.

Signed: …….. Date: ……..……

Mr Clydene Emmanual Reddy

COLLEGE OF AGRICULTURE, ENGINEERING AND SCIENCE

DECLARATION 2 - PUBLICATIONS

Details of contribution to peer-reviewed publications that include research presented in this dissertation. The undersigned agree that the following submissions were made and accepted as described and that the content therein is contained in this research.

Publication 1: SAIIE 29 Conference

Reddy, C.E., Padayachee, J. and Bright, G. (2018) 'A RECONFIGURABLE ROBOTIC END-EFFECTOR FOR MACHINING AND PART HANDLING – MACHINE TOOL SIMULATION', SAIIE 29 Conference of The South African Institution of Industrial Engineering, [Published], October 2018. This conference paper contains work done in chapters two to four of this dissertation.

Publication 2: SAJIE Journal

Reddy, C.E., Padayachee, J. and Bright, G. (2019) 'DEVELOPMENT AND ANALYSIS OF RECONFIGURABLE ROBOTIC END-EFFECTOR FOR MACHINING AND PART-HANDLING', SAJIE Journal of the South African Institution of Industrial Engineering, [Submitted], December 2019. This journal paper contains work done in chapters two to seven of this dissertation.

Signed: ……..… Date: …….…….…….…...

Mr Clydene Emmanual Reddy

Acknowledgements

This research is made possible by my Lord and Saviour Jesus Christ. In times of difficulty, lowliness and confusion He has given me the will and motivation to complete this study.

I would like to take this opportunity to express my sincere gratitude and appreciation to my supervisor Dr Jared Padayachee for all the help, support, advice and guidance whilst on this journey.

I wish to also thank Professor Glen Bright for the financial support given for the SAIIE 29 Conference, advice and suggestions.

I acknowledge my dearest parents, who have relentlessly encouraged me to complete this study. Without their love and support throughout the years, this research would not be possible.

I will like to thank my brother for the assistance and company he provided during the late nights and early mornings in the laboratory. My loving sister, for accompanying me to the SAIIE 29 Conference and listening to me when difficulties arose.

I would like to express my gratitude to my friends and colleagues who have provided me with valuable advice and assistance.

I would also like to express gratitude to the following people and organisations:

- NRF Thuthuka for financial support under the grant number TTK170421228180.
- Mechanical engineering workshop staff and admin staff for all their assistance.
- Mr Pravesh Moodley and VRTC for assisting with vibration equipment.

Abstract

The manufacturing landscape is shaped by human advancement. As such, the industry is continuously changing to cater to customer requirements. Manufacturers need to be flexible in terms of producing more variety within the same factory. The development of robotic systems for machining is increasing due to the flexibility of robotic manipulators compared to CNC machines. Industrial robotic manipulators require an end-effector to perform tasks such as part handling or processing operations. Commercially available part handling systems and machine tools are designed for specialised operations.

The purpose of this study is to research and develop a reconfigurable robotic end-effector for machining and part handling. The device eliminates the need for separate robots to perform part handling and manufacturing operations. Additionally, it eliminates lengthy end-effector changes. An end-effector that is able to retrofit to most serial and parallel robots will offer a higher level of flexibility in manufacturing.

This research presents the mechanical conceptualisation, design, structural analysis and manufacturing of the novel reconfigurable end-effector. Additionally, stability analysis, testing and benchmarking was conducted. The end-effector utilises a flexible, cable-driven gripper system in conjunction with a compact, lightweight milling cutter, capable of machining non-ferrous metals. The underactuated gripper finger integrates robust mechanical linkages and compliant rubber joints. This allows for the grasping of a variety of geometric profiles. Design of the reconfigurable end-effector is scalable and adaptable.

Dynamic behaviour of the machine tool spindle is predicted in FEA and determined experimentally. The prediction of milling forces is achieved by Mechanistic Cutting Force model. The compliant behaviour of the flexible rubber joint is predicted using non-linear FEA. Machine tool chatter causes poor surface quality in milling operations. Chatter prediction is conducted for the machine tool of the reconfigurable end-effector utilising Stability Lobe Diagram.

The results demonstrate the versatility and high compliance of the gripper and machine tool. The maximum grasp volume, grasp strength and payload of the gripper is 0.007 cubic metres, 21 N and 2235 g. The machine tool of the end-effector mills pinewood, HDPE plastic and Aluminium 6061. The maximum rated speed, torque and depth of cut is 15000 RPM, 0.6 Nm and 1 mm. The cycle time of the reconfigurable robot is 1.35 s.

An experimental study revealed the influence of reconfigurability on spindle dynamics and its implication on machine stability. Benchmarking of the end-effector further validates its applicability. The end-effector demonstrates that obtaining feasible and optimal characteristics in terms of the size and weight, cost and manufacturability, actuation mechanisms, robustness against machining forces, and susceptibility to mechanical vibrations are possible.

Table of Contents

List of Acronyms

3D	Three Dimensional
3R	Three Revolute
AC	Alternating Current
BEMF	Back Electromotive Force
BLDC	Brushless Direct Current
CAD	Computer-Aided Design
CNC	Computer Numerical Control
DAQ	Data Acquisition
DC	Direct Current
DH	Denevit-Hartenberg
DML	Dedicated Manufacturing Line
DOF	Degree of Freedom
DTI	Dial Test Indicator
EE	End-Effector
EMA	Experimental Modal Analysis
EOAT	End of Arm Tooling
ER	E collet Rego-Fix
ESC	Electronic Speed Control
FEA	Finite Element Analysis
FEM	Finite Element Method
FMS	Flexible Manufacturing System
FRF	Frequency Response Function
GU	Gripper Unit
HoQ	House of Quality
MAC	Modal Assurance Criterion
MOSFET	Metal-Oxide Field Effect Transistor

MSR	Modular Self Reconfigurable
MT	Machine Tool
NEMA	Natural Electrical Manufacturers Association
PKM	Parallel Kinematic Machine
PAM	Pneumatic Artificial Muscle
PLA	Polylactic Acid
PSU	Power Supply Unit
PWM	Pulse Width Modulation
QFD	Quality Function Deployment
RMS	Reconfigurable Manufacturing System
RMT	Reconfigurable Machine Tool
RM	Reconfiguration Mechanism
RREE	Reconfigurable Robotic End-Effector
SKM	Serial Kinematic Machine
SLD	Stability Lobe Diagram
UBEC	Universal Battery Elimination Circuit
UKZN	University of KwaZulu-Natal
VAP	Vertically Actuated Platform

List of Nomenclature

a	Edge contact length
a_e	Radial Depth of Cut
a_p	Axial Depth of Cut
a_r	Robot Acceleration
A	Center Distance
b_{lim}	Minimum chip width
b_x	Damping Constant, x
b_y	Damping Constant, y
c	Damping coefficient, Feed rate
c_x	Spring Constant, x
c_y	Spring Constant, y
d	Cutter diameter
d_a	Bearing Inner Race Support Diameter
d_b	Sphere diameter
d_c	Collar diameter
d_m	Pitch Diameter of Pulley, Mean Diameter
d_p	Pitch Diameter
d_w	Pulley pitch diameter
$delay$	Delay Time
D	Tool Diameter
D_a	Bearing Outer Race Support Diameter
D_b	Double Bearing Outer Race Support Diameter
f	Frequency, Chatter frequency, Coefficient of friction between the screw and nut
f_c	Coefficient of friction of the collar
f_z	Tooth Feed, Chip Load
F_a	Axial Force, Applied Force
F_g	Gripping Force
F_r	Radial Force, Radial load of the bearing
F_t	Tangential Force
F_x	Feed Force

F_y	Normal Force
F_z	Axial Force
G	Shear Modulus
h	Chip Thickness
i	Number of columns
k	Stiffness
K_{ac}	Axial cutting force coefficient
K_{ae}	Axial edge force coefficient
K_r	Radial stiffness
K_{rc}	Radial cutting force coefficient
K_{re}	Radial edge force coefficient
K_{tc}	Tangential cutting force coefficient
K_{te}	Tangential edge force coefficient
L	Lead
L_R	Belt Length
m	Mass
n	Rotational Speed, Spindle speed, Lobe number
n_c	Critical Rotational Speed
n_t	Number of teeth on the cutter
N	Number of Flutes, Spindle speed
Q_r	Radial load of one rolling element
r	The ratio of chatter frequency to the natural frequency
r_a	Radius from axis of rotation
r_d	Abutment Radius Double Bearing
r_t	Ratio between tooth frequency and natural frequency
r_s	Abutment Radius Single Bearing
R	Resolution of stepper
S	Steps

SF	Safety Factor
t	Pitch
T	Torque
T_R	Torque Required to Raise Load
u	Coefficient of Static Friction
UTS	Ultimate Tensile Strength
v	Surface Speed
v_c	Cutting Speed
v_f	Feed Rate
v_l	Linear Speed
v_s	Surface Speed of Belt
W	Applied load
Y	Young's Modulus
z	Number of Teeth
z_c	Number of rolling elements per column
z_g	Number of teeth of the large pulley
z_k	Number of teeth of the small pulley
α	Contact angle
α_n	Thread Angle
β	Helix angle, Wrap angle
δ_r	Radial deformation
ϵ	Phase shift angle
ζ	The ratio of damping coefficient to critical damping coefficient
θ_a	Angle between Lever Arm and Axis of Rotation
ν	Poisson Ratio
ρ	Mass Density

σ_y	Yield Strength
φ_{ex}	Exit immersion angle
φ_{st}	Start immersion angle
$\Phi(t)$	Tooth-normal Angle
ω_n	Angular Velocity

List of Figures

List of Tables

This page was intentionally left blank.

Chapter 1 Introduction

1.1 Project Background

The manufacturing landscape is shaped by human advancement. As such, the industry is continuously changing to meet customer requirements. The product life cycle has dramatically reduced in favour of new product models and updates. Manufacturers need to increase production flexibility to produce more variety with the same factory. Product customisation has challenges to employ; these challenges indicate the need for increased process variation and fabrication at elevated rates [1].

There are many reasons why machining with industrial robots is beneficial as compared to using traditional Computer Numerical Control (CNC) machines. In the past, workforces consisted of manual machines (Mills and Lathes) with skilled machinists. The evolution of technology and consumerism has induced competition among manufacturers. Flexibility was introduced, and manufacturers needed to upgrade to CNC machines in order to keep up with the increasing demand. The cost of industrial CNC machines is in the millions of Rands, even though the technology has been around for many years.

A recent solution to the problem of expensive and large form factor CNC machines is the use of robotic manipulators as machine tools. Robotic machining has advantages over traditional CNC machines. Machining with robots offers reconfigurability as multiple tooling, and fixturing components are usable instead of dedicated options. Control programming is adaptable and changeable. Not every machining application demand the precision and power of CNC machines, softer metals and roughing operations are well-suited for robotic machining. Such applications which require flexibility, extended working space, complex surfaces, and rapid prototype machining operations are compliant with the current capabilities of industrial robot machine tools [2].

According to Pandremenos et al. [3], the primary objectives of current manufacturing engineering are evolving. In order to face global competition, market trends indicate that precedence should be given to low-volume and large-variety processes. Industrial robots are cost-efficient, time-efficient and flexible means of materials processing. Furthermore, robots are not being used for industrial material removal processes. Serial Kinematic Manipulator (SKM) robots have accuracy issues since each of the linkages is supported by motors, brakes and reduction gears. These drivers introduce inaccuracies into the positioning of the End-Effector (EE). Vibrations induced by robot machining are not ideal as chattering is a circumstance of this effect. Figure 1-1 outlines the estimated global operational stock of industrial robots.

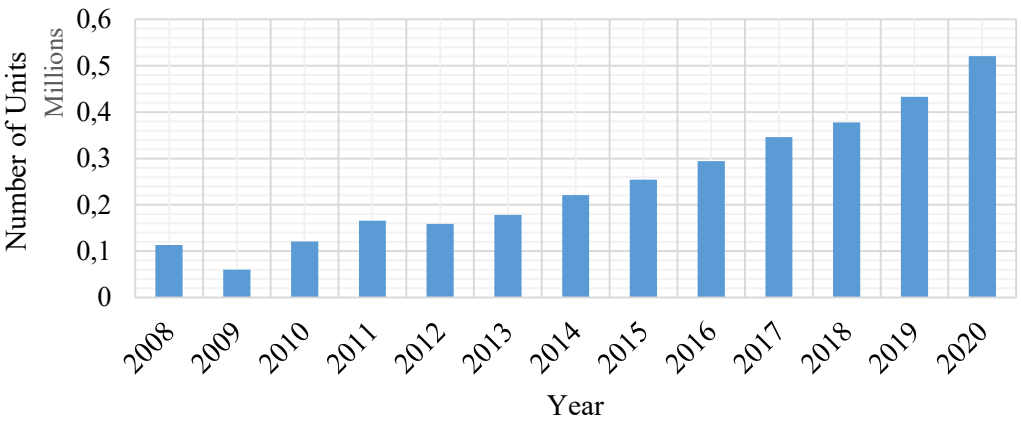

Figure 1-1: Estimated Worldwide Operational Stock of Industrial Robots [4]

1.2 Project Motivation

The high cost of imported CNC machines and other modern manufacturing technologies creates difficulty for South African manufacturers to remain competitive in global markets. The high cost of conventional CNC machines is attributed to their size and weight. Robot-based machining is an alternative to CNC machining. In contrast to CNC machines, industrial robots are characterised by low capital investment and application flexibility to a wide variety of situations. Nonetheless, barriers exist concerning the wide-scale adoption of robots for machining. Presently, global research efforts aim to explore how recent advances in Parallel Kinematic Manipulator (PKM) robotic architectures can overcome these barriers.

Robots have become a necessity in several manufacturing industries. They are used extensively by automotive, food and electronics manufacturers. Smaller production environments have difficulty with robot-based automation. Installation, safety, machine modification, interfacing grippers, and programming of the robot are some of the concerns raised by smaller manufacturers. Figure 1-2 presents the use of a KUKA serial robot for tending a CNC machine.

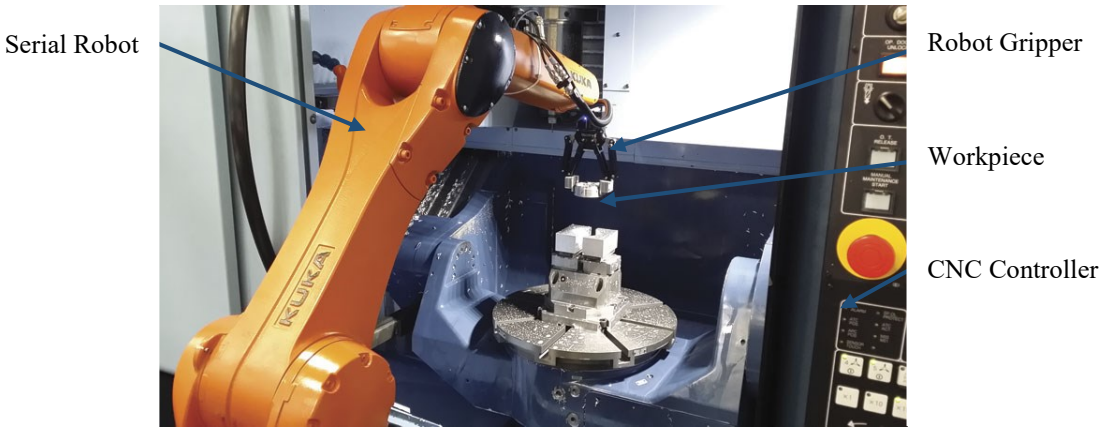

Figure 1-2: CNC Machine with KUKA Tending Robot [5]

The market requires a compact two-in-one solution to machining and part handling [6]. An end-effector that can retrofit to most serial robots and parallel robots will offer a higher level of flexibility in manufacturing [6]. Industrially available part handling systems and machine tools are designed for explicit

operations. Dedicated machine tools are used for milling, drilling, and boring. Industrial grippers are each typically designed to grip objects of similar geometry; this means that multiple grippers are needed for different parts. Most small scale manufacturers cannot afford the initial investment and often do not require the level of precision of industrial machine tools and grippers [6].

1.3 Current Research in Robotic Machining

Several studies on serial robotic systems for machining focus on trajectory planning, control system development, advanced and flexible programming, and the optimisation of mechanical stiffness. Schneider et al. [7] developed a position control system for robotic machining using an optical measurement system. Schneider et al. [8] also proceeded to combine advanced programming and simulation to create an ideal path for robot machining. These innovations improved robot machining accuracy. Domroes et al. [9] developed a flexible programming concept, which enabled the robot to mill water pump impellers along dynamically adapted path autonomously. This innovation enhanced the quality of robot-machined components and improved productivity. Klimchik et al. [10] studied the modelling of manipulator stiffness and cutting force estimation. The method was used to rank the performance of available industrial robots concerning several machining tasks. Lin et al. [11] also studied manipulator stiffness but from the perspective of posture optimisation. Through all of these studies, researchers agree that there are obstacles to using robots for machining applications. Researchers also agree that the designs of existing industrial robots are not optimised for machining operations [8],[9],[10],[12],[13].

Makinde et al. [14] presented a bio-inspired multifunctional end-effector capable of conducting maintenance tasks. The device consisted of a simple two jaw gripper that was centrally actuated by a worm gear module. Major shortfalls in their design is the limited workspace and drive mechanism. Pini and Leali [15] investigated the feasibility of employing a reconfigurable platform to conduct a human-machine collaborative relationship for polishing and quality assessment operations. The flexible device mounted onto a serial manipulator and produced promising results, however, the polishing process required extensive human input. Canali et al. [16] developed a highly reconfigurable gripper for industrial manufacturing. They aimed to pick parts of various sizes, shapes and materials from a moving conveyor. Additionally, the gripper was able to manipulate the parts for assembly operations. The gripper is theoretically capable of a 10 kg payload and uses Robot Operating System to communicate between the gripper and the robot. Avram and Valente [17] presented an algorithm for automated trajectory planning of serial robotic manipulator for high precision manufacturing.

Researchers such as Klimchik et al. [10] have identified parallel robots as a possible alternative to serial robots for machining applications. Parallel kinematic robots have a load-bearing advantage over serial robots as forces are distributed among multiple links. Parallel robots are also capable of higher accuracy and repeatability than serial systems. Serial robots are prone to error accumulation as an error in a single joint propagates throughout the serial kinematic chain [18]. Parallel robots are also recognised for the low inertial forces in the system and are, therefore, capable of speeds higher than that of serial robots [19].

Review of current research revealed the need for alternative machining platforms. Low-volume, high variety processes require multiple machines. The development of stronger robotic platforms will support machining and the need for multiple tools will require reconfigurable end-effectors.

The research question was identified: Can a reconfigurable robotic end-effector perform both machining and part handling?

1.4 Research Aims and Objectives

Aim

The aim of this study was to research and develop a reconfigurable robotic end-effector that is capable of both machining and part handling applications.

Project Objectives

1. Research and establish the state of the art in robotic end-effectors and establish the state of the art in design methods for reconfigurability.
2. Research and develop the complete mechanical design blueprints for the complete fabrication of the reconfigurable robotic end-effector.
3. Research and predict the performance of the end-effector using tools such as FEA and modal analysis.
4. Research, construct, assemble and test the performance of the end-effector in real-world machining applications.
5. Benchmark the performance of the end-effector against existing cutting technologies through data analysis and interpretation.

1.5 Scientific Contribution of Research

Research is being conducted globally, on robot architectures that will enable robust machining capabilities. Additional research on the design of suitable end-effectors for machining applications was also necessary. Presently, there are no end-effectors available that are capable of both machining and part handling. In order to switch between machining and part handling, robots typically undergo a time-consuming change of the end-effector, which increases robot downtime and reduces productivity. Manufacturers often use a dedicated part handling robot to move parts after machining, which inflates the capital investment required for a fully automated system.

This research aimed to meet the challenge of the development of a Reconfigurable Robotic End-Effector (RREE) that is suitable for machining applications. In order for a robot to maintain its flexibility while being used for machining applications, the end-effector must be capable of both part handling and machining.

An end-effector that is capable of both part handling and machining presented a significant research challenge on multiple fronts. Research challenges include obtaining feasible and optimal characteristics concerning the end-effectors (1) Size and weight (2) Cost and manufacturability (3) Actuation mechanisms (4) Robustness against machining forces (5) Susceptibility to mechanical vibrations.

The end-effector demonstrates the practicality of a multi-purpose tool. Additionally, it provides insights on the further development of End of Arm Tooling (EOAT) technology.

This research addressed the challenge of developing an end-effector that is capable of both machining and part handling, through a reconfigurable design. A reconfigurable design eliminates the need for an end-effector change or an additional dedicated part handling robot.

1.6 Research Methodology

The engineering design process was utilised in the development of the reconfigurable robotic end-effector. Definition of the problem was presented in Sections 1.2, 1.3 and 1.4 to clearly identify the gap in knowledge. Background research is conducted in Chapter 2 to outline the relevance of the research question. Requirements, specifications and evaluation are presented in Chapter 3 to define design constraints. Concept development and analysis are presented in Chapters 3, 4, 5 and 6 to solve the research problem. Testing and validating of the prototype is reported in Chapters 7 and 8 to evaluate the performance of the design. Finally, the results of the successful design are communicated in Chapters 9 and 10 through discussion and interpretation of results. Figure 1-3 presents the research methodology used for the novel design.

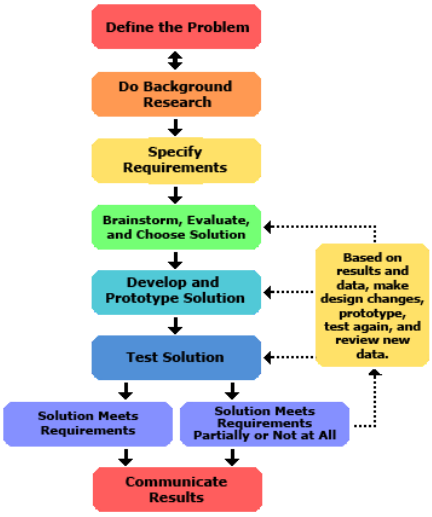

Figure 1-3: Engineering Design Process [20]

In conjunction with conventional engineering design methods, the mechatronics design philosophy was adopted. The convolution of mechanical, electronic, control and computer systems is essential in robotic design. The design of a mechatronic system requires the integration of these central systems.

1.7 Outline of Dissertation

Chapter One: Presents the background of the research project and provides the motivation for the study as well as the resultant scientific contributions. The objectives of the project are also presented.

Chapter Two: A literature review of essential background topics related to the research is presented. The state of the art in robotic end-effectors and design methods for reconfigurability are established.

Chapter Three: Synthesises the architectural layout of the reconfigurable robotic machine. Presents schemes of reconfiguration and conceptualises the mechanical architecture of the end-effector. Requirements and specifications are defined with the aid of Quality Functional Deployment (QFD).

Chapter Four: Presents the prototype design of the reconfigurable robotic gripper. Three subsystem designs are presented, machine tool, gripper and reconfiguration mechanism.

Chapter Five: Presents system modelling and analyses. Cutting force model is used to determine the milling forces encountered by the milling cutter during a specified cutting operation. Finite Element Analyses are conducted to validate the designed components.

Chapter Six: Presents manufacturing and system integration. Manufactured prototype end-effector is assembled to Fanuc SKM, and the integration of electronics for process automation is given.

Chapter Seven: Presents cutting dynamics theory, Experimental Modal Analysis (EMA) on the developed end-effector and stability analysis for machining operation.

Chapter Eight: Involves experimentation and validation of the RREE. Performance and structural characteristics of the machine tool are investigated. Adaptability characteristics of the gripper are determined. A review of the overall effect of subsystem operational behaviour concludes the chapter.

Chapter Nine: Summarizes the effectiveness and viability of the reconfigurable end-effector. Examination of the performance of the end-effector is conducted. Presents the benchmark of the RREE against dedicated tools and grippers. The implications of RREE are presented and concerns identified.

Chapter Ten: Concludes the dissertation with an evaluation of research objectives and aim. Research contributions are followed by recommendations of future research.

1.8 Chapter Summary

The background and motivation of the reconfigurable end-effector were presented as a requirement for robotic machining and part handling implemented for evolving manufacturing environment. The research gap in the development of such an end-effector was established. The aims and objectives of the research were listed, the methodology to achieve the objectives and aim was presented. The research contributions obtained were summarised before an overview of the dissertation was listed.

Chapter two presents a review of pertinent literature in an attempt to survey the landscape of robotic end-effector technology.

Chapter 2 State of the Art Review

2.1 Introduction

Industrial robots perform hazardous, precise, or repetitive tasks. Such tasks were initially performed by human hands, or by tools held by human hands. Robots are therefore required to mimic the effect of human hands. The robotic devices that accomplish the work of human hands are called end-effectors, End of Arm Tooling (EOAT) or manipulators. Robotic manipulators are split into two sections: body-and-arm assembly and wrist assembly. Both sections typically maintain three degrees-of-freedom, with the wrist sometimes requiring two for simpler operations. The device located at the wrist of a manipulator which performs a task is called an end-effector. This device is used to interact with the environment [21]. The end-effector is either a gripper, for part handling or, it is a tool for performing a specialised process. The body-and-arm of the robot is used to position the end-effector, while the robot's wrist is used to manoeuvre the end-effector to the required position. End-effectors are typically designed for a specific function as robots offer multi-faceted processes [22].

This chapter presents the research and establishment of state of the art in robotic end-effectors. Fundamentals of gripping end-effectors, industrial grippers, soft robotic grippers, and developing gripping technologies are reviewed. State of the art review in design methods for reconfigurability is established. Reconfigurability in manufacturing and in robotic grippers are investigated.

Taxonomy defines the different architectures of gripping systems. Existing gripper classification systems need to be updated to include new technologies such as soft grippers and friction grippers. Comparable end-effectors are reviewed to guide the design of the reconfigurable end-effector in terms of currently available options.

2.2 Gripping End-Effectors

The research and development of a part handing end-effector is essential for this research. As such, a review of gripping end-effectors and technologies is presented. Khurshid et al. [23] defined a gripper as any mechanism which can grasp various objects. It is a type of grasping mechanism for temporary contact with an object. The core function of any gripper is to position and orientate the object that is grasped in a manner that constrains the object sufficiently for the process that is to be performed.

Grippers are end-effectors tasked with grasping and manipulation of objects in a manufacturing system. Such objects are, typically work parts that need to be transported from one location to another in the cell. Grippers are predominantly used for loading and unloading applications. Due to the vast diversity of part shapes, sizes, and weights, grippers are usually custom-designed. Robotic grippers are classified on the basis of three criteria; type of contact-induced, the number of fingers, and the gripping method employed. Each of these three criteria will be discussed.

2.2.1 Contact Type

The three basic types of contact are; point contact, line contact, and area contact. A point contact occurs when the appendages and object are in contact at specific points. There is typically a minimum of three points of contact. Line contact occurs when the object to be grasped has a flat shape so that the imaginary

lines created during contact are relatively parallel. The area contact creates a surface contact region between the object and the gripper to constrain the object. This type of grasp is similar to the human finger grasp.

2.2.2 Number of Fingers

Grippers can be categorised according to the number of fingers they possess. Two-finger grippers are limited by their dual fingers and generally use area contact due to the lack of dexterity offered by two fingers. Three-finger grippers can be designed to operate for both contact types. Generally, as the number of fingers increases, control and design become more complex. Four finger grippers can either be dual two-finger grippers or four independent fingers. Given the complex nature of four finger grippers, they are generally used for applications which require precision manipulation. Grippers which consist of more than four fingers, are not commonly used in industry due to their complicated control. These grippers are still being developed on a research basis for dextrous gripping [24].

2.2.3 Gripping Methods

Robot gripping methods are categorised into the following classes: impactive, ingressive, contigutive, and astrictive. The resultant effect of grasping non-solids is grouped as permeating and non-permeating. Table 2-1 below describes the four gripping methods and their effects.

Table 2-1: Synopsis of Gripping Types and Effects [25]

Gripping Method	Gripping Effect on Material	
	Non-permeating	Permeating
Impactive	Jaws: Clamps, chucks, Collets	Pinch: Clu-picker, Walton devices, Pincers
Ingressive	Brush: Wire, hook, and loop	Pins: Picklift, Polytex, Hackles
Contigutive	Chemical adhesion, Surface tension forces	Thermal adhesion
Astrictive	Magnetic, electroadhesive	Vacuum suction

According to Monkman [25], impactive prehension is used in conventional robot gripper designs. Typically, in the form of a two or three-fingered claw or chuck mechanism. These fingers can be configured to grasp an object by encompassing the exterior or encompassing the interior. Ingressive methods depend on object penetration. Contigutive methods require the gripping surface to make contact with the object surface before a holding force is generated. In contrast, astrictive grippers provide a jamming force that makes grasping possible without contact.

2.2.4 The Taxonomy of Common End-Effector Types

There is a wide variety of end-effectors available nowadays, from simple mechanical grippers to intricate dextrous hands. The taxonomy of common end-effectors is similar to that of human grasps. Passive grippers can grasp objects but cannot move them while grasping or adjust the gripping force. Active grippers can actively control the grasp force. Passive and active end-effectors are further discussed.

Passive end-effectors emulate grasps without manipulation of the robotic fingers. Although many commercially available passive end-effectors incorporate sensors into their design, these sensors are limited for use by the robot arm and not the wrist. The first branch of passive end-effectors is the non-prehensile type which includes vacuum, electromagnetic and Bernoulli grippers. The term non-prehensile is given to these grippers because they do not need fingers to grasp an object; the object is grasped using a contracting force. Figure 2-1 outlines the taxonomy of robot grippers.

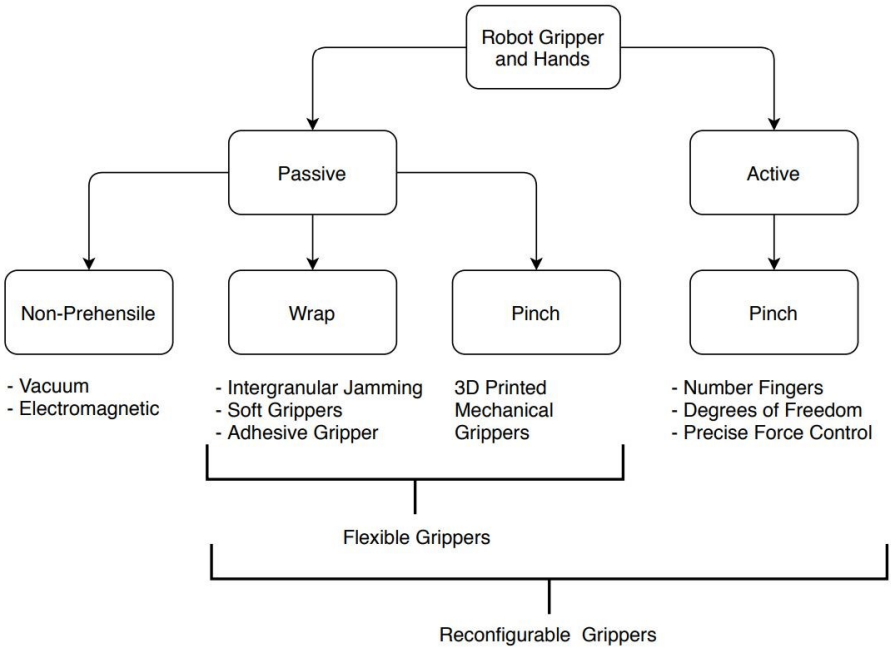

Figure 2-1: Taxonomy of Robot Grippers [26]

Grippers are based on different physical effects used to produce stable grasping between the gripper and the object being held. In industry, gripper designs are either mechanical, vacuum or magnetic.

2.3 Industrial Grippers

Typical industrial grippers are (1) Mechanical grippers: linkage actuation gripper; gear and rack actuation gripper; cam actuation gripper; screw actuation gripper (2) Vacuum grippers (3) Magnetic grippers (4) Adhesive grippers (5) Servo-electric grippers. Industrial manufacturers are prioritising improvement of production efficiency and supply chain processes. Rapid wide-scale automation across regions is increasing the demand for robot grippers with manufacturers adopting semi-professional 3D printed robot grippers [27].

2.3.1 Mechanical Grippers

A mechanical gripper is utilised as a robot end-effector for grasping objects via mechanically operated fingers. These grippers come in many different configurations. This type of gripper is most prevalently used in industry due to its simple structure and predictable actuation. Advancements in mechanical grippers are presented in this section [22].

Dual grippers – This type of mechanical gripper is best suited for machine loading and unloading. Single grippers require one load operation, and a following unload operation, this can lead to downtime and ultimately result in decreased production. The dual gripper allows the next part to be picked-up whilst the machine is processing the other work part. This means that the robot reaches in once to load and to unload. Figure 2-2 presents an ABB Serial Robot Arm with an attached Dual Gripper EOAT.

Interchangeable fingers implement a modular gripper design that allows different fingers to be installed to the end-effector to suit different parts. Sensory feedback involves sensor integration into the gripper to allow for the sensing of objects or to limit the force applied to a work part during the gripping manoeuvre. Multiple fingered grippers allow for a more dextrous grasp.

The principle of mechanical grippers is to apply friction when grasping an object to secure it for movement. Friction between the gripper and the object depends on two factors, surface roughness and surface force.

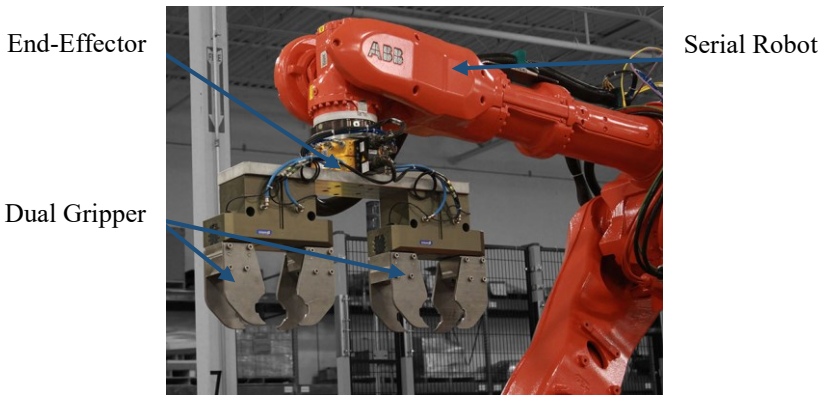

Figure 2-2: ABB Serial Robot Arm with an Attached Dual Gripper EOAT [28]

These grippers are commonly fitted with additional finger padding made from polyurethane as this increases the surface friction of the gripper, and reduces potential surface damage to the work part. Mechanical grippers are designed for specific applications and can be adapted to the size of the object [29]. The robotic gripper encounters the weight of the object and the additional forces and moments induced from the motion of this weight. Mechanical grippers assume the following types (1) Finger grippers (2) Multiple grippers (3) Expandable grippers (4) Internal grippers and (5) External grippers.

2.3.2 Vacuum Grippers

A vacuum gripper is a standardised tool used by robots in manufacturing due to its high level of flexibility. The tool employs a suction cup to maintain contact between the gripper and work part. The suction cup is generally fabricated of rubber or polyurethane which can be used at temperatures between -50 – 200°C.

The principle operation of a vacuum gripper is under pressure. The suction cup is connected via tubes with pressurised air to allow for the picking up and releasing of objects. Figure 2-3 below projects the half sections of the four different types of suction cups.

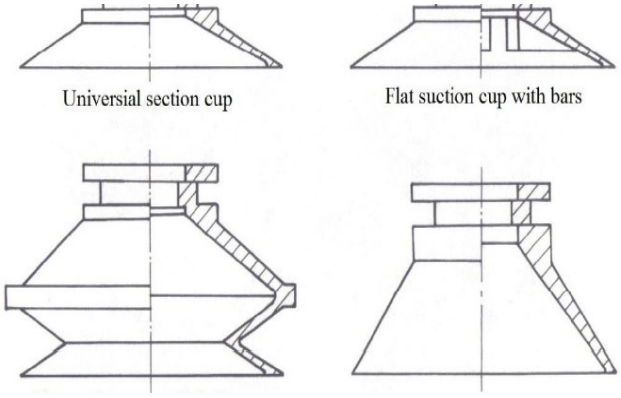

Figure 2-3: Four Types of Suction Cups [30]

Universal suction cups are utilised for flat or slightly contoured surfaces and are one of the cheaper options. A disadvantage to this suction device is increased wear at higher under pressures. Flat suction cups with bars are suitable for flat or flexible objects that require assistance when lifted. The flat suction cup is restricted to a small movement under load, which permits the contact pressure area to be well maintained. This decreases the wear on the suction cup, which results in an accelerated, more controlled movement.

Suction cups with bellows are generally utilised for objects with curved surfaces. These suction cups permit increased movement while gripping a component, although there is reduced stability due to the small under pressure. The depth suction cup is used for applications that require irregular or curved objects to be moved. An acute disadvantage of any form of vacuum gripper is that they cannot grip any object that does not permit a vacuum contact area. Objects with rough surfaces, holes, gaps on the surface, and porous surfaces, will all not permit a suction area to be formed [30].

2.3.3 Magnetic Grippers

Magnetic grippers are prevalently used for grasping ferrous materials. There are two types of magnetic grippers which operate with either permanent magnets or electromagnets. Electromagnetic grippers need both a controller and Direct Current (DC) power to handle materials. Permanent magnets have a distinct disadvantage over electromagnets due to the non-releasing ability of the permanent magnet. Additional machinery is required to remove a gripped object from the permanent magnet [31].

The manufacturing process must incorporate a demagnetising operation to remove residual magnetism in the work part. These grippers use a simple magnetic circuit to cause ferrous materials to adhere to the magnet. When a ferrous object makes contact with an electromagnet, the object provides a pathway for magnetic flux to flow through and complete the magnetic circuit. The attractive force created by this circuit holds the part against the electromagnet [32]. Figure 2-4 below is an image of a magnetic gripper.

Figure 2-4: Schunk Electromagnetic Gripper [33]

2.3.4 Hydraulic/Pneumatic Grippers

Hydraulic grippers are used when a large amount of force is needed. The lifting force is created by pumps that generate up to 137 bar of pressure. A significant drawback of these grippers is that they are prone to fluid leaks from the fluid transmission lines. Maintenance is substantial on these grippers due to the massive amounts of force they are expected to handle [34].

2.3.5 Adhesive Grippers

This type of gripper design utilises an adhesive substance to perform the grasping action. These types of grippers are used for handling fabrics and other lightweight materials. Adhesive content is continuously fed into the feeding mechanism, which is attached to the end effector [29]. Table 2-2 presents the specifications of standard industrial grippers.

Table 2-2: Specifications of Industrial Grippers

Gripper	Specification	Value
Vacuum [35] On-robot RB-GP-VG10VACUUM-OR	Payload	10 kg
	Repeatability	0.01 mm
Magnetic [36] SCHUNK EGM-B-L-30-1x2	Payload	20 kg (vertical), 60 kg (horizontal)
	Repeatability	0.01 mm
Pneumatic [37] SCHUNK MPG 16	Grasp Force	25 N
	Repeatability	0.02 mm
Adhesive [38] On-robot Gecko gripper	Payload	4.1 kg
	Repeatability	0.01 mm

2.4 Soft Grippers

Innovations in the field of robotics have seen a rise in unique gripper technology. Such technologies include soft grippers and friction grippers; these grippers diversify into heterogeneous architecture. These grippers offer an extensive range of compliance, as such elements of soft grippers may be taken forward in the gripper design.

2.4.1 Trends in Soft Robotics

Advancements in material science, soft robotics and deformable electronics have greatly hastened the development of soft grippers. The improvement of silicone elastomers, shape memory materials and active polymers has resulted in simpler and lighter flexible grippers. Challenges for the technology are miniaturization, robustness, integrity of sensing, speed and control [39]. Conventional robotics and machines are fabricated from rigid materials which limit their range of shape adaption. Hard robots experience adversity when tasked with handling fragile objects or dealing with adapting through complex environments [40]. In contrast to this convention, a soft robot has either minimal rigid material or no rigid material. These soft robots are formed of fluids, gels, soft polymers, and other easily deformable matter. A unique advantage of soft robots is their ability to operate when stretched or squeezed. The matter of compliance matching, which is the principle that contacting materials should be rigidly compatible with distributing the internal load and reducing contacting stress concentration evenly. A measure of material rigidity which is commonly used to compare the materials that go into a soft robot is the modulus of elasticity. Compliance matching is becoming increasingly important as robots become suitable for a broader range of tasks across multiple domains. The surface of a soft robot must be compliantly soft and deformable, so to broaden force application areas and eliminate interfacial stress concentrations [41].

2.4.2 Shape Adaption in Robotic Inspired Gripping

According to Wang [42], researchers worked on passive shape adaption of grippers constructed of compliant structures in pick and place operations in the 1970s. The research confirmed that such grippers could conform to irregular contours, and it also affirmed that morphology defines the function. Rolf Pfeifer introduced the philosophy of embodied intelligence. This philosophy has propelled robotic system technology to be developed for morphology changes to cater to alterations in the environment. Morphology can be assumed either actively or passively via internal actuation or external forces. Various functionality

is a desirable outcome of shape adaption. Two methods can accomplish active shape adaption of robots. One method of shape adaption occurs in a robotic system that is formed of many modules. These systems actively modify the association between robotic modules according to a motion planning algorithm [43]. Figure 2-5 below is a sketch of a Modular Self Reconfigurable (MSR) Robot concept, Roombot.

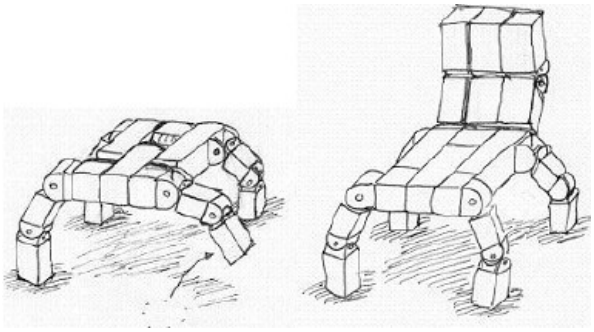

Figure 2-5: MSR Robot Concept Roombot [44]

The second means of attaining active shape adaption is via controlled deformation of soft materials. The concept of controlled deformation has sparked great interest in the robotic research labs of institutes in the past ten years. The Festo Bionic Handling Assistant is a flexible gripper arm which mimics an elephant's trunk. It is an excellent example of dynamic shape adaption through controlled deformation. Figure 2-6 presents an image of the Festo Bionic Handling Assistant.

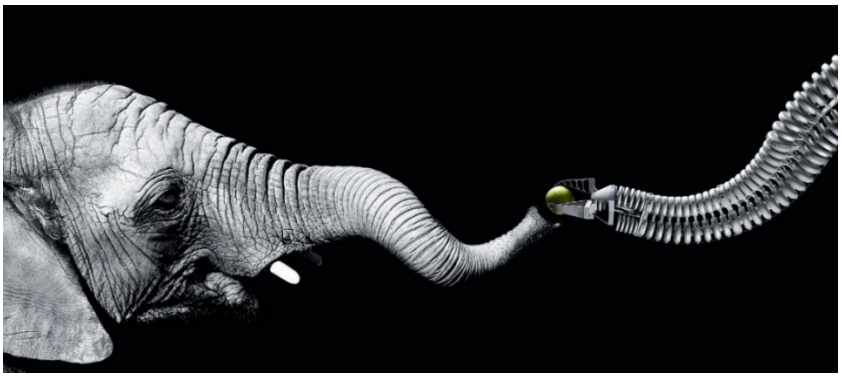

Figure 2-6: Festo Bionic Handling Assistant [45]

2.4.3 Review of Deformation in Soft-Matter Robots

A universal characteristic of soft matter is its delayed non-linear response to a stimulus. Polymers are commonly used in past and existing machine designs due to the cheaper cost and suitable mechanical properties. The use of rubber as a surface coating is commonly employed to absorb impact or maximise surface contact stresses. Robots are machines designed to interact in physical environments; in such environments, there is a chance that these machines will encounter soft matter. According to Wang [43], soft matter is a well-established field in materials science, and due to technological advancements, the amount of new synthesised soft matter grippers has increased. There are many new alternatives to the fabrication and manufacturing techniques made accessible. The amount of research being published on utilising soft matter deformation in robotics is on the increase.

A significant advantage in soft robots is the inherent ability to adapt behaviour in unanticipated task-environments. The three types of deformation behaviour in soft matter robots will be discussed. Elongation/Shortening is the simplest type of deformation in rigid bodies. From the case study on the behaviour of soft-matter under elongation and shortening performed by Wang [43], three distinct functions were determined. These are; actuator for linear actuation, reaching actions, and peristaltic locomotion.

The McKibben-type artificial muscle actuator is a type of Pneumatic Artificial Muscle (PAM). The pneumatic actuator, which is usually used in the cylinder variety, are widely used in factory floor automation. Pneumatics has gained much traction in the field of robotics as a mainstream motion source. Pneumatic Artificial Muscles albeit less well-known, form part of the pneumatic actuator family. PAMs contract on inflation, making them inverse bellows. The exertion force is dependent on pressure and the state of inflation. PAMs are notably lightweight but can transfer the same amount of energy as cylinders [46]. Figure 2-7 indicates the Pneumatic Artificial Muscle operation at constant load.

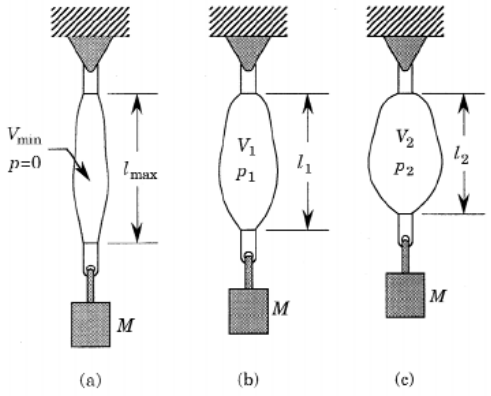

Figure 2-7: PAM Operation at Constant Load [47]

Bending is the most common deformation behaviour in solid structures. Flowing of soft matter results in deformation in a passive form. The utilisation of flowing of fluids or granular materials requires phase transition when applied to grippers. This is due to shape conformation, which permits the gripper to maintain the basic shape and force to move an object [42].

2.4.4 Soft Robotic Hand Design with Proprioception

According to Homberg et al. [48], soft robotic hands have a few advantages over traditional hard hands. The added compliance of soft grippers enables an efficient response to uncontrolled grasping. These grippers offer manipulation over a broader range of objects and versatile interactions. Due to the higher compliance offered by soft robots, a common disadvantage is that the grippers configuration is difficult to track. It is essential to understand the exact configuration of the gripper to ensure effective manipulation of items. The hand configuration determines the success of a grasp. Figure 2-8 (a) illustrates an implementation of the soft gripper design that was fabricated with proprioception.

Some disadvantages of soft grippers are the complicated fabrication methods required, the low gripping force, inability to grasp sharp/hot objects, unpredictable motion behaviour, and demanding control.

2.4.5 Baxter Easyhand

According to Franchi et al. [49], Three Dimensional (3D) printed robot hands are fast becoming a cheaper alternative to commercially available robot hands. The native Baxter gripper actuates the finger mechanism; this means that the gripper is more comfortable to control. The design was partially reconfigurable as the fingers were manually moved to different positions on the hand to vary the grasping range. Figure 2-8 (b) presents a side view of the Baxter Easyhand gripper. Figure 2-8 (c) presents the finger design. Actuation of each finger was provided by one tendon that flexes, thus closing the finger. A notable disadvantage of the gripper design lies in the native Baxter gripper actuator, as it can apply a limited force. Franchi et al. [49] noted that the limited force provided by the native actuator could result in problems with grasping because tendons usually need to apply more force than the gripper will apply at the fingertip. Advances in material science contribute to the flexible joints in the finger design.

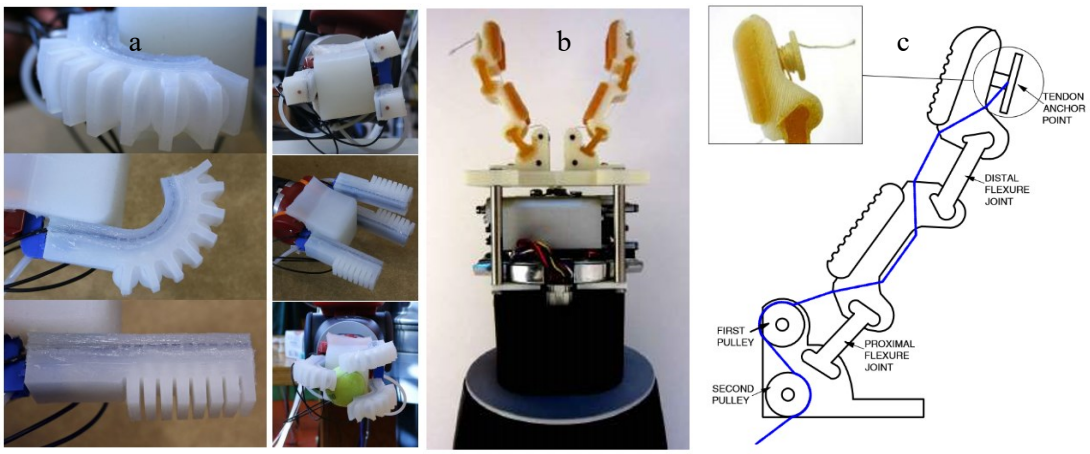

Figure 2-8: (a) Soft Robotic Hand Design with Proprioception [50]
(b and c) EasyHand Finger Design [49]

2.4.6 Universal Gripper

Universal robot grippers are capable of grasping many different geometries. Amend et al. [51] proposed a simple passive universal gripper. The gripper consisted of a quantity of granular material enclosed in an elastic membrane. The mechanism grasped due to a combination of negative and positive pressure, as it conformed to the shape of a target object. The vacuum pressure created by the actuation of the membrane held the unique geometry of the target part and thus clamped the part onto the contoured surface of the gripper. One advantage of this gripper architecture was that it did not require motors, cables, or linkages. Suction pressure was generated from a pump to remove air from the membrane. Another advantage of this gripper type was the simplistic design. Jamming grippers of this kind have the ability to grasp multiple closely spaced objects at the same instant. The structural integrity of the membrane is a potential disadvantage of the design. Sharp, hot or cold objects may damage the membrane. Further research is currently being conducted on the betterment of the membrane. Table 2-3 presents the specifications of soft grippers. Figure 2-9 depicts the operation of a universal jamming gripper.

Table 2-3: Specifications of Soft Grippers

Gripper	Specification	Value
Baxter Easy Hand	Grasp Force	25 N
IRobot Universal Jamming Gripper	Grasp Force	30 N
	Repeatability	0.01 mm
Soft Robotics mGrip	Payload	1,13398 kg
	Repeatability	0.01 mm

Figure 2-9: Universal Jamming Gripper [51]

2.5 Gripper Control and Automation

Automation is the main driving factor in manufacturing and robotics. There is a variety of automation technologies that are used in robot gripper designs. Traditionally, there are four levels of gripper automation; these are manual, electric, pneumatic, and hydraulic. Manual grippers are actuated by manual inputs such as levers, wheels and cranks. Electric grippers are actuated by electric Alternating Current (AC) AC/DC servo/stepper motors, and solenoids. Pneumatic grippers are actuated by the compression of air in a cylinder, and hydraulic grippers are actuated by a hydraulic fluid acting on a cylinder [52].

Manual grippers are the simplest to model and control as the user directly produces input. Automation achieved by electrical actuators can become complicated as the gripper design increases in complexity. Problems with modelling electrical systems arise when the operational parameters of the electrical components are not correctly specified. Electric motors are generally coupled to gearboxes, pulley or cables to drive gripper fingers. This collaboration between electrical and mechanical design is often difficult to model correctly and accurately. Control issues arise when system models are inaccurate, electrical systems are preferred to pneumatic or hydraulic systems due to the increased control offered. Pneumatic actuators do not directly offer incremental actuation; the gripper is either fully open or fully closed. Controlling the gripper force in pneumatic systems is achieved by controlling the pressure, this is often difficult to program. Another problem with pneumatic grippers is the lack of speed control; the gripper generally contacts the object at full speed which can result in the part moving if it is insufficiently fixed [53]. Hydraulic actuators have similar issues to pneumatic actuators.

Modelling the physical behaviour of pneumatically actuated soft robot grippers is a difficult task due to their elastic nature, the behaviour of the gripper is dependent on the internal structure of the gripper, and the magnitude of pneumatic pressure supplied. Advanced Finite Element Analysis (FEA) is currently being used to model the gripper behaviour; however, due to the fabrication methods of the gripper, the material structure is heterogeneous.

2.6 Machining End-Effectors

Bologa et al. [54] investigated the use of serial industrial robots in CNC milling processes. Serial robots easily attain point-to-point movements. Milling processes require precise control over the tool path; every point on the trajectory must be reached with high accuracy. Interpolation algorithms estimated intermediate points. Two critical issues with utilising serial robots for machining processes are the difficulty of path control and insufficient stiffness.

Jie and Shu-Hui [55] performed a study on the design method for the robotic drill end-effector. The proposed end-effector was developed to be used in conjunction with a six-axis serial manipulator. A disadvantage of the serial robot relates to high compliance; this causes perturbations and deformations in machining applications. Drilling processes generate thrust forces which caused vibration due to the serial robot joint configuration. A solution to this problem was suggested by altering the end-effector to a serial robot mounting platform. The clamping force should be higher than the thrust force in order to stabilise the system. A vital issue in the drilling operation was the lack of accuracy in the serial robot.

Karpiel and Petko [56] proposed an innovative parallel manipulator design for milling, Figure 2-10 (a) illustrates the design. A novel 3-RRPRR platform capable of three translational Degree of Freedom (DOF), this attributed to large payload capacity, workspace and accelerations. The manipulator design amalgamates the advantages of the Steward-Gough platform and Delta. The end-effector caters for mill spindles, and the machine was capable of handling forces of 100 N, which is sufficient for the milling of aluminium. The design employed direct actuation to the platform; this increased the payload and overall stiffness of the robot. A vital issue with parallel manipulators and machining is the sophisticated control that is required.

There are limited attempts to merge both cutting and gripping into a single system. Rahman et al. [57] had attempted to design a robot-farmer for gripping and cutting crops. The design incorporated a cutter and a two-finger robotic manipulator. The cutter subassembly consists of the cutting blade, blade holder, and gearbox mechanism that allowed the cutter to extend and retract into and out of the holder linearly. The robotic arm subassembly consisted of four parts. The proposed model cuts crops similar to a human farmer. A DC servo motor actuated the two-finger gripper. The design is presented in Figure 2-10 (b).

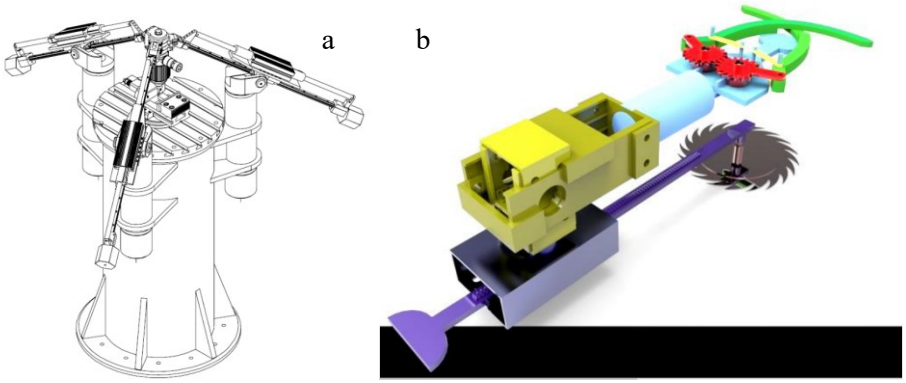

Figure 2-10: (a) 3-RRPRR Manipulator For Milling [56] (b) Farmer Robot Arm and Cutter [57]

There are many methods of handling parts after a machining operation is performed. Loading blanks and unloading machined workpieces; these operations are usually the requirement of part handling systems. In an industrial environment, automation of part handling is a norm, as such robot manipulators are used for part handling. These manipulators are predominantly serial robots with grippers attached to the end-effector. Traditionally, a manipulator robot will load a blank into the fixture of the machining centre or robot cutter. Once the machining operation is completed, a second manipulator robot will unload the workpiece, and the first manipulator robot will load a blank. Notice that two manipulator robots were required; this is due to the gripper, it is specifically suited to the geometry of the blank and the machined workpiece. There are other, less efficient methods of part handling such as manual labour.

2.7 Design Methods for Reconfigurability

New innovative approaches to manufacturing are essential for cost-effective response to market changes. The thrust of the new approach is to combine a high volume of Dedicated Manufacturing Line (DML) with the flexibility of Flexible Manufacturing System (FMS) in a manner that allows the system to act rapidly. To achieve this approach, Koren [58] defined two principles:

1. The manufacturing system and its machines must be designed with a flexible structure. This enables scalability of the manufacturing system to respond to market demands and machine adaptability to high product variety. Structure of the manufacturing system is altered at the system level and machine level.
2. The manufacturing system must be designed for a part family. The part family approach ensures customised flexibility for the production of all parts in the part family.

Flexibility is becoming increasingly important in manufacturing decision-making. It is essential to allow changes in the operating environment. FMS utilises flexibility as an adaptive response to strange situations [59]. They output different variants of products with changeable volume and mix [60].

According to Black and Kohser [61], a significant amount of the cost of manufacturing and assembly is determined during the design phase. Furthermore, approximately 70% of the life-cycle cost of a product is planned during the design phase. Choices in design dictate materials, fabrication methods, material handling and inspection techniques.

According to Cardin [62], the design of engineering systems for flexibility is not a simple task. Pre-requisites include guidance from research experience and industry applications. There is a lack of certainty

in identifying where to focus the design effort, how much flexibility is worth and costs, and how much flexibility is enough. The difficulty has led to the development of systematic procedures to aid engineering designers.

According to Black and Kohser [61], early design decisions determine about 60% of the cost, and all activities up to the start of full-scale development determine about 75%. Later decisions can make only minor changes to the result unless the design of the manufacturing system is changed.

Reconfigurability affects design decisions in several ways. According to Lee [63], adequate selection of components and manufacturing processes for system reconfiguration reduces the complexity of the design and the number of resources needed. The structure of components and manufacturing systems is closely linked to the ability of the manufacturing system to be reconfigured. Therefore, the structure of components, and the manufacturing system as well as resources, should all be considered at early design stages. Lee identified that system reconfigurability, serviceability and disposability are generally not determined early in the design process. The link between the structure of components and the manufacturing system should be investigated for the design to be reconfigurable.

Furthermore, Lee motivated that these components and manufacturing systems should incorporate minimum cost and physical movement of equipment for reconfiguration. The research highlighted three key areas of designing for reconfigurability; these were the design of manufacturing systems for reconfigurability, the design of components for reconfigurability, and integrated design of components and manufacturing systems for reconfigurability. Many reconfigurable designs fail due to the separation of component design and manufacturing system design.

Due to the dynamic nature of the consumer demands and its direct influence on the global market, manufacturers have no choice but to evolve with technology to meet requirements. Mehrabi et al. [64] have identified several factors which are concurrently contributing to these consequent market fluctuations. These include globalisation of the economy, saturated market and rapid advances in technology. This has resulted in an unpredictable market with reduced product cycles. Appropriate business strategies together with relevant manufacturing technologies, allow manufacturers to respond timeously to market changes.

The reconfigurable manufacturing system is able to meet the requirements of market-oriented manufacturing. The design architecture of RMS is modular; this means that reconfiguration is used as a strategy to adapt to market demands. These technologies give the manufacturing system the ability to adjust timeously to new production models, precise capacity requirements, and the ability to integrate new technologies.

Corves et al. [65] maintained that accuracy and repeatability of manufacturing and assembly operations must increase while improving quality and productivity. The gripper performs grasping operations and provides the machine-to-object interface. Most automated systems utilise guidance mechanisms or versatile robots which are customisable to perform various tasks without changing their architectures or dimensions. The type of gripper used dictates the size and shape of the object that can be handled. Industrial grippers are predominantly designed to perform specialised grasping tasks with known object specifications. These grippers are therefore limited in terms of versatility and dexterity to handle a wide variety of objects.

Most industrial grippers need to be changed out depending on the workpiece and task, this directly decreases production rates which increases costs. The solution to the problem of changing grippers is the reconfigurable gripper. As the name suggests, the reconfigurable gripper has the ability to assume different configurations depending on the task. Reconfigurable grippers enable manufacturers to reduce robot downtime by not having to change grippers per task; hence production rates increase.

2.8 Reconfigurable Robotic Grippers

Much research has been conducted to develop reconfigurable grippers. Different examples of reconfigurable grippers are reviewed in order to establish the state of the art in reconfigurable gripping systems. Zhang et al. [66] proposed a compensatory grasping design for a parallel jaw gripper. The research aimed to reposition the part to the required orientation by rotation during grasping. The design utilised four tips, two on each of the parallel jaws of the gripper. Ease of reconfiguration to handle different industrial parts was an advantage of compensatory grasping.

Riedel et al. [65] developed an adjustable gripper as a reconfigurable robot with a parallel structure. The work proposed a robot system which combined an adjustable gripper with a parallel manipulator. The operation consisted of four individual phases. The main idea was to generate a closed-loop kinematic chain which was formed by the object and the robot's fingers. Figure 2-11 (a) shows the developed parallel reconfigurable gripper design.

Molfino et al. [49] proposed a low-cost reconfigurable gripper for assembly and disassembly tasks. The gripper mechanism was required to grasp both prismatic and cylindrical shape families. Two parallel fingers generated planar grasp while the third finger was fixed and allowed cylindrical geometries to be grasped. The gripper has three degrees of freedom. The parallel fingers were actuated by pneumatic cylinders. The proposed gripper design is shown in Figure 2-11 (b).

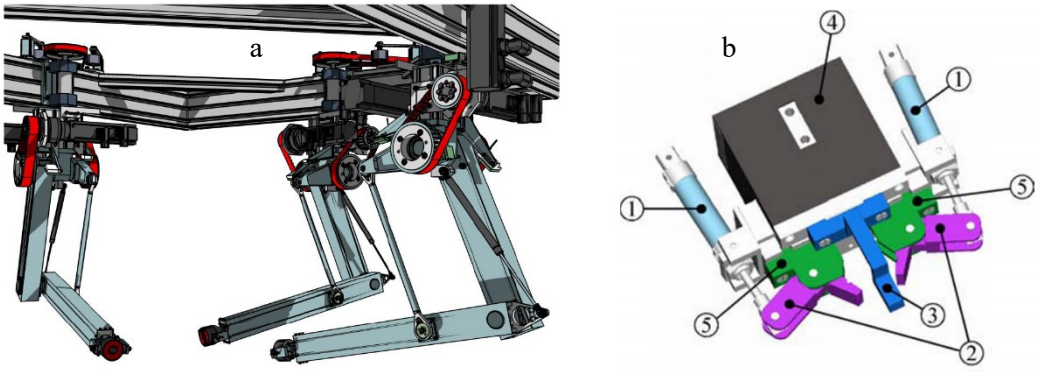

Figure 2-11: (a) Parallel Reconfigurable Gripper [65] (b) Multipurpose SPI3 Gripper [49]

Ziesmer [48] worked on a reconfigurable end-effector for in-hand manipulation without finger gaiting or regrasping. The proposed gripping mechanism made use of the concept of part-finger interface. The key to this concept existed when the interfaces were modelled as joints; this means that the end-effector and part form a closed-loop mechanism. As a result, the part-finger interface allowed reconfigurability between hard finger contacts and planar contacts. Actuation of the gripper mechanism was provided by two two-position linear actuators. Figure 2-12 (a) presents the prototype of Ziesmer's gripper design.

Dottore et al. [67] proposed a tendon-driven modular continuum arm with soft reconfigurable gripper. The reconfigurable gripper was underactuated; it consisted of four soft fingers linked to an independent actuation module. The gripper fingers were mounted on parallel discs at 180° intervals; this means that there are two fingers per disc. The discs are concentric about a centre axis, rotation of the discs was effected by a geared DC motor. The cables are actuated by geared DC motors which controlled the finger movement. The gripper mechanism is illustrated in Figure 2-12 (b).

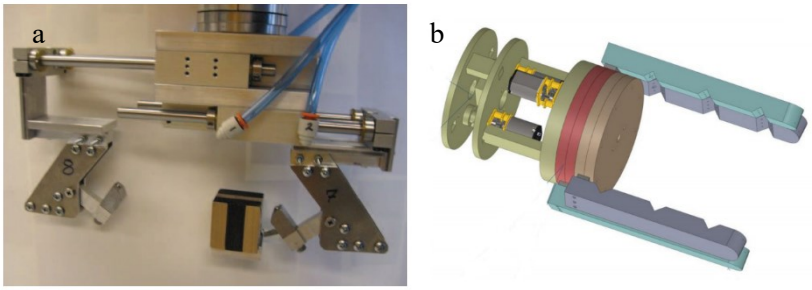

Figure 2-12: (a) Ziesmer Reconfigurable Gripper Prototype [48] (b) SIMBA Soft Reconfigurable Gripper [67]

Makris et al. [68] presented a reconfigurable gripper for dextrous manipulation in flexible assembly. The design was intended to result in a high-speed multi-fingered gripper. The gripper consists of three fingers with a total of eight DOF. The gripper attained a wide range of grasping modes, the centripetal grasp, the parallel grasp, and the encompassing and pinching grasps. Figure 2-13 presents these different grasp orientations. Each of the fingers received actuation from a motor and is directly coupled to the output shaft of the motor. The fingertips are also motor-driven at the tendons.

Figure 2-13: Grasping Poses [68]

According to Yeung [69], a gripper must have multiple fingers with reconfigurable positions to be capable of handling various shaped objects. Furthermore, each of the fingers must have movable joints so that the finger is able to conform to the shape of the object. The design of a reconfigurable gripper should be simple, light-weight and incorporate position correction. Simplistic designs reduce cost and increase reliability while maintaining a minimalistic design with fewer parts and mechanisms, lowers the manufacturing cost and chance of failure. The robot payload, moments generated by the end-effector, and inertia due to the change in velocity of the gripper fingers, all determine the magnitude of components. Position-correction removes the need for accurate object location and pre-planning grasps.

Methods of reconfigurability that can be taken forward in this project include a reconfigurable robotic design and a reconfigurable gripper design. The project demands reconfigurability as the robot must adapt itself to grasping tasks as well as machining tasks.

Cipra et al. [70] investigated a reconfigurable and foldable hexapod robot inspired by Origami, HexaMorph. The HexaMorph is unlike most modular robotic systems with tree or open-chain architecture as it does not have a central body. It has a closed-loop form which permits the robot to seamlessly envelope itself. Since there is no interconnection of modules, the robot reconfigures its orientation by actuating servo motors. The two main methods of reconfigurability for motion are self-deploying and locomotive squirming.

Figure 2-14 shows a time-lapse of the HexaMorph in motion.

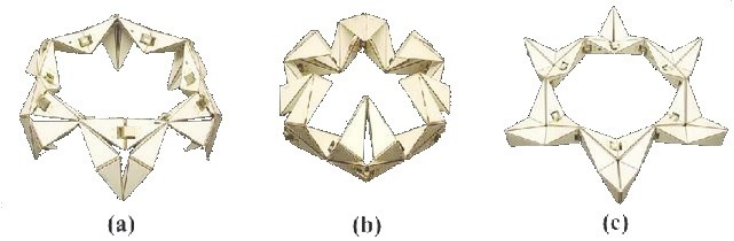

Figure 2-14: HexaMorph Time Lapse [70]

A single reconfigurable robot for part handling and machining tasks has not been realised in industry to date. The critical method of reconfigurability in this design is the transformation of the robot to perform different tasks. In the proposed design the gripper mechanism is reconfigurable as it is able to grasp and retract.

Figure 2-15 illustrates the historical developments of end-effectors. da Vinci designed the first sophisticated robotic arm in 1495 with four degrees-of-freedom and an analogue on-board controller supplying power and programmability [71]. Marvin Minsky had developed the Tentacle Arm in 1968 at MIT [72]. The arm received its name based on its movement like an octopus. It comprised of twelve joints and was designed to move around like an octopus. The arm was controlled by a PDP-6 computer and was powered by hydraulic fluids. The arm was designed to be mounted on a wall and could lift the weight of a person. The late 1970's offered a variation, the two fingered angle gripper. Each of the two fingers swings on a pivot point, closing like a gate or lobster claw on target objects. The Stanford Hand was built in 1983 and is equipped with tactile sense contacts on the fingers which are to imitate the human sense of touch [73]. The gripper was equipped with just three fingers but could still manipulate the work piece in its hand. Air-powered grippers are those that are not fingered types, generally utilize suction and flexible cups to grasp and are used to handle flimsy and breakable objects. Suction grippers are installed at the ends of regular robot arms or alternatively at the bottom of ceiling-mounted delta robots. Robotic hands have been used in industry but have been subject to two and three finger grippers. The timeline shows that flexible grippers are becoming increasingly popular over the recent years due to the advancements in soft robotics.

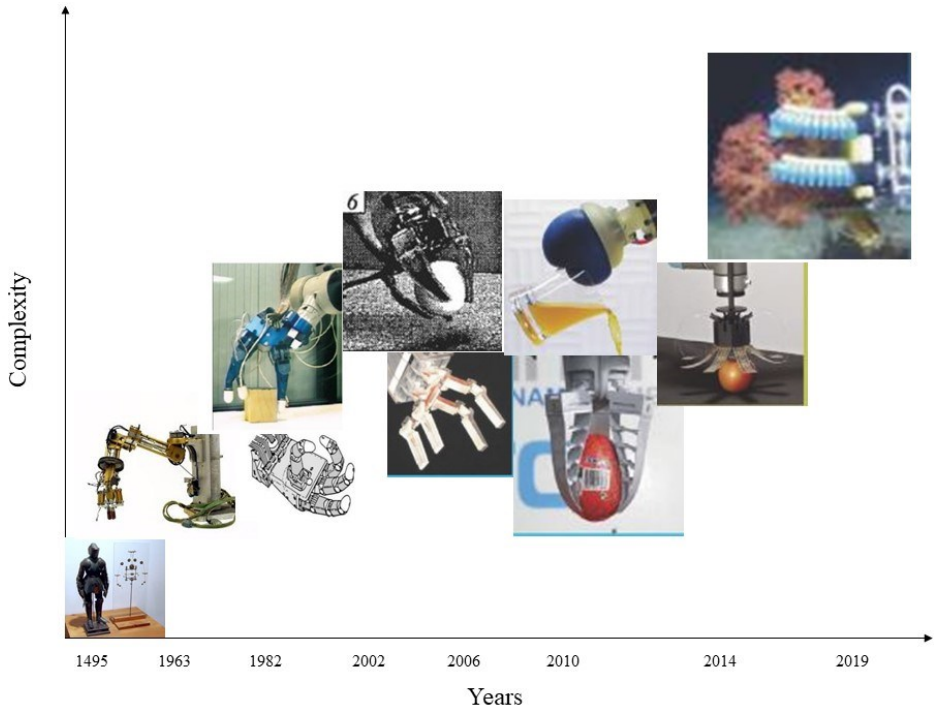

Figure 2-15: Graphical Timeline of Historical Developments of End-Effectors

2.9 Comparable End-Effectors

End-effectors that are capable of milling are not readily available for small scale applications. Therefore, it would be meaningless to compare powerful machines to the developed prototype. Three milling spindles are instead compared; these spindles require additional mounting mechanisms to be coupled with a robot. The metrics of three 3-finger adaptive grippers are compared to the metrics of the developed gripper.

2.9.1 Comparable Machine Tools

1. The Dremel 4000 is a lightweight, compact rotary tool. It is available globally and has the power requirements for milling softwoods, plastics and organic material. Keating [74] used the spindle in his doctoral research on the use of robotic arms in digital fabrication. Figure 2-16 (a) presents the tool in action milling a pumpkin. The tool has proprietary tooling with many small tools and end mills available.
2. The Kress 1050 FME-1 is a popular mill spindle in the small mill machine market. The German-engineered spindle produces high power and precision, given its size and price. The spindle is equipped with an ER16 collet system and does not require additional drivers to run. Figure 2-16 (b) presents the spindle mounted on a STEPCRAFT three-axis machine [75].
3. ISEL Germany AG ISA500 spindle motor is a high precision, compact machine tool spindle. The integral AC asynchronous motor is coupled to a three bearing spindle shaft. The spindle is equipped with ER11 collet; the clamping range of tool is 1 mm – 7 mm. This spindle is used in high precision, compact applications. Figure 2-16 (c) presents the spindle [76].

Figure 2-16: Mill Spindles (a) Dremel 4000 [74] (b) Kress 1050 FME-1 [77] (c) ISA 500 mill spindle [76]

2.9.2 Comparable Grippers

1. The Model O is an open-source derivative of the RightHand Robotics' gripper design, the result of the collaboration between Yale, Harvard, and iRobot. It includes three independently driven, underactuated fingers, as well as a fourth actuator that controls abduction and adduction. Figure 2-17 (a) presents the Yale OpenHand Model O Gripper [78].
2. The RobotiQ 3-Finger adaptive gripper is the best option for maximum versatility. It is well-suited for manufacturing and robotic research. Good shape adaption ensures a solid grip. With force, position and speed control for each individual finger, the RobotiQ 3-Finger gripper is one of the most advanced industrial three-finger adaptive grippers on the market [79]. Figure 2-17 (b) presents the gripper.
3. DH grippers are designed for multi-purpose gripping applications, which can pick objects of different sizes and shapes without changing the end-of-arm tools. Figure 2-17 (c) presents an image of the gripper. The gripper improves the gripping and manipulating capability of robots used in different scenarios such as electronics and automobile [80].

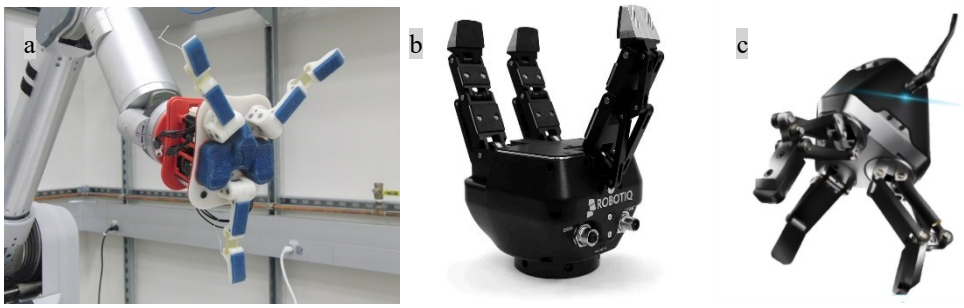

Figure 2-17: Three Finger Grippers (a) Yale Model O Gripper [81] (b) RobotiQ 3 Finger Adaptive Gripper [82] (c) DH Robotics DH3 Gripper [83]

2.10 Chapter Summary

The literature review was insightful; it brought up many more questions than answers in terms of applicability to the project. The concept of designing a reconfigurable end-effector for both part-handling and machining is not yet a popular topic for researchers. Currently, separate industrial robots are used for each operation. Serial manipulators are used extensively in the manufacturing industry.

Robotic end-effectors are becoming increasingly complex as the demand for reconfigurability grows in the manufacturing industry. Manufacturers are widely adopting robotic systems to fast-track production. End-effectors are traditionally dedicated to perform a specialised function. If a process changes, these traditional

end-effectors need to be replaced or modified. Robust grippers such as the Schunk MPG 16 pneumatic gripper reviewed in Section 2.3 will always have their place in the industry. However, grippers such as the RobotiQ Adaptive are fast becoming a norm in many manufacturing circles. These grippers offer process flexibility and adaptability, both factors are becoming critical as manufacturers push to keep up with evolving customer demand. In this research, an adaptive, flexible gripper capable of multi-geometry grasping is desirable.

In conjunction with gripping end-effectors, robots capable of machining were reviewed. The interest of machining with robotic manipulators is becoming increasingly popular in industry. These manipulators require dedicated end-effectors that are capable of material removal. Such end-effectors are large, heavy and are not reconfigurable.

The following chapter presents the initial requirements, specifications and conceptual designs for the reconfigurable robotic end-effector. Methods of reconfiguration are investigated, and subsystem concepts are presented.

Chapter 3 Conceptualisation of Reconfigurable Architecture

3.1 Introduction

This chapter covers the conceptualisation process of reconfiguration schemes for the Reconfigurable Robotic End-Effector (RREE). Quality Function Deployment (QFD) is used to determine design requirements, specifications and ranking of significance. Reconfigurability largely influences initial customer requirements. Customer requirements define RREE functional requirements. The functions of the RREE are defined and desirable characteristics presented. Subsystem requirements based on RREE functional requirements are defined. The methodology used for the synthesis of architectural concepts presents guidelines for the design process. Three mechanisms of reconfiguration highlight the development of concepts. Machine tool spindle and gripper concepts based on integrated reconfigurability provide directions for system embodiment design. Decision matrices aid in the selection of the final reconfigurable mechanism and gripper concept. Selection of final machine architecture is conducted based on the extent of success and practicality. The configuration of RREE and its subsystems provides a detailed representation of its operation. Subsystem specification based on QFD House of Quality (HoQ) requirements concludes the conceptualisation of the RREE.

3.2 Definition of Initial RREE Requirements

Constraints of the reconfigurable architecture are threefold. The first constrain originates from the usage of the robot. The RREE functions as an end-effector as such, it cannot operate when incorrectly coupled to a manipulator. Attachment criteria for robotic manipulators yield insights in design. That is, PKMs and SKMs. The second of which stems from the functionality of the robot. The robot must perform two primary functions based on this constraint. That is a machining operation and a part handling operation.

The machining operation taken forward in this research was the vertical milling process. As discussed in the literature, milling is a broadly utilised form of machining in subtractive manufacturing. More specifically, end-milling of non-ferrous metals was desirable for this research. More specifically, the down milling process will be taken forward as the machining operation for the RREE.

Part handling systems are used frequently in the manufacturing industry. As reviewed in the literature [84] [21] [40], there are many forms of grippers, ranging in complexity and application. Most industrial grippers perform a specific function for an object geometry at high frequency. While robotic hands are difficult to control and implement in manufacturing environments. Multiple link three-finger grippers form a reasonable “middle ground”. Thus, an underactuated multi-link three-finger robotic gripper is suitable for this research.

Secondly, the robot must possess characteristics of RMS on a machine-level as defined in the literature [58]. The responsiveness of a system depends on the transformability of design for structural and software changes. Scalability and adaptability are critical factors in the design of the RREE.

The robot must perform a secondary function based on this constraint. Reconfiguration of structural components was necessary to achieve process adaptability. Based on this constraint and the primary

functions, the design of a Reconfiguration Mechanism (RM) which alters the structure of the robot was required.

QFD enhanced design development based on the requirements of prospective users of the reconfigurable robot. The first step of QFD involved the identification of customer requirements. Customer requirements stem from the literature review and consultation with machine builders. Table 3-1 presents the input requirements of QFD. Weighting assignment is based on the significance of each requirement and was given a score from 0 to 10, 10 being critically important. Refer to Appendix A for the complete QFD House of Quality diagram.

Table 3-1: QFD Customer Requirements

Demanded Quality/Customer Requirements	Weight/Importance	Maximum Relationship Value in Row	Relative Weight
Lightweight	8.0	9.0	10.5
Powerful Gripper	5.0	9.0	6.5
Grasp objects of multiple geometries	8.0	9.0	10.5
Compact design	7.0	9.0	9.2
High-precision machining of aluminium 6xxx	8.0	9.0	10.5
Low cost	7.0	9.0	9.2
Compatible with SKMs and PKMs	9.0	9.0	11.8
Reconfigurable design	9.5	9.0	12.4
Design for manufacturability	7.0	9.0	9.2
Scalable architecture	8.0	9.0	10.5

While all of the customer requirements listed in Table 3-1 contribute to the design – not all of these constitute the same importance. The goal system behaviour requires the end-effector to be reconfigurable, and compatible with popular serial and parallel robotic manipulators – these characteristics assumed the highest weights. The mass of the end-effector dictates the movement characteristics of the device, therefore a rating of 8.0 was assigned. Equally important to mass are part flexibility, precision machining of non-ferrous metals and scalability of architecture. The end-effector was required to have a compact design, this contributes to the overall aesthetic and usability of the device – therefore a weight of 7.0 was justified. The robot was to be designed to be as low-cost as possible with design for manufacturability cognisant from the onset. These two requirements were equally important to the compact design and therefore received a congruent weight. The least important customer requirement was assigned a weight of 5.0 due to the "proof of concept". This research derived a unique end-effector, therefore the extent of grasping power was not of critical importance.

Based on these requirements, three subsystems were defined. The first subsystem is the Machine Tool (MT); this system performs the specified cutting operation. The second subsystem is the Gripper Unit (GU); this system performs the part handling operation. Lastly, the third subsystem is the Reconfiguration Mechanism (RM); this subsystem unifies both the systems mentioned above. It satisfied the functional requirement of reconfigurability that is characteristic of the RREE. Two architectural requirements of the reconfiguration mechanism are listed below.

- Mechanisms must be designed to get the tool out of the gripper space during part handling.
- Mechanisms must be designed to get the gripper out of the cutting space during machining.

In order to achieve a machine capable of both processes, the reconfiguration system must provide individual environments for each operation. The gripper should be unhindered by the machine-tool and vice-versa. Identification of quality characteristics ensured the satisfaction of customer requirements. Figure 3-1 presents fifteen engineering metrics identified from customer requirements.

Column #	1	2	3	4	5	6	7	8	9	10	11	12	13	14	15
Direction of Improvement: Minimize (▼), Maximize (▲), or Target (x)	▼	▼	▼	▲	▲	▼	▼	x	x	▲	▼	▼	▼	▼	▼
Quality Characteristics (a.k.a. "Functional Requirements" or "Hows") / Demanded Quality (a.k.a. "Customer Requirements" or "Whats")	Cost of Gripper	Weight of Gripper	Repeatability of Gripper	Grasp Volume	Payload of gripper	Cost of Machine Tool	Weight of Machine tool	Runout	Spindle Speed	Spindle Torque	Spindle Power	Maximum Tool Diameter	Weight of End-Effector	Reconfiguration Time	Volume of End-Effector

Figure 3-1: QFD Functional Requirements

The functional requirements were assigned a direction for improvement. They are either minimised, maximised or targeted. Refer to Appendix A for the complete QFD House of Quality diagram.

3.3 Reconfiguration Concepts

The definition of system structure required synthesis of reconfigurable architectures. The conceptual design process of three subsystems utilised reconfigurable mechanisms. There are three subsystems, machine-tool for metal cutting, gripper for material handling, and linear actuator for reconfiguration of the end-effector. The machine-tool design was considered at the onset as this subsystem maintains a significant portion of the goal system behaviour. The gripper system was integrated into the machine-tool system through the linear actuator. Reconfiguration of both systems was fundamental in the design. Figure 3-2 outlines the conceptualisation process of the robotic end-effector.

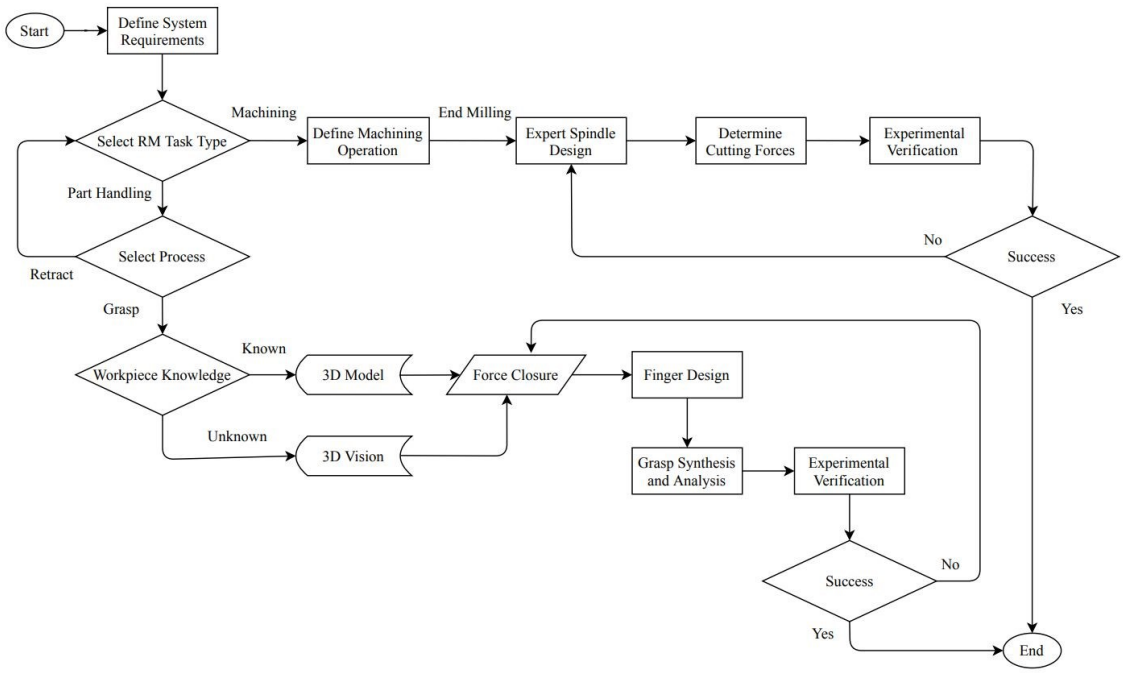

Figure 3-2: Conceptualisation Flowchart

3.3.1 Reconfigurable Design Methodology

According to Farid et al. [85] and Amro et al. [86], there are four requirements for reconfigurability. Requirements taken forward in the design methodology of the RREE, are described as:

1. Definition of the system and its boundary.
2. Definition of system configuration, this is equivalent to system structure.
3. The description and rationale of the system. Based on a desired set of reconfigurations.
4. Description of time/cost/effort of potential reconfigurations.

System structure, as defined by Oliver et al. [87], is the parts of a system and the relationships amongst them. A three-step approach was developed. Firstly, a list of all the components that form the system structure. The portion of goal system behaviour undertaken by each component was defined. Lastly, the interconnectivity of these components concluded the process.

3.3.2 Directly Coupled Platform Concept

Figures 3-3 and 3-4 present a configuration that aimed to use the robotic manipulator to reconfigure the end-effector. The mounting platform is rigidly coupled to the SKM or PKM, the machine tool and gripper subsystems are mounted onto this platform. This concept did not utilise a dedicated reconfiguration mechanism. The robotic manipulator moves the device for machining and gripping on one standard axis. Vertical reconfiguration was not possible in this design due to the shared drive shaft.

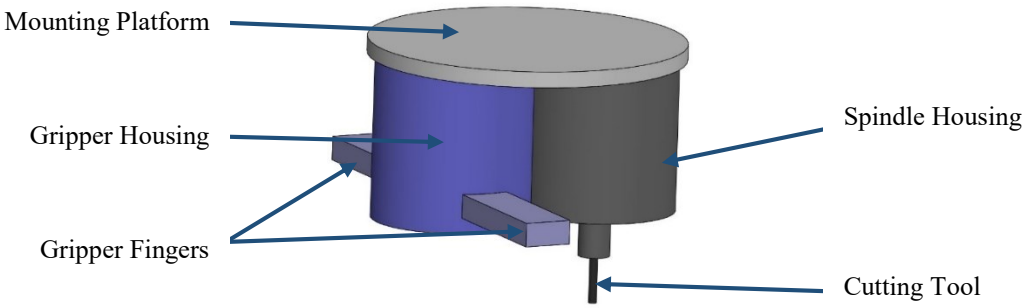

Figure 3-3: Schematic Side View of Single Motor Concept

The component layout is presented in Figure 3-4. A single motor drives the machine tool and gripper systems. The gripper system requires slow speed (100 RPM) and high torque for precise positioning of the gripper fingers. Precise control of such a mechanism will be difficult to attain with the drive system of this concept. The cutting system requires a high speed (12000 RPM) and low torque for the milling of aluminium.

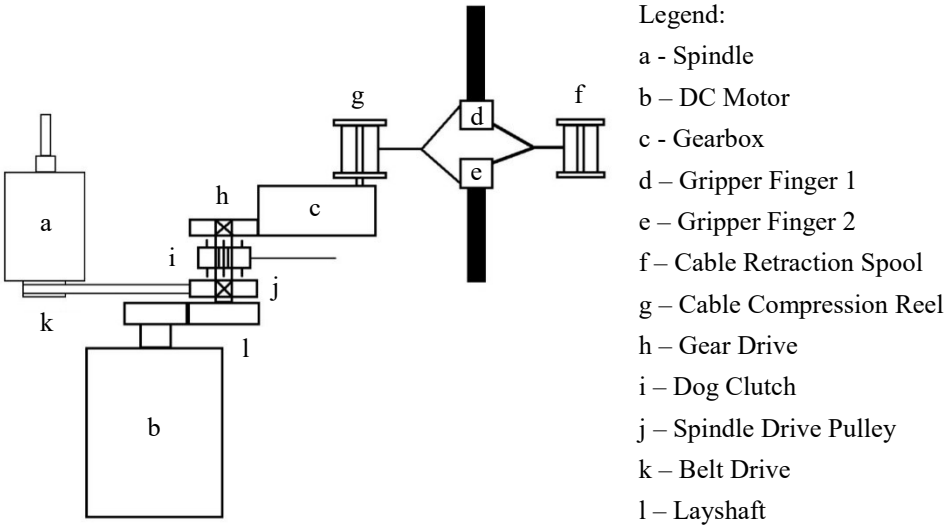

Figure 3-4: Component Layout of Single Motor Concept

A vital disadvantage of this configuration is the need for custom drive components and the high possibility of malfunction. Since both systems utilise the drive from a single motor, if the motor fails, the device stops functioning completely. The architectural configuration of the concept is presented in Figure 3-5.

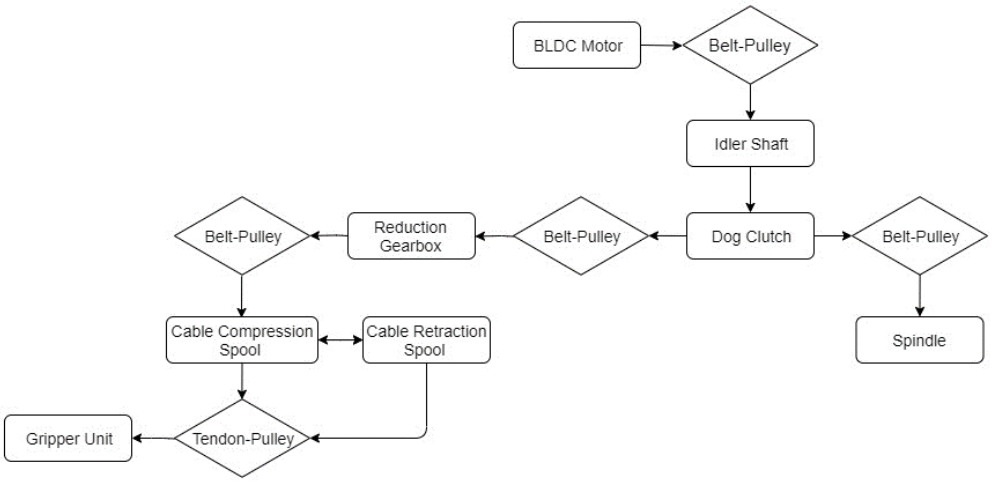

Figure 3-5: Schematic Diagram of Single Motor Concept

3.3.3 VAP: Fixed Gripper Concept

The machine tool spindle is used as the support structure of the end-effector due to its rigidity. System embodiment was utilised to position the spindle directly below the vertical axis of the PKM or SKM end-effector. Positioning the spindle along this axis permitted ideal force transfer through the robotic manipulator, which will reduce X-Y planar force transfer. A Vertically Actuated Platform (VAP) moves the machine tool but not the gripper; this permits the independent operation required for the design. However, the rigidity of the actuation mechanism will determine the effectiveness of the machine tool. Fixturing of the machine tool on the actuated platform will require the platform to have a large mass. This will result in increased weight of the end-effector and evades the light-weight specification. An additional problem characteristic of these results in the design of the spindle. If the spindle is not of the integral type, the MT drive motor will have to be actuated with the spindle.

3.3.4 VAP: Fixed Machine Tool Concept (Two Motor)

The method of reconfiguration utilised the vertical motion to transport the gripping system to the work-level. The gripper process does not require as much resolution as the machine tool. This is true due to the operational characteristic of underactuated gripper mechanisms. A fixed machine tool allowed for a rigid coupling and support of the machine tool spindle. The drive of the spindle may be of any type. There is no restriction due to the static nature of the machine tool. The architecture presented in Figure 3-6 satisfied the functional requirements of RREE design prescribed in Section 3.2.

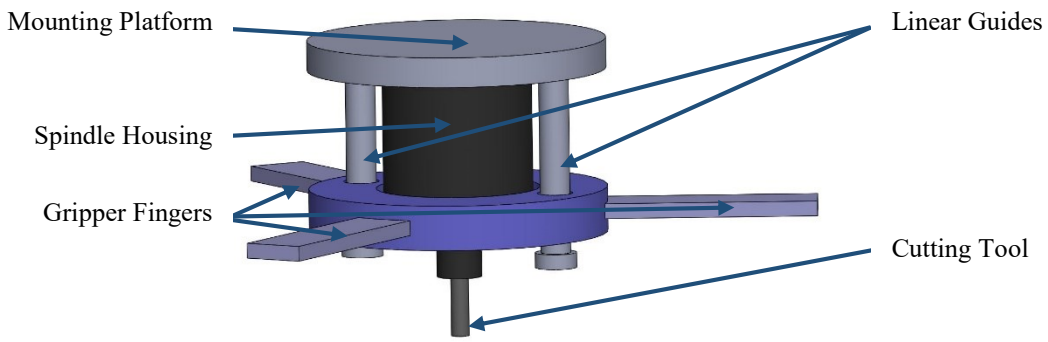

Figure 3-6: Schematic Side View of VAP

The dual-motor architecture is presented in Figure 3-7. The linear actuator creates the vertical displacement required to move the gripper platform.

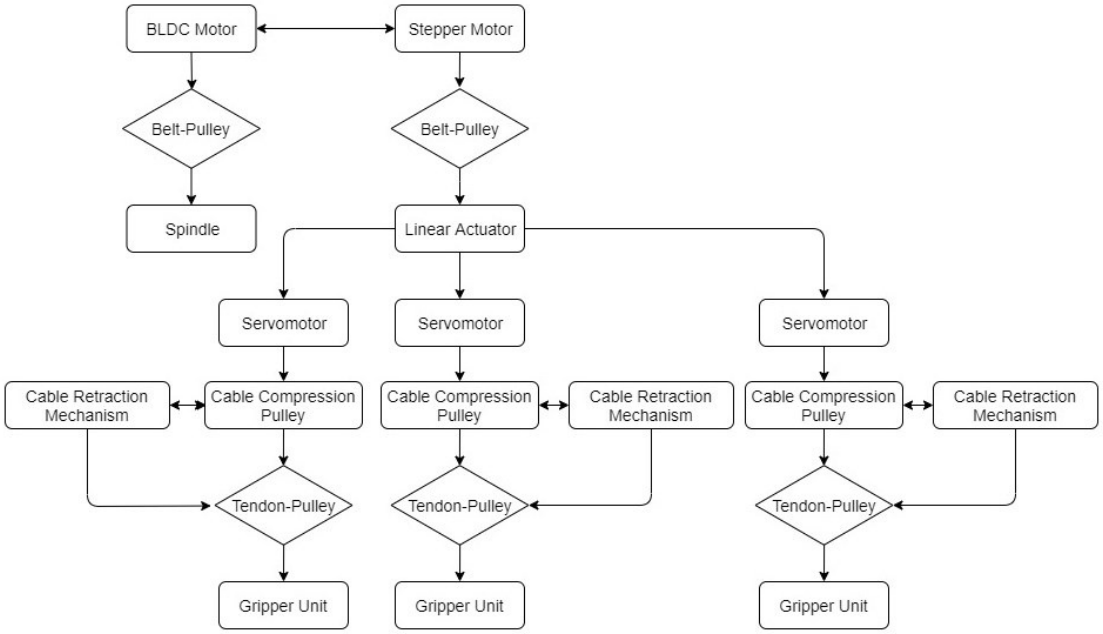

Figure 3-7: Two Actuator VAP Component Architecture

3.3.5 VAP: Fixed Machine-tool (Five Motor) Concept

Lastly, a five actuator architecture which utilises five electric motors is presented. A stepper motor is required for the linear actuation of the vertically moveable gripper platform. The stepper motor will provide the fast but precise actuation required to reconfigure the system. These motors are cost-effective, provide significant torque and are easily integrated and controlled while maintaining a lightweight and rigid design. A high-speed brushless DC motor is required for the machine-tool. Three compact servomotors are used to drive each of the gripper fingers independently. The proposed design incorporated both part handling and machining features on one end-effector. Reconfiguring the end-effector was accomplished by a linear actuated platform. The platform is extended toward the work surface to deploy the gripper and retracted to deploy the machining spindle.

The end-effector consists of three subsystems, the machine tool subsystem for metal cutting, the gripper for material handling and the reconfiguration subsystem for switching between these functions. An

overview of the system architecture is presented in Figure 3-8. There are five distinct levels of the design; the first level is the attachment surface to the robot through a bolted coupling. The second level is the central platform, upon which the reconfiguration subsystem and spindle subsystem are attached through a bolted coupling. The third level represents a moveable platform onto which the gripper subsystem is attached. The gripper fingers are designed to be actuated from the base of each finger mount. The fourth level consists of the gripper fingers and the tendon-driven actuation mechanism. The fifth level represents the gripper palm, which functions simultaneously as a structural part of the reconfiguration mechanism and provides a contact surface for gripping operations.

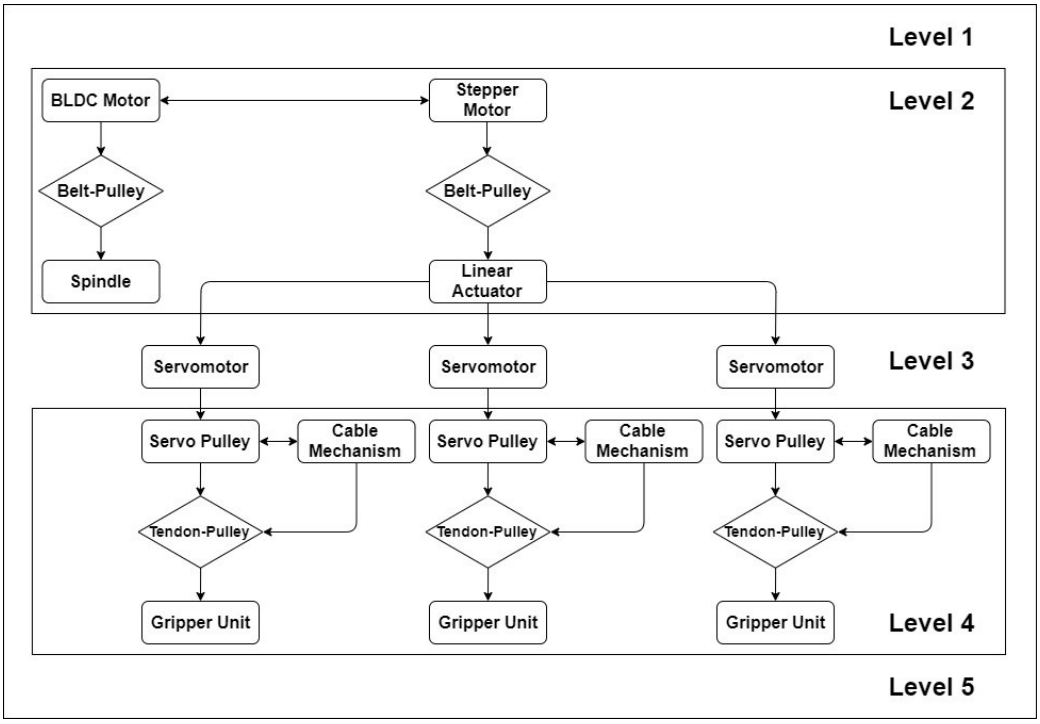

Figure 3-8: Architecture of RREE

Reconfiguration of the machine was accomplished utilising a linear actuator. The linear actuator transports the gripper subsystem between both ends of its stroke length. This allows the system to reconfigure between two states. These states are defined as reconfiguration modes.

- The first mode of reconfiguration is attained when the linear actuator is at zero stroke length.
- The second mode of reconfiguration is attained when the linear actuator is at maximum stroke length.

The rationale for these two reconfigurations was presented throughout this chapter. It is based on the functional requirement of reconfigurability defined in Section 3.2. Additionally, each of the two modes are characterised by the operation they permit. These are:

- Machining occurs at the first mode of reconfiguration.
- Part handling occurs at the second mode of reconfiguration.

The efficiency of the linear actuator constrains the reconfiguration time. However, given the compact specification of the RREE, the stroke length of the linear actuator should not exceed 100 mm. Electric screw actuators provide rapid linear motion, and reconfiguration time is envisioned to be in a matter of seconds.

The proposed design incorporated both part handling and machining features on one end-effector. There are five distinct levels of the design. The first level contains the mounting surface that attaches the end-effector to the robot through a bolted-joint coupling. The second level is the central platform, upon which the reconfiguration mechanism, spindle motor, stepper motor and spindle are attached through-bolted joint couplings. The middle level represents a reconfigurable platform onto which the gripper-finger modules are attached. The gripper fingers are designed to be actuated from the base of each respective finger mount. The fourth level forms support bracket for the linear actuator; this plate is rigidly mounted to the spindle. The final level represents the gripper palm; this surface performs two functions simultaneously. It is a structural part of the RM and provides a contact surface for gripping operation. The developed concept is presented in Figure 3-9. The concept employs a vertically actuated gripper subsystem.

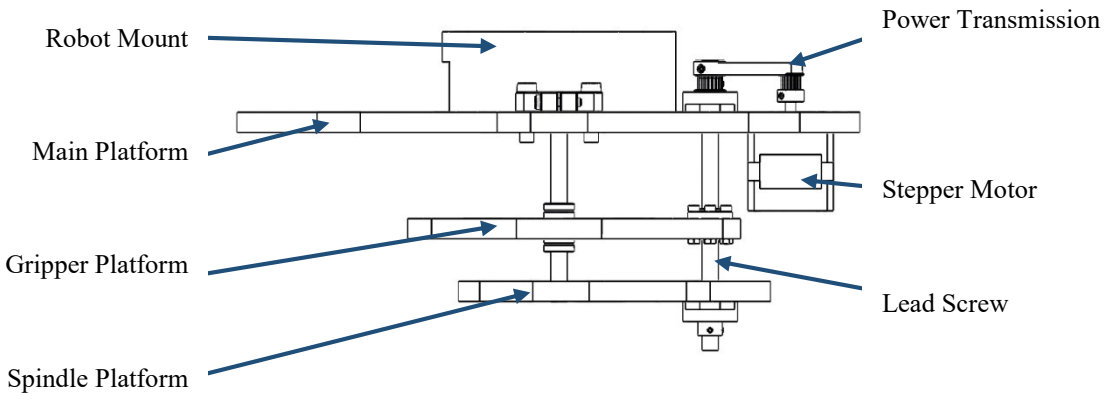

Figure 3-9: Sketch of Reconfigurable Concept

3.4 Spindle Concept

The expert spindle design method [88] was used in conjunction with methods of reconfigurability to generate the conceptual model. The method presented in Section 4.2 indicates the configuration of Machine Tool (MT) design. In general, MT is composed of the spindle shaft, bearings, bearing housing, electric motor, tool system, drive system and cooling system. The machine-tool must be compact, light-weight, rigid and capable of machining Aluminium 6xxx. Figure 3-10 presents a sketch of the conceptual model of the spindle assembly, electric motor and drive system. The concept is scalable, low-cost, compact and light-weight. Most importantly, reconfigurability is central to the design. The spindle is fixed on a base, and the motor is mounted to the same base. The concept utilises universal E collet Rego-Fix (ER) collet tooling. The spindle shaft is supported by two stiff, high-speed precision bearings. The system is air-cooled as the motor is outside the spindle.

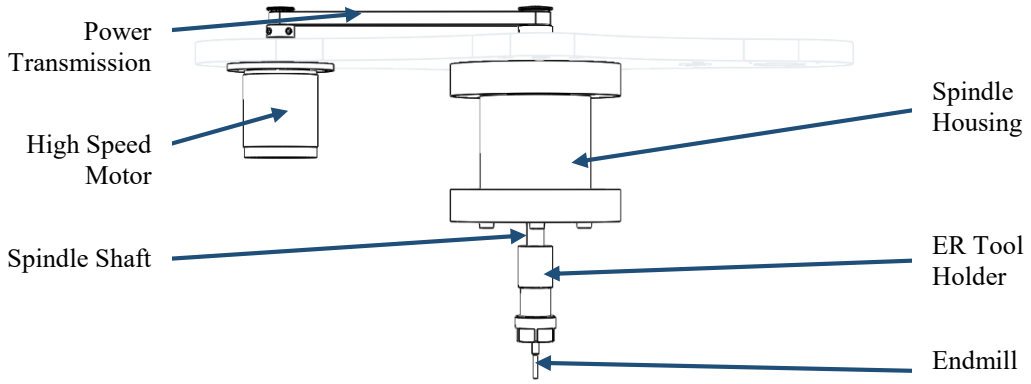

Figure 3-10: MT Concept Sketch

3.5 Gripper Concepts

The gripper was based on flexible multi-tendon fingers. These fingers aimed to mimic the prehensile capacity of the human finger. Each link is dense; cavities exist for the attachment of the tendons. Initially, rubber tendons were used in the fabricated finger prototype. Rubber creates the flexure required for the finger to conform around the object. The finger is cable actuated, a high strength, lightweight cable starts at the external link, passes through the middle link and base link through a series of guides located within all the links. The working principle of the first end-effector design is illustrated in Figure 3-11. The gripper fingers are attached to the end-effector. DC servomotors drive the cables in this approach to the concept.

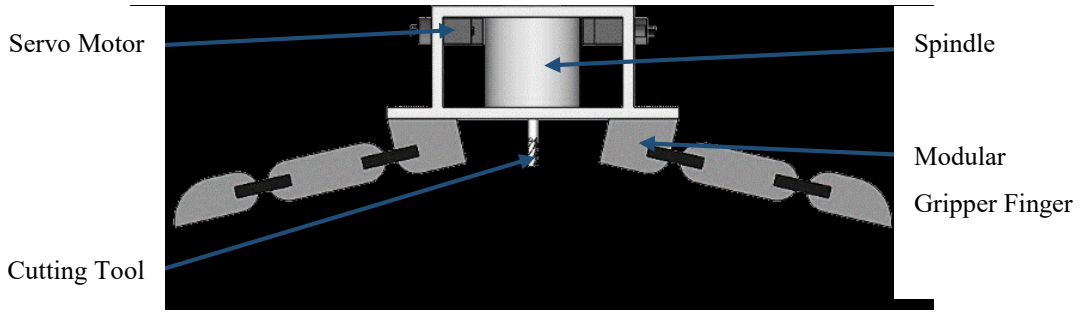

Figure 3-11: Tendon Gripper Concept Model

Grasp mode of a gripper is an important criterion that is considered at the onset of design. It specifies the scope of gripping formats that the mechanism must provide. Given the specifications of the research, two grasp modes are required. The enveloping grasp and pinch grasp, priority was given to the enveloping grasp. Figure 3-12 presents a standard two-finger multi-link gripper. Two revolute planar mechanisms provide both grasp modes. Enveloping grasp contains the volume of the object within that of the gripper fingers; it is presented Figure 3-12 (a). All links in the mechanism maintain contact with the object. The pinch grasp mode in Figure 3-12 (b) allows for the grasping of smaller objects. These smaller objects require significantly more grip force as compared to the enveloping grasp. This is due to the decreased contact area that the gripper and object have.

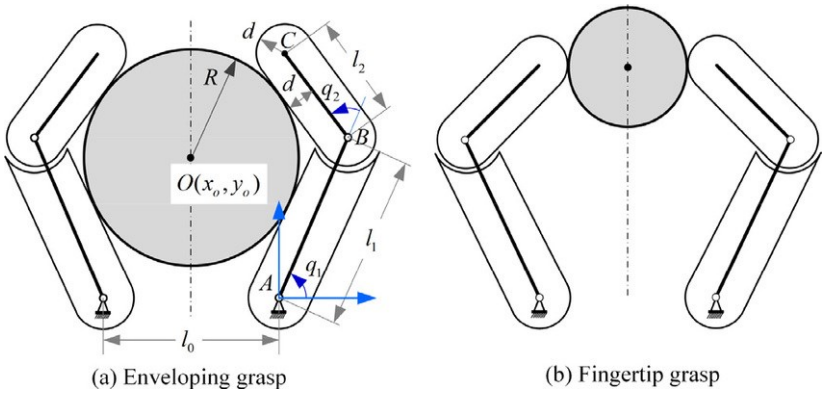

Figure 3-12: Two Grasp Modes [89]

3.5.1 Dual Rubber Joint Concept

The first attempt at the finger design made use of three links. The base link is attached to the end-effector and forms the base of the entire finger assembly. Two further links provide the required compliance around objects. Figure 3-113 shows the finger in (a) retract pose and (b) grasp pose. All of the joints in this design are flexible rubber joints. While the flexible rubber tendons provide a significant degree of compliance, it generated uncontrolled twist about the length of the finger. This twist resulted in failure to grasp objects properly.

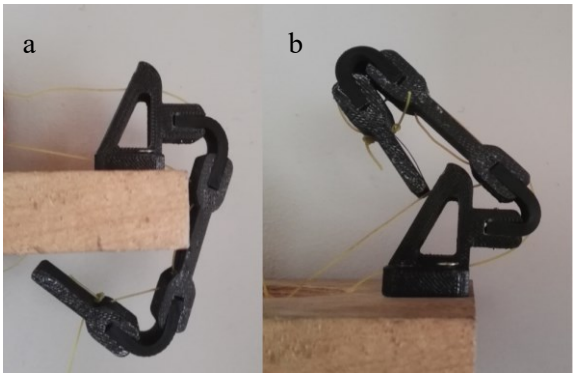

Figure 3-13: Dual Rubber Joint Concept

3.5.2 Single Rubber Joint Concept

The second attempt at the finger design made use of four links. The base link is attached to the end-effector and forms the base of the entire finger assembly. Three further links provide the required compliance around objects. Figure 3-14 shows the finger in (a) grasp pose and (b) retract pose. Starting at the base link; the first two joints are revolute while the last joint in this design has a flexible tendon. The addition of two pinned joints and another link significantly improved the stability of the finger when grasping objects. No considerable twist was observed from the prototype testing. The first link is termed proximal phalanx, the second link is termed middle phalanx, and the last link is termed distal phalanx.

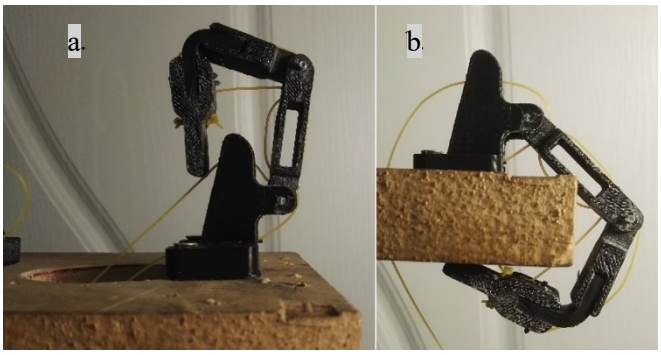

Figure 3-14: Single Rubber Joint Concept

3.6 Concept Selection

Demanded quality characteristics were defined in Section 3.2. These requirements are used as selection factors to determine the rating of each concept. This research involved the conceptualisation of three subsystems. The Decision Matrix is commonly used to select the most viable solution when presented with many options. Tables 3-2 and 3-3 present the concept decision matrices for the reconfiguration mechanism and the gripper, respectively.

Table 3-2: Reconfiguration Mechanism Decision Matrix

Criterion	Weight	3.3.2	3.3.3	3.3.4	3.3.5
Lightweight	8	8(X4)=32	8(X3)=24	8(X3)=24	8(X2)=16
Compact design	7	7(X3)=21	7(X2)=14	7(X2)=14	7(X4)=28
Low cost	7	7(X3)=21	7(X2)=14	7(X2)=14	7(X4)=28
Compatible with SKMs and PKMs	9	9(X3)=27	9(X3)=27	9(X3)=27	9(X4)=36
Reconfigurable design	9.5	9.5(X1)=9.5	9.5(X2)=19	9.5(X2)=19	9.5(X5)=47.5
Design for manufacturability	7	7(X2)=14	7(X2)=14	7(X3)=21	7(X4)=28
Scalable architecture	8	8(X2)=16	8(X3)=24	8(X3)=24	8(X4)=32
Total Rating		140.5	136	143	215.5

The lightweight weighting multiplier scored each of the four concepts according to their approximate mass, The Directly Coupled Platform has the least components, hence it scores the most. The VAP Five Motor concept has the most components; hence it was assigned twice the weight of the first concept. In terms of compatibility and manufacturing costs, the VAP Five Motor concept was the highest weighted. The VAP Fixed MT concept benefited from the highest rankings for manufacturability and scalability due to its design architecture. In terms of reconfigurable design – which carried the highest weighting, the first three concepts did not match the reconfigurability in design of the VAP Five Motor concept.

Table 3-3: Gripper Decision Matrix

Criterion	Weight	3.5.1	3.5.2
Lightweight	8	8(X4)=32	8(X4)=32
Powerful gripper	5	5(X2)=10	5(X3)=15
Grasp objects of multiple geometries	8	8(X4)=32	8(X4)=32
Compact design	7	7(X3)=21	7(X3)=21
Low cost	7	7(X3)=21	7(X4)=28
Compatible with SKMs and PKMs	9	9(X3)=27	9(X3)=27
Reconfigurable design	9.5	9.5(X4)=38	9.5(X4)=38
Design for manufacturability	7	7(X2)=14	7(X4)=28
Scalable architecture	8	8(X2)=16	8(X3)=24
Total Rating		211	245

The Single Rubber Joint Concept was assigned a higher weighting for its powerful gripper mechanism, reduced manufacturing expense, design for ease of manufacturing and scalable architecture. In general, the one less rubber joint provided more control and strength. The trade-off between flexibility and usability did not leave much between the two concepts. Based on the performance of the prototype grippers presented in Figures 3-13 and 3-14, the Single Rubber Joint Gripper performed a fraction better than the Dual Rubber Joint alternative.

Based on the decision matrix, the VAP: Fixed Machine-tool (Five Motor) concept had the highest weighting for reconfiguration mechanism. The Single Rubber Joint concept had the highest weighting for the gripper concepts. These conceptual designs were taken forward into prototype development.

3.7 Target Specifications of the RREE

Specifications of the reconfigurable robotic end-effector were determined based on the results from the QFD, as indicated in Section 3.2. The relationship matrix identified the relationships between demanded quality and quality characteristics. Figure 3-15 presents an excerpt from the House of Quality (HoQ) developed for the RREE. Refer to Appendix A for complete QFD HoQ.

Direction of Improvement: Minimize (▼), Maximize (▲), or Target (x)	▼	▼	▼	▲	▲	▼	▼	x	x	▲	▼	▼	▼	▼	▼
Quality Characteristics (a.k.a. "Functional Requirements" or "Hows") / Demanded Quality (a.k.a. "Customer Requirements" or "Whats")	Cost of Gripper	Weight of Gripper	Repeatability of Gripper	Grasp Volume	Payload of gripper	Cost of Machine Tool	Weight of Machine tool	Runout	Spindle Speed	Spindle Torque	Spindle Power	Maximum Tool Diameter	Weight of End-Effector	Reconfiguration Time	Volume of End-Effector
Lightweight	▲	⊙			▲	▲	⊙						⊙		○
Powerful gripper	○	○		○	⊙								○		▲
Grasp objects of multiple geometries	⊙	▲	⊙	○	⊙										○
Compact design	▲	○		⊙	⊙	▲	○				○	⊙	⊙	▲	⊙
High-precision machining of aluminium 6xxx						○	○	⊙	⊙	⊙	⊙	○	▲		
Low cost	⊙	▲	○	▲	▲	⊙	▲	⊙	○	○	○	○	▲	▲	
Compatible with SKMs and PKMs		⊙		○	⊙		⊙					○	⊙		⊙
Reconfigurable design	▲	⊙	⊙	⊙	⊙	▲	⊙	○	○	○	○	⊙	⊙	⊙	⊙
Design for manufacturability	○	▲				○	▲					▲	▲	○	⊙
Scalable architecture	⊙	⊙		○	○	⊙	⊙		⊙	⊙	⊙	○	○	○	⊙
Target or Limit Value	R20 000	20 N	5 mm	0,001 m3	9,81 N	R20 000	20 N	0,01 mm	15 000 RPM	0,35 Nm	800 W	5 mm	60 N	60 s	0,027 m3
Difficulty (0=Easy to Accomplish, 10=Extremely Difficult)	6	2	9	7	7	6	6	9	5	6	6	7	5	6	8
Max Relationship Value in Column	9	9	9	9	9	9	9	9	9	9	9	9	9	9	9
Weight / Importance	349,7	481,7	233,3	320,9	503,9	267,3	483,0	213,7	252,9	252,9	280,4	328,8	473,9	188,9	545,8
Relative Weight	6,8	9,3	4,5	6,2	9,7	5,2	9,3	4,1	4,9	4,9	5,4	6,4	9,2	3,6	10,5

Figure 3-15: QFD Relationship Matrix and Output Specifications

The quality parameters were determined from the customer requirements, these performance metrics provided key information on the working requirements of the device. The input parameters are tied to the performance of each subsystem – "powerful gripper" is linked "cost of gripper", "weight of gripper", "grasp volume", and "payload of gripper". It is also connected to the overall performance of the device as it has a relationship with "weight of the end-effector" and "volume of the end-effector". While, "grasp objects of multiple geometries" was linked to the GU performance metrics only. Reconfigurable design requirement is directly linked to all the quality parameters of the device – this was representative of the extent to which reconfigurability affects design decisions as mentioned in Section 2.8. Overall, the link between the input and quality parameters was pivotal in realising the potential of the RREE.

Based on the results of the QFD, the volume of the end-effector is most important. Therefore, the overall footprint of the machine is critical in the designing of subsystems. The payload of the gripper accrued the second-largest relative weight. The payload must be maximised for the design to satisfy customer requirements. The parametric design originates at the weight of machine-tool and gripper subsystems as they carry an average relative weight of 9.3. Weight of the end-effector received a relative weight of 9.2, the weight of gripper and machine-tool subsystems have a strong positive correlation with the weight of the end-effector. Table 3-4 presents the initial design specifications for the RREE, target/limit specifications from QFD and desired improved specifications are given.

Table 3-4: System Specifications

Subsystem	Specification		Unit	Target or Limit Value
Gripper	1	Cost	ZAR	20 000
	2	Weight	N	20
	3	Repeatability	mm	5
	4	Grasp Volume	m^3	0.001
	5	Payload	N	9.81
Machine Tool	6	Cost	ZAR	20 000
	7	Weight	N	20
	8	Runout	mm	0.01
	9	Spindle Speed	RPM	15 000
	10	Spindle Torque	Nm	0.35
	11	Spindle Power	W	800
	12	Maximum Tool Diameter	mm	5
Reconfiguration Mechanism	13	Weight of End-Effector	N	60
	14	Reconfiguration Time	s	60
	15	Volume of End-Effector	m^3	0.027

Additional specifications from 15 are listed below:

1. The length between the axis of rotation of the spindle and machine tool drive motor should be less than or equal to 120 mm.
2. The length between the axis of rotation of the lead screw and stepper motor should be less than 40 mm.

3.8 Chapter Summary

This chapter presented the conceptualisation process of reconfiguration mechanisms for the RREE. Requirements of the RREE were identified, and specifications determined. The functions of the RREE were defined, and desirable characteristics were presented. Subsystem definition and specification was presented. Methods of reconfigurable design were explored, and concepts employing three different reconfiguration methods were presented. Selection of final machine architecture was conducted based on system integration. Specifications of each of the end-effector were determined with the aid of QFD.

The following chapter details the complete mechanical design and blueprints for the RREE. The design of each of the three subsystems is covered from specific requirements and specifications to final assembly. Engineering design principles are utilised for the design of each subsystem.

Chapter 4 Prototype Design

4.1 Introduction

This chapter presents the detailed specification, methodology and mechanical design of the machine tool subsystem, gripper subsystem and reconfiguration mechanism. The machine tool subsystem section uses elements from the expert model [88] in conjunction with methods of reconfigurable design [60] to develop an integrated machine tool design. Requirements and specifications of the machine tool are briefly reiterated. The research methodology is explained, cutting conditions and requirements are determined. The power transmission components of the MT spindle are determined based on the calculated cutting parameters. Bearing configuration is selected for the spindle, mechanical design principles are utilised for the design of the spindle shaft and housing. Complete mechanical assembly is presented.

The gripper subsystem section presents an integrated gripper design. Requirements and specifications of the gripper system are briefly overviewed. The design methodology of the multilink gripper is discussed. The initial design considers the essential structural elements of the finger, positions, dimensioning and actuator selection. Secondary elements, such as the operational mechanisms of the gripper finger, are described. The geometric design of gripper finger components follows the mechanical design of power transmission components. The complete gripper assembly is followed by workspace analysis of a gripper finger is computed to approximate volumetric grasp range. The workspace of the gripper finger is specified by Denevit-Hartenberg (DH) parameters and solved with MATLAB.

The reconfiguration subsystem section defines the linear actuator design. The linear actuator forms the method of reconfiguration of the RREE. Design requirements and specifications are briefly revisited, as these were previously defined in Chapter 3. The design methodology of the linear actuator is presented. Selection of linear drive components is followed by load estimation of the linear axes. Reconfiguration time is estimated based on drive component specifications and the approximated load. Mechanical design of the fixturing mechanism used to join the RREE to popular manipulators is described. Complete mechanical assembly of the mechanism is presented. The platform is extended toward the work surface to deploy the gripper and retracted to deploy the machining spindle. The machining configuration is shown in Figure 4-1 (a), and the grasping pose is shown in Figure 4-1 (b). Figure 4-2 presents the functional decomposition diagram of the RREE.

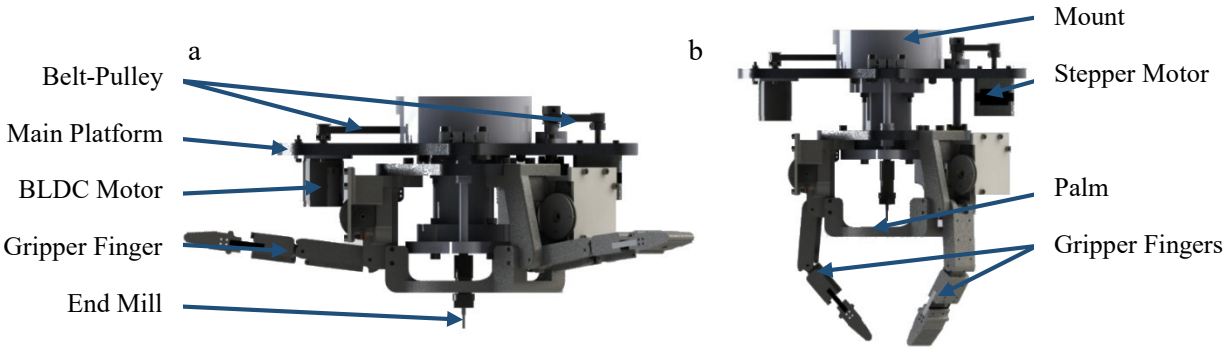

Figure 4-1: **Rendering of Reconfigurable Robotic End-Effector**

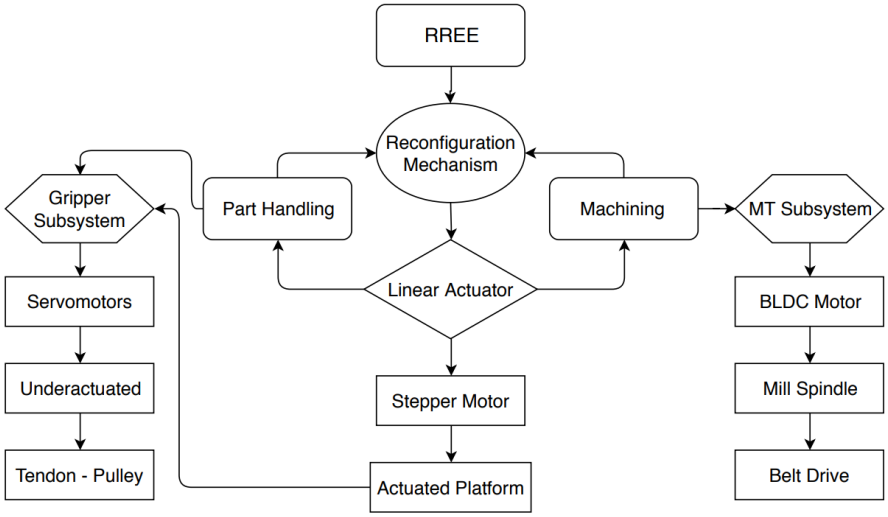

Figure 4-2: Functional Decomposition Diagram of RREE

4.2 Machine Tool Subsystem

4.2.1 Requirements and Specifications of MT

Requirements of the Machine Tool (MT) stem from Section 3.2. The Reconfigurable Machine Tool (RMT) was designed to meet the primary function of machining aluminium. In summary, the developed machine tool is required to perform down end-mill machining operation. Aluminium 6061 was selected as the profile of aluminium as it is widely machined in industry [90-92]. A MT capable of machining this non-ferrous metal is able to cut softer materials. Therefore, softwoods and soft plastics become readily machineable [93]. Based on the requirement of scalability, the machine tool drive components must be upgradable. The mechanical design must be compact, inexpensive and lightweight.

Table 3-4 in Section 3.7 defined the specifications of the machine tool. The cutter diameter was minimised below 5 mm. 2 mm end mills provide high precision cuts and are commonly used in small-scale CNC machines [94, 95].

4.2.2 Methodology – MT subsystem

The machine tool design comprised of a high-speed brushless motor, machine spindle and pulley-belt drive coupling. The design methodology was adapted from Maeda's Expert Spindle Design [88]. The engineering design process was followed for the machine tool; the process is summarised in Figure 4-3.

Figure 4-3: Machine Tool Design Methodology

Cutting conditions such as tool and workpiece material data were needed to determine the cutting requirements. These cutting requirements depended on the tool geometry and material properties of the workpiece. The required torque, speed and power were determined based on the set cutting conditions. The power transmission system was designed to deliver the required torque and rotational speed. The rotating

spindle shaft was coupled to a system of bearings. The selection of a viable, cost-effective bearing system was, therefore, determined. The geometric design of the spindle shaft and shaft housing are produced in SolidWorks Computer-Aided Design (CAD). Finally, a complete machine tool assembly model was presented.

4.2.3 Cutting Conditions

4.2.3.1 Tool Selection

Part of the aim of the research was to design a machine tool capable of machining operations. Milling has been selected as the machining operation; as such, the tool that was selected should be capable of milling. The workpiece material for the research is aluminium 6061, as defined in Chapter 3. The tool required for end-milling aluminium is the two flute carbide end mill [96]. A cost-effective, short end mill is Cleveland C76050. It is compatible with non-ferrous metal milling and is designed for high-speed material cutting. Specification of Cleveland C76050 is presented in Table 4-1.

Table 4-1: Cleveland C76050 Specification [97]

Helix Angle	30°
End Mill Material	Carbide
Milling Diameter	2.00 mm
Shank Type	Straight
Shank Diameter	3.18 mm
Length of Cut	6.00 mm
Overall Length	38.10 mm
Number of Flutes	2

4.2.3.2 Workpiece Material Data

Workpiece material specification was critically essential in machine tool design. The recommended cutting parameters for the end milling of aluminium 6061 were sourced from tool manufacturers. Two such parameters are surface cutting speed and tooth feed rate. These values are specified based on workpiece material mechanical and strength properties, tool diameter and tool material.

The recommended surface cutting speed for end milling wrought aluminium alloy is 76.2 m/min [98]. The recommended tooth feed rate for end milling wrought aluminium alloy with two flutes, 2 mm diameter carbide tool is 0.0254 mm/tooth [98]. These parameters, in conjunction with Equations 4.1 and 4.2, are used to compute the required spindle speed, feed rate, depth of cut and width of cut. The solution is presented in Appendix B.1.

$$N = \frac{1000.v_c}{\pi.D} \tag{4.1}$$

$$v_f = n.z.f_z \tag{4.2}$$

Using the recommended cutting parameters [98], and Equations 4.1 and 4.2, a rotational cutting speed of 12127.61 RPM and a feed rate of 616.08 mm/min was calculated. The width of cut is 2 mm for an end milling process. The depth of cut is 2 mm.

4.2.4 Cutting Requirements: Torque, Speed and Power

The metal cutting mechanics involved in the end milling process defines tangential force as the limiting load to determine cutting torque. The required cutting torque was calculated from cutting conditions specified above. Equations 4.3 and 4.4 below compute the instantaneous cutting torque and maximum cutting torque, respectively. The numerical solution is provided in Appendix D.1.

$$T_c = \frac{D}{2}\sum_{j=1}^{N} F_{tj}(\varphi_j) \tag{4.3}$$

$$T_{max} = \max(T_c) \tag{4.4}$$

Equations 4.5 and 4.6 were computed to determine the required tangential force.

$$F_{tj}(\varphi_j) = K_{tc}ah(\varphi_j) + K_{te}a \tag{4.5}$$

$$h(\varphi_j) = c\sin\varphi_j \tag{4.6}$$

Equations 4.7, 4.8 and 4.9 were used to compute the cutting power, cutting speed, and maximum cutting power, respectively.

$$P_t = V\sum_{j=1}^{N} F_{tj}(\varphi_j) \tag{4.7}$$

$$v_c = \frac{\pi Dn}{60} \tag{4.8}$$

$$P_{max} = \max(P_t) \tag{4.9}$$

The numerical simulation based on Equations 4.3 to 4.9, produced a maximum tangential cutting force of 173 N, cutting speed of 1.27 m/s, maximum cutting torque and power of 0.173 Nm and 219.71 Watts respectively.

4.2.5 Power Transmission Selection

4.2.5.1 Selection of Drive Motor

Given the torque and power requirements from the end milling process presented in Section 4.2.4, a drive motor was selected. Machine tools require high precision components to perform high accuracy machining operation. The spindle drive motor is a critical component in the design as it provides the rotational speed, torque and power. High-speed DC motors were best suited for the design requirement of compactness. Typically, high precision DC drives require expensive speed controllers and power supplies. The low-cost specification of the design required an alternative to expensive components.

Brushless DC motors provide high rotational speed, are cost-effective and readily available. The NTM PROP DRIVE 3548 out-runner brushless DC motor was selected for the spindle motor based on power, speed and torque requirements. Specifications of the motor are presented in Table 4-2. The motor has a maximum rotational speed and torque of 15000 RPM and 0.6 Nm respectively. This exceeded the rotational speed and torque requirements of 12127.61 RPM and 0.173 Nm for the specified machining operation. Therefore, it is well suited to drive the machine tool spindle as higher material removal rates are possible.

Table 4-2: Specification of NTM PROP DRIVE 3548 1100KV Motor [99]

Maximum Speed	15000 RPM	* 12127.61 RPM
Maximum Torque	0.6 Nm	* 0.173 Nm
Maximum Power	640 Watts	* 219.71 Watts
Weight	185 g	
Maximum Current	70 A	
Maximum Voltage	14.80 V	
Shaft Diameter	5 mm	
Length	70.00 mm	
Diameter	35.00 mm	

*Required theoretical values

4.2.5.2 Selection of Tooling System

Mill machine tool holders are diverse, and there are many options. Each type is designed for a specific application in terms of machine size, stiffness and tooling requirements. Two standard tool holding systems are the ER system and the BT system; each has a place in the machine-building industry. The ER tool holder has several advantages over BT tool holders [100]. It offers flexibility for drill, tap, and reaming operations. The holder prolongs tool life by decreasing runout with standard accuracy. It has a wide clamping range for tools less than 7 mm in shank diameter. ER standard collets are simple to use, change and maintain as the collet is self-extracted from the holder. ER tool-holders do not need dedicated tap-holders. Due to the compact requirement of the design, a drawbar retention clamping mechanism was not feasible. ER11 collet with 3.18 mm diameter shank is used for the Cleveland C76050 endmill. ER11 Tool Holder material is 40 CR Steel, clamping range is 1 – 7 mm, spindle shaft bore diameter is 8 mm and length is 37 mm.

4.2.5.3 Design of Transmission System

Power transmission was a critical component of the machine tool. The rotational motion generated by the drive motor must be transferred efficiently from the motor shaft to the spindle shaft. There are several options for power transmission between these components. Each of the transmission types is ideally suited for different applications. Based on the low-cost requirement of the design, the belt-pulley power transmission system was selected. Expert Spindle Design Method [88] in conjunction with calculated torque and speed was used to confirm the transmission system. Three standard belt-pulley conventions are used for machine tools; these are the flat belt, the v-belt and the timing belt. For synchronous power transmission, the timing belt type was selected. There are many types of timing belt-pulley conventions. The calculated speed and torque were used in conjunction with manufacturer specification chart [101] to select the type of timing belt. The 2 mm pitch GT2 configuration was selected due to support of speed, availability and cost. The pulley should have a minimum of 16 teeth [101]. Due to availability of belt and pulley components, 6 mm width belt and pulley were chosen for the design. Maximum surface speed for GT2 timing belts was found to be 38 m/s [102]. The maximum rotational speed of the belt was determined by Equation 4.10.

$$n = \frac{v_s \times 60}{\pi \times d_m} \tag{4.10}$$

The pitch diameter of the motor pulley was 12.7 mm. The resultant maximum rotational speed of the belt was 29029.86 RPM. The calculated rotational cutting speed was 12127.61 RPM, therefore the GT2 belt was ideally suited for the application.

To select a belt combination - design considerations of the spindle and brushless motor were considered. The approximate distance between centres of the spindle shaft and the spindle drive motor was defined in Section 3.7. Given this length of 120 mm, the approximate belt length was determined using Equation 4.11. The specification of the selected tool holder and spindle motor required pulleys of inner diameter 8 mm and 5 mm respectively. GT2 pulleys with these inner diameters and 20 teeth are available and cost-efficient. Both pulleys have the same number of teeth; this was selected due to the ideal speed and torque output of the NTM BLDC motor. Therefore, the power transmission ratio is 1:1; Equation 4.11 is simplified to Equation 4.12. Appendix B.1 contains the design calculations.

$$L_R = 2 \times A \times \sin\left(\frac{\beta}{2}\right) + \frac{t}{2} \times (z_g + z_k + (1 - \frac{\beta}{180}) \times (z_g - z_k) \quad (4.11)$$

$$L_R = 2 \times A + \pi \times d_w \quad (4.12)$$

The pitch diameter of the motor pulley is 12.7 mm. Using the centre distance of 120 mm - the calculated belt length was 279.90 mm. Due to the unavailability of a belt with this specific length, a 280 mm belt was selected. Belt tensioning mechanism was incorporated to adjust pretension of the belt and pulley assembly. Tolerance for allowable tensioning and adjustment of the belt-pulley was incorporated in the designed mount.

4.2.6 Bearing Selection

4.2.6.1 Selection of Bearings

One of the most critical components of the machine tool spindle was the bearing system. The bearing system must be suitable for the range of rotational speed and load capacity required by the machining operation. There are three commonly used bearings in high-speed spindles; these are Angular contact ball bearing, Roller bearing and Taper roller bearing. Based on the Expert Spindle Design method [88], angular contact ball bearings were selected. This was due to the relatively low load, high-speed application of the tool system. A minimum of two bearings is required for machine tool spindles.

4.2.6.2 Selection of Bearing Arrangement

The magnitude of preload on angular contact ball bearings is an essential factor to consider as it impacts the maximum speed and stiffness. There are typically three magnitudes of preload, light, medium and heavy. Lighter preloads used for high rotational speed applications which contain small loads, while higher preloads used for low rotational speed applications which require increased stiffness [103].

There are three commonly used bearing mounting configurations. The back-to-back arrangement is best suited for applications which require good accuracy and rigidity. Face-to-face arrangement is commonly used for applications which require both axial and radial loading. Tandem arrangement is used for larger spindles, the front bearings are stacked, and the rear bearings are also stacked. This results in a higher moment loading capacity and increased spindle performance [103].

The back-to-back arrangement was selected for the front bearing of the spindle; this is the side closest to the end mill cutter. Majority of the support of the spindle shaft originates from the front bearing. This is due to the proximity of the support to the location of loading. Double row angular contact bearings are more straightforward to assemble than two single row angular contact bearings; therefore, a double row angular contact ball bearing was used for the front shaft support. The rear shaft was supported by single row angular contact ball bearing, the rear of the shaft supports the power transmission pulley and a portion of the cutting forces. The bearing arrangements are presented in Figure 4-4.

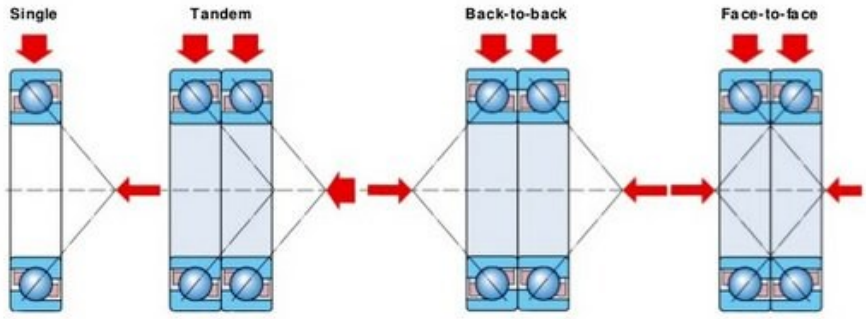

Figure 4-4: Arrangements of Angular Contact Ball Bearings [104]

The shaft was attached to the BLDC motor through GT2 Pulley on one end and the ER11 Tool Holder on the other. The diameter of the shaft is constrained to 8 mm at both ends to accommodate these attachments. Design for manufacturability was considered, following consultation with the Machinist – the inner diameter of the bearing was selected as 12 mm. This allowed for ease of manufacturing with the available equipment. The specifications of both bearing NSK 7201 BW single row angular contact ball bearing and NSK 3201 double row angular contact ball bearing are listed in Table 4-3.

Table 4-3: NSK 7201 BW [105] and NSK 3201 [106] Bearing Specifications

Bearing	NSK 7201 BW	NSK 3201
Dimensions	12 mm x 32 mm x 10 mm	12 mm x 32 mm x 15.9 mm
Dynamic Load Rating	8.15 kN	10.60 kN
Static Load Rating	3.75 kN	5.85 kN
Grease Speed Limit	18000 RPM	15000 RPM
Oil Speed Limit	26000 RPM	20000 RPM
Weight	0.038 kg	0.051 kg

4.2.6.3 Bearing Stiffness

Angular contact ball bearings were used in the machine tool spindle design. Bearings are usually modelled as solid rigid structures in simulation, though this does not produce a realistic result. For successful design, bearing stiffness was computed to evaluate the dynamic stiffness of these supports. It is for this reason that the bearing stiffness was analysed for both bearings in the model. The Hertz contact model [107] was used to approximate radial deformation using Equation 4.13 and radial stiffness using Equation 4.14. Equation 4.15 solved for the radial load of one rolling element. Table 4-4 contains the results of the Hertz contact model for angular contact ball bearings. Figure 4-5 indicates the four spring-dampers elements arranged in right angles for the spindle shaft.

$$\delta_r = \frac{0.436}{\cos\alpha}\sqrt[3]{\frac{Q_r^2}{d_b}} \tag{4.13}$$

$$Q_r = \frac{5}{iz_c \cos \propto} \tag{4.14}$$

$$K_r = \frac{dF_r}{d\delta_r} = 1.18\sqrt[3]{F_r d_b (iz_c)^2 \cos^5\alpha} \tag{4.15}$$

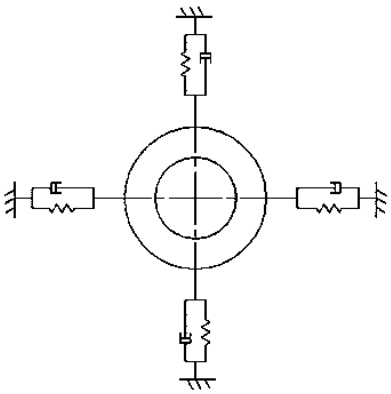

Figure 4-5: Arrangement of spring-damper on spindle shaft [108]

Table 4-4: Hertz contact model results

Symbol	Front bearing (double row)	Rear bearing (single row)
δ_r	$4.275587808 \cdot 10^{-6}$	$5.344195505 \cdot 10^{-6}$
K_r	$0.23158 \cdot 10^{9}$	$0.12555 \cdot 10^{9}$
α	25	40
d_b	5.95	6
i	7	10
z	2	1
Q_r	$10.6 \cdot 10^{4}$	$7.6 \cdot 10^{4}$
F_r	$1.06 \cdot 10^{4}$	$0.761 \cdot 10^{4}$

4.2.7 Machine Tool Spindle Design

4.2.7.1 Spindle Shaft

Two angular contact ball bearings support the spindle shaft. The bearings require mounting specifications and tolerances as indicated by the manufacturer. These parameters were used in the dimensioning of the spindle shaft. The manufacturers recommended fillet and abutment specifications are presented in Appendix B.1.

Design for manufacturability was considered throughout the design of the end-effector. After consultation with the machinist, the fillets were excluded from the shaft design. Due to the small scale of the spindle shaft, it was difficult to manufacture this fillet. Nevertheless, the recommended abutment dimensions were used in the shaft design. The diameter of the tool holder and drive pulley are 8 mm. Therefore, the diameters of both ends of the shaft were selected to be 8 mm with 0.1 mm clearance fit. Using the manufacturer's abutment specification - a stepped shaft design was required. The end diameters are 8 mm, the first step on both ends are 12 mm in diameter due to the inner races of NSK bearings. Both bearings are coupled to the

shaft by an interference fit. The middle section or second step diameter was designed based on the minimum abutment diameter of 17 mm and ease of manufacture. The diameter of this section is therefore 20 mm. The length of the shaft was determined based on the thickness of bearings, length of tool holder and length of the pulley. This design parameter was constrained by reconfigurability specification of maximum volume defined in Section 3.7. The designed spindle shaft assembly is presented in Figure 4-6; the length of the shaft is 134 mm. Appendix K.2 contains the dimensioned engineering drawing.

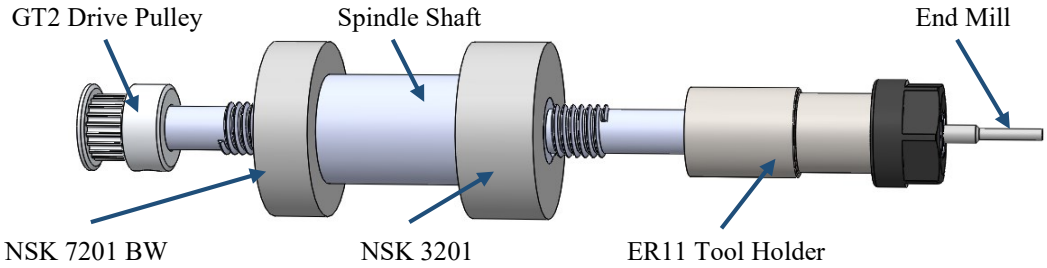

Figure 4-6: CAD Model of Spindle Shaft Design

Many factors influence material selection in a machine tool spindle design. The high rotational speeds generate a significant amount of friction between contact surfaces; increased heat dissipation is a result of this. The spindle shaft material must have high strength and decreased susceptibility to torsion. Solid AISI 4340 Alloy Steel was selected as the spindle shaft material. It is a nickel-chromium-molybdenum alloy steel that is commonly used in machine tool applications due to its high toughness and strength. AISI 4340 has excellent machinability characteristics and is machined using conventional methods.

4.2.7.2 Shaft Housing

The spindle shaft bearings require adequate support to operate effectively. The housing design was primarily influenced by the requirements and specifications of the reconfigurable system. The bearing manufacturer specifies the mounting of the angular contact ball bearing. The manufacturers recommended fillet and abutment specifications [109] are used in the housing design. Design for manufacturability was considered throughout the design of the end effector. Bearing outer race diameter of 32 mm was used to dimension the surface contact diameters. Clearance fit was used to mount the outer race of the bearing into the surface contact. The smallest diameter of the housing is 25 mm; this abutment supports the inner mounting faces of both bearings. Preload clamps restrain the outer mounting faces of both bearings. The preload clamp was clearance fitted to both sides of the housing. These clamps are fastened onto the housing by four metric screws. The internal thread was therefore cut for these screws, Appendices K.3 and K.4 contain the dimensioned engineering drawings of these clamps. The footprint of the spindle housing is constrained by reconfigurability as defined in Section 3.7 and the length of the spindle shaft. Appendix K.1 contains the dimensioned engineering drawing. The length of the housing is 74 mm, and the outermost diameter is 80 mm. Figure 4-7 presents the spindle housing design.

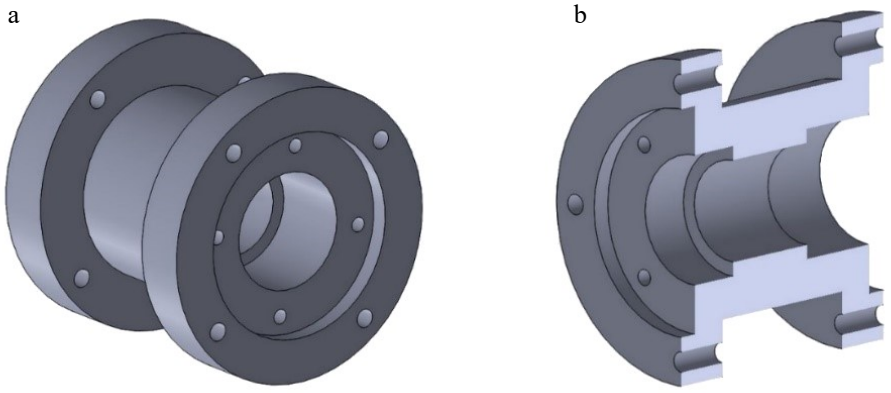

Figure 4-7: (a) Full CAD Model of Spindle Housing Design (b) The 3D Sectional View of the Spindle Housing Design

The spindle housing should be lightweight and support the shaft and bearing effectively. Many factors influenced material selection, the high rotational speeds generate a significant amount of friction between contact surfaces; increased heat dissipation is a result of this. Loading caused by the metal cutting process is propagated from the tooltip through the spindle shaft, bearings, and then spindle housing. The housing material is solid aluminium 6082-T6 due to its lightweight characteristic. Weight specification defined in Section 3.7 affects material choice as stiffer materials are generally heavier. Conventional machining methods easily machine wrought aluminium. The above process took material and resource availability into consideration, while maintaining the structural integrity requirements of the machine tool design.

4.2.7.3 Machine Tool Assembly

The compact, high-speed spindle performs machining. The spindle was designed to machine woods, plastics and non-ferrous metals such as aluminium, copper and bronze. The compact, brushless motor was coupled to the spindle via a pulley-belt drive system. It was engineered for high-speed end milling. Angular contact bearings are stacked in the front and back of the spindle shaft in the configuration. The machine-tool was designed to work with ER11 metric collets, and the collet holder can clamp a maximum end mill of 7 mm diameter. The end-effector can be mounted onto serial robots, parallel robots and three-axis machines. The design of the unit permits easy adaption to different mounting configurations [6]. Figure 4-8 presents a rendering of the final design; all subcomponents can be seen. Table 4-5 indicates the specifications of the machine tool design.

Table 4-5: Machine Tool Final Specifications

Maximum Speed	15000 RPM	* 12127.61 RPM
Maximum Torque	0.6 Nm	* 0.173 Nm
Maximum Power	640 Watts	* 219.71 Watts
Weight	1058.33 g	
Spindle Material	AISI 4340 Alloy Steel, Aluminium 6082-T6	
Power Transmission	GT2 Belt Drive	
Tooling	ER11 Collet, 7 mm Diameter Endmill	

*Required theoretical values

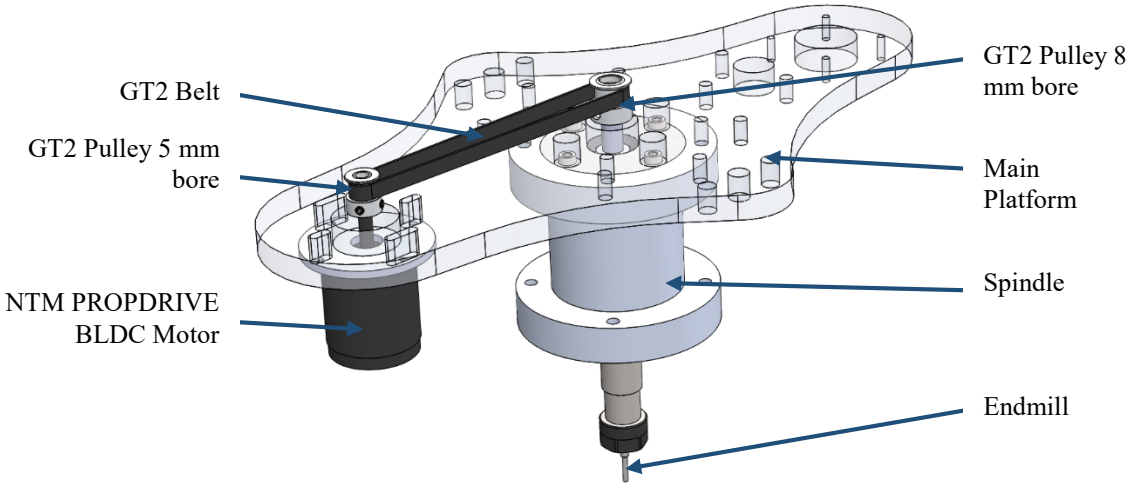

Figure 4-8: Machine Tool CAD Design

4.3 Gripper Subsystem

4.3.1 Requirements and Specifications of GU

The requirements of the Gripper Unit (GU) stem from Section 3.2. The gripper was designed to meet the primary function of part handling. In summary, the developed gripper system was required to perform material handling of objects with multiple geometric definitions. The gripper conformed to the integrated "demanded quality" requirements of the RREE listed in Table 3-1. Based on the requirement of scalability, the gripper drive components must be upgradable. The mechanical design must be compact, inexpensive and lightweight. Based on the literature review on state of the art in reconfigurable robotic grippers, a gripper with underactuated drive mechanism was required.

Table 3-4 in Section 3.7 defined the specifications of the gripper system. Maximum grasp volume of the gripper is 0.001 cubic metres; this volume is cubic. Therefore, an object of 100 mm – length, breadth and depth, must be grasped. The gripper must have a minimum payload capacity of 9.81 N. The gripper must maintain repeatability of 5 mm. The gripper should be fabricated by additive manufacturing methods such as 3D printing to save cost. Additive manufacturing in engineering is a current trend in rapid prototyping. 3D printing offers useable components for efficient prototyping and testing, it saves development resources such as time and money.

4.3.2 Methodology – GU subsystem

The methodology for the development of the gripper subsystem is summarised in Figure 4-9. The basic properties of the gripper system are defined; these properties include the number of linkages, finger positions, manufacturing and dimensions. The actuation mechanism was selected based on the defined gripper. The mechanical gripper mechanism which produced the grasping motion is defined. The gripper assembly follows the mechanical design of the linkages and transmission components. Workspace analysis was conducted to determine the grasp range of the gripper system.

Figure 4-9: Gripper Subsystem Design Methodology

4.3.3 Number of Fingers, Phalanges, and Actuators

Robot grippers consist of fingers, phalanges and actuators. The selection of the quantity of these components is critical to effective operation. Object geometry, size, mass and surface temperature are vital characteristics that must be defined. Figure 4-10 illustrates the performance to flexibility comparison of different gripper architectures. Reconfigurable architecture requires compact gripper finger with shape adaptability characteristics. The gripper must have intermediate flexibility to grasp objects of various geometries. Each gripper must be actuated independently to satisfy integration in reconfigurable architecture. The gripper must have an acceptable performance to execute part handling processes on serial and parallel robots.

Three-finger, three-phalange grippers provide average performance and intermediate flexibility. According to specifications defined in Section 3.7; three fingers, three phalanges and three actuators were selected.

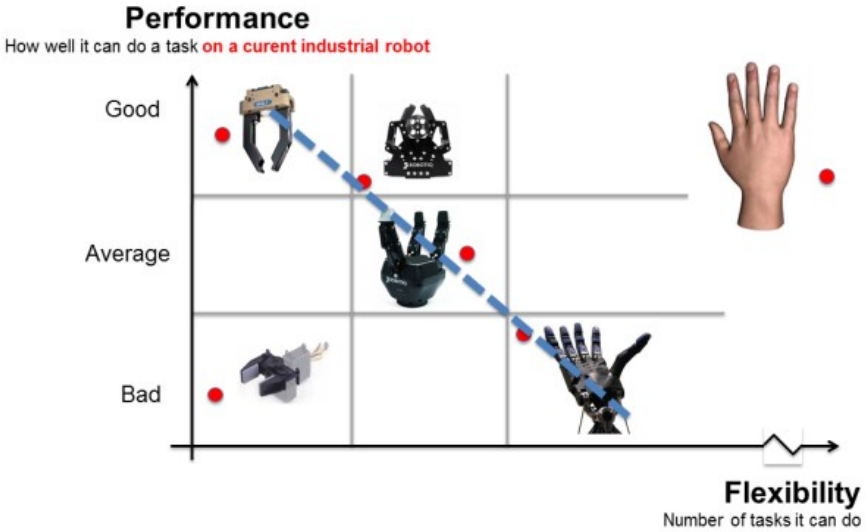

Figure 4-10: Range of Grippers [110]

4.3.4 Finger Positions

The purpose of this part was to describe the finger positions and why we need these finger positions. Finger positions were defined by three states, as indicated in Figure 4-11. Figure 4-11 (a) characterises the retracted position of the gripper; this pose is a specification requirement of the reconfigurable architecture. Figure 4-11 (b) characterises the intermediate position of the gripper; this position engages parts of broader diameter. Figure 4-11 (c) illustrates the fully closed position of the gripper finger.

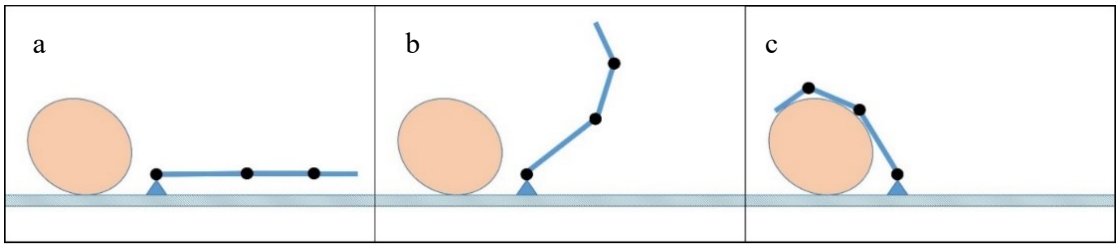

Figure 4-11: Finger Positions of Architecture

4.3.5 Manufacturing and Dimensions

Additive manufacturing is a fast and efficient method of rapid prototyping. The gripper components were fabricated through FDM 3D Printing. This manufacturing process yielded useable plastic components for minimal cost and manufacture time. Polylactic Acid (PLA) filament is widely used for rapid prototyping due to its excellent printability and reliability. PLA plastic was selected as the filament material for the designed gripper components. PLA is a low-cost, rigid, light-weight material that has acceptable mechanical properties for the application. Rubber joint material is BUTYL Durometer 60. Dimensions are 30 mm x 30 mm x 5 mm. Figure 4-12 presents a CAD model of the overall dimensions of the gripper. Appendix K.20 contains the detailed drawing.

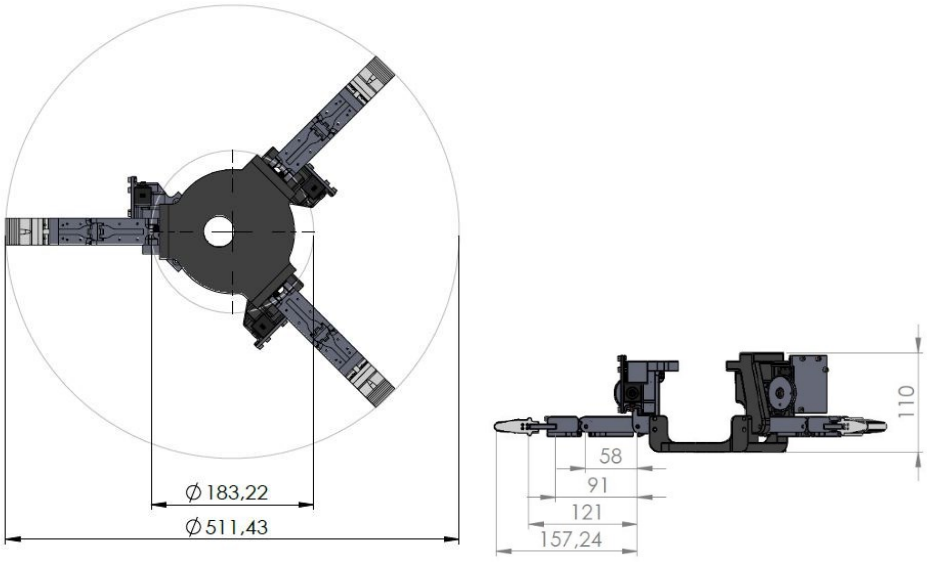

Figure 4-12: Dimensioned Gripper Subsystem

4.3.6 Actuator Selection

Electric motors were selected for actuation of the gripper. Robot servo motors were selected due to the kinematic structure. The tendon had to be driven from the gripper housing for it to remain modular. Robot servo motors have a relatively small size and high power to mass ratio. The design requires a lightweight actuator; pneumatic and hydraulic actuators are costly and often add weight.

Servo motors vary in size, output torque, cost, efficiency, controllability, speed, current and voltage. Specification of the gripper requires the motor to be lightweight, compact, simple to control and cost-

effective. There are many compact, low-cost servo motors available. The output torque required for gripping specification of 9.81 N must be determined to select appropriate servo motor. Equation 4.16 was used to determine the minimal gripping force. The gripping force is the sum of all individual finger force. Distal phalanx has a friction coating for increased grasp ability. The glove material was polyurethane with a static coefficient friction factor of 2.2 [111]. The complete calculation is contained in Appendix B.2.

$$F_g > \frac{m(g + a_r)}{u}(SF) \tag{4.16}$$

$$T = r_a F_a \sin\theta_a \tag{4.17}$$

Total gripping force of 13.464 N was required for 9.81 N payload. Since there are three fingers, grasp force per finger is 4.488 N. Torque was estimated using Equation 4.17 as 0.706 Nm using the lever arm of gripper finger and required grasp force of one finger. The FEETECH FR0115M Robot Servo Motor was selected due to its specifications. The servo motor specifications are tabulated in Table 4-6.

Table 4-6: Specifications of FEETECH FR0115M [112]

Dimensions	40.0 × 20.0 × 40.5 mm	
Operating Voltage	4.8 V ~ 7.4 V	
Nominal Current	2 A	
Speed	0.18 sec /60° (4.8V), 0.16sec / 60° (6V)	
Torque	1,37 Nm (4.8V), 1,47 Nm (6V)	* 0.706 Nm
Control Signal	Digital	
Signal Range	500 µS ~ 2500 µS	
Direction	Counter Clockwise	
Operating Angle	180°	
Weight	59 g	

*Required theoretical values

4.3.7 Definition of Kinematic Architecture

An underactuated linkage mechanism was utilised in the finger design. A three-bar planar mechanism was selected to supply each finger with a single degree of under actuation. The geometric and kinematic design process follows the description of the mechanism. Underactuated fingers have a fewer number of actuators compared to degrees of freedom. These mechanisms have a relatively simple design compared to fully actuated mechanisms. The underactuated finger mechanism conforms to the shape of different geometries due to the adaptive grasping ability. The mechanism has the advantage of a low-cost mechanical system which meets design requirements. The proposed gripper finger has three degrees-of-freedom and one degree-of-actuation by Grubler's formula [113]. Actuation occurs on the third joint between the middle and distal phalanxes. A tendon – pulley transmission system is used to couple all three phalanges to the motor pulley. Finger design schematic is presented in Figure 4-13. Each finger consists of three links, two revolute joints and a flexible end joint. Appendices K.18 and K.19 contain the detailed gripper subassembly drawings.

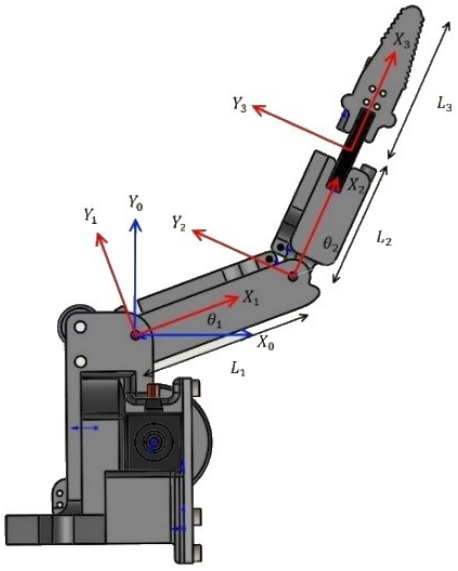

Figure 4-13: Definition of the Kinematic Structure

The design incorporated revolute joints to couple the proximal phalanx to the motor housing and middle phalanx to the proximal phalanx. A flexible rubber joint is used to couple the middle-distal phalanges. The rubber joint was evaluated in the concept stage. This type of joint increases the compliance of the gripper mechanism, aids in adaptability. The kinematic structure requires a lightweight cable-pulley power transmission system. Gear and Linear drives do not suit the kinematic architecture of the gripper. Cable drives offer added flexibility and manoeuvrability of the drive system. Length of the proximal phalanx, middle phalanx and distal phalanx are 58 mm, 48 mm and 54.5 mm respectively. Maximum joint angles from horizontal position are 90°, 45° and 46° for proximal, middle and distal joints respectively.

4.3.8 Design of Transmission System

Figure 4-14 gives a side diagrammatic view of a single gripper-actuator subassembly. The underactuated design is described by the two cable systems shown. The red cable represents the retraction system; this was coupled to a set of extension springs. The retracted pose of the gripper is a requirement for reconfiguration. The retraction system is composed of five extension springs per finger. The blue cable represents the grasping system; this is coupled to the robot servomotor. The servo motor shaft is coupled to a pulley, and the pulley is connected to the blue cable, as indicated in Figure 4-14. The servomotor rotates through 180°, in a clockwise direction. This translates the rotational torque from the servo motor to a tension force in the cable. Appendices K.18 and K.19 contain the detailed gripper subassembly drawings.

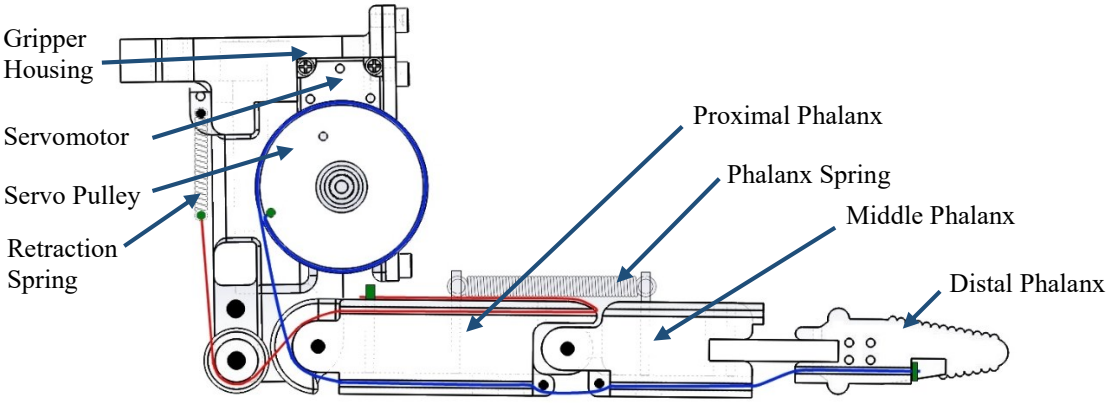

Figure 4-14: Definition of Dual Cable Routing System

Waxed Thread 475 was selected as the cable for the actuation system. Fishing line, while smaller in diameter, did not possess the required strength upon trial testing. Cable diameter is 1.02 mm; it has a strength rating of 22.23 kg [114]. It was assumed that the cable is inextensible at loads less than the indicated strength.

4.3.8.1 Grasp System

Grasp operation was achieved by actuation of the cable-pulley mechanism. Actuation of the grasp is provided by FEETECH servomotor. The cable was routed from the cable mounting screw on the distal phalanx. The cable passes through the pulleys on the middle and proximal phalanges. The revolute joint of the proximal phalanx provides the moment arm of the mechanism. The cable is then attached to a pulley on the horn of the servomotor. The servo pulley provides an additional function of collecting the cable as it the gripper is actuated.

4.3.8.2 Retraction System

The function of this system is to maintain the gripper in the retracted position, as presented in Figure 4-11 (a). An array of extension springs is used for this purpose. Selection of these springs is necessary for the successful operation of the mechanism. Figure 4-15 presents a schematic of the finger with the proposed spring configuration. Table 4-7 presents the definition of lengths to determine spring criteria. Frictional effects in the cable are neglected in the calculation. Therefore, it can be assumed that the gravitational force of the gripper is equal to the force that the spring must provide. Fixed pinned constraints are applied to both springs and pulleys.

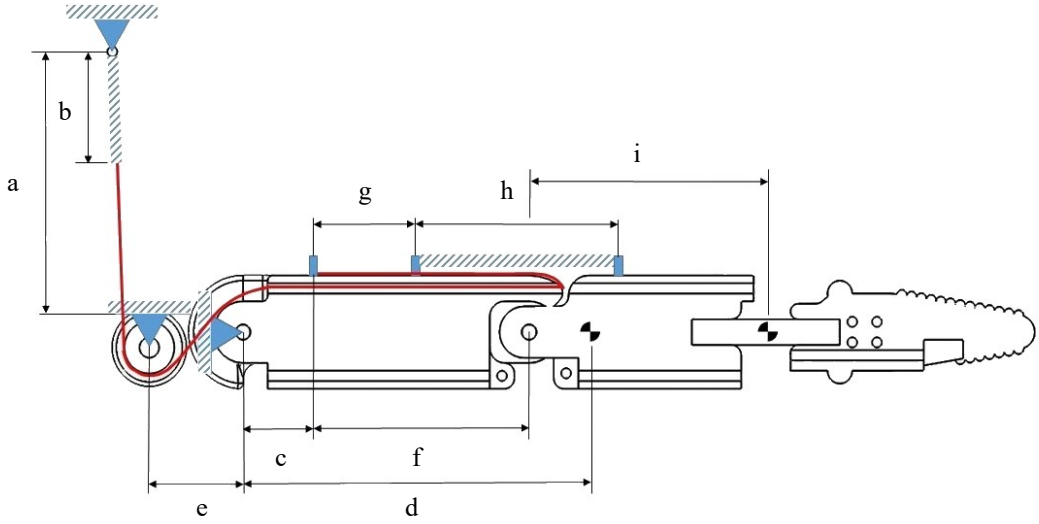

Figure 4-15: Dimensioned Finger

Table 4-7: Spring Selection Criteria

a	Maximum spring extension	58.95 mm
b	Mainspring length (no extension)	li
c	Length from base phalange pivot to cable mount	12 mm
d	Length from base phalange pivot to the centroid of finger	69.06 mm
e	Length from retraction pulley to base phalange pivot	19 mm
f	Length from cable mount to middle phalange pivot	46 mm
g	Length from cable mount to the base phalange spring mount	20 mm
h	Length from proximal phalanx spring mount to the middle phalanx spring mount	44 mm
i	Length from middle phalanx pivot to the centroid of the middle joint and distal phalanx	47.31 mm

The weight of the finger assembly (three phalanges and joints) is approximately 0.76 N. Refer to Appendix I for detailed mass calculation. A moment of 0.053 Nm was required to support the weight of the finger.

The cable is mounted 31 mm from the retraction pulley. A force of 1.69 N is required to generate the moment to support the finger weight. The mainspring should have an extension of no more than 2 mm when loaded by the fingering weight. This was to prevent movement of the finger when the end-effector is in motion. The mainspring stiffness for 2 mm extension is 846.85 N/m.

The mainspring must possess approximately this spring stiffness, diameter less than 5 mm and length less than 56.95 mm. A spring with these parameters was not found as an “off-the-shelf” product. Smaller springs with the required length and diameter were readily available. The spring was used in parallel to provide an estimated equivalent spring stiffness. Details of available mainspring are listed in Table 4-8. The equivalent stiffness of three parallel springs is 882 N/m. Since the equivalent stiffness is slightly larger than the required stiffness, the deflection is less than 2 mm when statically loaded.

The weight of the middle, distal phalanges and rubber joint is approximately 0.43 N. A moment of 0.0202 Nm is required to support the weight of these links. The cable is mounted 18 mm from the pivot of the middle phalange. A force of 1.12 N was required to generate the moment to support the weight of these components. The secondary spring should have an extension of no more than 3 mm when loaded by the finger weight. This was to prevent movement of the finger when the end-effector is in motion. The secondary spring stiffness for 3 mm extension was 373.87 N/m. The secondary spring must possess

approximately this spring stiffness, diameter less than 5 mm and length less than 41 mm. A spring with these parameters was not found as an "off-the-shelf" product. Smaller springs with the required length and diameter were readily available. The spring was used in parallel to provide an estimated equivalent spring stiffness. Details of available mainspring are listed in Table 4-8. The equivalent stiffness of two parallel springs is 392 N/m. Since the equivalent stiffness is slightly larger than the required stiffness, the deflection is less than 3 mm when statically loaded.

Table 4-8: Retraction System Spring Specification

Mainspring		Secondary spring	
Diameter	5 mm	Diameter	5 mm
Length (no extension)	20.5 mm	Length (no extension)	40 mm
Length (full extension)	55.5 mm	Length (full extension)	75 mm
Spring stiffness	294 N/m	Spring stiffness	196 N/m

4.3.9 Palm and Transmission Components

The palm structure serves three functions. It forms base support for the gripper modules which add structural rigidity to the gripper. Secondly, it provides a barrier between the endmill and the grasped object. This prevents any contact between the object and endmill. Lastly, the palm constricts the grasped object in the gripper mechanism, which is essential for enclosed grasped mode. The palm is manufactured by 3D printing, as is all of the gripper components. Figure 4-16 presents the solid CAD model of the palm structure. Appendix K.16 presents the detailed engineering drawing of the gripper palm.

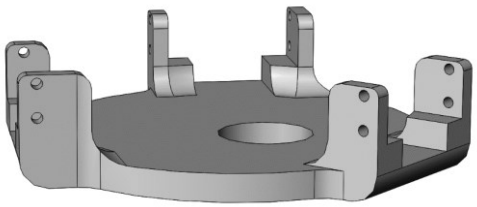

Figure 4-16: Palm Structure

Figure 4-17 (a and b) present component-level diagrams of the pulley and retraction systems. Compression tendon is attached to the servo pulley through tying the end of the cable to the mounting hole. The compression tendon passes over the base pulley of the proximal phalanx through the upper tendon guide. The end of the compression tendon is fixed to the distal phalanx by 2.9 x 6.5 mm screw. Retraction tendon (Wax Thread 375) is attached to spring mount; it passes over the retraction pulley through the lower tendon guide. The end of the retraction tendon was fixed to the proximal phalanx by 2.9 x 6.5 mm screw as indicated by the green rectangle in Figure 4-14. The spring mount couples the retraction tendon to the extension springs. Three extension springs are used to maintain the retracted position of gripper. The base spring mount couples the extension springs in parallel to the finger housing as indicated in Figure 4-17 (b).

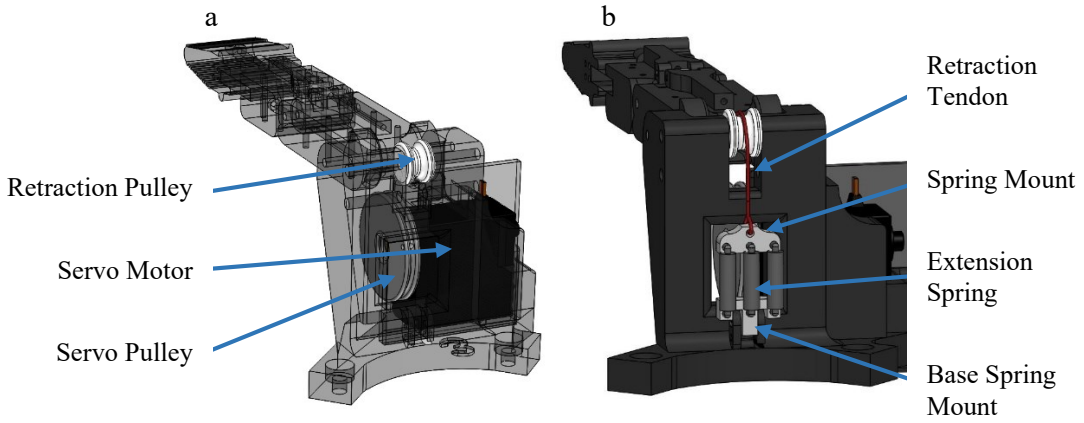

Figure 4-17: CAD Model (a) Pulleys (b) Retraction System

4.3.10 Finger Design

An exploded view of the gripper module subassembly is presented in Figure 4-18. Dimensioning of each component was essential for the integration and implementation of the underactuated mechanism. FEETECH servomotor forms the basis of the housing design. The servomotor is fixed in housing by cover plate and four screws. The servo pulley is 3D printed to interference fit onto the servo horn. The gripper finger housing mounts to the linear actuator through two bolted joint connections. Shaft pins are interference fitted into place to prevent slippage. The weight of each finger module assembly is approximately 3.45 N.

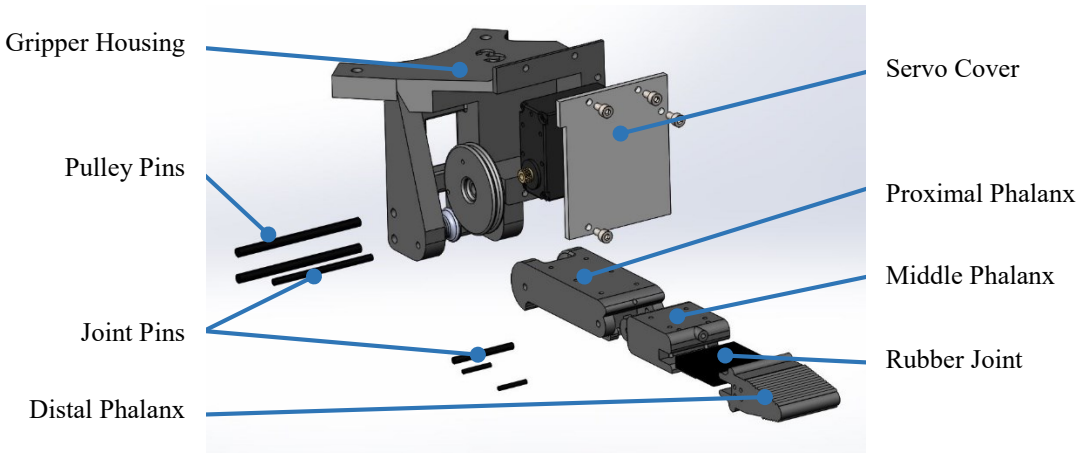

Figure 4-18: CAD Model of the Gripper Module Subassembly

Pulley pins were mounted the gripper module to the palm and couple the retraction pulley to the gripper housing. The joint pins create revolute joint connections between gripper housing – proximal phalanx and proximal phalanx – middle phalanx. The geometry of each component was designed for 3D printing. The dimensions of each component were restricted by the overall footprint of the reconfigurable end-effector.

4.3.11 Glove Design

A cover-over glove was incorporated for each gripper finger. The function of the glove is to provide additional compliance in grasp and to improve the friction characteristics of the gripper. Polyurethane was used to fabricate the glove due to its favourable deformation and friction properties. Smooth-On Ecoflex 00-30 was selected for fabrication of the glove. Notable properties of the silicone are its useful temperature range – 65 – 450 °C [115] and a coefficient of friction of 2.2 [111]. Appendix K.28 presents the drawing

of the mold assembly. Fabrication of the glove requires a mold to set the shape and contour of the exterior of the distal phalanx. Mold design feature in SolidWorks was utilised for this purpose. A two-part mold was designed as three gloves are required. 3D printing is used for fabrication of the mold; the liquid silicone is poured into the top of the mold. Figure 4-19 presents a cross-sectional view of the two-part solid model that is used.

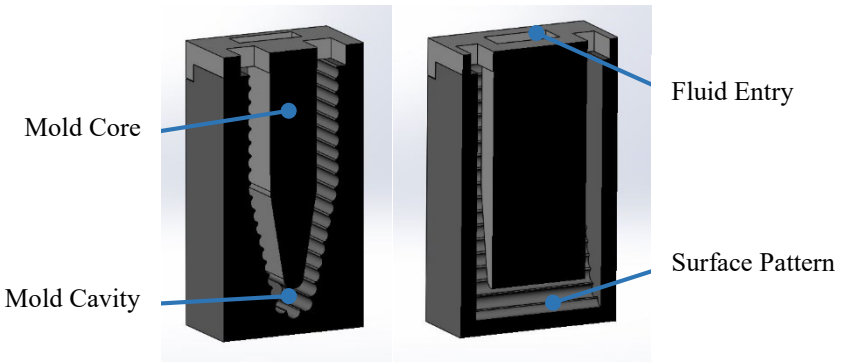

Figure 4-19: Cross Section of Mold Design

4.3.12 Gripper Assembly

Gripper subsystem assembly consists of multiple components. The complete part list and mass calculation for the gripper system are presented in Appendix I. The assembly consists of three-finger modules and palm structure. The total weight of the gripper subsystem is approximately 12.38 N. Figure 4-20 presents the gripper in retracted mode. Appendix K.20 contains the detailed gripper assembly drawing.

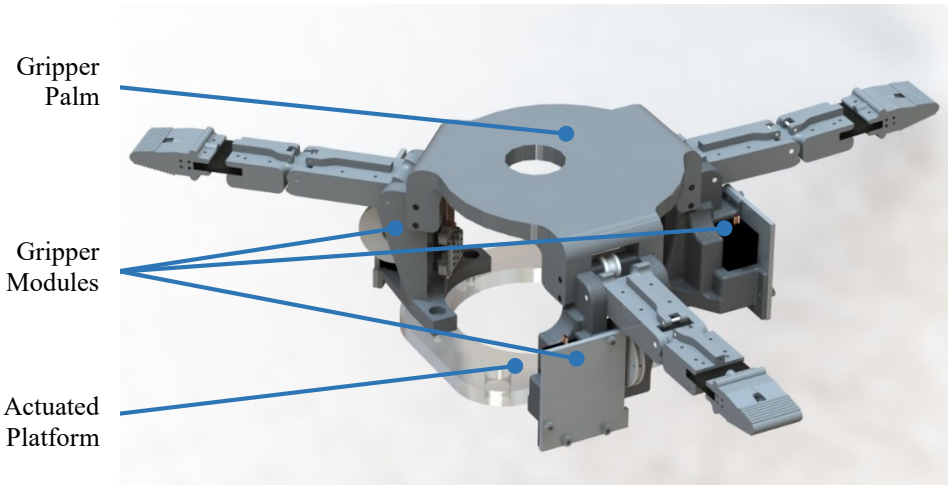

Figure 4-20: Gripper Subsystem Assembly

Integration of the gripper subsystem with the machine tool subsystem and reconfiguration subsystem impacted the geometric design of the gripper subsystem. This is evident in the proportions of the gripper, hole in the gripper palm, kinematic structure of each gripper module and gripper subsystem as a whole. Each of the gripper housing is attached to the linearly actuated platform that was presented in Section 4.4. The resultant gripper structure forms a closed-kinematic chain. Each gripper module receives support from the gripper palm and the linear platform. This prevents deformation between the fingers, which causes slippage.

4.3.13 Workspace of Finger – 3R Approximation

The workspace of a gripper is an essential measure of the capability of the design. Gripper workspace may be approximated by treating all three joints as revolute. The kinematic equations of the finger mechanism can be computed using equations for x and y position as the mechanism is characteristic of a Three Revolute (3R) planar mechanism. The Denevit-Hartenberg (DH) method was used. Figure 4-21 presents the attributed DH parameters and Table 4-9 assigns the parameters.

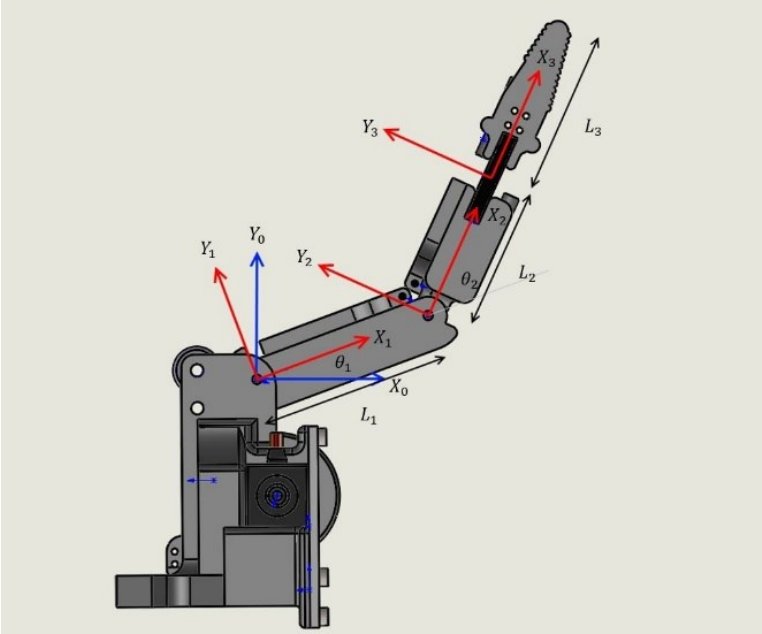

Figure 4-21: Annotated Side view of 3R planar mechanism

Table 4-9: Denevit-Hartenberg parameters

Joint i	a_{i-1}	α_{i-1}	d_i	θ_i
1	0	0	0	θ_1
2	L_1	0	0	θ_2
3	L_2	0	0	θ_3
4	L_3	0	0	0

Individual Homogenous Transformation Matrices:

$$ {}^{0}_{1}T = \begin{bmatrix} \cos\theta_1 & -\sin\theta_1 & 0 & 0 \\ \sin\theta_1 & \cos\theta_1 & 0 & 0 \\ 0 & 0 & 1 & 0 \\ 0 & 0 & 0 & 1 \end{bmatrix} $$

$$ {}^{1}_{2}T = \begin{bmatrix} \cos\theta_2 & -\sin\theta_2 & 0 & L_1 \\ \sin\theta_2 & \cos\theta_2 & 0 & 0 \\ 0 & 0 & 1 & 0 \\ 0 & 0 & 0 & 1 \end{bmatrix} $$

$$ {}^{2}_{3}T = \begin{bmatrix} \cos\theta_3 & -\sin\theta_3 & 0 & L_2 \\ \sin\theta_3 & \cos\theta_3 & 0 & 0 \\ 0 & 0 & 1 & 0 \\ 0 & 0 & 0 & 1 \end{bmatrix} $$

$$ {}^{3}_{4}T = \begin{bmatrix} 1 & 0 & 0 & L_3 \\ 0 & 1 & 0 & 0 \\ 0 & 0 & 1 & 0 \\ 0 & 0 & 0 & 1 \end{bmatrix} $$

Product of Homogenous Transformation Matrices:

$$ {}^{0}_{4}T = \begin{bmatrix} \cos(\theta_1+\theta_2+\theta_3) & -\sin(\theta_1+\theta_2+\theta_3) & 0 & L_3\cos(\theta_1+\theta_2+\theta_3)+L_2\cos(\theta_1+\theta_2)+L_1\cos(\theta_1) \\ \sin(\theta_1+\theta_2+\theta_3) & \cos(\theta_1+\theta_2+\theta_3) & 0 & L_3\sin(\theta_1+\theta_2+\theta_3)+L_2\sin(\theta_1+\theta_2)+L_1\sin(\theta_1) \\ 0 & 0 & 1 & 0 \\ 0 & 0 & 0 & 1 \end{bmatrix} $$

MATLAB is used to determine all possible points of the tip of the distal phalanx. Refer to Appendix D.6 for the MATLAB simulation code. The resultant point cloud is presented in Figure 4-22.

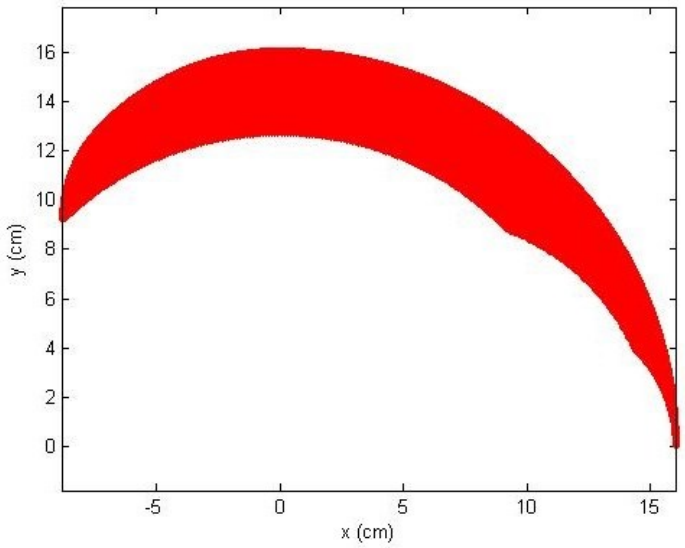

Figure 4-22: MATLAB Two-Dimensional Point Cloud of Finger indicating Workspace

Based on the result of the workspace of each finger, the grasp range of three-finger gripper assembly is approximated. Figure 4-22, in conjunction with Appendix K.20, is used to approximate minimum and maximum x and y parameters of the gripper system. Minimum radius and height are 50 mm and 90 mm respectively, maximum radius and height are 120 mm and 155 mm, respectively.

The working envelope was calculated as a cylindrical volume due to the geometry of the gripper configuration. A minimum and maximum volume of $0.00071\ m^3$ and $0.00701\ m^3$ are approximated for the gripper finger.

4.4 Reconfiguration Subsystem

The function of the linear actuator was to provide linear motion through a motor-driven screw assembly. Consideration of performance factors includes stroke, maximum rated load and maximum rated speed. Screws are commonly driven through the direct coupling, belt and pulley or gear mechanism.

4.4.1 Requirements and Specifications

The requirements of the Reconfiguration Mechanism (RM) link from Section 3.2. The reconfiguration system was designed to meet the secondary function of changing orientations between machining and part handling. In summary, the developed mechanism was required to perform linear actuation of the gripper system. The linear actuator must conform to the integrated “demanded quality” requirements of the RREE listed in Table 3-1. Based on the requirement of scalability, the actuator drive components must be upgradable. The mechanical design must be compact, inexpensive and lightweight.

Table 3-3 in Section 3.7 defined the specifications of the gripper system. Maximum volume of the RREE is 0.027 cubic metres; this volume is cubic. Based on the dimensions of the machine tool and gripper subsystems, the stroke length of the linear actuator must be less than 100 mm. This is to achieve reconfiguration between machining and part handling. The maximum cycle time between modes was 60 s.

4.4.2 Methodology – Linear Actuator

The methodology for the development of the reconfiguration subsystem is summarised in Figure 4-23. The principal mechanism of linear motion was determined based on the design requirements and specifications. Estimation of the actuated load was calculated for drive motor selection. This is followed by the selection of the power transmission system. The time between reconfiguration modes was predicted based on the properties of the mechanism. Finally, the CAD model of the linear actuator subassembly is presented.

Figure 4-23: Linear Actuator Subsystem Design Methodology

4.4.3 Selection of Linear Mechanism

Conversion of rotational motion to linear motion was achieved by linear screw and nut. ACME Lead screw typically hold loads without power, provide good positional accuracy, reduced friction and consume less power to turn. The screw is readily available and provides fast linear motion for a few rotations. These screws are low cost as compared to ground ball screws. The lead screw material is stainless steel, and nut material is brass. Specification of the lead screw is presented in Table 4-10.

Table 4-10: Specification of Linear Screw

Screw Pitch	2 mm
Screw Lead	8 mm
Screw Angle	29°
Threaded Length of Screw	74 mm
Screw Diameter	8 mm
Thread Type	Trapezoidal
Number of Starts	4

The lead screw was mounted at both ends utilising radial bearings. Flange pillow block bearings were selected for this purpose. 608 2RS ball bearing, of inner diameter 8 mm provide smooth bi-directional rotation. These supports provide a low-cost option that is easy for assembly. Power screw is coupled using two grub screws.

Linear guides are essential for successful implementation of the linear actuator. Rails provide accurate linear motion but are expensive and bulky. Linear shaft and linear bearing are utilised for this purpose. The mechanism provides reasonably accurate linear motion, is cost-effective and readily available. Linear shaft diameter must be minimised due to compact specification - solid stainless steel shaft of diameter 8 mm due to this factor. The linear shaft was mounted at both ends through 8 mm linear shaft support. These supports provide a low-cost option that is easy for assembly. Linear shaft was coupled using two grub screws.

4.4.4 Load Estimation of Linear Axes

The estimation of torque required to drive a power screw was necessary for the selection of electric motor. The torque required to raise the load T_R is estimated by Equation 4.18. The efficiency of the linear actuator was calculated using Equation 4.19. Detailed calculation is contained in Appendix B.3.

$$T_R = \frac{Wd_m}{2}\left[\frac{f\pi d_m + L(\cos\alpha_n)}{\pi d_m \cos\alpha_n - fL}\right] + \frac{Wf_c d_c}{2} \quad (4.18)$$

$$\eta = \frac{WL}{2\pi T_R} \quad (4.19)$$

Taking into account friction losses from linear guides, the torque required to raise the load was 0.058 Nm. To account for losses in the system - a safety factor of 2 was used. The minimum torque of the motor was 0.12 Nm. The efficiency of the linear actuator was calculated 55.71% means of Equation 4.19.

4.4.5 Selection of Drive Motor

Given the torque and power requirements to raise the load in Section 4.4.4, the drive motor was selected. The drive motor is a critical component of the linear actuator design as it provides the speed, torque and power. Stepper motors provide accurate motion control and are commonly used in low-cost CNC machines. The Natural Electrical Manufacturers Association (NEMA) 17 Stepper motor was selected based on output specification, low-cost, and ease of control. The variant that was selected for the prototype produces 0.12 Nm at 1500 RPM. This satisfies the torque required to raise the load with a safety factor of 2. Specifications of NEMA 17 HWPSMT609 stepper motor are presented in Table 4-11.

Table 4-11: Specifications of NEMA 17 Stepper Motor [116]

Step Angle	1.8°	
Voltage Rating	3.4 V	
Current Rating	1.7 A	
Holding Torque	0,392266 Nm	* 0.12 Nm
Frame Size	42.3 x 42.3 mm	
Shaft Diameter	5 mm	
Body Length	40 mm	
Mass	240 g	

*Required theoretical value

4.4.6 Selection of Power Transmission

Power transmission is a critical component of the linear actuator design. The rotational motion generated by the drive motor must be transferred from the motor shaft to the lead screw. Gear, belt-pulley and direct coupling transmission systems are commonly used in linear actuators. Each of the transmission types is ideally suited for different applications. Based on the low-cost and compactness requirement, belt-pulley power transmission was selected. A timing belt was required for stepper motor drives. There are many timing belt-pulley conventions. The calculated speed and torque were used in conjunction with the chart presented in Appendix G.2 to select the type of belt-pulley system. The 2 mm pitch GT2 configuration was selected due to support of speed, availability and cost. The pulley should have a minimum of 16 teeth. Due to availability of belt and pulley components, 6 mm width belt and pulley were chosen for the design. Maximum surface speed for GT2 timing belts was found to be 38 m/s [102]. The maximum rotational speed of the belt was determined by Equation 4.20.

$$n = \frac{v_s \times 60}{\pi \times d_m} \quad (4.20)$$

The pitch diameter of the motor pulley is 12.7 mm [102]. The resultant maximum rotational speed of the belt was 29029.86 RPM. To select belt combination, design considerations of the power screw and NEMA 17 stepper motor were considered. Appendix B.3 contains detailed calculations. The approximate distance between centres of the power screw and the stepper motor is defined in Section 3.7. Given this length of 40 mm, the approximate belt length is determined.

The specification of the selected lead screw and electric motor require pulleys of inner diameter 8 mm and 5 mm respectively. GT2 pulleys with these hub diameters and 20 teeth are available. The transmission ratio was 1:1, as NEMA 17 motor provides estimated torque and speed for the operation. The length of the timing belt was determined by means of Equation 4.21. Since the drive ratio is 1:1, Equation 4.21 was simplified to Equation 4.22.

$$L_R = 2 \times A \times \sin\left(\frac{\beta}{2}\right) + \frac{t}{2} \times (z_g + z_k + (1 - \frac{\beta}{180}) \times (z_g - z_k) \quad (4.21)$$

$$L_R = 2 \times A + \pi \times d_w \quad (4.22)$$

Using the centre distance of 40 mm - belt length was 119.90 mm. Due to the unavailability of a belt with this specific length, a 120 mm belt was selected.

4.4.7 Estimated Reconfiguration Time

Given required torque of 0.12 Nm, the corresponding speed was determined from Appendix G.2 as 1500 RPM. Linear speed in mm/s is determined by Equation 4.23. Travel time in seconds for 74 mm length of the lead screw is calculated by Equation 4.24. Detailed calculation is contained in Appendix B.3.

$$v_l = nL \quad (4.23)$$

$$\Delta t = \frac{\Delta x}{v_l} \quad (4.24)$$

The maximum permissible linear speed of the linear actuator is 200 mm/s. The drive takes 0.34 seconds to move 74 mm at maximum linear speed.

4.4.8 Robot Mount Design

The connection of the end-effector and robotic manipulator occurs through a customised bolted coupling. The coupling has multiple mounting holes for attachment to many industrial robots. The mounting standard has been adhered to; however, different manufacturers use different hole-diameters and mounting specifications. As with any end-effector, a coupling is required. In the case of the proposed design, this coupling is not difficult to adapt depending on the available robot. Figure 4-24 presents the attachment mount for the developed end effector. The eight red holes are the locations of bolted joint coupling between robot and end-effector. The end-effector has been adapted for use with Fanuc M10IA robot. Aluminium 6082-T6 stock is used in the design. Refer to Appendix K.21 for the detailed drawing.

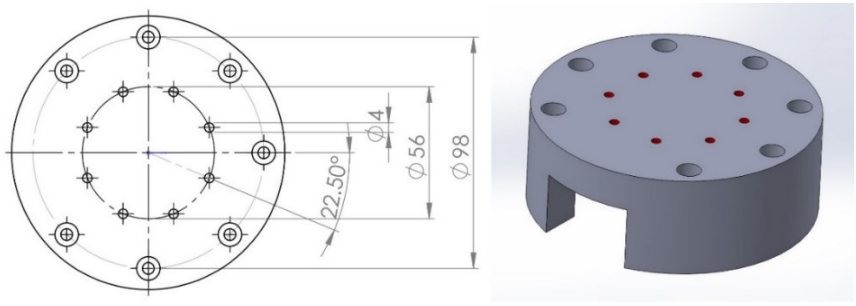

Figure 4-24: End effector-robot mount

Table 4-12 presents specifications of four different serial manipulators. Some specifications of the robots are the payload and mounting dimensions. The end-effector mount shown in Figure 4-24 is adaptable to the mounting specifications of these robots by merely adding the desired holes. The mounting dimensions specify hole-centreline diameter, hole diameter, number of holes and the degree of recurrence.

Table 4-12: Popular Industrial Robot General Specifications

Industrial Robot	Payload (kg)	Reach (mm)	Mounting dimension (mm)
Fanuc M10iA	10	1422	56 x 4 (8) 22.5°
KUKA KR AGILUS	6-10	706.7-1101	31.5 x 5 (8) 22.5°
ABB IRB 1660	6-10	1200	80 x 6.8 (6) 45°
STAUBLI TX2-90	20	1450	50 x 5 (4) 90°

4.4.9 Linear Actuator Assembly

Assembly of all components is presented in Figure 4-25. Scalability of the end-effector was realised in the mechanical design of each subsystem. Figure 4-25 (a) presents the main platform, which functions as a central mount. The gripping, mounting and cutting systems are attached to the main platform. It is robust, lightweight and rigid as it supports the entire machine. Aluminium 6082-T6 plate of 10 mm thickness was used in the design. Figure 4-25 (b) illustrates the gripper platform, which is the mounting point for the gripper modules. The plate is linearly actuated and satisfies the reconfiguration requirement. Actuation is achieved by two linear guides and a lead screw. The plate has the lead screw nut, and two linear bearings press fitted for stability. Aluminium 6082-T6 plate of 10 mm thickness was used in the design.

Figure 4-25 (c) presents the solid model of the spindle mount. This component functions as the mounting point for the free end of the gripper and spindle subsystems. The plate is mounted to the base of the spindle housing. Aluminium 6082-T6 plate of 10 mm thickness was used in the design. The actuator is suited for rapid reconfiguration of the end-effector. The linear bearings are press-fit into the gripper platform. The thickness of the aluminium plate is 10 mm and the length of the linear bearing is 24 mm; therefore, the bearing is assembled so that the excess 14 mm is spaced in 7 mm intervals at the top and bottom. This enhances the stability of the gripper platform during motion. The lead nut is press-fitted and fastened using 4 bolted joint connections. Refer to Appendices K.22 – K.24 for detailed drawings of plate components.

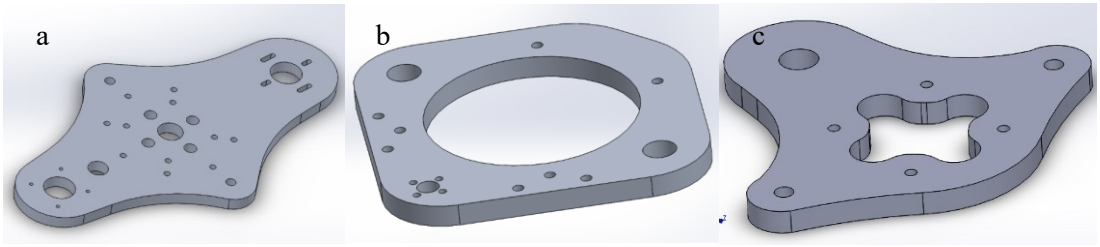

Figure 4-25: CAD Model (a) Main Platform (b) Gripper Platform (c) Spindle Mount

The robot mount is connected to the main platform by seven bolted joints. Rod end mounts secure the linear rails onto the main platform and is interference fit to the spindle mount. The lead screw is mounted on the main platform and spindle mount through flange pillow block bearings. The stepper motor is mounted to the main platform, as indicated in Figure 4-26. Components of the linear drive system are readily replaceable; additionally, the reconfiguration system is robust and compact.

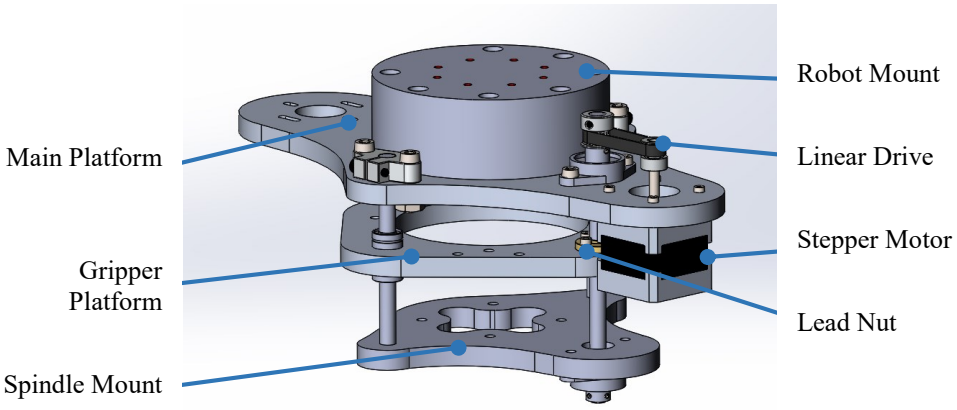

Figure 4-26: Assembly of Linear Actuator System

The integration of all subsystems produced a mechanically stable all-metal design. A bottom view of the system is presented in Figure 4-27 (a); the end-effector is in machining mode. The ER11 collet nut is easily accessible to loosen and tighten using a wrench tool. The gripper fingers remain above the gripper palm, and the retraction system ensures that no contact occurs between the gripper fingers and machining operation. Figure 4-27 (b) presents an elevated view of the end-effector. All components are below the robot mount which simplifies attachment of the end-effector to robotic manipulators.

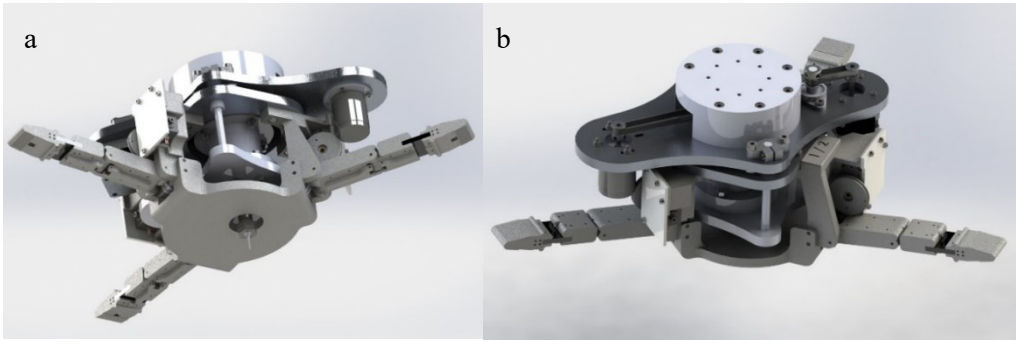

Figure 4-27: CAD Rendering of Reconfigurable End-Effector (a) Bottom View (b) Top View

4.5 Chapter Summary

This chapter discussed the mechanical design of all three subsystems. The design specifications of each subsystem originated from quality function deployment conducted in Chapter 3. A methodologic approach for the design of each subsystem was presented. Expert design models were utilised for the machine tool (Section 4.2) and gripper (Section 4.3) subsystems. Detailed mechanical design was conducted for each designed element. Manufacturability was considered at each stage of the design process. The selection of each motor was validated based on the performance specification. The workspace of the developed gripper was computed, and work volume was approximated in Section 4.3.7. Estimated reconfiguration time was calculated based on the theoretical performance of the linear actuator. Finally, complete assemblies of each subsystem were presented in Sections 4.2.7.3, 4.3.12 and 4.4.9. Figure 4-28 presents two CAD renderings of the RREE assembled to the Fanuc M10IA serial industrial robot.

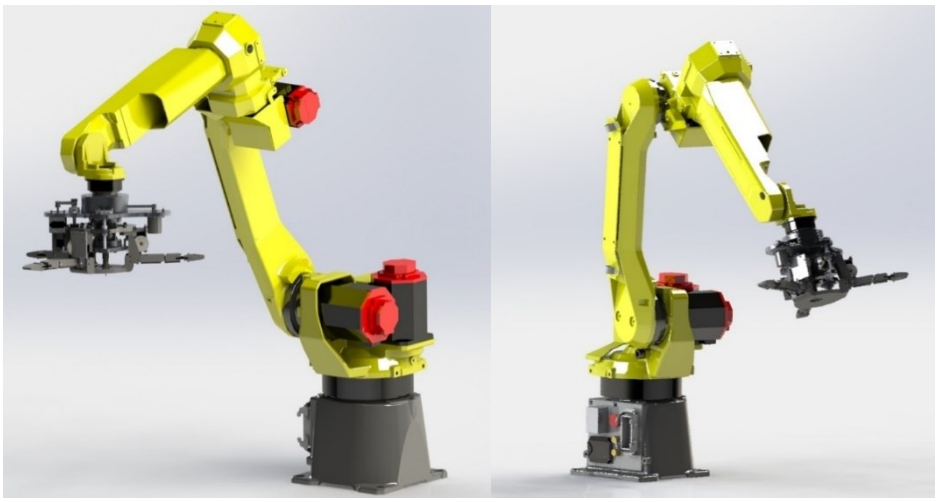

Figure 4-28: Rendering of RREE assembled to Fanuc Robot

The next chapter presents system modelling and analysis. Engineering methods, such as FEA and FEM, are used to validate the structural integrity of the designed components. Cutting force prediction models are used to determine the cutting forces induced by the metal cutting operation. Dynamic behaviour of subsystems of the RREE is determined using modal analysis.

Chapter 5 System Modelling and Analysis

5.1 Introduction

Engineering methods of modelling are used to determine the characteristics of the designed RREE. FEA is used to compute the strength and operational properties of the designed components of the RREE. FEM is used to predict the cutting forces produced in the milling process. Dynamic behaviour of the machine tool spindle is predicted through modal analysis in NX Nastran environment. Mechanistic cutting force model is used in conjunction with MATLAB to predict forces at the tooltip for milling aluminium 6061. Finite Element Analysis of the spindle shaft is predicted through structural analysis in NX Nastran environment. Compliant behaviour of flexible rubber joint is predicted using non-linear FEA in SolidWorks simulation environment. Strength analysis of reconfigurable mechanism is conducted using NX Nastran solver. Modal analyses are conducted on the developed spindle shaft and end-effector subassembly. The modal analysis is used to determine the resonant-natural frequencies of each structure. This type of analysis is independent of loading conditions; however, it does depend on the constraints of the model and its geometry. The purpose of such analysis for this research is inductive to the safe operation of the machine tool. These natural frequencies induce large deformations and stresses in each structure. Thus, the critical speeds of rotation are determined for these computed natural frequencies.

5.2 Mechanistic Cutting Force Simulation

To proceed with the machine-tool design - the cutting forces were needed. The cutting forces constrain the spindle design as motor power and torque are strongly related to cutting forces. Altintas and Budak [117] developed a Mechanistic Cutting Force model to determine the forces generated by the end milling process. These forces are used in FEA to determine the structural characteristics of the designed shaft. Tangential, radial and axial forces acting on a differential flute element with height dz are computed by Equations 5.1, 5.2 and 5.3. The elemental cutting forces are resolved into feed, normal, and axial directions. These forces are computed by Equations 5.4, 5.5 and 5.6, respectively [6].

$$dF_{t,j}(\varphi, z) = \left[K_{tc} h_j(\varphi(z)) + K_{te}\right] dz \tag{5.1}$$

$$dF_{r,j}(\varphi, z) = \left[K_{rc} h_j(\varphi(z)) + K_{re}\right] dz \tag{5.2}$$

$$dF_{a,j}(\varphi, z) = \left[K_{ac} h_j(\varphi(z)) + K_{ae}\right] dz \tag{5.3}$$

$$dF_{x,j}\left(\varphi_j(z)\right) = -dF_{t,j}\cos\left(\varphi_j(z)\right) - dF_{r,j}\sin\left(\varphi_j(z)\right) \tag{5.4}$$

$$dF_{y,j}\left(\varphi_j(z)\right) = dF_{t,j}\sin\left(\varphi_j(z)\right) - dF_{r,j}\cos\left(\varphi_j(z)\right) \tag{5.5}$$

$$dF_{z,j}\left(\varphi_j(z)\right) = dF_{a,j} \tag{5.6}$$

These equations were used to simulate the cutting forces generated in the end milling of Aluminium 6061. Table 5-1 indicates the assumptions that were made based on the work material and cutter geometry defined in Section 4.2.1.

Mechanistic Cutting Force model is used in conjunction with MATLAB to solve Equations 5.4, 5.5, and 5.6 at the tooltip for milling Aluminium 6061. The MATLAB code and complete numerical solution are contained in Appendices D.2 – D.4 and D.5, respectively.

Table 5-1: Cutting Force Simulation Assumptions

Symbol	Assumption	Symbol	Assumption	Symbol	Assumption	Symbol	Assumption
K_{tc}	805 MPa	K_{te}	6 N/mm	a and d	2 mm	φ_{st}	85°
K_{rc}	418 MPa	K_{re}	6 N/mm	c	0.1 mm/tooth	φ_{ex}	100°
K_{ac}	227 MPa	K_{ae}	1 N/mm	N	2	β	30°

To compute the total cutting force; the cutting flute is segmented into a finite number of differential elements along the cutting flute curve [6]. The total cutting force components acting on the flute at an instant are obtained by numerically integrating the force components on a differential element [117]. These forces were integrated over an axial depth of cut to produce the three elemental cutting forces using Equations 5.4, 5.5, and 5.6. The graph presented in Figure 5-1 presents the horizontal (feed) cutting force as the cutter enters and exits the material. The normal cutting force is plotted as a function of the immersion angle in Figure 5-2. All three cutting forces are plotted against the immersion angle of the tool. The axial cutting force is plotted against the immersion angle and is presented in Figure 5-3.

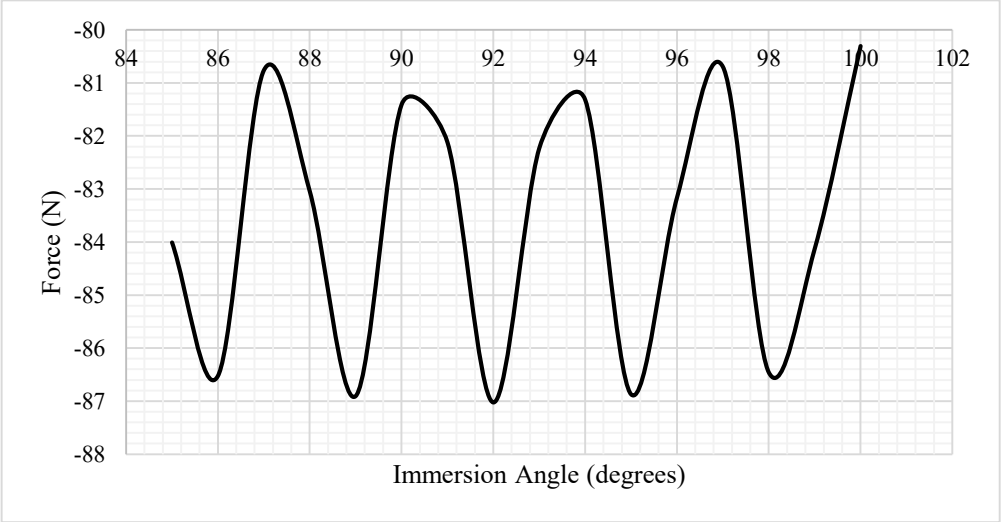

Figure 5-1: Simulated Feed Cutting Force versus Immersion Angle

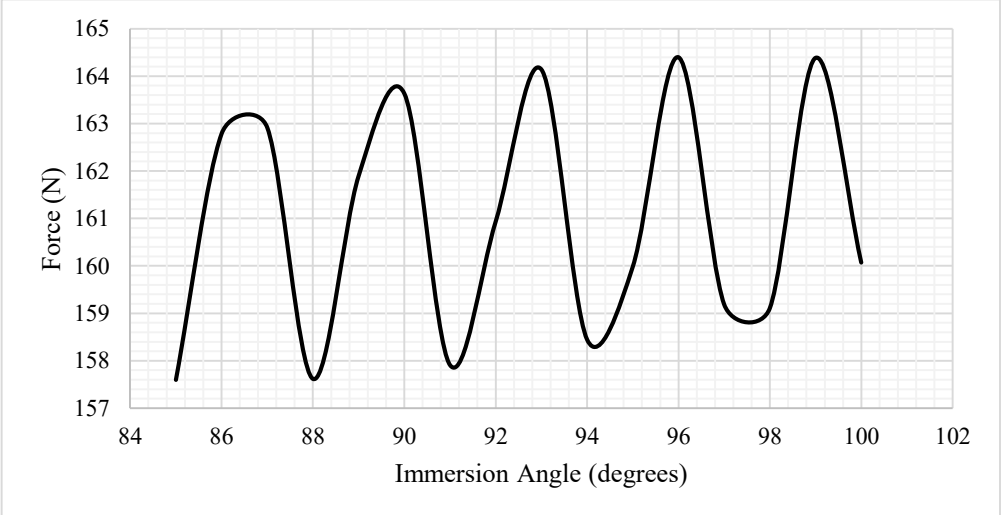

Figure 5-2: Simulated Normal Cutting Force versus Immersion Angle

Figure 5-3: Simulated Axial Cutting Force versus Immersion Angle

The theoretical cutting forces represent the forces generated at the tooltip workpiece engagement. The numerical simulation yielded maximum forces of – 87.0245 N, 164.397 N and 4 N for feed, normal and axial respectively. The solution of the forces is necessary as it represents part of the input loads in FEA.

5.3 Structural Simulation of Spindle Shaft

5.3.1 Model Setup and Solver Selection

Metal cutting is a delicate process; machine tools are often used for prolonged periods. As such, machine tool failure as a result of fatigue fracture of the spindle shaft is not uncommon [118]. A static structural analysis NX10 SOL101, Linear was conducted to determine the Von-Mises stress and displacement of the shaft. The solid model consists of the designed spindle shaft, GT2 pulley, ER11 tool holder assembly (collet holder, nut and 3.175 mm collet) and endmill cutter. The purpose of this simulation study is to determine the magnitude and location of the maximum elemental stress on the designed spindle shaft. The spindle shaft experiences combined loading by the axial, normal and feed cutting forces. The motor torque on the spindle shaft adds to the loading on the shaft.

5.3.2 Material Assignment

Spindle shaft material is AISI 4340 Alloy Steel, GT2 Pulley material is Aluminium 6061, ER11 Collet assembly material is AISI 5140 Alloy Steel, and endmill material is Tungsten Carbide. Table 5-2 contains the material properties of these components.

Table 5-2: Material Properties [119, 120]

Material	ρ	Y	ν	G	σ_y	UTS
AISI 4340 alloy steel *	7.85	193000	0.284	80000	470	745
Aluminium 6061 *	2.711	68980	0.33	24000	241.70	275.95
AISI 5140 alloy steel	7.85	200000	0.285	80000	295	570
Tungsten Carbide	15.88	686000	0.22	283000	360	530

*These material properties were used from the NX Material Database

5.3.3 Loads, Constraints and Contact Regions

Table 5-3 indicates the loading conditions on the spindle shaft. These are the maximum cutting forces computed in section 5.2 and the maximum torque of the NTM BLDC motor. The applied loads are

visualised by the red vectors presented in Figure 5-4. The non-translational constraint was applied on the radial surfaces at the location of bearing mount to the shaft. This constraint fixes all translational degrees of freedom and frees all rotational degrees of freedom. The constraints are visualised by the blue vectors presented in Figure 5-4. The solid model contains multiple components with different material assignments. The relation and association between components are necessary to obtain a realistic solution. The surface-to-surface glueing simulation object type was used to constrain all bodies together. Figure 5-5 presents an image of the association vectors that were generated by the simulation object. The symmetric gold shapes visualise these vectors.

Table 5-3: Specification of Loading Conditions

Load type	Load location	Magnitude	Direction
Torque	GT2 pulley inner race	0.6 Nm	Clockwise
Force	Tooltip	164.397 N	y
Force	Tool tip	87.0245 N	-x
Force	Tooltip	4 N	z

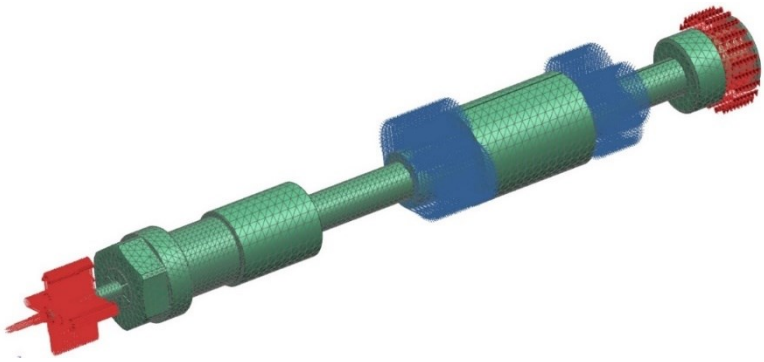

Figure 5-4: Simulation Loads and Constraints on Spindle Shaft

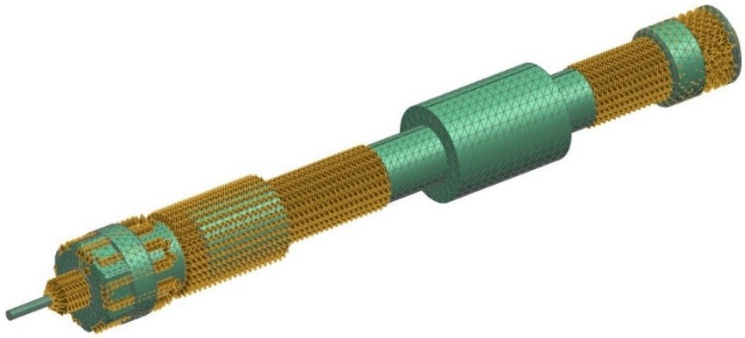

Figure 5-5: Simulation Surface Gluing on Spindle Shaft

5.3.4 Mesh Configuration

Three-dimensional volume meshes are automatically generated for solid geometric models. The volume mesh has a tetrahedral shape with several Jacobian points. Siemens NX 10 Advanced Analysis provides two such mesh elements – a four Jacobian point element and a ten Jacobian point element. Ten-point

element is best suited for three-dimensional models with complex curvature and many geometric details. Figure 5-6 presents the three-dimensional tetrahedral ten-point element. The object has four faces with six edges; each edge contains three Jacobian points.

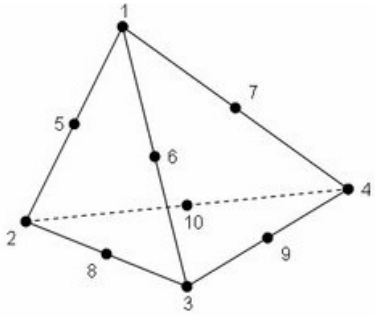

Figure 5-6: 3D Tetrahedral 10 Node Mesh Element [121]

A 3D tetrahedral mesh element CTETRA10 was used. Refer to mesh element definition in Section 5.3.5. NX element quality checker was used to confirm mesh information and mesh metrics. All elements passed the check with values within the standard range. Find the settings for mesh testing in Appendix C.1. Four volume meshes were generated as the model consists of thirteen components. Endmill meshed with 1 mm CTETRA10 elements; Spindle shaft meshed with 1 mm CTETRA10 elements, ER11 collet holder meshed with 1 mm CTETRA10 elements and the GT2 pulley meshed with 1 mm CTETRA10 elements.

Additionally, Free mapped meshing was attempted, the mid node method was mixed, surface curvature-based size variation was 50%, and the element growth rate through volume was set at 50%. A minimum of two elements through-thickness was used, and the transition element size was used. Small feature tolerance of 10% element size was used. 265544 mesh elements and 447434 mesh nodes were generated. The maximum and minimum element size is 3.64504 mm and 0.05566 mm, respectively. The Jacobian ratio of the 3D mesh is 1, and the aspect ratio is 26.40602. The Jacobian ratio is excellent, while the aspect ratio is within the acceptable range [122].

5.3.5 Mesh convergence of CTETRA10 Element

Mesh quality is pivotal to a successful simulation result. While mesh metrics such as Jacobian and aspect ratio provide useful tolerance checks, they do not ensure that the mesh provides an accurate solution. Loads and constraint are equally crucial to meaningful FEA. A mesh convergence study was conducted to validate the CTETRA10 element used for analyses conducted in Sections 5.3, 5.4, 5.5, 5.8 and 5.9. Mesh convergence determines whether or not the critical stresses converge to a specific value [123]. FEA convergence investigates the relationship between mesh density and a critical design parameter. In this study, element size defines mesh density as smaller size mesh elements produce a denser mesh. Maximum Von-Mises stress is selected as the critical parameter. A minimum of four data points is advised for a successful mesh convergence plot [124]. The spindle shaft model was used for the analyses. Additional components such as the pulley, tool holder and endmill were removed. Five data points were generated for five simulation runs, from 5 mm to 1 mm element size in 1 mm increments. Figure 5-7 presents the mesh convergence plot for the study. The maximum Von-Mises stress converged to approximately 354 MPa as 2 mm element size was reached.

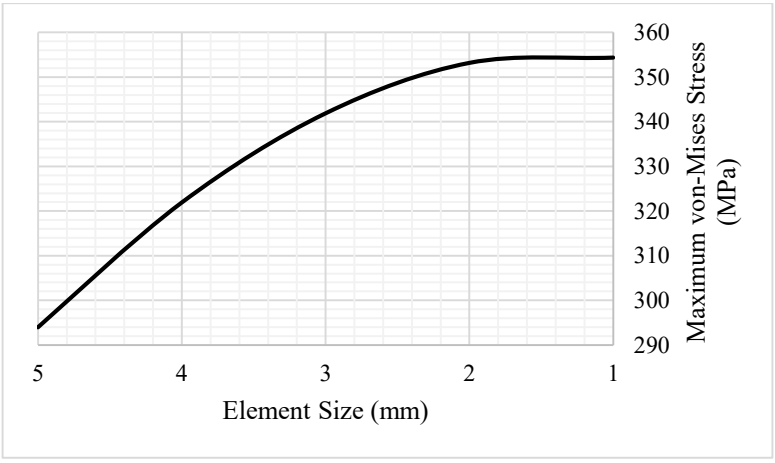

Figure 5-7: Mesh Convergence Plot for CTETRA10 Element

5.3.6 Simulation Result

Figures 5-8 and 5-9 present the Von-Mises elemental stress and nodal displacement simulation results, respectively. Maximum elemental stress of 1071.25 MPa occurred at the neck of the endmill, as indicated in Figure 5-8. The endmill geometry was simplified for the simulation model; therefore, the flute geometry was not included. These cutting peripheries add structural rigidity to the tool; nevertheless, the resulting maximum Von-Mises stress of 1071.25 MPa occurred in a similar direction to the normal force. Maximum nodal displacement of 0.913 mm was observed at the tooltip, as indicated in Figure 5-9. This deformation is sub-millimetre and is acceptable due to the small scale design of the machine tool. These results are not the primary concern of this analysis. The maximum Von-Mises stress and deformation of the designed spindle shaft are investigated.

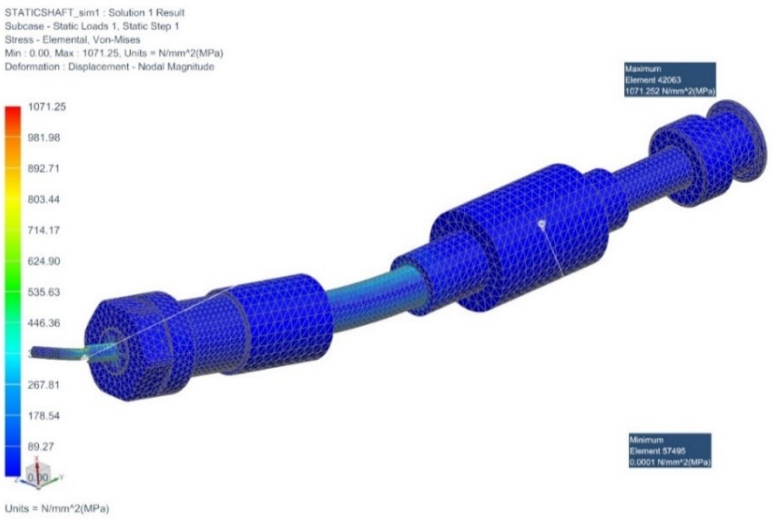

Figure 5-8: Spindle Shaft Assembly Von-Mises Elemental Stress Fringe Plot

Since the analysis was based on the designed spindle shaft, the failure criterion is not based on the entire assembly. Instead, it is based on the maximum Von-Mises stress of the spindle shaft. The purpose of this simulation was to validate the designed spindle shaft. To determine the Von-Mises elemental stress and nodal displacement of the spindle shaft, the post view feature in NX was used.

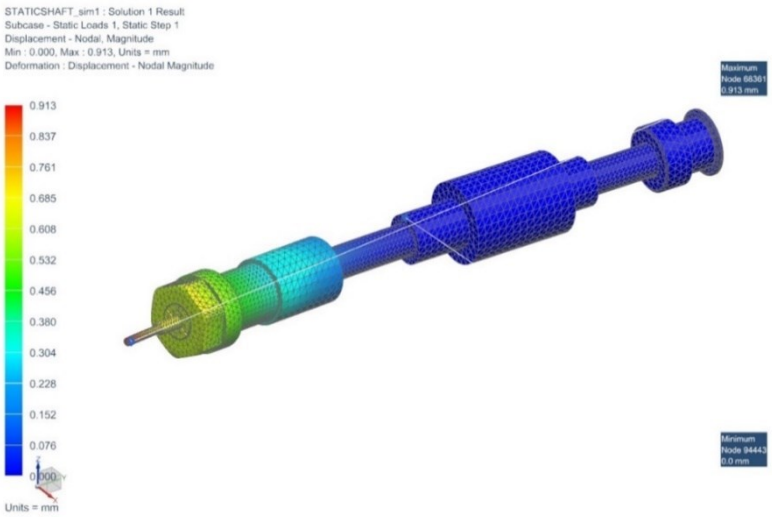

Figure 5-9: Spindle Shaft Assembly Nodal Displacement Fringe Plot

The fringe plots presented in Figures 5-10 and 5-11 indicate the range of stresses and deformation that occur in the shaft as a result of the imposed loading conditions. A maximum Von-Mises elemental stress of 353.16 MPa occurred at the first step of the shaft (collet holder – front bearing collar) as indicated in Figure 5-10. A localised stress concentration was expected at this location as fillets were not used in the shaft design. These fillets are challenging to manufacture on a manual lathe due to the small size of the shaft. Nonetheless, the Von-Mises failure criterion for UTS yielded a safety factor of 2.11 for the shaft design. This safety factor is acceptable, and the design is validated. Maximum nodal displacement of 0.388 mm was observed at the collet holder mounting-end of the shaft, as indicated in Figure 5-11. The resultant deformation is sub-millimetre and is acceptable.

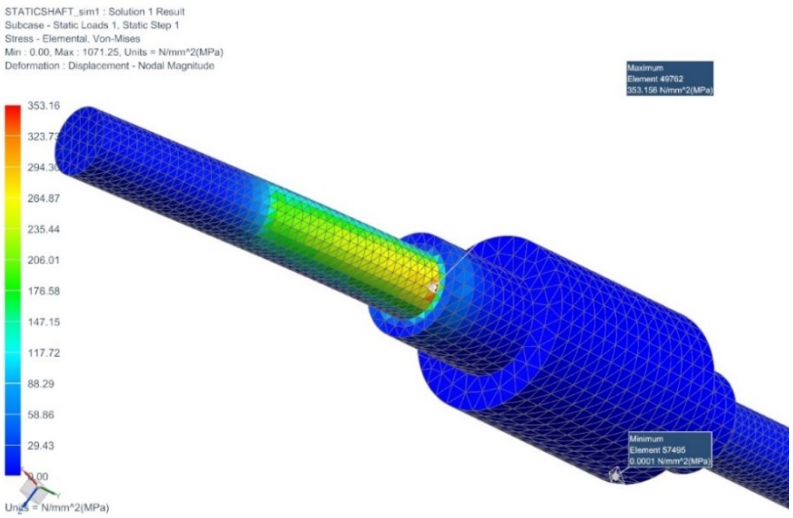

Figure 5-10: Spindle Shaft Von-Mises Elemental Stress Fringe Plot

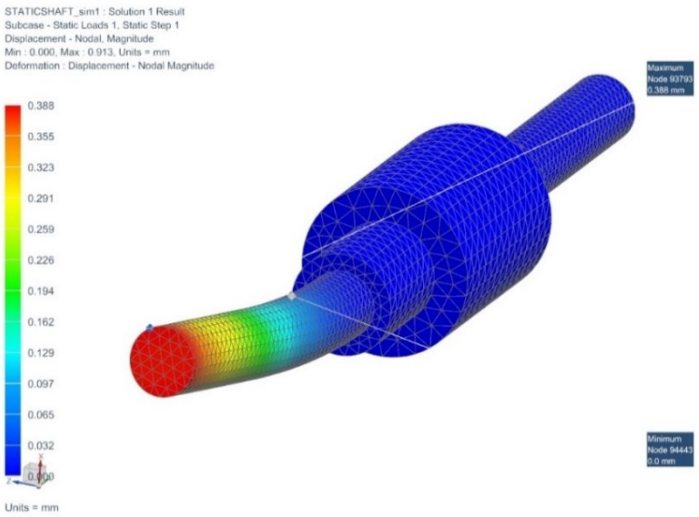

Figure 5-11: Spindle Shaft Nodal Displacement Fringe Plot

5.4 Modal Simulation Spindle Shaft

5.4.1 Model and Solver Selection

Machine failure as a result of large spindle deformation caused by self-excited vibration is uncommon. However, there is a possibility that these vibrations might occur. The purpose of this dynamic simulation was to predict these natural frequencies. The modal deformation characteristics at these frequencies are significant as critical speeds are determined. The simulation model is composed of the solid geometry of the spindle shaft. Threaded regions on the shaft were removed to reduce computation time, adding small features requires denser mesh. This requires more solution iterations and hence a longer computation time. The spindle shaft geometry was imported into the NX Nastran modelling environment. SOL103 Real Eigenvalues structural simulation was conducted using NX NASTRAN solver. The Lanczos eigenvalue parameter was selected; seven vectors were defined. MASS method for normalizing eigenvectors was used. The simulation computed the first ten-mode shapes.

5.4.2 Material Assignment

Mesh collector was used for Isotropic AISI 4340 material property assignment for the spindle shaft. Table 5-2 contains the material properties of AISI 4340 alloy steel.

5.4.3 Loads, Constraints and Contact Regions

A non-translational constraint was applied on the radial surfaces at the location of the bearing mount to the shaft. This constraint fixes all translational degrees of freedom and frees all rotational degrees of freedom. The constraints are visualised by the blue vectors presented in Figure 5-12.

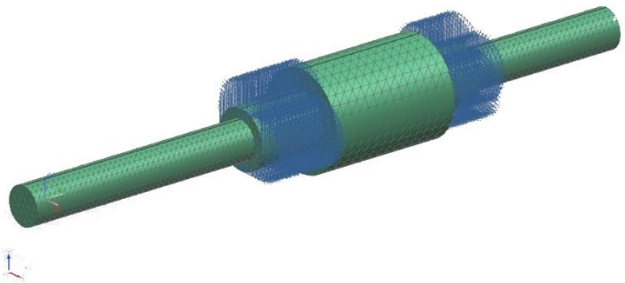

Figure 5-12: Simulation Constraints on Spindle Shaft

5.4.4 Mesh Configuration

A 3D tetrahedral mesh CTETRA10 of 1 mm element size was used. Refer to mesh element definition in Section 5.3.5. NX element quality checker was used to confirm mesh information and mesh metrics. All elements passed the check with values within the standard range. Find the benchmark for mesh testing in Appendix C.1. Additionally, Free mapped meshing was attempted, the mid node method was mixed, surface curvature-based size variation was 50%, and the element growth rate through volume was set at 50%. A minimum of two elements through-thickness was used, and the transition element size was used. Small feature tolerance of 10% element size was used. 47448 mesh elements and 74629 mesh nodes were generated. The maximum and minimum element size is 3.00919 mm and 0.34129 mm, respectively. The Jacobian ratio of the 3D mesh is 1, and the aspect ratio is 10.14806. The Jacobian ratio is excellent, while the aspect ratio is well within the acceptable range [122]. Jacobian ratio is a measure of correlation from a meshed element to the ideally shaped element [125]. Aspect ratio defines the measurement of the equality of all sides of a mesh element [126]. These mesh metrics measure the accuracy and reliability of the 3D Mesh; it is essential to check that these are within acceptable ranges to ensure a viable computation.

5.4.5 Simulation Result

The mode shapes were solved by the NASTRAN solver. Table 5-4 presents the results of nodal displacement and elemental stress of the dynamic simulation. Figures 5-13 to 5-17 present the deformation behaviour of the spindle shaft for the first ten natural frequencies. These frequencies are used to calculate the critical speed of the rotating shaft in Section 5.6. Refer to Appendix C.2 for the complete set of plots for all modes.

Table 5-4: Dynamic Simulation Results

Mode	Frequency (Hz)	Nodal Displacement (mm)	Elemental stress (MPa)
1	2045	14.12	20560000
2	2046	14.13	20070000
3	4286	16.84	60010000
4	4287	16.84	49770000
5	12000	14.26	107000000
6	12010	14.26	104700000
7	15040	14.11	88390000
8	21900	16.89	164500000
9	23470	9.89	112100000
10	23640	17.15	289300000

Figure 5-13 presents the modal deformation plots for the first two-mode shapes. The first mode shape shows bending about the 8 mm diameter shaft step at the tool holder coupling. A deformation of 14.12 mm occurs at the end of the shaft at 2045 Hz. The second bending mode occurs at the second mode shape. At 2046 Hz the shaft deforms 14.13 mm in the y-direction at the location of the tool holder coupling.

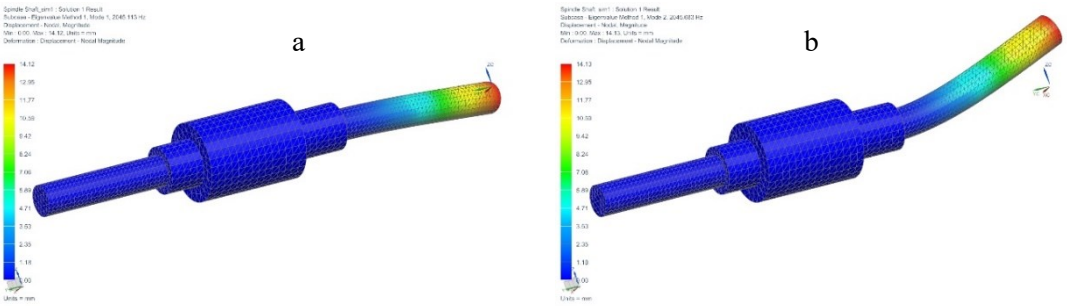

Figure 5-13: Mode 1 and 2 Deformation Plot

Figure 5-14 presents the modal deformation plots for modes three and four, both of which are first-order bending modes. A deformation of 16.84 mm occurs in the third in the location of the pulley mount at 4286 Hz. In the fourth mode, an equivalent deformation as in the third mode occurs at the same location but in the – x-direction. Both modes occur at approximately the same frequency.

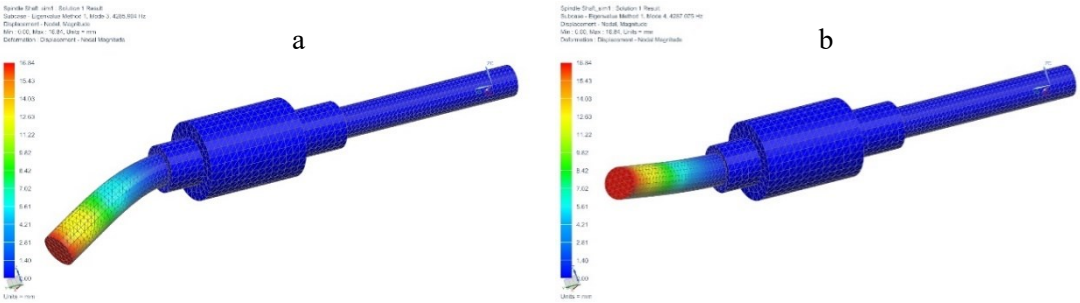

Figure 5-14: Mode 3 and 4 Deformation Plot

Mode five indicates the fifth bending mode of vibration; it is presented in Figure 5-15 (a). At 12000 Hz, a deformation of 14.26 mm occurs at the tool-holder coupling end of the spindle shaft. The sixth mode presented in Figure 5-15 (b) displays elements of bending and radial expansion at the tool-holder coupling end of the spindle shaft. At 12010 Hz, the first-order mode of bending produces unstable deformation that inhibits any possibility of machining.

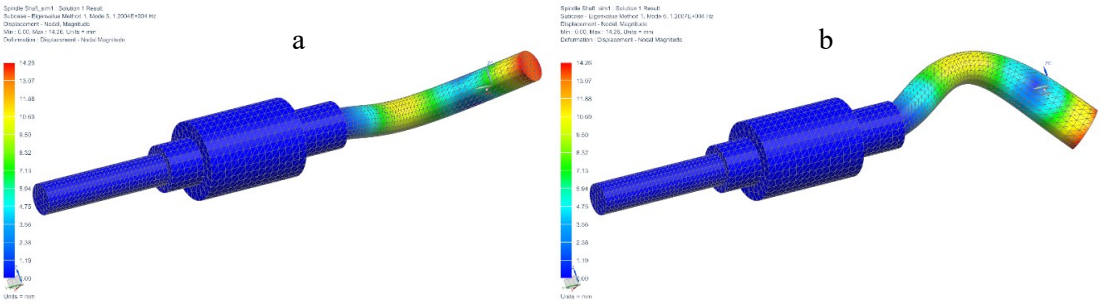

Figure 5-15: Mode 5 and 6 Deformation Plot

Figure 5-16 presents the modal deformation plots of the seventh and eighth modes. Both mode shapes display characteristics of radial expansion. Maximum radial expansion occurs at either end of the spindle

shaft. The seventh mode shape (Figure 5-16 (a)) produces a radial deformation of 14.11 mm, the coupled ER11 tool-holder has a bore diameter of 8 mm. The resultant deformation will induce significant stresses in this component. While, at the other end of the spindle shaft, the eight mode shape produces a radial deformation of 16.89 mm. This deformation occurs in the mounting location of the motor-pulley mount, as presented in Figure 5-16 (b). Significant stresses are therefore produced in the coupling as the pulley has a bore diameter of 8 mm.

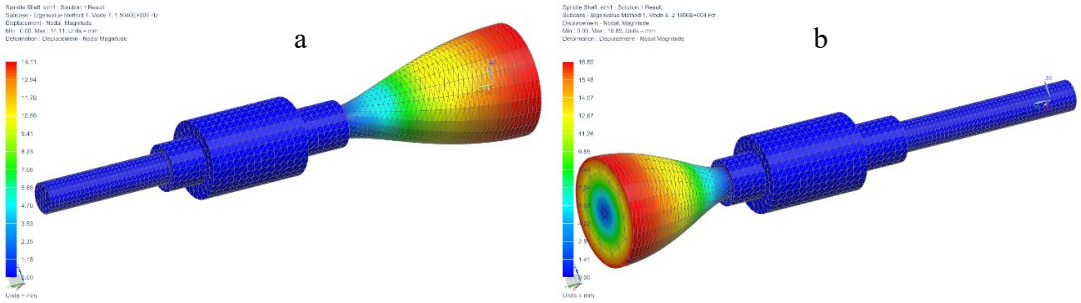

Figure 5-16: Mode 7 and 8 Deformation Plot

The ninth mode shape is prescriptive of elongation along the rotational axis of the spindle shaft. A maximum deformation of 9.89 mm occurs in the y-axis at 23470 Hz. This large deformation occurs at the tool holder shaft 8 mm diameter step, as presented in Figure 5-17 (a). Figure 5-17 (b) presents the mode shape of the tenth natural frequency. Large torsional, bending and expansion are produced at 23640 Hz in the location of the motor-pulley mount. The excitation frequency is a forced frequency whereas the modal or natural frequency is a fundamental unforced frequency of the structure. Resonance occurs when the excitation frequency is equivalent to the natural frequency.

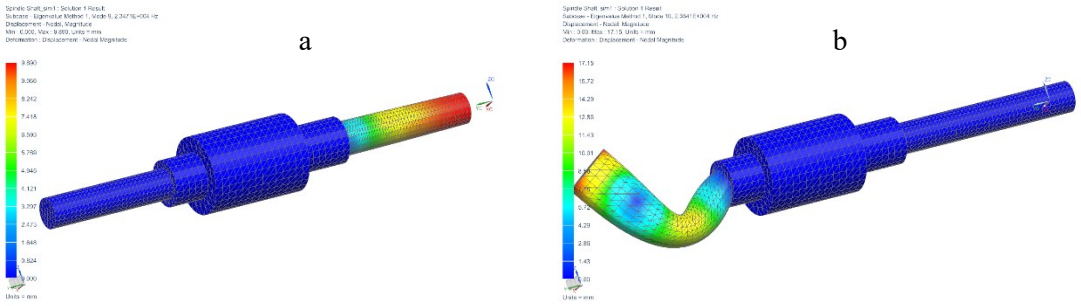

Figure 5-17: Mode 9 and 10 Deformation Plot

5.5 Modal Simulation of Machine Tool

5.5.1 Model and Solver Selection

Machine failure as a result of large spindle deformation caused by self-excited vibration is uncommon. However, there is a possibility that these vibrations might occur. The purpose of this dynamic simulation is to predict these natural frequencies for the machine-tool subassembly. The modal deformation characteristics at these frequencies are significant as critical speeds are determined. A dynamic modal analysis SOL103 Real Eigenvalues was conducted for this purpose. The Lanczos eigenvalue parameter was

selected; seven vectors were defined. MASS method for normalizing eigenvectors was used. The simulation computed the first ten-mode shapes.

5.5.2 Material Assignment

Spindle shaft and bearing material is AISI 4340 Alloy Steel, GT2 Pulley material is Aluminium 6061, ER11 Collet assembly material is AISI 5140 Alloy Steel, and endmill material is Tungsten Carbide. Table 5-2 contains the material properties of these components. The main platform and spindle mount material is aluminium 6082-T6; the mechanical and strength properties are presented in Table 5-5.

Table 5-5: Material Properties [127]

Material	ρ	Y	ν	G	σ_y	UTS
Aluminium 6082-T6	2.7	70000	0.33	26000	260	310

5.5.3 Loads, Constraints and Contact Regions

No loads were applied to the model as the fixed-free frequency response was to be determined. The model was constrained by fixed constraints located at the bolted joint connection holes on the robot mount. Figure 5-18 presents the meshed model; blue vectors represent the constraint. The solid model contains multiple components with different material assignments. The relation and association between components are necessary to obtain a realistic solution. The surface-to-surface glueing simulation object type was used to constrain all bodies together. Simulation object vectors are visualised by the symmetric gold shapes in Figure 5-18.

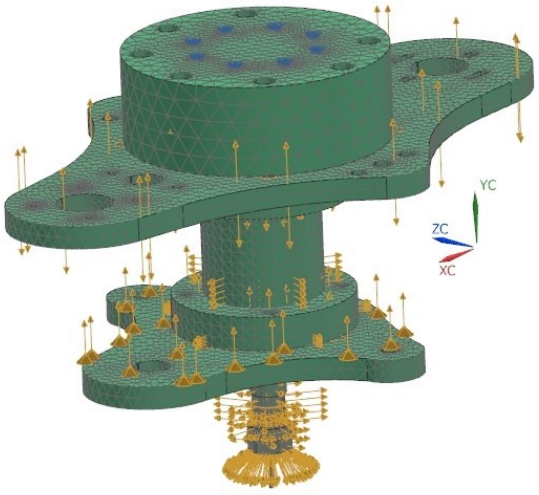

Figure 5-18: Prepared Solid Meshed Model

5.5.4 Mesh Configuration

A 3D tetrahedral mesh element CTETRA10 was used. Refer to mesh element definition in Section 5.3.5. NX element quality checker was used to confirm mesh information and mesh metrics. All elements passed the check with values within the standard range. An element assessment was conducted using NX Nastran standard error limit and warning limit, an aspect ratio greater than 10 but less than 100 is acceptable.

Furthermore, a skew angle of less than 45 degrees but greater than 30 degrees is acceptable. Find the settings for mesh testing in Appendix C.1. Five volume meshes were generated as the model consists of thirteen components. CTETRA10 1.5 mm elements were used for the endmill; the spindle shaft was meshed with 4 mm CTETRA10 elements, ER11 collet holder used 2 mm CTETRA10 elements and the bearings - 4 mm CTETRA10 elements. CTETRA10 elements of 4 mm size were used for the gripper platform, spindle platform, robot mount and main platform.

Additionally, Free mapped meshing was utilised, the mid node method was mixed, surface curvature-based size variation was 50%, and the element growth rate through volume was set at 50%. A minimum of two elements through-thickness was used, and the transition element size was used. Small feature tolerance of 10% element size was used. 66569 mesh elements and 107708 mesh nodes were generated. The maximum and minimum element size is 19.74443 mm and 0.25 mm, respectively. The Jacobian ratio of the 3D mesh is 1 and aspect ratio is 16.67294. The Jacobian ratio is excellent, while the aspect ratio is well within the acceptable range.

5.5.5 Simulation Result

The resultant mode frequencies, nodal displacements and elemental stresses are presented in Table 5-6. The displacement and stress-induced in the first ten natural frequencies are tabulated for both the end-effector subassembly and the spindle shaft.

Table 5-6: Simulated Mode Frequencies, Displacements and Equivalent Stresses

Mode	Frequency (Hz)	Assembly Displacement (mm)	Shaft Displacement (mm)	Assembly Equivalent stress (MPa)	Shaft Equivalent stress (MPa)
1	540.7	7.187	3.688	2611.83	2611.83
2	542.3	7.211	3.694	2524.82	2524.82
3	776.7	4.785	0.191	333.3	284.62
4	998.4	5.256	0.293	638.34	404.8
5	1221	1.618	0.897	1151.93	1047.88
6	1226	2.751	0.772	948.66	948.66
7	1828	6.071	0.447	923.05	390.44
8	2232	2.505	0.453	806.81	540.22
9	2320	5.239	0.162	1051.65	188.63
10	2841	3.419	1.249	1074.78	1074.78

Figures 5-19 to 5-23 present the deformation behaviour of the machine tool subassembly at the first ten natural frequencies. These frequencies are used to calculate the critical speed of the spindle shaft. Refer to Appendix C.3 for the complete set of plots for all modes.

Figure 5-19 presents the modal deformation plots for modes one and two. Both of these mode shapes are first-order bending modes. Figure 5-19 (a) presents the modal deformation plot of the subassembly at 540.7 Hz. While Figure 5-19 (b) presents a deformation of 7.211 mm at 542.3 Hz. These large deformations occur at the tool holder and are induced on the spindle shaft.

The third and fourth mode shapes are presented in Figure 5-20. A deformation of 4.785 mm occurs at 776.7 Hz in the third mode at the spindle motor mount of the main platform, as indicated in Figure 5-20

(a). Both mode shapes are first-order bending modes of the main platform. In the fourth mode at 998.4 Hz, a deformation of 5.256 mm occurs on the mounting platform. However, in this mode, the deflection occurs in the location of the stepper motor mount.

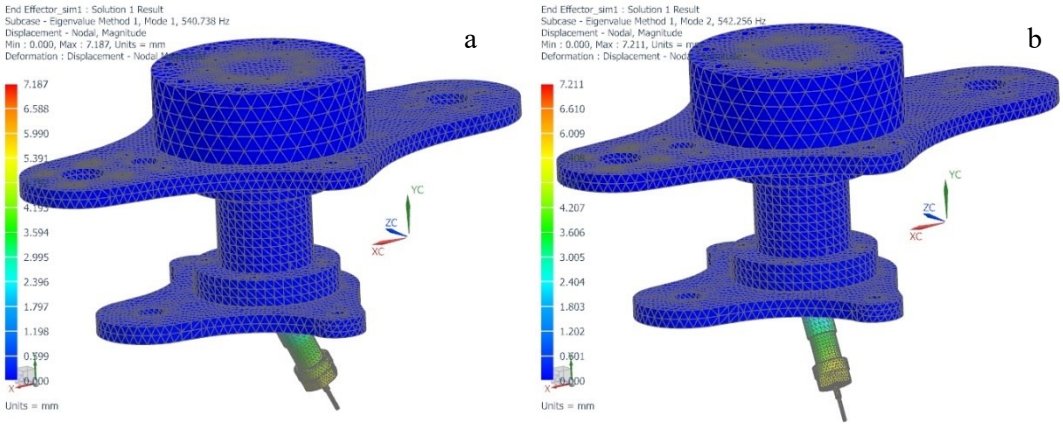

Figure 5-19: Mode 1 and 2 Deformation Plot

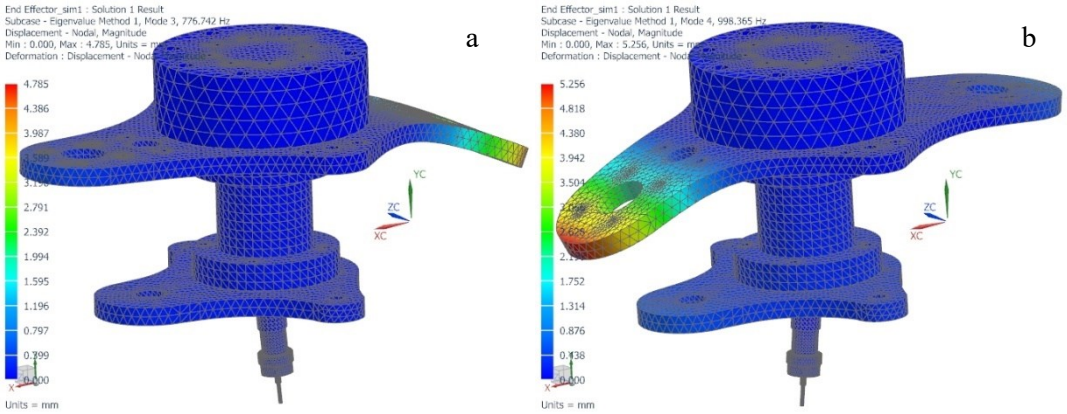

Figure 5-20: Mode 3 and 4 Deformation Plot

The fifth mode shape is presented in Figure 5-21 (a), large bending deformations are present in both the spindle mount and the spindle shaft-tool holder. A deformation of 1.618 mm occurs at the spindle mount plate at 1221 Hz. Figure 5-21 (b) presents the deformation plot of the machine tool subassembly at 1226 Hz. A maximum deformation of 2.751 mm is induced in the spindle mount platform at this resonant frequency. The sixth mode displays bending of the spindle shaft-tool holder, main platform and spindle mount.

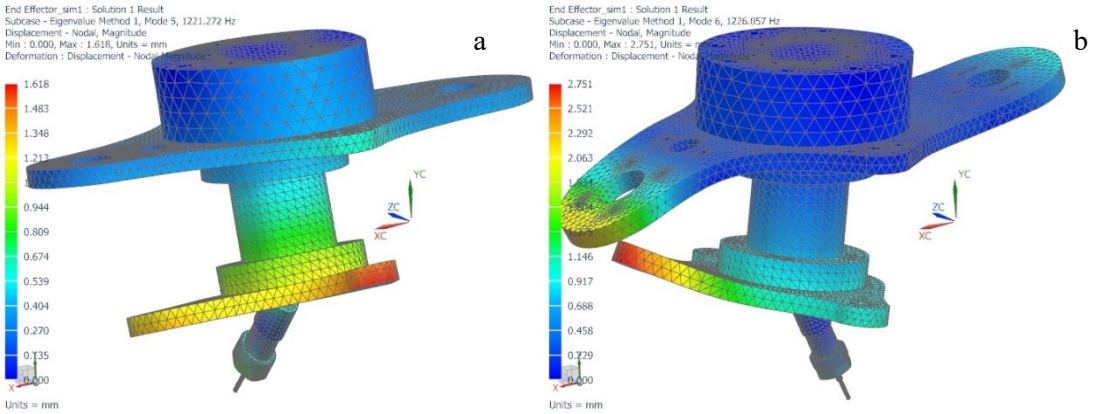

Figure 5-21: Mode 5 and 6 Deformation Plot

Figure 5-22 presents the mode shapes of the seventh and eighth resonant frequencies. At the seventh natural frequency, a first-order bending mode induces critical deformation of 6.071 mm. Figure 5-22 (a) presents the mode shape; the red region depicts the maximum deformation in the spindle mount location. Mode eight is characteristic bending of the spindle mount and twisting in the main platform. A maximum deformation of 2.505 mm occurs at this mode at 2232 Hz, as presented in Figure 5-22 (b).

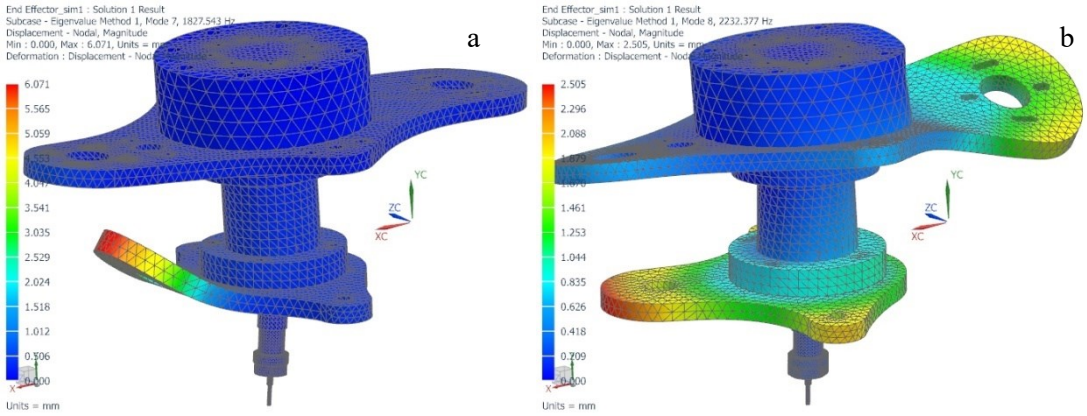

Figure 5-22: Mode 7 and 8 Deformation Plot

Figure 5-23 presents the modal deformation plots for modes nine and ten. Twisting deformation in the ninth mode occurs at the spindle motor mount of the main platform. A maximum deformation of 5.239 mm occurs at 2320 Hz, as presented in Figure 5-23 (a). In the tenth mode, a maximum deformation of 3.419 mm occurs at the spindle platform. At 2841 Hz, torsional mode shape is produced at the main platform, and bending mode shape is induced in the spindle platform. This is presented in Figure 5-23 (b).

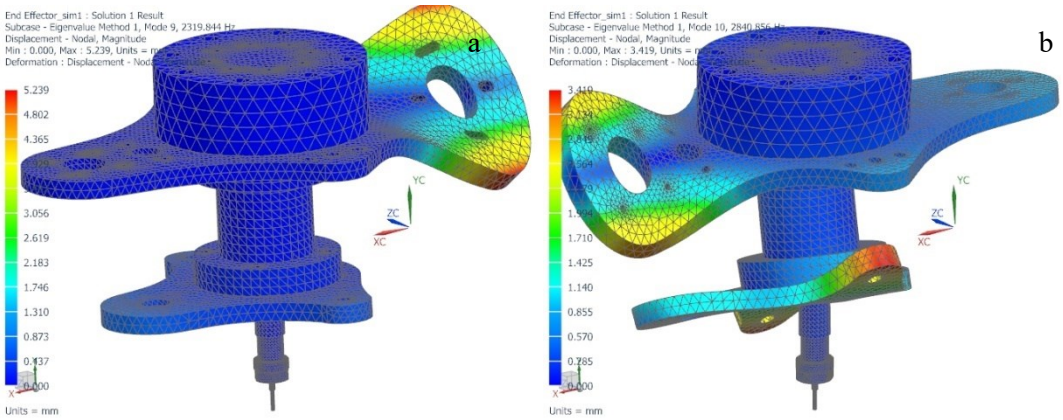

Figure 5-23: Mode 9 and 10 Deformation Plot

Referring to Table 5-6, in conjunction with Figures 5-19 to 5-23 define the natural frequencies of the end-effector subassembly. The subassembly and spindle shaft both have critical deformation at the second natural frequency of 542.3 Hz. This is, therefore, the critical mode from FEA analysis.

5.6 Critical Speed of Shaft

The natural frequencies of the designed Spindle Shaft and Spindle subassembly were determined in Sections 5.4 and 5.5. The critical speed of the spindle shaft was determined for each of these frequencies. This is used to validate the shaft design for the required speed of rotation as calculated in section 4.2.3.2. The required rotational speed for end milling aluminium 6061 with Cleveland C76050 tool at the specified feed rate and depth of cut is 12127.61 RPM. Using this speed as a benchmark, the critical speeds of the spindle shaft are determined. The rotor dynamics are determined based on the calculated natural frequencies using Equations 5.7 and 5.8. Table 5-7 presents the calculated critical speeds for both the spindle shaft (determined in Section 5.4) and machine tool subassembly (determined in Section 5.5).

$$\omega_n = 2\pi f \tag{5.7}$$

$$n_c = \frac{60\omega_n}{2\pi} \tag{5.8}$$

Table 5-7: Calculated Critical Speeds

	Spindle Shaft		Machine Tool Subassembly	
Mode	Frequency (Hz)	Critical Speed (RPM)	Frequency (Hz)	Critical Speed (RPM)
1	2045	122700	540.7	32442
2	2046	122760	542.3	32538
3	4286	257160	776.7	46602
4	4287	257220	998.4	59904
5	12000	720000	1221	73260
6	12010	720600	1226	73560
7	15040	902400	1828	109680
8	21900	1314000	2232	133920
9	23470	1408200	2320	139200
10	23640	1418400	2841	170460

5.7 Non-Linear Simulation of Flexible Joint

5.7.1 Model and Solver Selection

The analysis aimed to determine the advantages of utilisation of flexible joint instead of the solid revolute joint. The simulation model was simplified to investigate the behaviour of this joint. The objective of this simulation is to determine the deformation characteristics of the rubber joint. The simulation model consists of middle phalange, distal phalange and rubber joint. The middle phalanx is constrained by applying a fixed boundary condition at the location of the revolute joint. The purpose of the simulation is to investigate the behaviour of rubber joint. Therefore, the proximal phalanx was not included in the simulation.

5.7.2 Nonlinear Material Model

The material assignment is a necessary step in FEA. Rubber materials are flexible and prone to deformation under small loading conditions. Flexible materials such as rubbers are categorised as hyperelastic materials. Due to its significant deformation characteristic, a suitable strain energy function is required for Finite Element solvers. The Mooney Rivlin material model is used to approximate the strain behaviour of rubber material. The curve-fit method uses polynomial approximations from test data, numerical values of coefficients resulting from the curve-fits are used in FEA programs for mechanical analysis. The FEA software bases the stiffness characteristics of the rubber on these coefficient values.

5.7.3 Material Assignment

Non-linear material model of Butyl Durometer 60 rubber was utilised. PLA material properties are assigned to the phalanges; properties of PLA are presented in Table 5-8. Figure 5-24 presents the stress-strain curve of the non-linear material model. Hyperelastic Mooney Rivlin material model was used in conjunction with the maximum Von-Mises stress failure criterion. SolidWorks simulation environment was used for the simulation.

Table 5-8: PLA Material Properties [128]

Material	ρ	Y	ν	G	σ_y	UTS
PLA	1.252	3500	0.36	1287	70	59

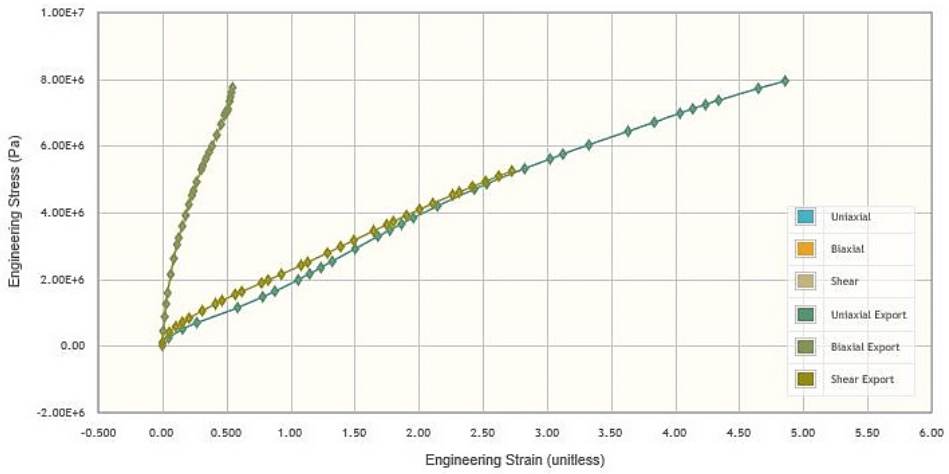

Figure 5-24: Butyl 60 Durometer Stress-Strain Curve [129]

5.7.4 Loads, Constraints and Contact Regions

Figure 5-25 presents the meshed model showing boundary constraint in green and force vector distribution in blue. Total distributed load of 4.488 N was applied to the contact surface of the distal phalanx. This surface will contact the grasped geometry in a pinch grasp. Fixed translational boundary constraint was applied to the middle phalanx, in the location of the revolute joint between the proximal and middle phalanges. Global bonded contact condition was applied to the assembly, to activate mate relations of each part with the other in the assembly. The boundary condition applied ensured that there were no penetration sets between the solid bodies.

5.7.5 Mesh Configuration

Curvature-based solid mesh with 2 mm maximum element size is used, the minimum element size is 0.4 mm. Sixteen Jacobian points with automatic transition and 0.1 mm tolerance were used for the solid assembly. The number of nodes and elements in the mesh was 214581 and 148000, respectively. A maximum aspect ratio of 8.336 with 0% distorted elements (Jacobian ratio) was present in the mesh. Both mesh metrics are within an acceptable range as defined by NAFEMS [124]. Figure 5-25 presents the meshed model.

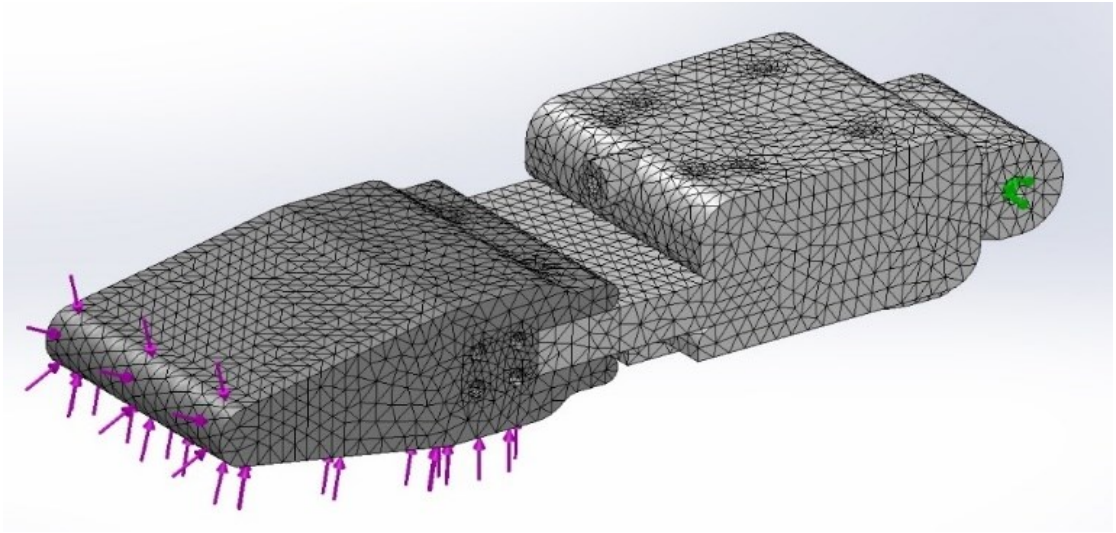

Figure 5-25: Volume Mesh of Finger Partial Assembly

5.7.6 Simulation Result

Figures 5-27, 5-28 and 5-29 indicate the deformation, Von-Mises stress and strain, respectively. The most substantial deformation occurred at the finger-tip while maximum stress occurred at the revolute joint of the middle phalanx. The maximum strain is located within the rubber joint. Figure 5-26 indicates the time-step stress convergence of the non-linear solution for node element 1. The time-step curve for the simulation illustrates the solution result approximation.

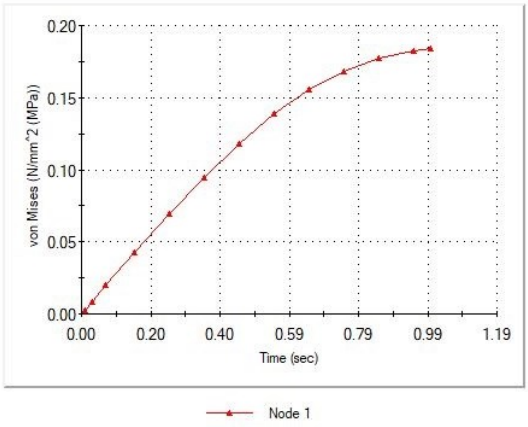

Figure 5-26: Time-step Response Solution Plot

Figure 5-27 presents the equivalent displacement plot of the nonlinear analysis. The distributed force of 4.488 N (indicated by the purple force vectors) induces a maximum displacement of 41.4 mm in the resultant direction of the force vector. This deformation occurs at the tip of the distal phalanx, as indicated by the red region in Figure 5-27. The translucent distal phalanx illustrates the initial position of the structure. Large deformation is observed due to the hyperelastic material property of the rubber joint.

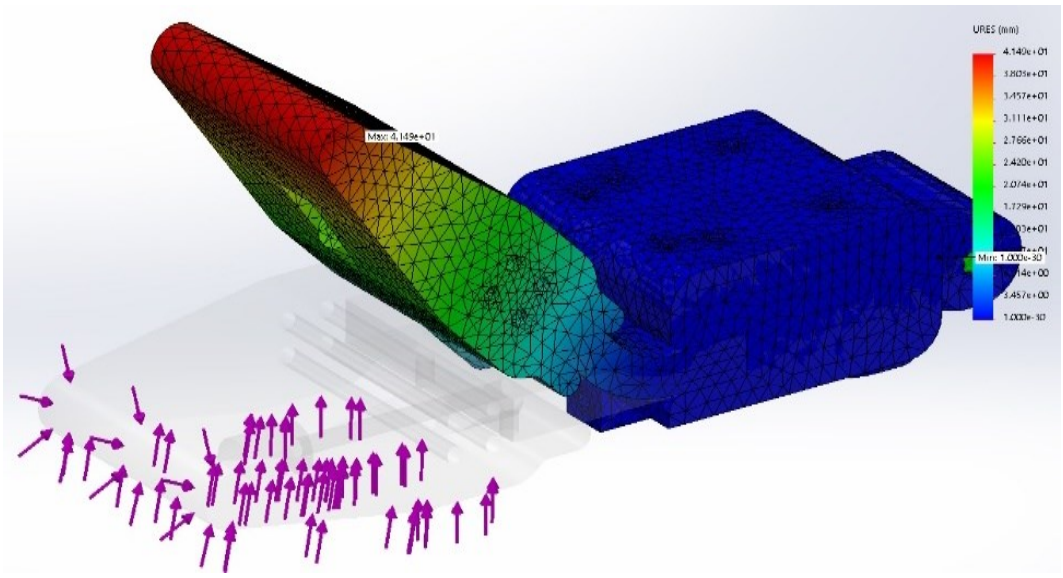

Figure 5-27: Equivalent Displacement Plot

In the nonlinear static analysis, the von-Mises stress result is calculated for the structure. Maximum Von-Mises stress of 3.26 MPa occurs at the joint located in the middle phalanx as indicated by the red region in Figure 5-28. This is due to the large deformation which is produced by the 4.488 N distributed force. The middle phalanx is coupled to the proximal phalanx through this joint. Nevertheless, the Von-Mises failure criterion for UTS yielded a safety factor of 18.1 for the PLA middle phalanx. This safety factor is acceptable, and the design is validated. Minimum Von-Mises stress of 0.00107 MPa occurs in the distal phalanx.

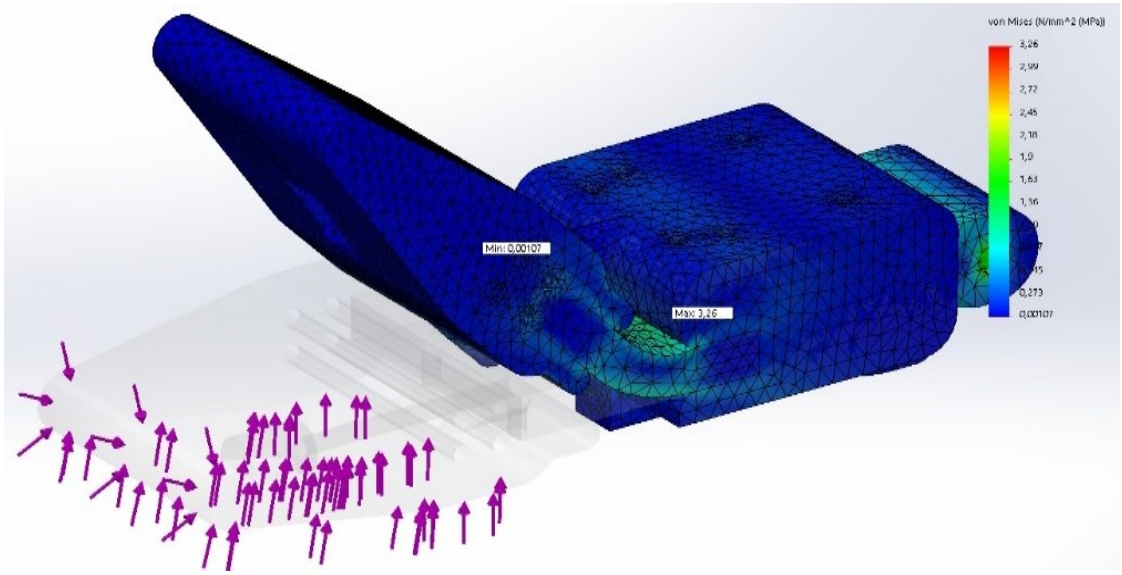

Figure 5-28: Von-Mises Stress Plot

A maximum strain of 0.1816 is produced in the rubber joint as indicated by the red region in Figure 5-29. The most substantial strain occurs on the bottom side of the rubber joint, closer to the exterior surface of the geometry. A small strain is produced at the middle volume of the rubber joint as indicated by the blue mesh region.

Further investigation is conducted in Sections 8.3 and 8.4, which determine the maximum force developed by the RREE gripper for different grasp geometries.

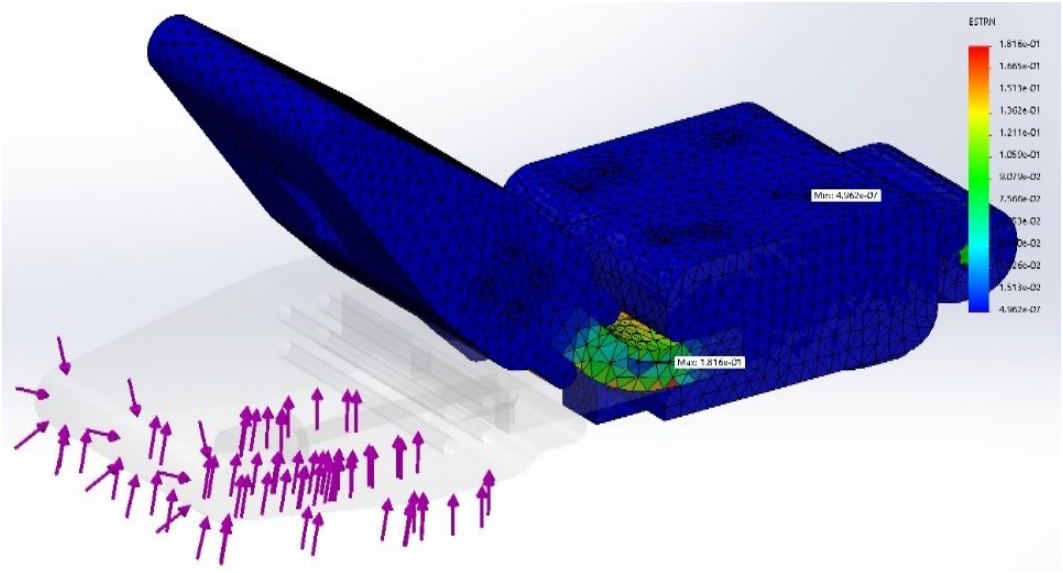

Figure 5-29: Equivalent Strain Plot

5.8 Structural Simulation Main Platform

5.8.1 Model and Solver Selection

A static structural analysis NX10, SOL101, Linear was conducted to determine the Von-Mises stress and maximum deflection of the main platform design [6].

5.8.2 Material Assignment

Table 5-5 contains the material properties of Aluminium 6082-T6.

5.8.3 Loads, Constraints and Contact Regions

Figure 5-30 indicates load conditions and constraints. Non-translational constraints are applied on the inner radial surfaces where the main platform couples to the robot mount. The constraints are indicated by the dark blue pattern in Figure 5-30. Loading conditions are described in Table 5-9. Each load is represented by a different colour vector, as indicated in Table 5-9 and Figure 5-30.

Table 5-9: Specification of Loading Conditions

Load type	Vector Colour	Load location	Magnitude	Direction
Force	Light Blue	Spindle assembly	14.5805049 N	y
Force	Red	Linear rails	1.579501 N	y
Force	Orange	Stepper mount	2.8127232 N	y
Force	Lime Green	Spindle mount	1.8850896 N	y

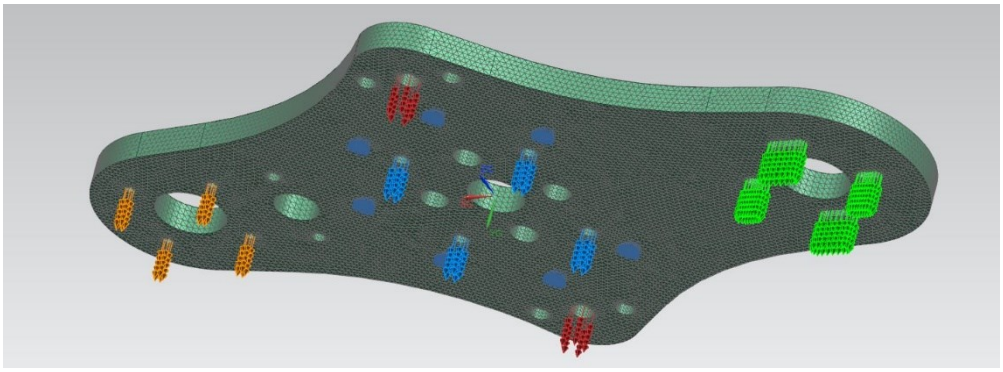

Figure 5-30: Meshed Main Platform with Loads and Constraints

5.8.4 Mesh Configuration

A 3D tetrahedral mesh CTETRA10 of 2 mm element size was used. Refer to mesh element definition in Section 5.3.5. NX element quality checker was used to confirm mesh information and mesh metrics. All elements passed the check with values within the standard range. Find the settings for mesh testing in Appendix C.1. Additionally, Free mapped meshing was attempted, the mid node method was mixed, surface curvature-based size variation was 50%, and the element growth rate through volume was set at 50%. A minimum of two elements through-thickness was used, and the transition element size was used. Small feature tolerance of 10% element size was used. 211364 mesh elements and 332488 mesh nodes were generated. The maximum and minimum element size is 5.14869 mm and 0.46423 mm, respectively. The Jacobian ratio of the 3D mesh is 1 and aspect ratio is 12.43249. The Jacobian ratio is excellent, while the aspect ratio is well within the acceptable range.

5.8.5 Simulation Result

Figures 5-31 and 5-32 indicate Von-Mises stress and maximum deflection, respectively. The most considerable deflection of 0.001352 mm occurred at the stepper motor mount while maximum stress of 0.457 MPa occurred at the mounting hole location. The function of the hole is to allow bolted joint

connection of the main platform with the robot mount. Nonetheless, the Von-Mises failure criterion for UTS yielded a safety factor of 678.34 for the aluminium plate. This safety factor is acceptable, and the design is validated.

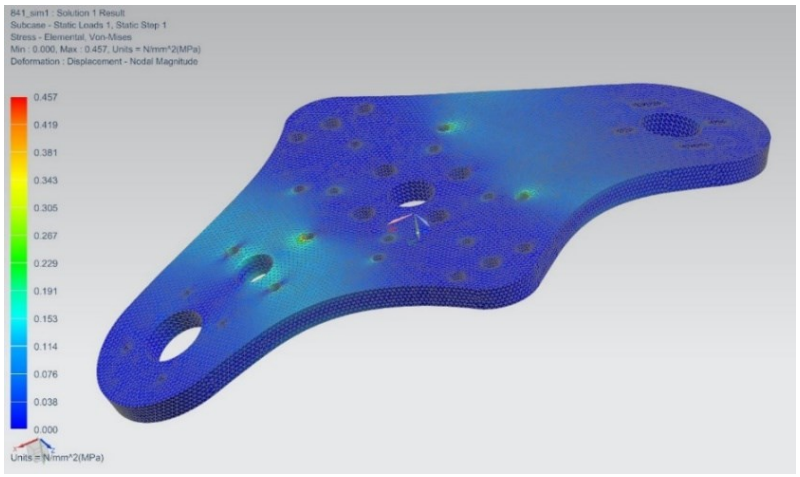

Figure 5-31: Main Platform Von-Mises Stress Plot

Deformation occurred on both ends of the main platform due to the combined loading of the stepper and spindle motors. This validates the geometric design of the platform as the plate is centrally mounted and supports the combined loading.

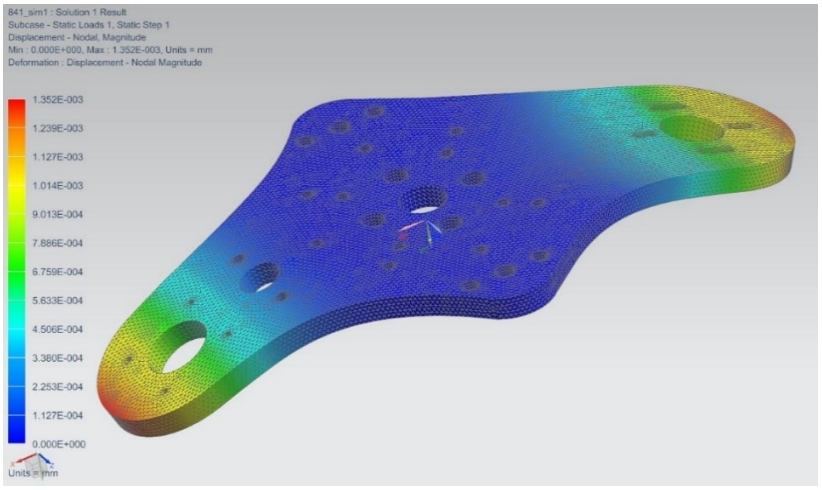

Figure 5-32: Main Platform Displacement

The main platform design was validated by the static structural analysis conducted. Aluminium was used due to its availability and ease of machining. Based on the results of this simulation, engineering plastics are a viable option. Plastics such as HDPE and Delrin have good structural rigidity and strength properties. The use of plastic material decreases the mass of the main platform while offering the required strength to support the combined loading as represented in Table 5-9 and Figure 5-30.

5.9 Structural Simulation Gripper Platform

5.9.1 Model and Solver Selection

Static structural analysis in NX10, SOL101, Linear was conducted to determine the Von-Mises stress and maximum deflection of the gripper platform [6]. The simulation result proves the effectiveness of the designed structure as combined loading cases and constraints are imposed on the model.

5.9.2 Material Assignment

Aluminium 6082-T6 is used as the material for the gripper platform. The isotropic material model is used. Table 5-5 contains the material properties of Aluminium 6082-T6.

5.9.3 Loads, Constraints and Contact Regions

Figure 5-33 indicates load conditions and constraints. Non-translational constraints are applied on the inner radial surfaces where the gripper platform couples to the linear rails. The constraints are indicated by the dark blue pattern in Figure 5-33. Loading conditions are described in Table 5-10. Each load is represented by a different vector, as indicated in Table 5-10 and Figure 5-33.

Table 5-10: Specification of Loading Conditions

Load type	Load location	Magnitude	Direction
Torque	Stepper motor mounting	0.392266 Nm	Clockwise
Force	Gripper assembly	12.3805143 N	y

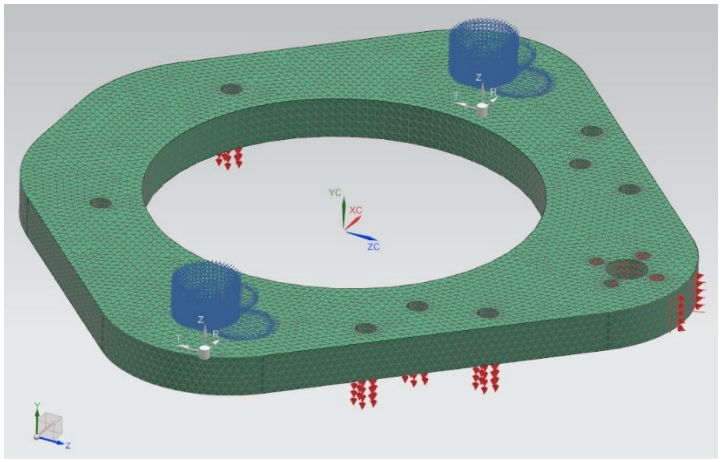

Figure 5-33: Meshed Gripper Platform with Loads and Constraints

5.9.4 Mesh Configuration

A 3D tetrahedral mesh CTETRA10 of 2 mm element size was used. Refer to mesh element definition in Section 5.3.5. NX element quality checker was used to confirm mesh information and mesh metrics. All elements passed the check with values within the standard range. Find the benchmark for mesh testing in Appendix C.1. Additionally, Free mapped meshing was attempted, the mid node method was mixed, surface curvature-based size variation was 50%, and the element growth rate through volume was set at 50%. A minimum of two elements through-thickness was used, and the transition element size was used. Small feature tolerance of 10% element size was used. 93918 mesh elements and 148990 mesh nodes were

generated. The maximum and minimum element size is 5.11148 mm and 0.44441 mm, respectively. The Jacobian ratio of the 3D mesh is 1 and aspect ratio is 11.87834. The Jacobian ratio is excellent, while the aspect ratio is well within the acceptable range.

5.9.5 Simulation Result

Figure 5-34 (a and b) indicate the Von-Mises stress and maximum deflection, respectively. The most substantial deflection of 0.002017 mm occurred at the lead nut mounting hole, as indicated by the red mesh region in Figure 5-34 (b). The maximum stress of 1.017 MPa is produced on the inner surface of the cylindrical hole for the brass lead nut.

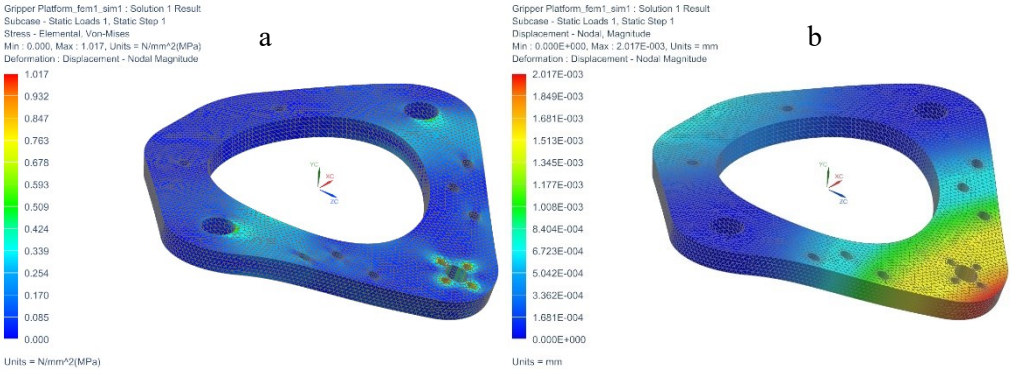

Figure 5-34: Fringe Plot (a) Gripper Platform Stress (b) Gripper Platform Displacement

This result of the Von-Mises failure criterion for Ultimate Tensile Strength yielded a safety factor of 304.82 for the aluminium plate. This safety factor is acceptable, and the design was validated.

Based on the results of this simulation, engineering plastics are a viable option. Plastics such as HDPE and Delrin have good structural rigidity and strength properties. The use of plastic material decreases the mass of the gripper platform while offering the required strength to support the combined loading is represented in Table 5-10 and Figure 5-33.

5.10 Chapter Summary

FEA was used to verify the critical stresses and deformations induced by the loading and constraint couples of the designed components. Modal analyses were used to determine the natural frequencies of the spindle shaft and spindle subassembly in Sections 5.4 and 5.5, respectively. Structural analyses were conducted to determine the Von-Mises failure criterion and maximum deformations of the spindle shaft in Section 5.3. Dynamic behaviour of the machine tool spindle was predicted by means of modal analysis in NX Nastran environment. Section 5.2 presented the mechanistic cutting force model used in conjunction with MATLAB to predict forces at the tooltip for milling aluminium 6061. Critical speeds of the spindle shaft and spindle subassemblies were determined in Section 5.6. Compliant behaviour of flexible rubber joint was predicted using non-linear FEA in SolidWorks simulation environment in Section 5.7. Strength analysis of the designed plate components of the reconfigurable mechanism was conducted using NX Nastran solver in Sections 5.8 and 5.9. The next chapter presents the manufactured full-scale prototype of the RREE. The RREE is an end-effector; as such, it is dependent on a robotic manipulator to perform operations. System integration of the RREE is therefore undertaken in the following chapter.

Chapter 6 Manufacturing and Systems Integration

6.1 Introduction

This chapter presents the manufactured full-scale prototype. In this research, part of the fourth objective (Section 1.4) is to construct and assemble the end-effector. Manufacture of each subsystem is presented with reference to the methods of manufacture. The RREE prototype is assembled onto Fanuc M10IA serial industrial robot. The selection of an electronic control system and software is implemented. Integrated control of all five electric motors is presented using the Arduino microcontroller.

6.2 Machine Tool Spindle Manufacture

The spindle housing and spindle were machined on a manual lathe. The holes on the spindle housing were manually drilled and threaded due to the soft material characteristic of aluminium. Thread on the spindle shaft was delicate to machine due to the small diameter of the shaft. Careful consideration was taken to apply the correct amount of force to prevent deflection in the spindle shaft. Figure 6-1 presents the assembly of the spindle shaft, housing and angular contact bearings. The mass and cost of the components used are presented in Appendices I and J, respectively. The assembly procedure follows the spindle subassembly, MT subassembly and RREE subsystem drawings in Appendices K.5, K.6 and K.27 respectively.

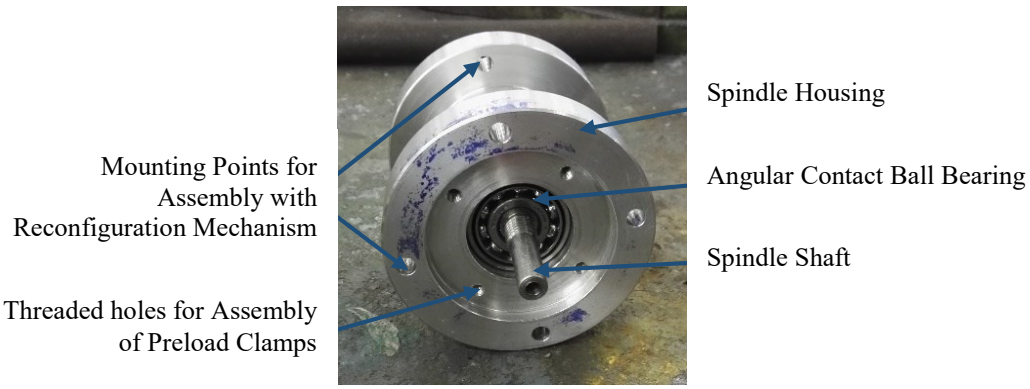

Figure 6-1: Subassembly of the Spindle

6.3 Robotic Gripper Manufacture

6.3.1 3D Printed Components

Rapid prototyping by means of plastic deposition was selected as the manufacturing process for producing the required components. The parts were produced using Creality CR10-S5 3D-printing system. Plastic is deposited layer by layer to build up the part from the base plate. Level calibration was done on the printing bed in order for the 3D print to be perfectly aligned for each layer. Preheat was required on machine bed according to a temperature of 200°C [130].

6.3.2 Mechanical Assembly

All components were printed for the gripper system, and the complete assembly is shown in Figure 6-2. The assembly procedure follows the gripper assembly, and RREE subsystem drawings presented in

Appendices K.20 and K.27, respectively. The mass and cost of the components used are presented in Appendices I and J, respectively.

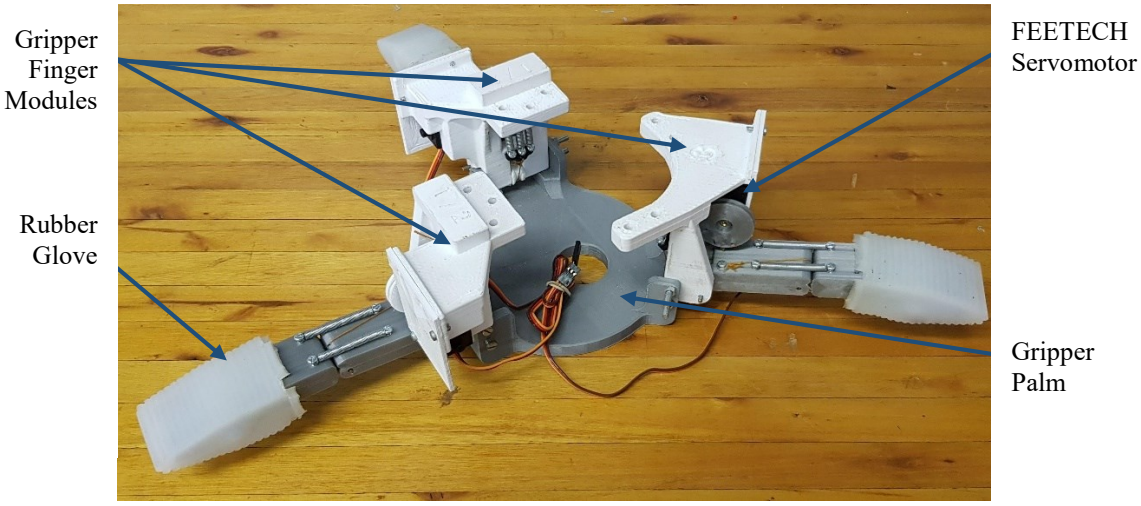

Figure 6-2: Assembled Gripper Subsystem

6.4 Linear Actuator Manufacture

The designed components of the reconfigurable subsystem were manufactured at low-cost using readily available materials and machining processes. The main platform, gripper platform and spindle mount are water jet cut. The jet cutter was unable to attain cuts of features smaller than 5 mm in diameter, therefore scale templates were used to drill out these holes using a drill press and cutting fluid. The robot mount was turned on a manual Lathe by a machinist. The linear shafts and lead screw were cut with an angle grinder. The ends of the shafts were ground to maintain tolerances for the assembly. Threads on the ends of the lead screw were rethreaded to allow the nut to be assembled. The mass and cost of the components used are presented by Appendices I and J, respectively. The assembly procedure follows the RM assembly, and RREE subsystem drawings in Appendices K.25 and K.27 respectively.

6.5 RREE Assembly

The RREE prototype was assembled by combining the machine tool, gripper and linear actuator subsystems. The components of the reconfiguration subsystem formed the attachment of both primary subsystems. The RREE was assembled onto the Fanuc M10IA serial kinematic industrial robot. The M10IA is a widely used industrial robot, integration and operation of the RREE on this robot verified the developed end-effector. The payload of the Fanuc robot is 10 kg, as stated in Table 4-12 in Section 4.4.8. Therefore, RREE is a suitable end-effector for this manipulator. The stiffness of the Fanuc SKM is insufficient for machining applications, therefore, the robot is used for part handling testing. Due to the unavailability of a PKM, machining was done with the aid of a vibration test frame. The purpose of the frame was to simulate a stiff mounting for the RREE, similar to the mounting configuration present in PKMs. Figure 6-3 presents the RREE assembled onto the Fanuc robot. Refer to RREE assembly drawing in Appendix K.27.

Figure 6-3: Assembled RREE on Fanuc M10IA Robot

The RREE was designed as a standalone end-effector, suitable to be adapted to operate in conjunction with different robotic manipulators. Due to this, the control system of the RREE was not permanently integrated with that of the manipulator. The control architecture of the Fanuc M10IA industrial robot was not easily accessible due to the "tamper proof" control system. Nevertheless, integration of the RREE and manipulator was achieved via the Path Plan Programme feature on the SKM. The desired robot motion profile was programmed via the Teach Pendent Human-Machine Interface (HMI). The RREE control system works in conjunction with the robot through triggering either subsystem. Triggering occurs at a specified location of the path, it can either be a machining or grasping operation. Figure 6-4 illustrates how each controller works together with the Fanuc M10IA to execute machining and handling operations.

Initially both subsystems are disabled. Loading of the stock material from storage occurs at position A, at which point the gripper was enabled via actuation of the three servomotors (Arduino control system – refer to Section 6.7). Unloading of the stock material into the work fixture occurs at position B, the SKM moves from position A to B through the pre-programmed path plan. Reconfiguration of the end-effector occurs – the gripper system retracts via the linearly actuated platform. The machine tool was then enabled by input triggering of the BLDC motor drive (Arduino control system – refer to Section 6.6). The motion profile of the RREE was controlled by the SKM, hence the milling tool path was pre-programmed into the path plan of the robot. Once machining has completed, the RREE reconfigures to gripping stance, grasps the work piece and moves to position C. At position C, the gripper releases the completed work piece in the collecting area and proceeds to the starting position A.

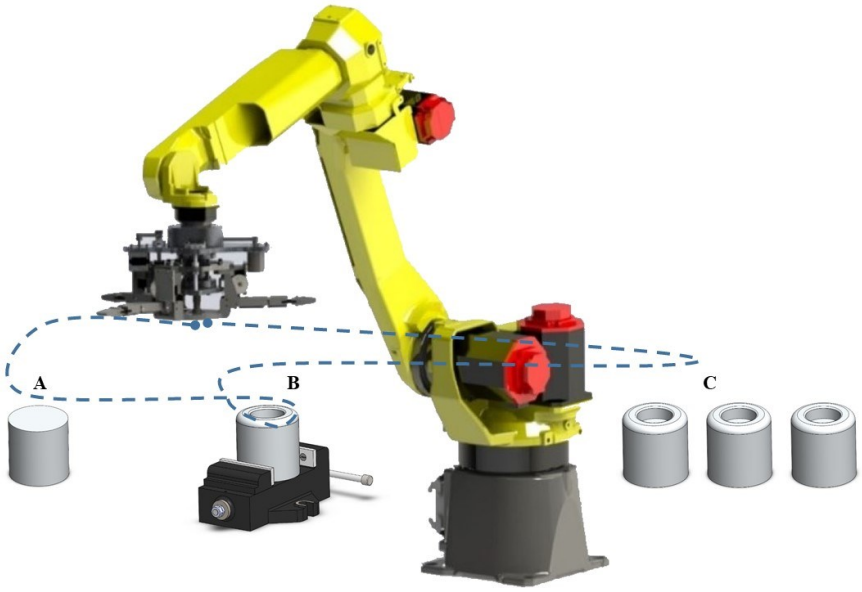

Figure 6-4: Integration of Control Architecture

6.6 Machine Tool Speed Control

The NTM PROP DRIVE Brushless Direct Current (BLDC) motor required specific drive electronics to operate effectively. The Brushless DC motor is three-phase, the permanent magnet arrangement forms the rotor and coil arrangement forms the stator. To control the rotation, adjustment of magnitude and direction of current in stationary coils must be made. Sensor-less BLDC motors Back Electromotive Force (BEMF) signals are monitored by the driver to commutate the signal. Position detection is not as accurate however, the cost of the motor and drive is reasonably less [131].

6.6.1 Electronic Speed Control

BLDC motors require power systems to drive them adequately. As such, most motors have specific controllers. NTM PROP DRIVE motor requires 80 A brushless Electronic Speed Controller (ESC) with a cell count of 3S – 5S to excite the motor. ESC working principle is discussed by referring to Figure 6-5.

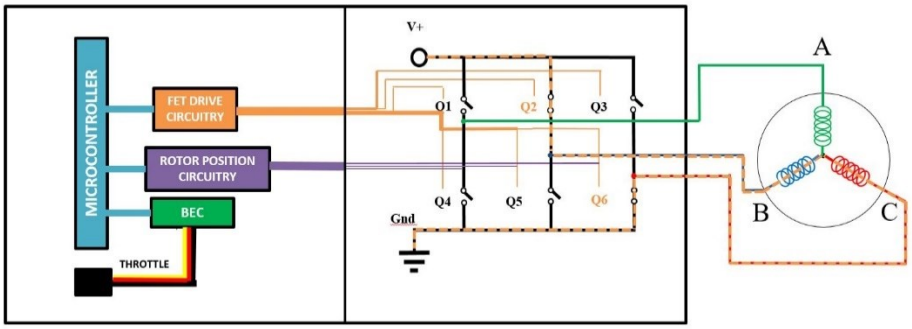

Figure 6-5: Circuit Diagram of ESC and Motor Connection [132]

An ESC controls the speed and motion of a brushless DC motor by activating the appropriate Metal-Oxide Field-Effect Transistor (MOSFETs) to create the rotating magnetic field. Higher frequencies correspond to faster processing of six intervals [133]. Based on the power requirements of NTM motor, Hobbywing Skywalker 80A Universal Battery Elimination Circuit (UBEC) ESC was selected. The specifications of the

ESC are presented in Table 6-1. UBEC is a voltage regulator, which converts the primary power source to a lower voltage and current to support additional devices.

Table 6-1: Specification of ESC [134]

Continuous Output Current	80 A
Nominal Input Voltage	18.5 V
Peak Input Voltage	21.0 V
Size	86.0 38.0 12.0
Weight	82 g
Communication	UBEC 5V, 5A Switching

The UBEC communication port was used to control the speed of the motor. A reliable Power Supply Unit (PSU) was required to supply the proper voltage and current to drive the motor. Based on the cutting requirements of the spindle motor and referring to the BLDC motor characteristic curve in Appendix G.1, the current required for the specified cutting operation torque and power is approximately 25 Amps. The Meanwell SE-600-24 Power Supply was selected to power the spindle system. Specification of the power supply is voltage input of 180 – 264 V AC. Voltage, current and power output is 24 V DC, 25 A and 600 W respectively.

6.6.2 Arduino Integration and Control

Control of BLDC motor is similar to Servo motor. Pulse Width Modulation (PWM) is used to control the speed of the motor via the signal wire on the UBEC of the ESC. Arduino control board was used for this purpose. The potentiometer was used to alter the speed between minimum and maximum. Figure 6-6 presents the circuit diagram including the Arduino board, potentiometer, ESC, motor, and power supply. Calibration of the ESC is necessary to set maximum and minimum speeds. Arduino potentiometer control code is presented in Appendix F.4 and the calibration code is given in Appendix F.3.

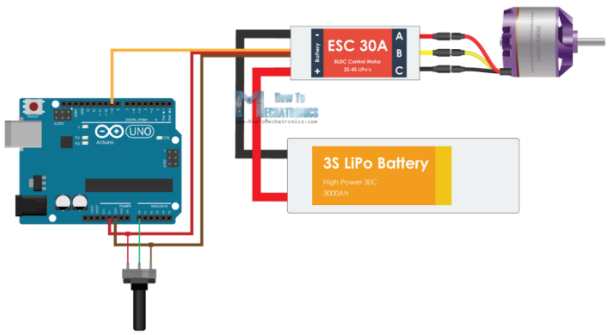

Figure 6-6: Main Circuit Diagram [135]

6.6.3 Brushless Motor Pseudocode

1. Include Servo Library;
2. Create a servo motor object to control ESC;
3. Define the analog pin as an integer value;
4. Attach ESC on pin 9;
5. Read the integer value of the potentiometer (0 to 1023);
6. Scale the read integer value to use with the servo motor library (0 to 180);
7. Send the signal to ESC.

6.7 Gripper Position Control

6.7.1 Pulse Width Modulation

The servo output shaft was positioned by an electrical pulse of variable width, through the control wire. There are a minimum and maximum pulse as well as repetition rate. A servo motor shaft turns 90° in either direction for a total of 180° angular range of motion. The PWM signal that the motor receives determines the position of the shaft. Pulse duration determines the speed of the rotor as it moves to the desired position [136].

Power source was required to supply the required voltage and current to drive the motor. Referring to specifications of FEETECH servo, the current and voltage required for the specified operational torque are approximately 2 Amps and 5 Volts respectively. Meanwell RS-15-5 Power Supply was selected to power each FEETECH servo motor. Voltage input ranges between 85 – 264 V AC, the voltage output is 5 V DC, output current range is 0 – 3 A and the output power is 15 W.

6.7.2 Arduino Integration

Arduino control board was used for this purpose. The potentiometer was used to alter the speed between minimum and maximum. Figure 6-7 presents the circuit diagram including Arduino board, potentiometers, motors, and power supplies. Arduino potentiometer control code is presented in Appendix F.1.

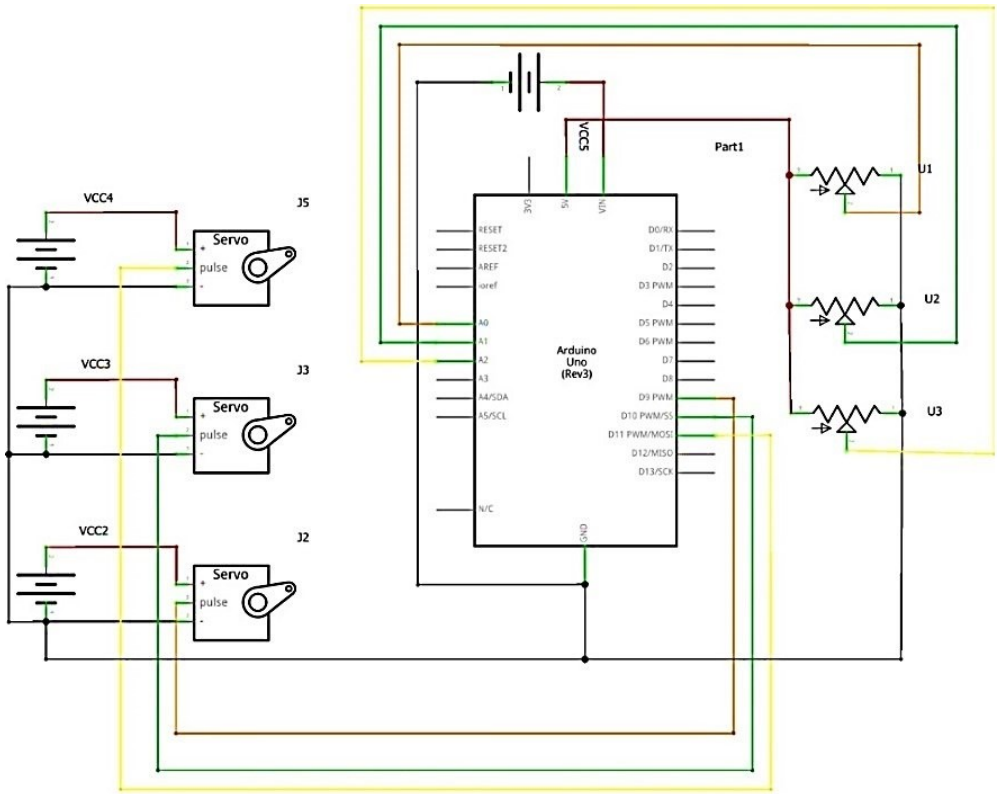

Figure 6-7: Gripper Circuit Schematic

6.7.3 Gripper Pseudocode

1. Include Servo Library;
2. Define three servo motors;
3. Define three potentiometer pins as integers;
4. Define three integer values;
5. Attach three servo motors;
6. Read potentiometer pin for servo motor;
7. Map integer value to servo motor scale (0 to 1023 – 0 to 180);
8. Write a scaled value to the servo motor;
9. Delay 25 microseconds.

6.8 Stepper Motor Position Control

Stepper motors require driver boards to excite their coils. Selection of stepper driver was critical as it determined the performance of the motor. Once the driver was selected, interfacing it with the controller was required. Linear travel and speed must be defined in the code for operation of the linear actuator.

6.8.1 Motor Driver Selection

The TB6560 microstepping driver is built around the Toshiba TB6560AHQ chip and is used to drive two-phase bipolar stepper motors. Given the requirements of NEMA 17 stepper motor, a compatible motor driver was selected. The driver is low-cost, reliable, and efficient and provides more than enough power than required. Figure 6-8 presents the layout of the driver board.

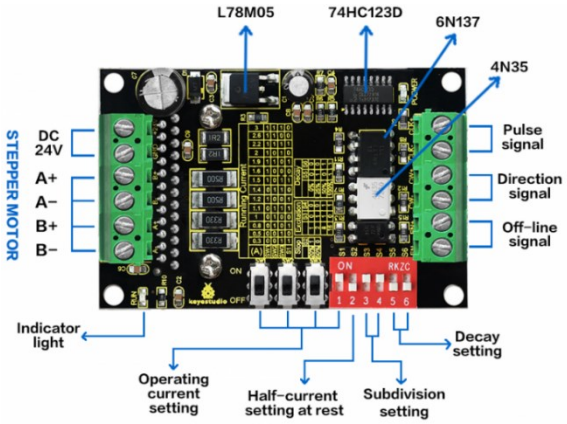

Figure 6-8: Layout of the TB6560 Driver Board [137]

The Switch settings for NEMA 17 stepper motor are given in Appendix H. Microstepping was not needed as end-to-end positioning of the actuator was required. Specifications of driver are operating voltage range of 10 – 5 V DC, recommended switch Power Supply with 25 V DC. Rated current output is 3 A; peak current output is 3.5 A. The driver offers four excitation modes, 1/1; 1/2; 1/8; 1/16 steps. The Meanwell SP-240-24 power supply was used to power the driver board. Specifications of power supply are voltage input range between 85 – 264 V AC. The output voltage, current and power is 24 V DC, 0 – 10 A, and 240 W.

6.8.2 Arduino Integration

Arduino control board was used for this purpose. The potentiometer is used to alter the speed between minimum and maximum. Figure 6-9 presents the circuit diagram including Arduino board, motor, and TB6560 driver.

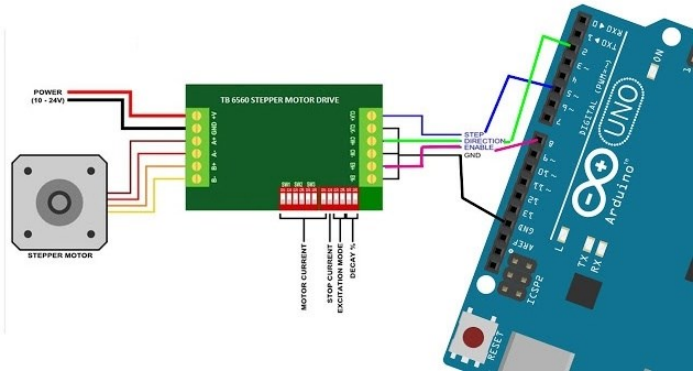

Figure 6-9: Circuit Diagram for NEMA 17 [138]

To determine the Arduino code for the stepper, steps and delay time were calculated. Steps required to rotate the motor through the length of the screw was determined by Equation 6.1. Delay time was calculated using the minimum traverse time and Equation 6.2. Detailed calculation is contained in Appendix B.3.

$$S = \frac{\Delta x \times 360}{R \times L} \tag{6.1}$$

$$\text{delay} = \frac{\Delta t}{S} \tag{6.2}$$

Steps required to traverse the length of the screw is 1850. Delay is calculated as 200 microseconds.

6.8.3 Stepper Pseudocode

1. Define Stepper motor pin numbers as constant integers;
2. Set stepper pins as outputs;
3. Change rotation direction when LOW;
4. Make 1850 pulses;
5. Delay 200 microseconds between pulses;
6. Change rotation direction when HIGH;
7. Make 1850 pulses;
8. Delay 200 microseconds between pulses.

6.9 Chapter Summary

The manufacturing of the RREE was presented, the prototype was assembled with Fanuc M10IA serial industrial robot. Electronic control system and software were implemented, and integrated control of actuation mechanisms was presented.

In the next chapter, the dynamics of the vertical milling process is presented in conjunction with methods of chatter prediction and prevention. Force prediction models are investigated to determine the cutting forces produced. Vibrational testing is conducted to determine the natural frequencies of the RREE. Machine stability is predicted using the Stability Lobe Diagram.

Chapter 7 Cutting Dynamics – Theory and Experimentation

7.1 Introduction

This chapter presents a review of recent literature on cutting dynamics. Furthermore, the geometry of milling cutters is investigated. Force prediction models, structural dynamics of machine tools and chatter prediction models are reviewed. An Experimental Modal Analysis (EMA) is conducted to determine the natural frequencies of the RREE. Modal parameter extraction is undertaken to calculate the damping ratio and experimental stiffness of the RREE. Chatter prediction is conducted employing the Stability Lobe Diagram (SLD). Stability analysis is performed utilising the experimental frequency response of the structure. Finally, experimental cut testing is undertaken to verify the predicted stability model.

7.2 Characteristic Quality of Milled Surfaces

Machined components are commonly described by four characteristics of quality. These are size tolerances, geometric characteristics, surface texture and integrity [139]. The size tolerances of machined parts are decreasing due to the advancement of machining equipment. Geometric characteristics describe the shape of the part which define the following characteristics: flatness, roundness, straightness, perpendicularity, parallelism and concentricity.

Tolerances of geometric characteristics are also being minimised; this is due to the higher specific load that results from geometric errors. These inaccuracies contribute to more substantial wear, unwanted operations, reduced efficiency and interchangeability issues. Surface finish is characteristic of machining operations. It is a description of the roughness and texture of the machined surface. It has a direct impact on fatigue strength, corrosion resistance and most importantly, force distribution. Surface integrity of machined components is the definition and control of multiple possible changes in a surface layer; this includes effects to material properties and the performance of the finished surface during operation.

According to Grzesik et al. [67], a machining process produces a surface defined by the topography, metallurgical and mechanical properties. Machined surfaces are very complex as they consist of many interrelated features which influence the functional performance of the surface.

7.3 Cutting Mechanics

In the past, the majority of manufacturing companies were not aware of the significance of cutting tool technology and merely considered it an afterthought. In present times, this is no longer the case; manufacturers realise that cutting tool technology ensures optimum production output and the consistency of machined products. Machining is a subtractive manufacturing process used in industry. It is a mainstream process due to its high flexibility and ability to produce parts with excellent quality [140].

It is a material removal process which uses a machine tool to cut away material leaving the required geometry. Machining is a high-precision manufacturing process. It is highly capable of producing multiple parts with diverse geometries.

7.4 Milling Processes

Material removal occurs due to the cutting edges of the rotating cutting tool [141]. The process involves a synchronised linear feeding motion of the rotating cutting tool as it moves across and into the workpiece [142]. Endmills are coupled to a rotating machine spindle. The milling process involves passing a workpiece against a revolving toothed-cutter. The cutting action induced by a multi-toothed tool created an efficient method of material removal. The workpiece surface may be flat, angular, or curved. The milling operation can produce any combination of shapes. According to Groover [140], there are two general types of milling processes; these are Peripheral and Face Milling. Peripheral Milling positions the axis of the tool parallel to that of the surface to be machined. Cutting is achieved by the sharp edges on the external periphery of the cutting tool. The direction of cutter rotation assumes two forms of milling: up and down. The direction of the cutter motion is the same as the feed direction during down milling. This results in longer tool life due to the decreased time per volume the cutter is engaged in the cutting process. In this case, the cutting force direction is tangential to the periphery of the cutter. Face Milling positions the axis of the cutting tool perpendicular to that of the surface which is too be milled. Material removal is undertaken by the cutting edges on dual cutting edges of the periphery.

7.5 Milling Geometry

Due to the various types of milling operations, the geometry of an end milling cutter will be discussed. The most common end mill designs are; roughing end mills, finishing end mills, square end mills, ball end mills, and corner rounding end mills [143]. Milling cutters are identified by diameter and pitch. The tooth, tooth face, and flute are essential components of the milling cutter. The lead angle is formed by the peripheral edge of the cutter and the centre axis of the cutter. Larger lead angles require more power to perform a cut. The axial rake angle determines the extent to which the peripheral cutting edge is leaning into or away from the centre axis. The radial rake angle describes the extent the end cutting edge leans into or away from the radius. The helix angle describes the relationship between the peripheral cutting edge and the centre axis of the cutter for solid tooling. Figure 7-1 highlights the necessary end mill terminology.

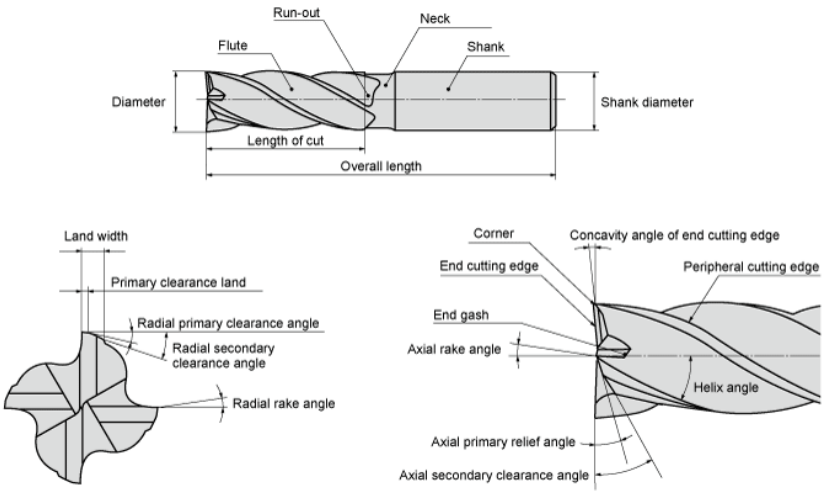

Figure 7-1: Endmill Terminology [144]

7.6 Force Prediction Models

Dynamic cutting process modelling is comprised of three methods, namely, analytical methods, experimental methods, and mechanistic and numerical methods [145]. Dynamic cutting force coefficients govern the cutting process; these coefficients are used to predict the unstable conditions of machine tools. Approximations link the instantaneous uncut chip thickness to the dynamic cutting force. Experimental methods are used to determine dynamic cutting force coefficients. This has led to many innovative methodologies. Research reflected dynamic methods derive the dynamic force coefficients by measuring displacements between the tool-workpiece contact. The stiffness method, the dynamometer method, and the time series method exist. Mechanistic and numerical methods make use of computer simulation techniques to compute enhanced empirical and analytical models. Mechanistic modelling methods outline the machining process as a set of components. The chip load-cutting force and tool-workpiece displacement are two of these components. Cutting tool, workpiece and process geometry, and machining conditions are also factors that influence the model. Displacement feedback alters cutting conditions and tool geometry [145]. Two commonly used finite element models for machining are the Lagrangian and Eulerian models. Lagrangian models are mostly used to simulate entry and exit phases of chip formation, and, intermittent and discontinuous machining processes. Disadvantages include unusable mesh distortion in the event of large plastic deformations, discontinuous tool path motion, and the expensive computation cost. Eulerian models achieve continuous material flow around the tool. Therefore, Euleurian models produce physically realistic results for ductile materials. Disadvantages such as remeshing and node splitting do not affect Eulerian models. Moreover, Eulerian models are computationally inexpensive; however, it does have drawbacks. It is not ideal for modelling intermittent machining, entry and exit phases and discontinuous chip formation. Lagrangian and Eulerian models are restricted to orthogonal machining.

Milling processes generate vibrations due to the rotating machine tool that provides periodic material removal. There are two primary sources of vibrations in milling; these are forced vibrations and chatter vibrations [146]. Stable periodic oscillations are common in practice and are generally negligible due to the stiffness of the machine tool structure. More significant cyclic forced vibrations usually occur close to the natural frequencies of the spindle speeds. These vibrations are likely to appear at low-damped modes. Some significant vibrations cause acceptable surface integrities; however, the surface location error and roughness induced are often unacceptable to manufacturers. Forced near-resonant oscillations unnecessarily increase the cutting forces. The problem of forced vibration poses a limitation to material removal rates and the utilisation of cutting variables.

According to Bachrathy [146], chatter is caused by the surface regeneration effect; this is the second type of vibration caused by the milling process. The resulting chaotic fluctuations occur when the static milling process becomes unstable. Unstable static periodic forced oscillations decrease surface integrity and create excessive cutting forces. This causes the path of each cutting edge to deviate from the estimated path. Depth of cut, spindle speed, and feed rate are input variables that determine the process output quality. These parameters are critical to prevent abnormal tool behaviour.

According to Zhang and Hwang [147], control of the cutting forces is related to the workpiece material characteristics. Cutting dynamics is a matter which deals with the cutting force during the machining

process. Tool vibration is caused mainly by the dynamic variation of the cutting force. Many researchers in the metal cutting industry have attempted to explore the possibility of predicting the cutting force and its effects on the structural dynamics of the machine tool.

According to Grossi et al. [54], machine tool dynamics is usually attained by the Frequency Response Function (FRF) at the tool-tip; this is conducted through an impulse test on the static cutter. High-Speed Milling is a dynamic machining operation, as such, tool-tip dynamics should change due to gyroscopic effects and centrifugal forces.

Dijk [56] proposed a model for the milling process. Material is removed from the workpiece by the joint motion of the cyclic cutting tool and the linear movement of the cutter in the feed direction. Figure 7-2 provides a schematic representation of the milling process.

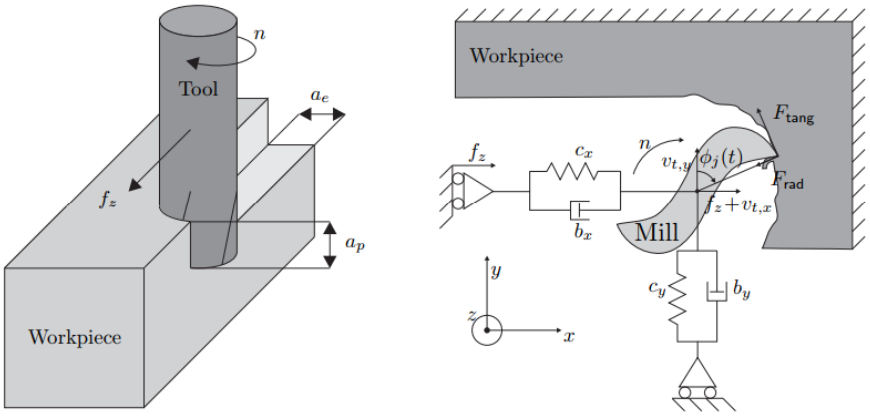

Figure 7-2: Schematic Representation of the Milling Process [56]

Hung et al. [148] found that bending vibration of the spindle shaft and bearing preload in a vertical milling machine influenced the dynamic characteristics of the machine tool. According to Hung et al. [148], the measurement of a spindles frequency response function, that is the transfer function of force input and displacement output, at the tooltip characterises dynamic behaviour. If the spindle does not exist, then the frequency response function cannot be found in the manner described above. A computational simulation of the spindle was done to optimise spindle design parameters. The maximum axial depth of cut for specific speeds was determined. Gyroscopic and centrifugal effects on dynamic spindle stability are significant at high rotational speeds.

Fundamental research in the dynamics of end milling processes has focused on the frequencies and mode shapes of the machine tool system which could have been excited during the cutting process [149]. The machine tool system comprises of the machine tool structure, spindle shaft, endmill cutter, fixtures, and workpiece.

7.7 Structural Dynamics

According to National Instruments [150], experimental modal analysis involves measuring and processing the dynamic response of a system. The system is energised by a stimulus of known magnitude. It is widely used in determining the modal parameters of a structure.

The two most commonly used methods of modal testing are Impact Hammer modal testing and Shaker modal testing. In either case, the energy of known frequency is supplied to the system. Doina [151] researched the dynamic properties of milling centres by measurements. An impulse force caused excitation in the machine tool, and the vibration response was recorded. Accelerometers were positioned at the spindle head, the table and the clamping device. The research allowed the determination of critical frequencies, damping and stiffness of the system. Shiak and Strinivas [152] investigated the modal characteristics of a spindle tool unit experimentally. Tooltip FRF and Stability Lobe Diagram (SLD) were obtained using Finite Element Method (FEM). The frequency response function of the endmill-tool system was also determined experimentally by means of Impact Hammer testing. A triaxial accelerometer was used. Input and output signals were recorded, and Fourier transforms obtained the frequency response. Average tooth angle method was used to predict the stability lobes. Figures 7-3 and 7-4 illustrate the test apparatus and typical result of impulse test.

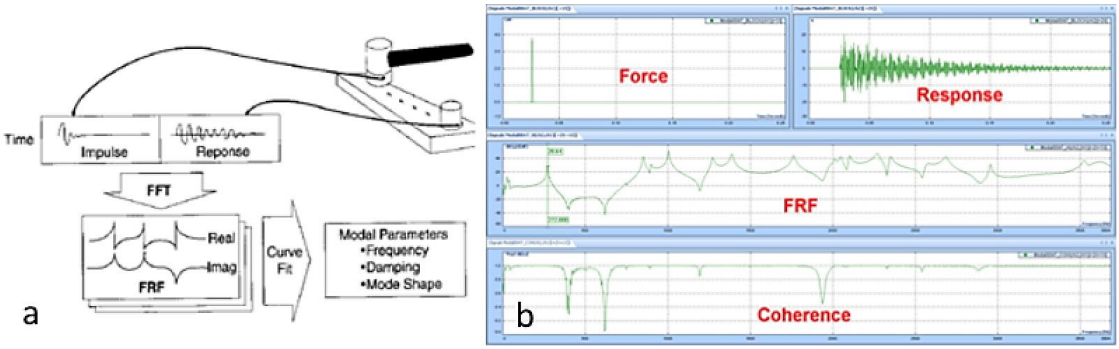

Figure 7-3: (a) Typical Impact Hammer Modal Test and Signal Processing (b) Typical Impact Hammer Modal Test Data [153]

Modal analysis is a prerequisite in determining the SLD. Modal parameters such as natural frequency, modal stiffness and damping coefficient are typically obtained from the analysis of the FRF of the structure. Obtaining the spindle-tool system transfer function was realised by impulse hammer testing [154]. Impulse testing is a widely-used form of modal testing; it involves both an input and an output signal. The input signal is the force generated by the impulse of the impact hammer; simultaneously, the output acceleration generated by the structure is measured by a carefully placed accelerometer. Data Acquisition (DAQ) equipment is necessary for EMA.

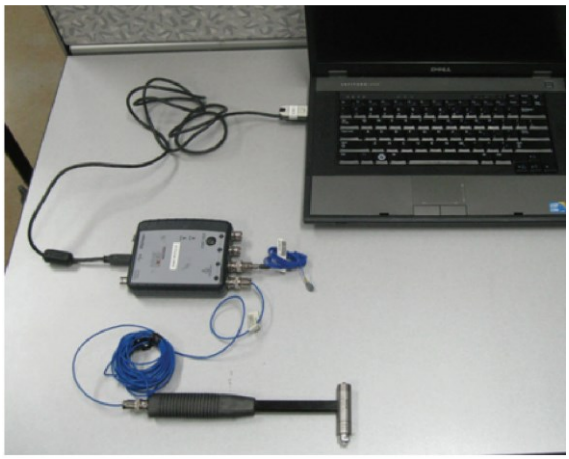

Figure 7-4: Apparatus Required for Impact Test [155]

7.8 Chatter Prediction in Milling

Research was conducted by Grossi et al. [54] on the topic of chatter stability prediction in milling using speed-varying cutting force coefficients. The accuracy of chatter prediction is primarily influenced by the reliability of cutting force coefficients and FRF. Spindle speed affects cutting force coefficients and FRF. The investigation of chatter prediction models has resulted in a chart called Stability Lobe Diagram (SLD); this chart identifies stable cutting parameters. The accuracy of Stability Lobe Diagrams is affected by both machine dynamics at the tool-workpiece interface and cutting coefficients. High-speed milling benefits greatly from an accurate SLD, at increased spindle speeds, typical diagram lobes have larger spaces, these larger spaces create stable zones at increased depth of cuts. Higher depth of cuts at faster spindle speeds increases productivity. Chatter stability is dependent on both machine tool dynamics and cutting force coefficients.

Deshmukh and Rajput [55] conferred that chatter prediction is fundamental in milling processes. Predicting chatter allows for the avoidance of vibrations by specifying the maximum possible, stable depth of cut and spindle speed. In turn, increased material removal rates at high accuracies are certain. Furthermore, it was determined that oscillations must be minimised in milling machines to ensure the highest possible material removal rates. A significant advantage of SLD is the maximisation of the metal removal rate.

Dijk [56] confirmed that a stable working point should be selected as predicted from the SLD. Furthermore, chatter prediction is possible from analysis of the stability properties of milling model. An analytical method based on the Nyquist criterion to determine the stability of the milling process was presented by Altintas and Budak [156]. Working points on an SLD either avoid chatter occurrence or ensure high material removal rates. These two options pose two problems; the first problem arises if a working point below the chatter boundary is selected. This point ensures stability but does not guarantee high material removal rates. Factors such as wear and temperature will eventually affect the milling machine and tool which will result in the working point shifting as time progresses. Therefore, maintaining systems for high material removal rates will not ensure eternal robustness against chatter. The other problem is that different workpieces often have different materials and hence require different cutting speeds. This limits the

material removal rate if no lobe is located at the specified speed. The solution to this problem is automated chatter control strategies; three such strategies will be discussed.

Spindle speed modulation: According to Dijk [56], the aim of this strategy is to perturb the regenerative effect by continuously changing the spindle speed. It is achieved through sinusoidal or random spindle speed variation. This strategy is restricted by the inertia and actuation power of the spindle system; it is therefore not advisable for high-speed machining. The strategy can also be achieved by the utilisation of non-equidistant tooth distribution tooling; it results in uneven chip load distribution and excessive wear of the tool.

Spindle speed selection: Changing working points are a real-world problem. Mitigation of this problem is realised by adjusting process parameters of the cutting process to ensure that a stable working point is maintained regardless of changing process conditions. The strategy is two parted, firstly, the detection of the onset of chatter and secondly, a control algorithm that selects a new working point for process parameters [56].

Alteration of spindle dynamics: This strategy involves the manipulation of spindle-bearing, tool holder and tool system dynamics. The idea behind this approach is to modify the SLD to result in higher material removal rates. The alteration of spindle dynamics can be achieved either by passively or actively controlling chatter [56].

Regenerative chatter theory is represented by the stability lobe diagram; it is, therefore, a useful tool to anticipate and control chatter. SLD's can increase productivity and improve material removal rate by optimising the axial depth of cut and the spindle speed. Figure 7-5 represents the typical format of a stability lobe diagram; the progressively wider scallop-shaped borderlines indicate stability. Intersection points represent the deepest stable cuts at different spindle speeds. Yue [157] proposed a simple method to analytically calculate approximate optimal depths of cut and determine the relative spindle speeds.

Two-dimensional stability lobe theory produces stability solutions for dynamical cutting systems; these solutions are spindle speed and axial depth of cut. Stability is achieved as a function of two cutting parameters, chatter-free cutting conditions exist in the region below the lobes in the diagram and unstable cutting conditions exist in the region above the lobes in the diagram [158].

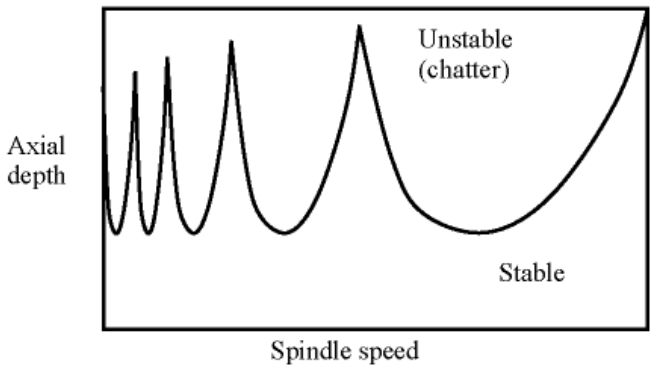

Figure 7-5: Example Stability Lobe Diagram [159]

The stability model for the end-milling process will ensure that the correct speed and depth of cut are selected for chatter-free machining. The avoidance of chatter allows decreased vibration of the machine-

tool hence, ensuring an excellent surface finish. To determine chatter stability lobes, FRF of the machine tool-workpiece system and mill process parameters must be determined [6].

7.9 Experimental Modal Analysis of RREE

7.9.1 Aim and Objectives

The aim of the experiment was to investigate the dynamic modal characteristics of the end-effector assembly. The objectives were to (1) Determine FRF of end-effector assembly through impulse testing (2) Extract modal parameters from FRF (3) Determine critical speeds of the spindle shaft.

7.9.2 Experimental Setup and Apparatus

The apparatus used are listed and shown in Figure 7-6. The Bruel & Kjaer 4507B uniaxial accelerometer has a sensitivity of 97.02 mV/g and range of 6000 Hz. Bruel & Kjaer 8206-002 Impulse Hammer has a sensitivity of 2.18 mV/N and a range of 2200 N. The data acquisition equipment was selected due to the acceptable sensitivity and measurement range.

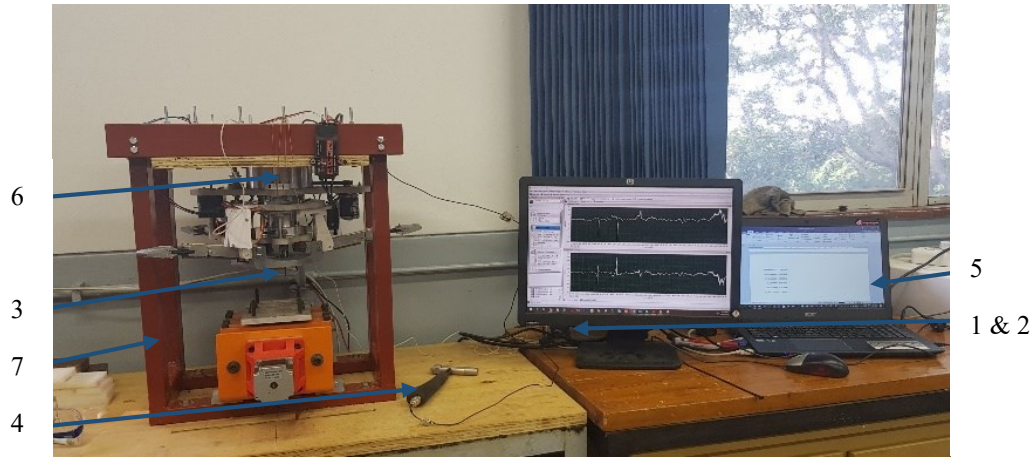

Figure 7-6: Experimental setup

1. National Instruments Data Acquisition Device (cDAQ-9171 CompactDAQ);
2. National Instruments Sound and Vibration module (NI-9234 C Series);
3. Uniaxial Accelerometer (Bruel & Kjaer 4507B);
4. Impulse Hammer (Bruel & Kjaer 8206-002);
5. Laptop with National Instruments Signal Express Software (2017);
6. End-effector;
7. Test frame.

7.9.3 Method

1. Turn off the machine tool spindle and disconnect it from the mains power supply;
2. Attach the accelerometer to the spindle head directed to the y-axis reference;
3. Turn on the DAQ and connect it via USB to the computer;
4. Open Signal Express software and configure the accelerometer and impulse hammer;
5. Calibrate accelerometer with calibrator;
6. Select frequency response testing and real and imaginary response and use Hanning window with force 50.0% and exponent 10.0%;

7. Strike the tip of the tool in the y-direction;
8. Generate the average frequency response function in Signal Express software. Figure 7-7 presents a portion of the block diagram developed to capture the input force signal from the Impulse Hammer and the Input Acceleration signal from the Accelerometer. Refer to Figure E 12-63 in Appendix E.14 for the complete block diagram;
9. Use the Peak-Picking method to extract modal parameters.

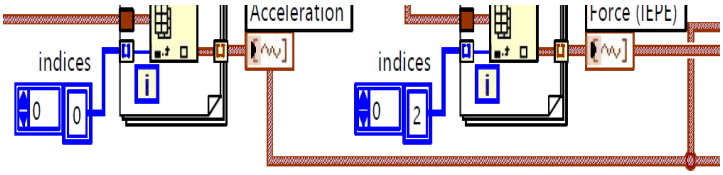

Figure 7-7: Part of the LabVIEW Block Diagram

7.9.4 Results

Figures 7-8 to 7-11 represent the Frequency Response Functions of the fully assembled end-effector. Excitation was provided by an impulse hammer at the tooltip. The output response was measured using a uniaxial accelerometer mounted at the tooltip in the direction of impact. Aluminium hammer tip was used due to the low-damping of the machine tool system. The real and imaginary responses are shown in Figures 7-10 and 7-11, respectively. Figures 7-8 and 7-9 present the magnitude and phase FRF's of the system. Modal parameters of the structure are tabulated in Table 7-1. The Peak-Picking method [150] is used to estimate the natural frequencies as used by [54, 152-155, 158, 160].

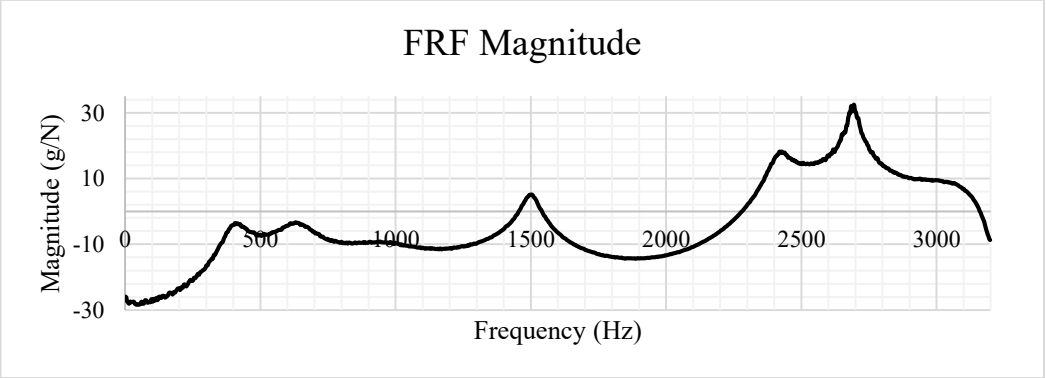

Figure 7-8: Frequency Response Function of Machine-tool (Magnitude)

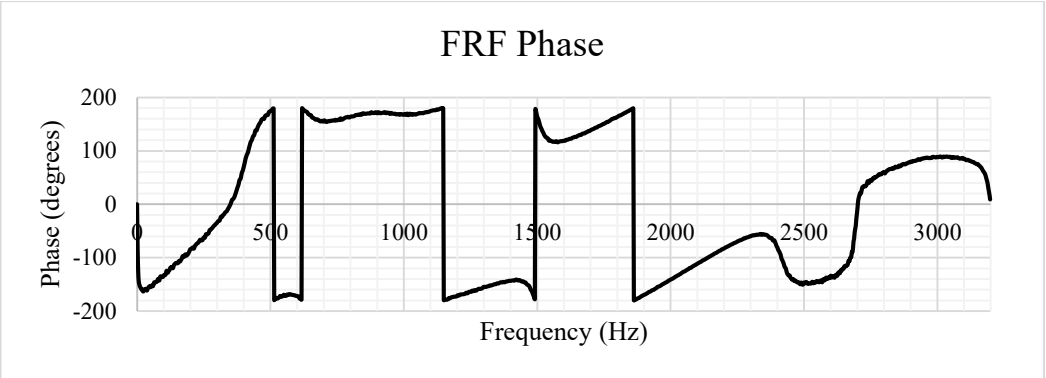

Figure 7-9: Frequency Response Function of Machine-tool (Phase)

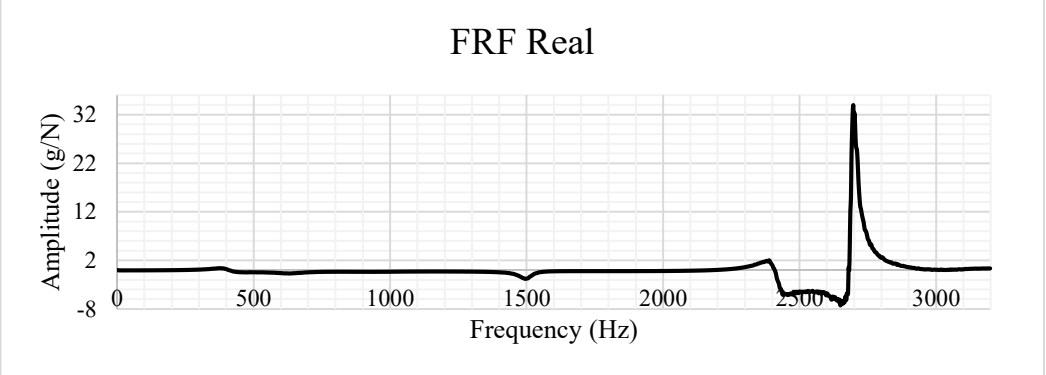

Figure 7-10: Frequency Response Function of Machine-tool (Real)

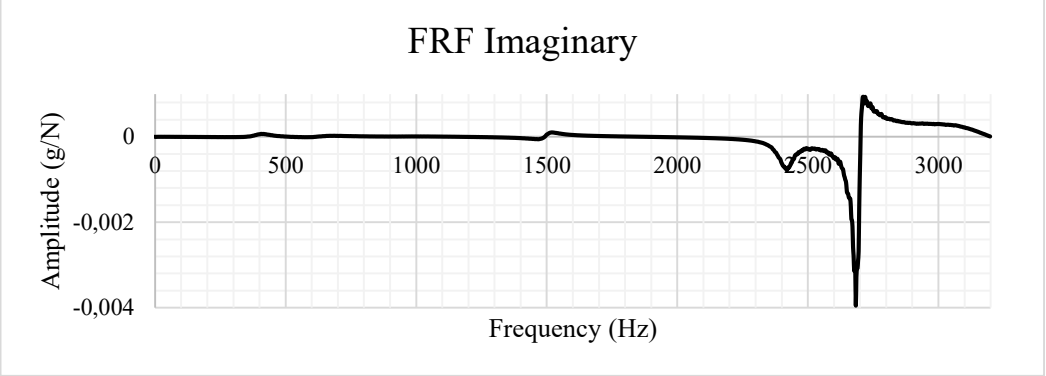

Figure 7-11: Frequency Response Function of Machine-tool (Imaginary)

Table 7-1: Modal parameters of the Machine-tool structure

Mode	Frequency (Hz)	Amplitude (g/N)	Critical Speed (RPM)
1	407.467	-3.558	24448.02
2	629.333	-3.324	37759.98
3	1501.87	5.119	90112.2
4	2427.73	18.22	145663.8
5	2694.4	32.45	161664

The inverted peak at 2694.4 Hz from Figure 7-11 corresponds to the critical frequency of the system. Natural frequencies of the system are represented by peaks in Figure 7-8. Five such frequencies were identified. Modal parameter extraction was conducted using the Half-Power method and Peak-Picking

method. The critical mode produced the largest amplitude; this was identified as 2694.4 Hz. A critical amplitude of -0.004 g/N was found at this frequency from Figure 7-11. The Half-Power method used by [161] was used to estimate the modal damping ratio given in Equation 7.1. Equation 7.1 yields acceptable damping ratio from spectral analysis; the damping ratio should be less than 0.05 [161]. The experimental stiffness was approximated using the damping ratio found by Equation 7.1 and the critical amplitude of the Imaginary part of the Frequency Response Function [155] via Equation 7.2.

$$\zeta = \frac{\omega_B - \omega_A}{\omega_n} \tag{7.1}$$

$$k_{exp} = \frac{-1}{2\zeta \mathrm{D}} \tag{7.2}$$

Where ζ is the damping ratio, ω_B is the frequency of the crest on the real part of the FRF, ω_A is the frequency of the trough on the real part of the FRF in the region of the critical frequency (ω_n). k_{exp} is the experimental stiffness and D is the amplitude of the minimum peak on the imaginary FRF.

The experimental stiffness k_{exp} and damping ratio ζ are 14500 N/m and 0,008708803 respectively. Critical speeds of the spindle shaft at each mode frequency was determined. This validated the designed spindle shaft. The rotational speed of the spindle should not exceed these critical values as modal frequencies will occur.

Modal correlation between the test and FEA data was beyond the scope of this research. This would have granted a meaningful comparison of the correlation between the EMA and FEA. The Modal Assurance Criterion (MAC) provides a measure of consistency between one modal and another reference modal vector. The omission of such criterion prevented any meaningful comparison between the test and FEA data [162]. However, some general inconsistency between the methods of obtaining modal data was observed. Referring to the modal simulation results obtained from Section 5.5 with the EMA results obtained in Section 8.10.1, there are some differences in the results. This may be attributed to the idealistic bearing model used in the simulation, inconsistencies in conducting the EMA and simplified constraints. This error offers implications on the reliability of the FEA modal simulation, parameters such as bearing stiffness and system damping cannot be disregarded. The EMA offers the most reliable modal characteristics of the two methods as this result is used to predict the stability regions presented in Section 7.10 and validated in Section 7.11.

7.10 Stability Analysis of RREE

Stable machining produces a high-quality surface finish on parts and reduces tool wear by keeping vibrations to a minimum. In unstable machining, variations in the magnitude of cutting forces excite the spindle, causing vibrations that lead to changes in the chip thickness. There are many methods of prescribing stable operating conditions in material removal operations. Stability diagrams are used in milling operations; these diagrams take into consideration the properties of the work material and cutting tool. These diagrams are computed for different tool-workpiece combinations. Stable milling on the reconfigurable end–effector was achieved, provided that a stability diagram is used when selecting process parameters.

Many studies have contributed to the advancement of regenerative chatter theory; these include Altintas and Budak [156], Merritt [163], Tlusty [164] and Smith [157]. The theory relates spindle speed to the depth of cut or critical chip width. This generates a stability lobe diagram which allows the selection of the highest stable material removal rate. Tlusty demonstrated that stability is dependent on both machine tool dynamics and cutting force coefficients [28]. Spindle speed affects both cutting force coefficients and the frequency response. The investigation of chatter prediction models has resulted in a chart called a Stability Lobe Diagram (SLD); this chart was used to select stable machining parameters. High-speed milling benefits greatly from an accurate SLD, at increased spindle speeds. Higher depth of cuts at faster spindle speeds increases productivity. In this research, cutting force coefficients were referenced from similar studies.

The SLD was generated by means of Altintas's [156] stability equations for multiple linear plots. Yue [157] proposed an iterative approach to the solution of the depth of cut and spindle speed as functions of milling parameters defined by Altintas and Budak's mechanistic force model. The area under the curves represents the regions of chatter-free cutting conditions.

The stability lobe diagram is formed by a series of intersected scallop-shaped borderlines of stability. The intersections of the lobes represent the deepest stable cuts at various ranges of spindle speed. The governing equations of machine chattering were derived from the general equation of vibration and the regenerative chatter equations [165]. In orthogonal cutting, cutting force F is proportional to the cutting area, according to Equation 7.3. Where k_s is the specific power, x is the displacement of the cutter normal to the cut, t is time, and T is the time interval between the previous and current cuts. The general equation of vibration is Equation 7.4.

$$F = k_s bh = k_s b[x(t-T) - x(t) \tag{7.3}$$

$$m\ddot{x} + c\dot{x} + kx = F \tag{7.4}$$

The chip width, b, should always be positive. The minimum chip width, b_{lim}, represents a limit in a machining process. Since it is independent of the chatter frequency, there is only a fixed value determined by the materials and geometries of the cutter and workpiece. A cutting process is unconditionally stable when the chip widths are under this critical value. A dimensionless chip width may be represented by the ratio of chip width to the minimum chip width according to Equation 7.5. G_R is the real part of the frequency response function. Equation 7.6 is the standard solution to the frequency response function.

$$b = \frac{-1}{2k_s G_R} \tag{7.5}$$

$$\frac{x}{F} = \frac{1-r^2}{k[(1-r^2)^2 + (2\zeta r)^2]} + i\frac{-2\zeta r}{k[(1-r^2)^2 + (2\zeta r)^2]} = G_R + iG_I = G \tag{7.6}$$

The ratio of chatter frequency to the natural frequency is related to the ratio of the damping coefficient to critical damping coefficient by Equation 7.7. Equation 7.8 computes the minimum chip width, which provides a limitation in the machining process. Equation 7.9 represents the relationship between the dimensionless chip width ratio and the chatter frequency ratio.

$$r = \sqrt{1 + 2\zeta} \tag{7.7}$$

$$b_{min} = \frac{-1}{2k_s G_{R,min}} = \frac{2k\zeta(1+\zeta)}{k_s} \tag{7.8}$$

$$r_b = \frac{b}{b_{min}} = \frac{G_{R,min}}{G_R} = \frac{(1-r^2)^2 + (2\zeta r)^2}{-4\zeta(1+\zeta)(1-r^2)} \tag{7.9}$$

Equations 7.10 and 7.11 are used to derive the equation of regenerative chatter given in Equation 7.12. Roughness or waviness always exists on the machined surface of workpieces due to vibrations. Equation 7.12 models the relationships among the chatter frequency, f, the tooth frequency, f_t ,and the lobe numbers, n.

$$\frac{f}{f_t} = \frac{r}{r_t} = n + \frac{\varepsilon}{2\pi} \tag{7.10}$$

$$\varepsilon = \pi + 2\tan^{-1}\frac{G_I}{G_R} \tag{7.11}$$

$$\frac{f}{f_t} = \frac{r}{r_t} = n + \frac{1}{2} + \frac{1}{\pi}\tan^{-1}\frac{-2\zeta r}{1-r^2} \tag{7.12}$$

The stability lobe diagram for the machine-tool system was computed using the system of equations (Equations 7.3 – 7.12) and results from frequency response testing using Yue's [157] method. Figure 7-12 presents the resultant stability lobe diagram. The cutting stiffness or specific power was calculated using the cutting force coefficients for Aluminium 6061. The cutting stiffness k_s was found to be approximately 907.055 N/mm^2 [166]. A two-flute cutting tool was used in the stability model. Refer to Appendix E.4 for simulation data points. The range of rotational speed attained by the machine-tool is 2300 – 17800 RPM. The areas under the lobe-lines represent regions of stable cutting conditions, areas above the lobe-lines represent regions of unstable cutting conditions.

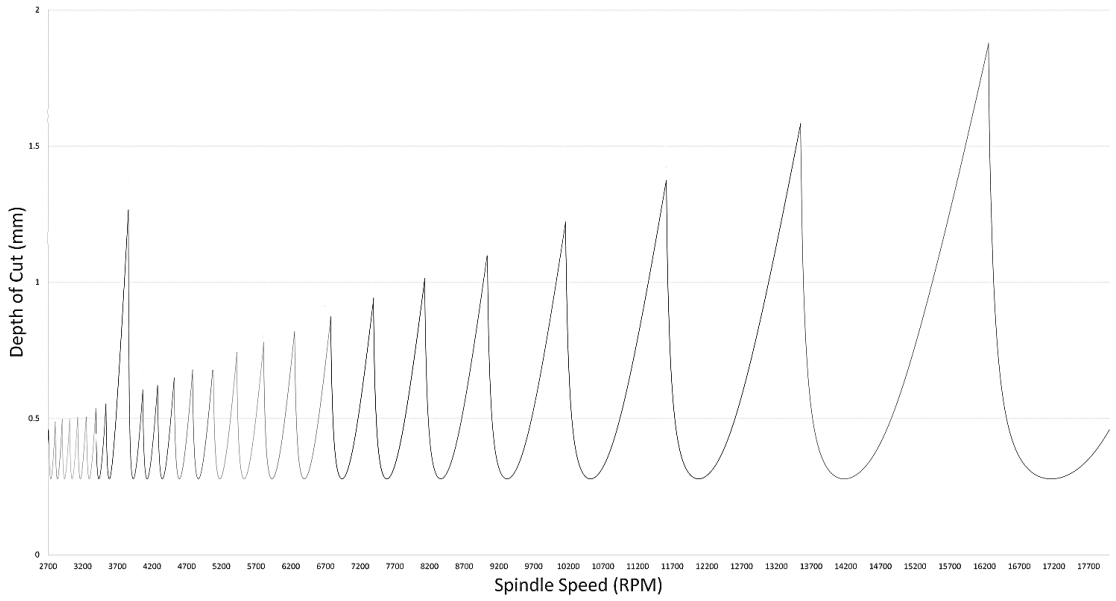

Figure 7-12: Stability Lobe Diagram of End-Effector Assembly

7.11 Stability Validation of RREE

Verification of the computed stability diagrams is of significance. It was for this reason that cut testing was conducted. Linear cut testing was undertaken to verify the stability lobe diagram. Slot milling of aluminium

6061 samples using ranging depths of cut and spindle speeds yielded data points for evaluation. The assembled end-effector was mounted onto a custom steel-framed structure. The end-effector was coupled to the Test Frame via the eight mounting bolts. Figure 7-14 (a) presents the experimental setup. Apparatus used was NI DAQ system (Refer to Section 7.9.2 for the components), Laser tachometer (Toptronic T6236), Linear Actuator Drive and Drill Press Vice (MAC-AFRIC 150 mm Engineers Drill Press Vice) and Test Frame. The Linear Actuator was used from a postgraduate Gantry machine developed in previous research at UKZN [167]. The diameter of the cutting tool was 2 mm, refer to Section 4.2.3.1 Table 4-1 for the properties of the endmill. Bruel & Kjaer 4507B uniaxial accelerometer was mounted on the spindle head, as presented in Figure 7-14 (b). The location of the accelerometer is referenced from the literature [55, 152].

Apart from the stability validation from milling aluminium 6061 samples, pinewood and HDPE samples were also milled. This was done to demonstrate the capability of the RREE for the milling of woods and plastics. Figure 7-13 (b and d) present the surface finish of HDPE and pinewood samples, respectively. Photographs of the milling process of HDPE and pinewood are presented in Figure 7-13 (a and c) respectively.

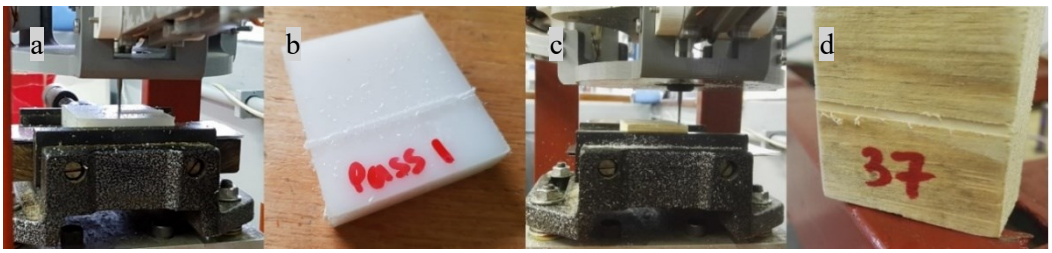

Figure 7-13: Milling Sample (a and b) HDPE Plastic (c and d) Pinewood

The feed rate, depth of cut and rotational cutting speed for the plastic sample was 0.73 mm/sec, 0.57 mm and 6000 RPM respectively. While the feed rate, depth of cut and rotational cutting speed for the wood sample was 0.73 mm/sec, 0.53 mm and 6000 RPM respectively.

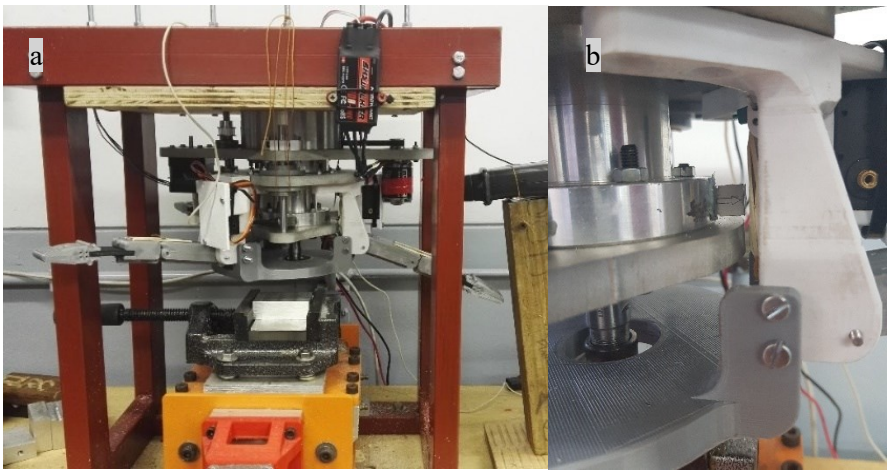

Figure 7-14: Experimental Setup (a) Aluminium Sample Cut (b) Accelerometer Mounting

The spindle speed ranged between 12700 RPM and 18000 RPM. The laser tachometer was used to determine the instantaneous rotational speed of the spindle motor and hence the spindle. The drive ratio of the spindle system is 1:1, due to the compactness of the design, it was difficult to measure the speed of the spindle shaft. The average detected acceleration for data points 3,4,7 and 8 were more significant than the rest of the test points. These large accelerations attributed to increased displacement; hence vibration was

more significant at these points. These vibrations occurred at slow and moderate feed rates; the depths of cut were below 0.5 mm. Table E 12-22 in Appendix E.15 presents the measured spindle speed, depth of cut, average acceleration, and set feed rate for the experiment.

The data from twenty-two samples are plotted on the stability lobe diagram (Figure 7-12) in Figure 7-15. The blue data points resulted in stable cuts with good surface finish, while red points produced unstable cuts with diminished surface quality.

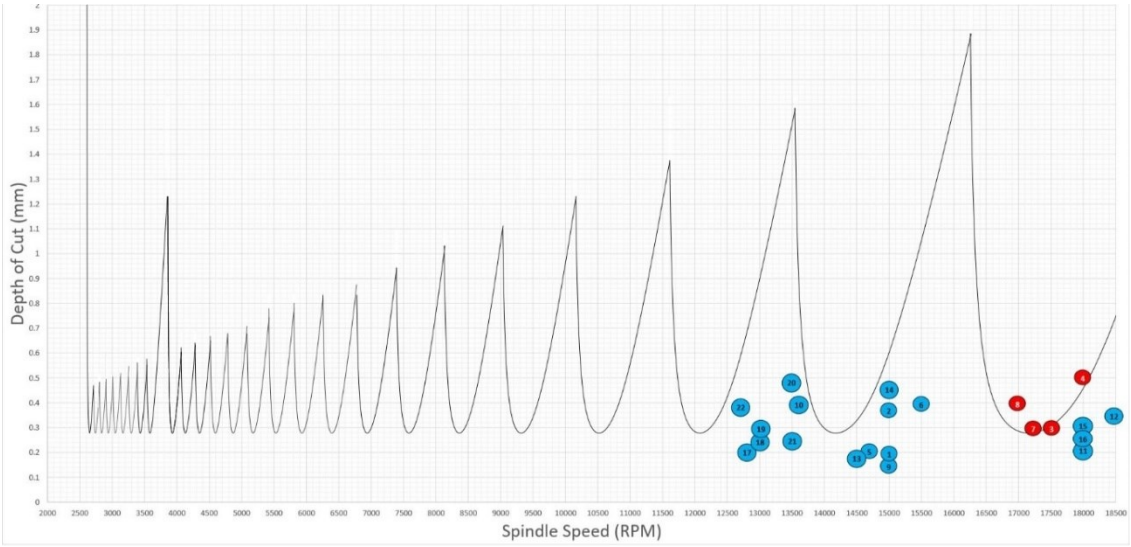

Figure 7-15: Stability Lobe Diagram Verification (Aluminium 6061-T6)

The difference between stable and unstable cut was visualised by means of the stability lobe diagram. Axial depth of cut is a function of spindle speed; the resulting graph presents a series of scalloped-shaped lines. The target was to seek parameter points below the lobe-lines. Process damping occurred at low rotational speeds. The surface finish of cutting process seventeen is presented in Figure 7-16 (b), while the machined surface of cutting process eight is presented in Figure 7-16 (a).

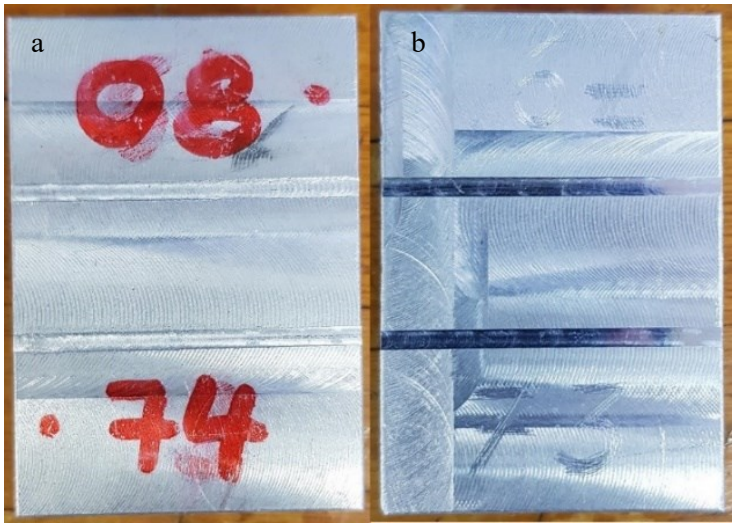

Figure 7-16: Cut Test Specimen for (a) Unstable and (b) Stable Cut

7.12 Chapter Summary

This chapter presented a review of pertinent literature on milling dynamics and the geometry of milling cutters. Force prediction models, structural dynamics of machine tools and chatter prediction models were reviewed. An experimental modal analysis was conducted to determine the natural frequencies of the RREE. Modal parameter extraction was undertaken to calculate the critical damping ratio and experimental stiffness. Chatter prediction was conducted by means of the Stability Lobe Diagram. Stability analysis was conducted based on the experimental frequency response of the structure. Finally, experimental testing was undertaken to verify the predicted stability model.

The following chapter presents the experimental testing and validation of the RREE by analysing the performance of each subsystem. Furthermore, the effect of dynamic interactions between gripping and machining is investigated.

Chapter 8 Experimentation and Validation

8.1 Introduction

This chapter discusses experimentation and evaluation of the developed end-effector. Testing is undertaken in two phases. The first phase involves individual testing and evaluation of performance metrics of each of the three subsystems. The second phase aims to investigate the extent of interaction between subsystems. Machine tool system is tested for spindle runout to determine the eccentric accuracy of the machine tool. Performance metrics of the gripper system are determined through experimental testing. Finger force, hand force, accuracy, repeatability, slippage load and geometric adaptability are determined. It is fundamental to assess the range and extent to the performance of the gripper to draw conclusions on the design. Reconfiguration mechanism is tested for cycle time, accuracy and repeatability. These measurements demonstrate the benefit of the reconfigurable end-effector as compared to dedicated systems. The cycle time provides a realistic measure of the capability of the RREE. Performance and interactions of the spindle and gripper subsystems are investigated. Multistage assembly testing of the end-effector investigated the effect that the subsystem has on spindle dynamics and stability. Dynamic interaction of the gripper is determined through vibration response testing. The vibration and stability testing produces invaluable data on the dynamic characteristics of the integrated system and the effects the combined systems have on each other.

8.2 MT Spindle Runout

Tool runout is a measurement of the deflection of rotating machinery. Inaccuracies in the alignment of the shaft have a direct impact on the accuracy of the machine tool. Shaft eccentricity is considered in the test. Determining the MT runout provides an understanding of the limitations of the manufactured prototype.

8.2.1 Aim and Objective

The aim of the experiment was to investigate the radial runout of the machine tool spindle. The objective to meet the aim was to determine the deflection of end-mill for a complete rotation of the spindle motor.

8.2.2 Experimental Setup and Apparatus

Figure 8-1 presents the experimental setup and apparatus that were used to determine spindle runout.

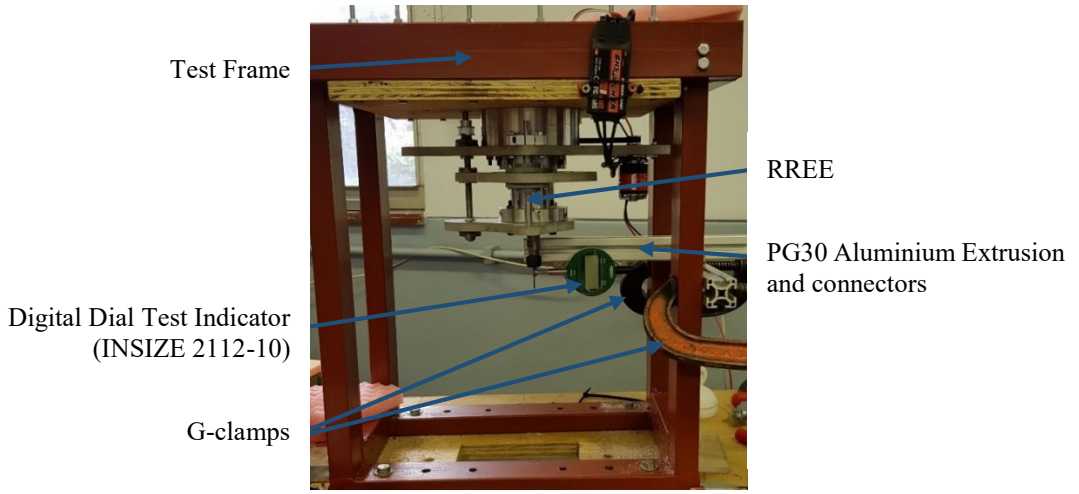

Figure 8-1: Spindle Runout Experimental Setup

8.2.3 Method

1. Mount and Zero the Digital Dial Test Indicator and align its edge to meet the plain shank of the tool.
2. Rotate the tool 18° clockwise.
3. Measure reading from Digital Dial Test Indicator (DTI).
4. Repeat steps three and four at 18° increments to 360°.

8.2.4 Results

Figure 8-2 presents the findings from the experiment in the form of a graph; the complete set of data points is presented in Appendix E.10. The INSIZE Dial Test Indicator has a range of 12.7 mm, an accuracy of 20 micrometres and a resolution of 0.01 mm. The black curve represents the radial runout of the MT spindle for one revolution.

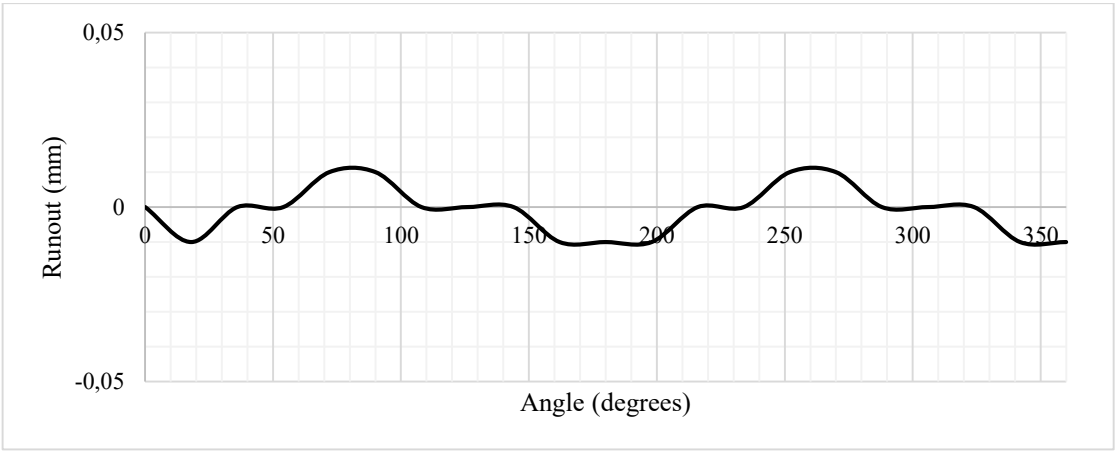

Figure 8-2: Graph of Spindle Runout versus Rotation Angle

Inaccuracies in the experiment are attributed to the stability of the DTI, eccentricity of the ER11 tool holder and measurement of angular position. The DTI was positioned along the shank of the endmill; this did not produce an accurate measurement of total tool runout. To measure total tool runout a blank tool with plain shank was used. The DTI was aligned using a set square. The bracket of PG30 profile was secured by two G clamps as presented in Figure 8-1. Mounting of the DTI was not ideal as the DTI was not completely secure.

However, the purpose of this experiment was to measure the runout produced by the spindle system. This was achieved, and inaccuracies of the investigation were discussed.

8.3 GU Grasp Force – Finger

Grasp strength is a key performance metric for a robotic gripper. It provides a realistic measure of the maximum grasp strength a gripper finger is able to exert on its environment in a pinch grasp mode. The load generated at the fingertip of each gripper finger is investigated. The maximum grasp force of the gripper mechanism is determined at three different approach angles.

8.3.1 Aim and Objectives

The aim of the experiment was to investigate the effect of approach angle on static grasp ability of each gripper finger. The objective was to determine the maximum force that each gripper finger exerts at three different approach angles which cover the range of the gripper.

8.3.2 Experimental Setup and Apparatus

1. Calibrated weight scale (Clover scales electronic balance MARK80V40).
2. Fanuc M10IA Serial Robot.
3. Reconfigurable End-Effector.
4. Calibration masses.
5. Laptop computer with Excel software.

8.3.3 Method

Figure 8-3 illustrates the three approach angles. Figure 8-3 (a) represents the 88° approach angle, Figure 8-3 (b) represents a 45° approach angle and Figure 8-3 (c) illustrates a 0° approach angle.

1. The scale was calibrated with 50 g, 100 g and 150 g mass elements up to 1 kg.
2. End-effector was positioned to position 1 using a Fanuc robot.
3. Finger 1 servo motor was engaged at maximum torque.
4. Finger 1 mass was measured from the scale.
5. Finger 1 servo motor was disengaged.
6. End-effector was rotated about the last joint to maintain its position.
7. Repeat steps three – six for Fingers 2 and 3.
8. End-effector was moved to positions 2 and 3 respectively. Steps three – seven are iterated for these positions. Repeat the test five times.

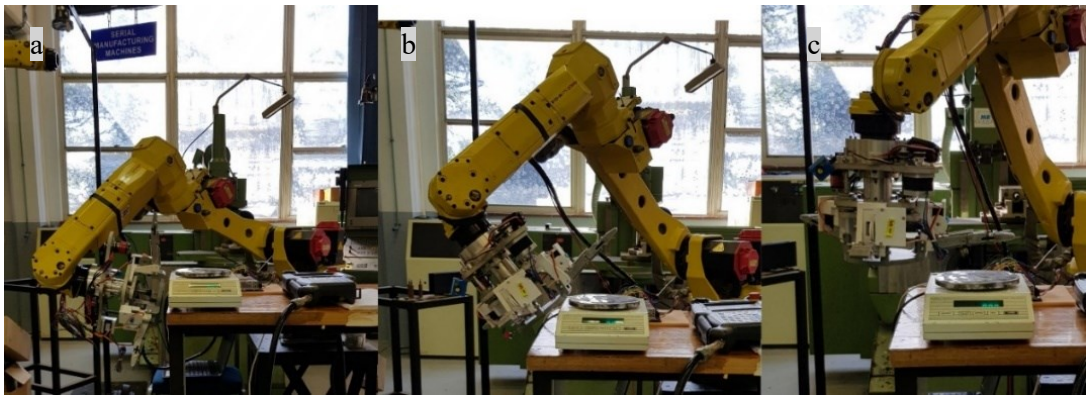

Figure 8-3: Approach Angles - Vertical Reference (a) 88° (b) 45° (c) 0°

8.3.4 Results

Figure 8-4 illustrates the relationship between the approach angle and output load generated by the gripper finger. The grasping force was approximated using the gravitational constant.

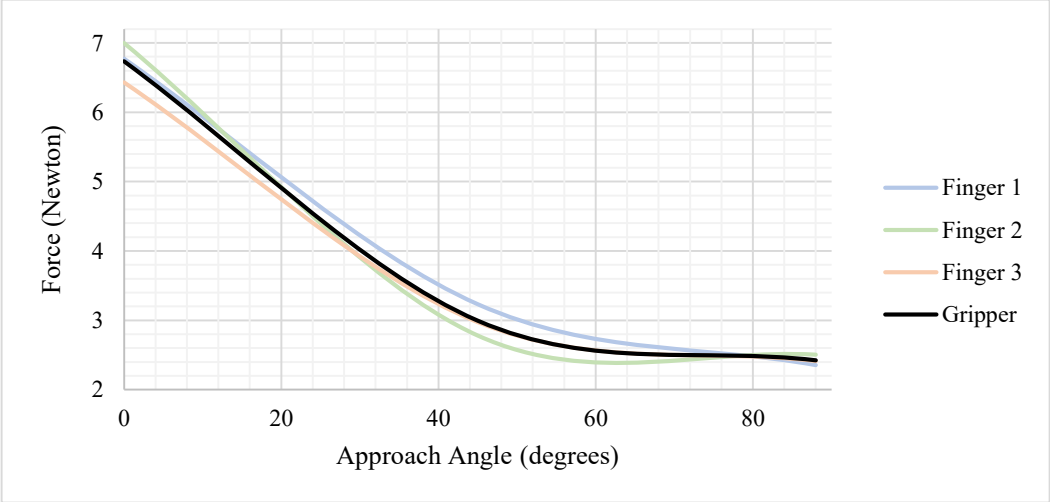

Figure 8-4: Maximum Grasp Force of Gripper versus Approach Angle

The experimental error resulted from the mass measurement. To minimise this error, the electronic scale was first calibrated with calibration masses up to 1 kg. The scale has a measurement range of 4100 grams. Therefore, the experimental measurements were within the measurement range of the scale. Each test was conducted three times, and the average result was taken, this was done to reduce inconsistencies in the measured data. The reading on the scale did not settle, as the servomotors were set to maximum output. The temperature of servomotors elevated when used continually for four minutes; the maximum force produced at increased temperatures decreased.

8.4 GU Grasp Force – Hand

Three-component test apparatus was developed for the purpose of this test. Technical drawings of the apparatus can be found in Appendix K.29. These devices are mounted at three circumferential diameter intervals. The distal phalanx of each gripper finger contacts the slider carriage. As the finger's servo motor is actuated, the finger pushes against the carriage and extends the spring.

8.4.1 Aim and Objectives

The aim of the experiment was to investigate the combined grasp force characteristics of the gripper. The objective of the experiment was to determine the maximum force that the gripper system exerts laterally on an object of varying diameter by measuring spring extension.

8.4.2 Experimental Setup and Apparatus

Figure 8-5 presents the experimental setup to determine the grasp force of the gripper. In conjunction with the apparatus shown in Figure 8-5, EIE SH20 Digital Vernier Calliper; Laptop computer with Microsoft Excel software and marker tape were used in the experiment.

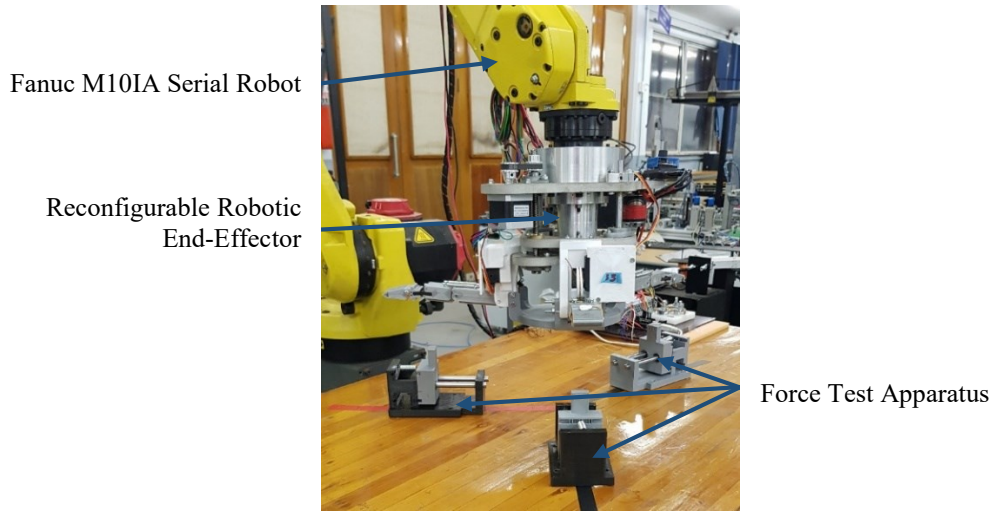

Figure 8-5: Hand Force Experimental Setup

8.4.3 Method

1. Actuate the reconfigurable mechanism to gripping mode.
2. Align the centre of the gripper to worktable and mark finger axes with marker tape.
3. Create 10 mm mark increments on the tape starting at the centre point.
4. Position the three force test apparatus finger contact at 144 mm diameter.
5. Engage gripper servo motors to maximum torque.
6. Measure the spring extension on each force test apparatus using Vernier calliper.
7. Disengage gripper servo motors.
8. Repeat steps four – seven for 244 mm, 344 mm and 384 mm grasp diameters.
9. Repeat the test ten times.
10. Calculate spring force using Hooke's law.

8.4.4 Results

Appendix E.12 contains the complete set of recorded data for the experiment. The result of the experiment was summarised in the Bar Graph presented in Figure 8-6.

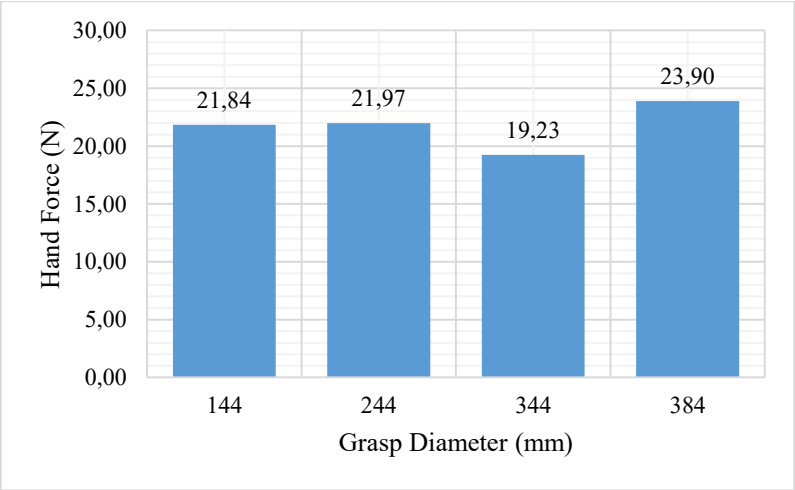

Figure 8-6: Hand Force versus Grasp Diameter

Multiple sources of inconsistency were present in the experiment. The developed force test apparatus (refer to Appendix K.29 for CAD drawing) operated on the measurement of spring extension to calculate force. The extension spring acts to pull the slider to the rest position, while the finger applies a resultant reaction force on the slider in the opposite direction. The extension of each spring was measured from a similar reference point on each of the apparatus with the digital Vernier calliper. Springs are elastic components, as such the elasticity of the device changes over time. It is not guaranteed that all three springs behave exactly the same; this was due to manufacturing tolerances and processing of the springs. This possible variation in spring stiffness has a direct influence on the spring extension and therefore the calculated grasp force. A digital Vernier calliper was used, the reference position of each displacement measurement was not exactly the same as three test apparatus were used. This inconsistency of measurement has a direct influence on the calculated grasp force. To minimise these errors in measurement, the average of ten measurements were taken. The temperature of servomotors elevated when used continually for four minutes; the maximum force produced at increased temperatures decreases.

8.5 GU Accuracy and Repeatability

Dimensional accuracy of each gripper finger gives the positional error of the mechanism. Repeatability of each gripper finger defines the reliability of consistent grasps. These measures predict the positional behaviour of the gripper system for predefined grasping operations. According to Tlach et al. [168], robots one-directional accuracy and repeatability are defined using Equations 8.1 to 8.7. AP defines the one-directional positional accuracy, as given by Equation 8.1. The one-dimensional coordinate of the barycentre mean value from the measured points is given by Equation 8.2. The variable x_j is the coordinate of the j^{th} location.

$$\mathrm{AP} = \bar{x} - x_c \tag{8.1}$$

$$\bar{x} = \frac{1}{n}\sum_{j=1}^{n} x_j \tag{8.2}$$

The one-dimensional positional repeatability (RP) is defined by Equation 8.3. Where $\bar{l}$ (mm) is the mean value of deviation between the barycentre mean and j^{th} location, and is calculated by Equation 8.4. Equation 8.6 computes the sample standard deviation.

$$\mathrm{RP} = \bar{l} + 3S_l \tag{8.3}$$

$$\bar{l} = \frac{1}{n}\sum_{j=1}^{n} l_j \tag{8.4}$$

$$l_j = \sqrt{(x_j - \bar{x})^2} \tag{8.5}$$

$$S_l = \sqrt{\frac{1}{n-1}\sum_{j=1}^{n}(l_j - \bar{l})^2} \tag{8.6}$$

8.5.1 Aim and Objective

The aim of the experiment was to investigate the repeatability and accuracy of each gripper finger. The objective was to determine the grasp force by measuring the spring extension.

8.5.2 Experimental Setup and Apparatus

Three-component test apparatus was developed for the purpose of this test. Technical drawings of the apparatus can be found in Appendix K.29. These devices were mounted at three circumferential diameter intervals. The distal phalanx of each gripper finger contacts the slider carriage. As the finger servomotor was actuated, the fingers pushed against the carriage and extended the spring. Figure 8-7 presents the test apparatus.

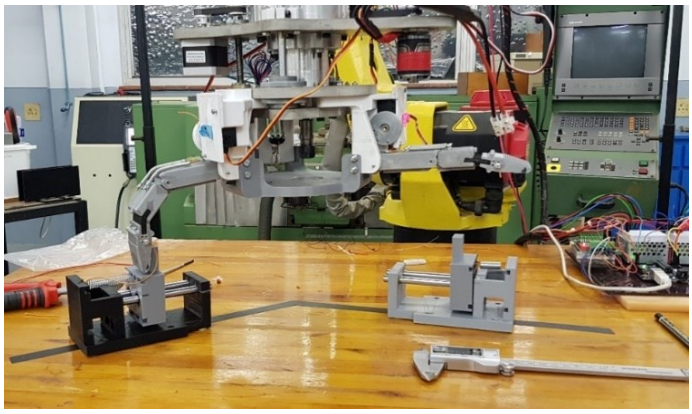

Figure 8-7: Experimental Setup for Repeatability and Accuracy Measurement

1. Fanuc M10IA Serial Robot.
2. Reconfigurable End-Effector.
3. Three Force Test apparatus.
4. Digital Vernier calliper (EIE SH20).
5. Laptop computer with Excel software.

8.5.3 Method

1. Actuate the reconfigurable mechanism to gripping mode.
2. Align the centre of the gripper to worktable and mark finger axes with marker tape.
3. Create 10 mm mark increments on the tape starting at the centre point.
4. Position the three force test apparatus finger contact at 144 mm diameter.
5. Engage gripper servo motors to maximum torque.
6. Measure the spring extension on each force test apparatus using Vernier calliper.
7. Disengage gripper servo motors.
8. Repeat steps four–seven for 244 mm, 344 mm and 384 mm grasp diameters.
9. Repeat the test ten times.

8.5.4 Results

Repeatability of grasp was determined for each gripper finger at four different grasp diameters. Ten iterations of each extension were measured. Appendix E.8 presents the repeatability measurement for each finger at each of the four grasp diameters. The result of the experiment was summarised in the Bar Graph presented in Figure 8-8.

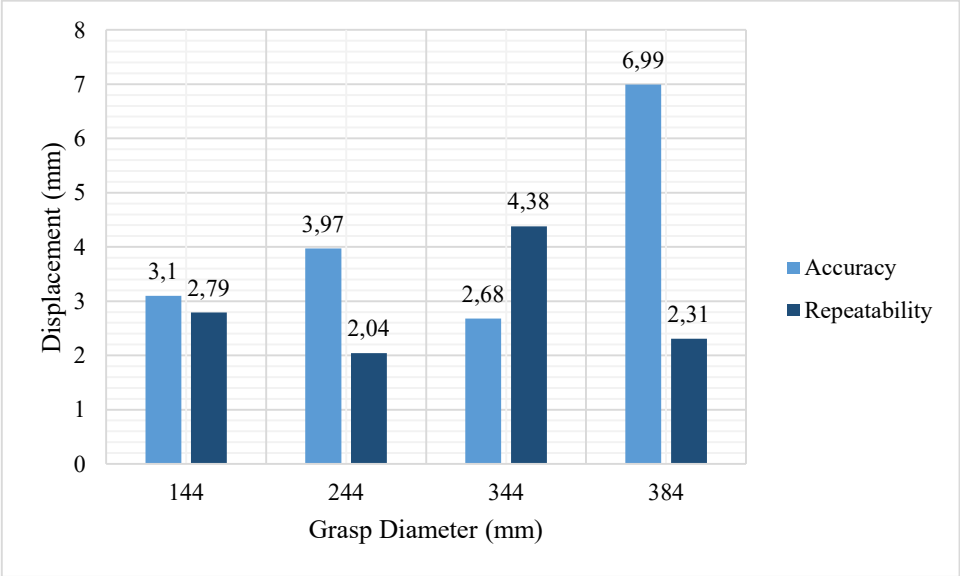

Figure 8-8: Accuracy and Repeatability versus Grasp Diameter

All three springs did not behave exactly the same; this was due to manufacturing tolerances and processing of the springs. This possible variation in spring stiffness has a direct influence on the spring extension and therefore the calculated grasp force. A digital Vernier calliper was used, the reference position of each displacement measurement was not precisely the same as three test apparatus were used. This inconsistency of measurement has a direct influence on the calculated grasp force. To minimise these errors in measurement, the average of ten measurements were taken. The temperature of servomotors elevated when used continually for four minutes; the maximum force produced at increased temperatures decreases.

The rubber joints in the gripper fingers added inaccuracies as the rubber did not maintain consistent initial and final positions between tests. This is due to the hyperelastic material property of rubber. The non-linear

simulation conducted in Section 5.5 provided insight on the stress-strain material characteristic of Butyl 60 durometer rubber.

8.6 GU Slippage of Static Load

Slippage in robot grippers provides a realistic evaluation of the maximum static loading the device holds. This measure of mass is critical to understanding the potential of the developed gripper in different holding configurations. Two such encompassing grasp configurations are investigated; the first grasp involves a cubic object while the second a cylindrical object. Seven test specimens where used, each with different geometric properties and size.

8.6.1 Aim and Objective

The aim of the experiment was to investigate the slippage characteristic of the gripper system. The objective of the experiment was to determine the maximum graspable static weight of the gripper system.

8.6.2 Apparatus

1. Fanuc M10IA Serial Robot.
2. Reconfigurable End-Effector.
3. Calibrated weight scale (Clover scales electronic balance MARK80v40)
4. Calibrated brass weights of 100 g increments.
5. Two weight holder specimens.

8.6.3 Method

1. Actuate the reconfigurable mechanism to gripping mode.
2. Position the first weight holder specimen within grasp range.
3. Engage gripper servo motors to maximum torque.
4. Add 100 g mass to the weight holder specimen.
5. Observe gripper and assess for slippage of the specimen.
6. Repeat steps four and five until the weight holder slips from the gripper.
7. Measure the mass.
8. Disengage gripper servo motors.
9. Position the first weight holder specimen within grasp range.
10. Engage gripper servo motors to maximum torque.
11. Add 100 g mass to the weight holder specimen.
12. Observe gripper and assess for slippage of the specimen.
13. Repeat steps ten and eleven until the weight holder slips from the gripper.
14. Measure the mass.
15. Disengage gripper servo motors.

8.6.4 Results

Figure 8-9 presents the visual slippage of the gripper mechanism under load. The first test specimen slipped at a mass of 1134.7 g. However, the second test specimen slipped at a mass of 2234.9 g.

Figure 8-9: Slippage Weights of Two Specimens

8.7 GU Geometric Adaptability

The gripper unit was developed with an underactuated tendon-driven finger architecture. This mechanism was selected due to simplification of control and its shape adaptability characteristic. Objects of various geometries are grasped by the gripper to determine the effectiveness of the adaptive gripper.

8.7.1 Aim and Objectives

The aim was to investigate the geometric adaptability of the gripper system. The objectives were to (1) Observe gripper finger position in the closed grasp of seven different geometries (2) Determine the success and failure rate of the gripper system for grasping seven different geometries.

8.7.2 Experimental Setup and Apparatus

Figure 8-10 and Table 8-1 present the geometric test specimens and their dimensional parameters, respectively.

Table 8-1: Properties of Test Geometries

Specimen Shape	Dimensions (mm)		Weight (g)
Sphere	Radius	65	135.02
Rectangular Prism	Length, Breadth, Height	215, 205, 75	152.52
Solid Cube	Length	60	134.70
Solid Cylinder	Height, Radius	100, 50	234.42
Filament Spool	Height, Outer Radius	60, 100	216.39
Solid Square Pyramid	Length, Perpendicular Height	80, 120	86.33
Solid Triangular Prism	Length, Height	80, 100	95.48

Figure 8-10: Geometric Test Specimens

8.7.3 Method

1. Actuate the reconfigurable mechanism to gripping mode.
2. Position the first test specimen within grasp range.
3. Engage gripper servo motors to maximum torque.
4. Observe gripper and assess for a firm grasp of a specimen.
5. Record result.
6. Disengage gripper servo motors.
7. Repeat steps three–six ten times.
8. Repeat steps two–seven for twelve specimens.

8.7.4 Results

Table 8-2 presents the success rate of each test specimen in orientation. Figures 8-11 to 8-15 present visual inspection of geometric adaptability of the gripper system.

Table 8-2: Results of Geometric Adaptability Test

Geometry	1	2	3	4	5	6	7	8	9	10	11	12
Success Rate (%)	100	80	100	100	80	100	100	90	100	100	70	100

The gripper had a 100% success rate when the object lay inside the workspace of the system. Enclosed grasp mode yielded a high success rate for the gripper. The polyurethane friction material assisted in increasing graspability of the gripper.

The pinch grasp mode was utilised for geometries one and two. The dimensions of these geometries exceeded the requirements of an encompassing grasp, as presented in Figure 8-11 (a and b) respectively. The third and fourth test geometries were enclosed within the internal workspace of the gripper. Figure 8-11 (c and d) present a side view of the encompassing grasp produced by the robot gripper. The sphere was grasped firmly and adhered well within the workspace of the gripper. The rectangular prism, when grasped along its length (as presented in Test 2, Figure 8-11 (b)) – relied on the grasp force of the gripper and the friction of the polyurethane glove. As such, slippage occurred at a rate of 20%. The third test geometry was grasped securely by the proximal and distal phalanges; the encompassing grasp mode prevented slippage

in all directions. The cube test geometry was constrained at its top, and bottom surfaces as the volume of the cube coincided with the maximum vertical reach of the gripper.

Figure 8-11: Side View of Grasped Test Geometries 1 – 4

The gripper was tasked with grasping objects with cylindrical geometry. Figure 8-12 (a – d) presents the visual grasp result of two different geometries with two different orientations. The fifth and seventh tests, presented in Figure 8-12 (a and d) respectively – reveal the strengths and weaknesses of the gripper. Test geometry five produced a similar result to that of Test 2, in that a pinch grasp was used. When grasped along the length of the cylinder (as presented in Test 5, Figure 8-12 (a)) the grasp hinged on the grasp force of the gripper and the friction of the polyurethane glove.

In contrast, the spool holder in Figure 8-12 (c) was grasped by enclosing the object within the working envelope of the gripper. The difference between test geometries five and seven are seen in the point of contact between the gripper and the object. Test five was pinched by the tip of the distal phalanx while test geometry seven was compressed by the distal phalanx closer to the middle phalanx. Test geometries six produced a 100% success rate; this is attributed to the pinch grasp and increased contact between the gripper palm and fingers. The spool holder failed to grasp effectively in 10% of grasps. Although the objects vertical length exceeded the grasp range of the gripper, the gripper system adapted by complying to the geometries surface features. One of the fingers entered the central hole; this created an anchor to prevent slippage, as seen in Figure 8-12 (d).

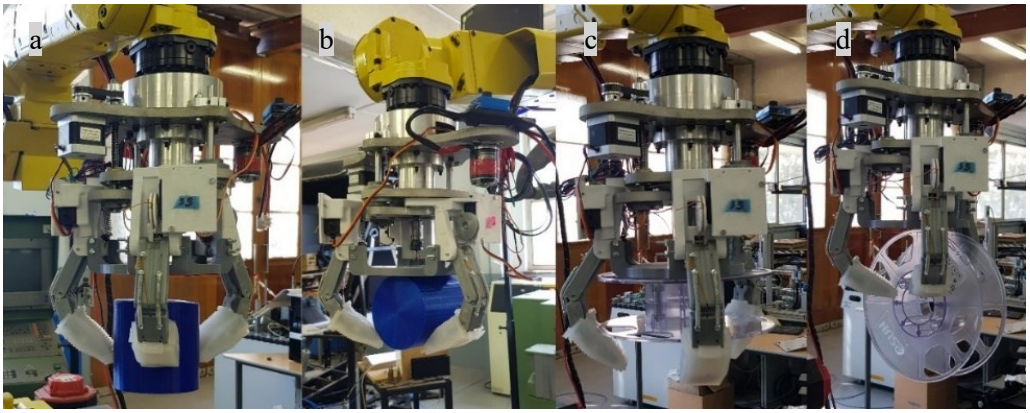

Figure 8-12: Side View of Grasped Geometries 5 – 8

The resultant grasps for test geometries nine, ten and twelve are presented in Figure 8-13 (a,b and d) respectively. These three grasps encompassed the object within the volume of the gripper fingers; as such, these grasps yielded a 100% success rate. The inverted rectangular prism (presented in Figure 8-13 (a))

maintained surface contact with the gripper palm and all three tips of all gripper fingers. Figure 8-13 (b) presents the grasp result of the same rectangular prism; however, the object was grasped along its side. The fingers adapted to the surface contours of the shape without precise positional control. This distinct advantage of the underactuated gripper system is repeated in test geometry twelve (Figure 8-13 (d)).

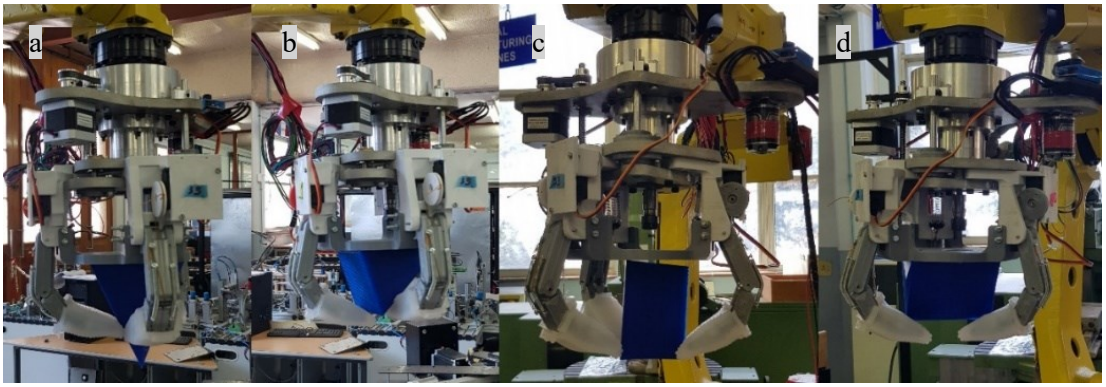

Figure 8-13: Side View of Grasped Geometries 9 – 12

Figures 8-14 and 8-15 produce the bottom view of the grasping operation for test geometries 3 – 6 and 9 – 12, respectively. The notion of increased graspability for enclosed grasps was corroborated by the position of the distal phalanxes of each gripper finger. The closer the tips of the fingers are together increased the grasp stability. This is due to the increased contact force that was generated by this form of grasp; it is shown in Figure 8-14 (b and d) and Figure 8-15 (a,b and d). Grasps that position the robot finger tips along the side surface and maintain a single point of contact – result in decreased grasp stability. This is shown in Figure 8-14 (a and c) and Figure 8-15 (c). The experiment was based on visual inspection; therefore, results were measured on success or failure. As such, the sources of recorded error are minimal.

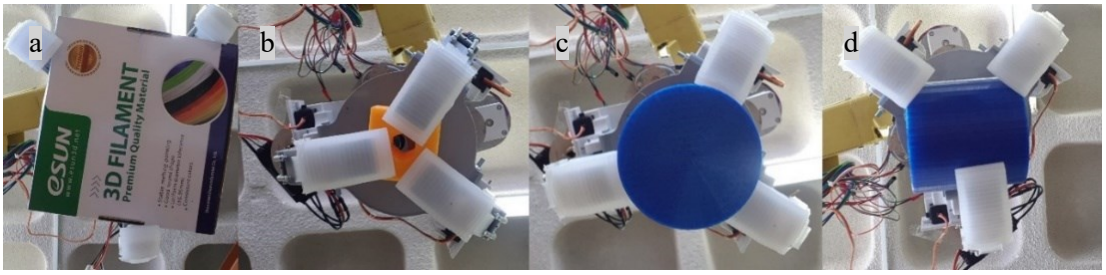

Figure 8-14: Bottom View of Grasped Geometries 3 – 6

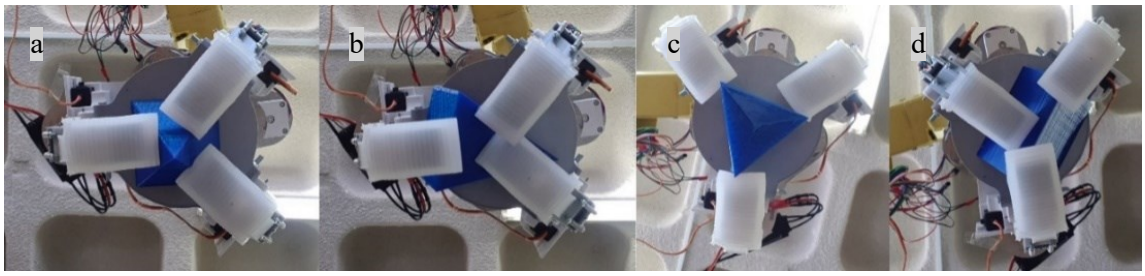

Figure 8-15: Bottom View of Grasped Geometries 9 – 12

8.8 RM Cycle Time

Change-of-operation is of primary significance in this research. The reconfiguration system utilises a linear mechanism to reconfigure the device between grasping and machining modes. The change-over-time is, therefore, a measure of efficiency of this subsystem. This is, the time in seconds the linear actuator takes to move through the length of the power screw from grasp mode to machining mode and return to grasp mode.

8.8.1 Aim and Objectives

The aim was to investigate the reconfiguration time of the end-effector. The objectives were to (1) Determine the duration of the linear actuator to reconfigure the end-effector from gripping mode to machining mode at multiple speeds (2) Determine the duration of the linear actuator to reconfigure the end-effector from machining mode to gripping mode at multiple speeds.

8.8.2 Apparatus

1. Digital Stop Watch (Microsoft Windows).
2. Laptop Computer with Arduino Software.
3. End-effector and control system.
4. Digital Vernier Calliper (EIE SH20).

8.8.3 Method

1. Upload Arduino code from Arduino UI to Arduino Microcontroller through the USB communication port for an 85.48 mm/s linear speed to actuate the RREE to machining mode. Refer to Appendix F.2 for the code.
2. Record the time it takes the platform to move to the machining stance.
3. Upload Arduino code from Arduino UI to Arduino Microcontroller through the USB communication port for an 85.48 mm/s linear speed to actuate the RREE to gripping mode. Refer to Appendix F.2 for the code.
4. Record the time it takes for the platform to move to the gripping stance.
5. Repeat steps one – four for linear speeds of 29.94 mm/s and 14.72 mm/s.

8.8.4 Results

The travel length between modes is 74 mm. Table 8-3 presents the acquired test data for both reconfiguration modes and the resultant cycle time. Three linear speeds were investigated.

Table 8-3: Summarised Results of Cycle Time

	Gripping Mode to Machining Mode		Machining Mode to Gripping Mode		One Cycle	
	Linear Speed (mm/sec)	Time (s)	Linear Speed (mm/sec)	Time (s)	Linear Speed (mm/sec)	Time (s)
1	85,48	0,73	85,48	0,62	85,48	1,35
2	29,94	1,91	29,94	1,77	29,94	3,68
3	14,72	3,79	14,72	3,60	14,72	7,39

Based on the time results from Table 8-3, reconfiguration between the gripping mode to the machining mode took additional time as compared to vice-versa. This is due to the increased load on the linear actuator when the gripper platform was moved upwards. Power screw theory confirms that the torque required to

raise a load is larger than that to lower the same load. Nonetheless, the fastest reconfiguration time was measured to be approximately 1.35 seconds. This was to transform the end-effector from gripping-machining-gripping modes. Stepper motor drive settings are defined in Appendix H. The primary source of error was due to the manually recorded time, which contributed delays in capturing the exact time. Signal delays from the microcontroller may have impacted the measured time result. However, since the same controller was used for all time measurements of the experiment, this error is minimal.

8.9 RM Accuracy and Repeatability

Dimensional accuracy of the linear actuator gives the positional error of the mechanism. Repeatability of the linear drive system defines the reliability of consistent positional motion. These measures predict the positional behaviour of the actuator. According to Tlach et al. [168], robots one-directional accuracy and repeatability are defined using Equations 8.1 to 8.7.

8.9.1 Aim and Objective

The aim was to investigate the repeatability and accuracy of the reconfiguration mechanism. The objective was to determine the deflection of the DTI from a reference position by raising and lowering the reconfiguration mechanism.

8.9.2 Apparatus

1. Digital Dial Test Indicator (INSIZE 2112-10).
2. Two G-clamps.
3. PG30 Aluminium Extrusion and connectors.
4. Laptop Computer with Excel.
5. Fanuc M10IA Serial Robot.
6. Reconfigurable End-Effector.

8.9.3 Method

Aluminium PG30 extrusion is mounted to the work table using G clamps. Digital dial test indicator is mounted to the end of the aluminium extrusion as presented in Figure 8-16.

Fanuc M10IA robot was used to position the end-effector above DTI. Reconfiguration mechanism was actuated to grasp mode (Figure 8-16 (a)) to obtain reference point. The reference position was marked on the bottom surface of the gripper palm. RM was actuated to machining mode (Figure 8-16 (b)), and the DTI was zeroed. Ten reconfiguration cycles were conducted for three different linear speeds. Results were recorded from digital dial test indicator in the grasping mode of each cycle.

Figure 8-16: Repeatability Testing of Reconfiguration Mechanism

8.9.4 Results

Accuracy and repeatability of the reconfiguration mechanism were determined. Table 8-4 presents the acquired data as well as accuracy and repeatability calculations. Refer to Appendix E.9 for the data and calculation.

Table 8-4: Accuracy and Repeatability Calculation of Reconfiguration Mechanism

Linear Speed (mm/sec)	85.48	32.12	14.72
Accuracy (mm)	0.29	0.31	0.21
Repeatability (mm)	0.13	0.05	0.17

Based on the results of accuracy and repeatability presented in Table 8-4, the best actuator accuracy measurement was attained at a linear speed of 14.72 mm/sec. While the most repeatable actuator measurement was produced at a linear speed of 32.12 mm/sec. The INSIZE Dial test indicator has a range of 12.7 mm, an accuracy of 20 micrometres and a resolution of 0.01 mm.

Multiple sources of inconsistency were present in the experiment. Inaccuracies in the experiment are attributed to the stability of the DTI and its mounting. Positioning error of the actuated platform due to missed steps by the NEMA 17 stepper motor, which occurred at high linear speeds. To minimise these errors in measurement, the average of ten measurements were taken. The aim of the experiment was met as the accuracy and repeatability of the linear mechanism was investigated.

8.10 Performance and Interactions – Spindle Subsystem

8.10.1 Dynamics of Multistage End-Effector Assembly

The frequency response functions of the machine tool spindle were computed to determine if the integration of the gripper subassembly and reconfiguration subassembly affect the dynamic structural characteristics of the machine tool. According to Grossi et al. [22], machine tool dynamics are usually represented by a frequency response function at the tool-tip. The function is generated by conducting an impact test on the stationary tool. Doina [23] researched the dynamic properties of milling centres by experimentation. An impulse force caused excitation in the machine tool, and the vibration response was recorded. Accelerometers were positioned at the spindle head, the table, and the clamping device. The research allowed the determination of critical frequencies, damping, and stiffness of the system. Shiak and Strinivas [24] investigated the modal characteristics of a spindle tool unit experimentally. Tooltip frequency response

and stability lobe diagrams were obtained using the finite element method. The frequency response function of the endmill-tool system was also determined experimentally by means of Impact Hammer testing. A triaxial accelerometer was used. Input and output signals were recorded, and Fourier transforms obtained the frequency response. The average tooth angle method was used to predict the stability lobes.

8.10.1.1 Aim and Objectives

The aim of the experiment was to investigate the effect of gripper and reconfiguration subsystem on spindle dynamics. The objectives to achieve the aim were to (1) Determine FRF of multiple assembly stages of the end effector through impulse testing (2) Extract modal parameters from multiple FRFs (3) Determine critical speeds of the spindle shaft.

8.10.1.2 Experimental Setup and Apparatus

The integration of machining and part handling into an end-effector required an investigation into the effect amalgamating these functions into a single device. The performance of spindle subsystem was therefore investigated individually and at various stages of integration with the reconfiguration and gripper subsystems. The apparatus used for the experimental modal analysis of the multistage assembly is the same as that used in Section 7.9.2. Figure 8-17 (a – d) provides the cases that were investigated.

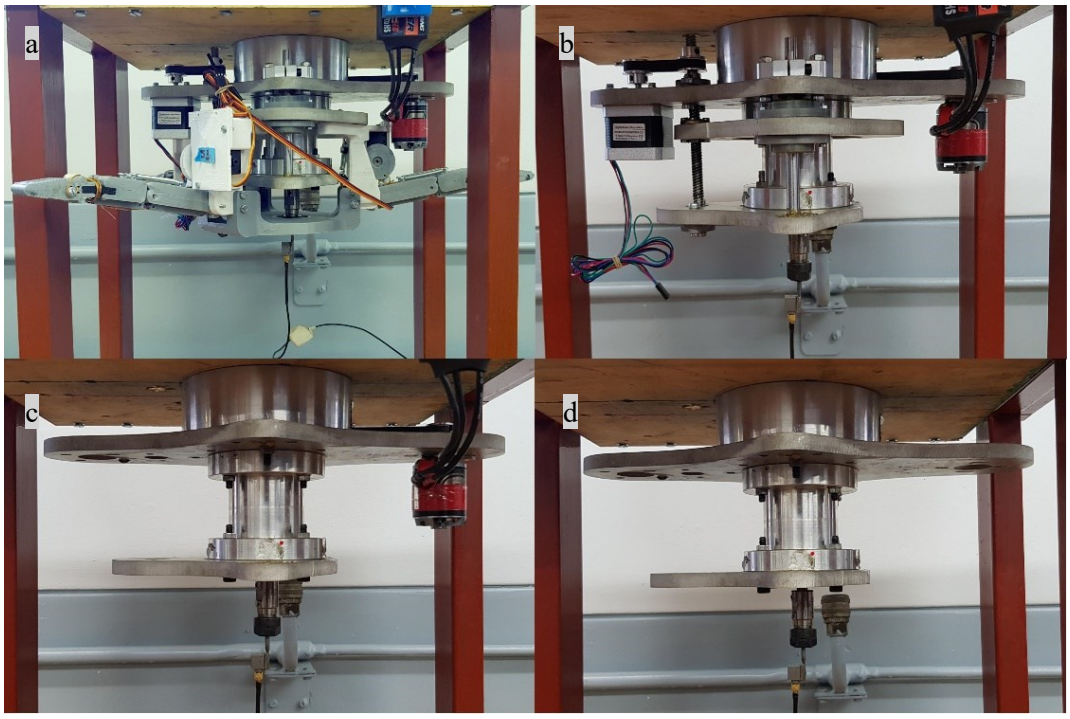

Figure 8-17: Four Stage Structural Decomposition (a) Complete System Assembly (b) Gripper Subassembly Removed (c) Gripper Subassembly and Reconfiguration Subassembly Removed (d) Spindle Only (Spindle Drive Removed)

8.10.1.3 Method

The experimental method used to determine the modal parameters of each of the four stages of the RREE is analogous to the method used in Section 7.9.3. Additionally, the method was repeated four times for each of the four stages of assembly.

8.10.1.4 Results

Figures 8-18 and 8-19 represents the acquired magnitude and imaginary frequency response signals of cases a-d, respectively. The black curves correspond to case a, the red curves correspond to case b, the green curves correspond to case c, and the blue curves correspond to case d. Table 8-6 represents the tabulated modal parameters of the four-stage structural response.

The inverted peak at 2348.8 Hz from Figure 8-19 corresponds to the critical frequency of the system [155]. Natural frequencies of the system are represented by peaks in Figure 8-18. Five such frequencies were identified. Modal analysis was conducted using the Peak-Picking method [151]. The critical mode produced the largest amplitude; this was identified as 2348.8 Hz.

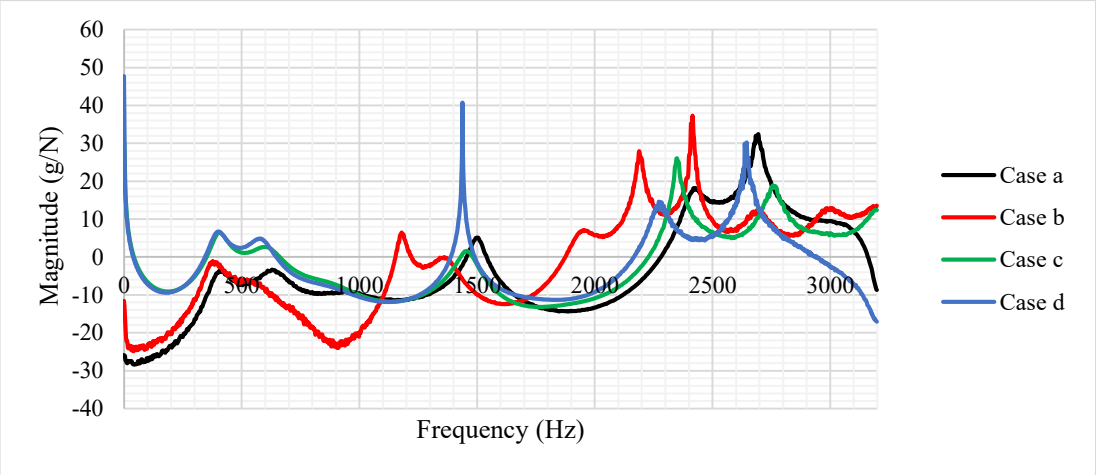

Figure 8-18: Frequency Response Function of Multistage End-Effector (Magnitude)

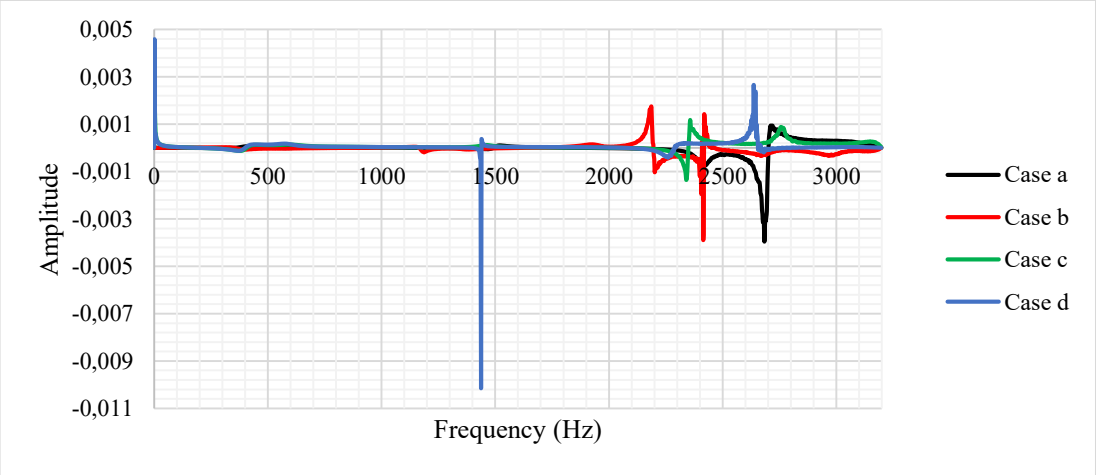

Figure 8-19: Frequency Response Function of Multistage End-Effector (Imaginary)

A critical amplitude of -0.00138 g/N at this frequency was found from Figure 8-19. The experimental stiffness k_{exp} and damping ratio ζ are 27510 N/m and 0.013171 respectively. The cutting stiffness or specific power was calculated using the cutting force coefficients for Aluminium 6061. The cutting stiffness k_s was found to be approximately 907.055 N/mm^2 [166]. Equations 7.1 and 7.2 were used to determine the experimental stiffness and damping ratio, respectively.

Critical speeds of the spindle shaft at each mode frequency was determined. This validated the designed spindle shaft. The rotational speed of the spindle should not exceed these critical values as modal frequencies will occur. Large deformations and unstable structural characteristics occur at these natural frequencies. The rotor dynamics were determined based on the calculated natural frequencies. The critical speeds for three stages of the end-effector are presented in Table 8-5. The critical speeds for case a were presented previously in Table 7-1. The modal parameters for multistage analysis of the end-effector are presented in Table 8-6. The modal parameters for case a were presented previously in Table 7-1.

Table 8-5: Mode Parameters of Assemblies b, c and d

Assembly	Mode	Frequency (Hz)	Amplitude (g/N)	Critical Speed (RPM)
b	1	375.467	-1.13	22528.02
	2	1179.73	6.46	70783.8
	3	1358.93	-3.84E-02	81535.8
	4	1956.27	7.063	117376.2
	5	2188.8	27.92	131328
	6	2414.93	37.27	144895.8
	7	2688	12.32	161280
	8	3001.6	12.88	180096
c	1	407.467	6.462	24448.02
	2	595.2	2.649	35712
	3	1459.2	1.579	87552
	4	2348.8	26.04	140928
	5	2756.27	18.88	165376.2
d	1	403.2	6.728	24192
	2	580.267	4.823	34816.02
	3	1437.87	40.73	86272.2
	4	2272	14.62	136320
	5	2645.33	30.24	158719.8

Table 8-6: Modal Analysis of Four Stage Structural Response

End-Effector Assembly	Critical frequency (Hz)	Critical Amplitude (g/N)	Experimental stiffness (N/m)	Damping ratio
a	2694.4	-0.004	14500	0.008709
b	2414.93	-0.0039	11609	0.0110438
c	2348.8	-0.00138	27510	0.013171
d	1437.87	-0.0102	3477	0.0141

8.10.2 Stability Analysis of Multistage End-Effector Assembly

Machine stability was effected by the addition of components. The reconfigurable system affects the region of stability attainable for the cutting operation. The most substantial depth of cut was attained by the third configuration of the assembly. This is the assembly with the gripper system removed, as presented in Figure 8-17 (c).

Figure 8-20 represents the Stability Lobe Diagram for the four assemblies. The area under the lines represents the areas of chatter-free cutting conditions. The stability plots are computed by means of

Altintas' [156] stability equations for multiple linear plots. The black line represents the SLD of subassembly a; the red line represents the lobe-line of subassembly b. The stability plot for subassembly c is given by the blue lobe-line, while the green curve represents the SLD of subassembly d. Refer to Appendix E.4 to E.7 for simulation data points.

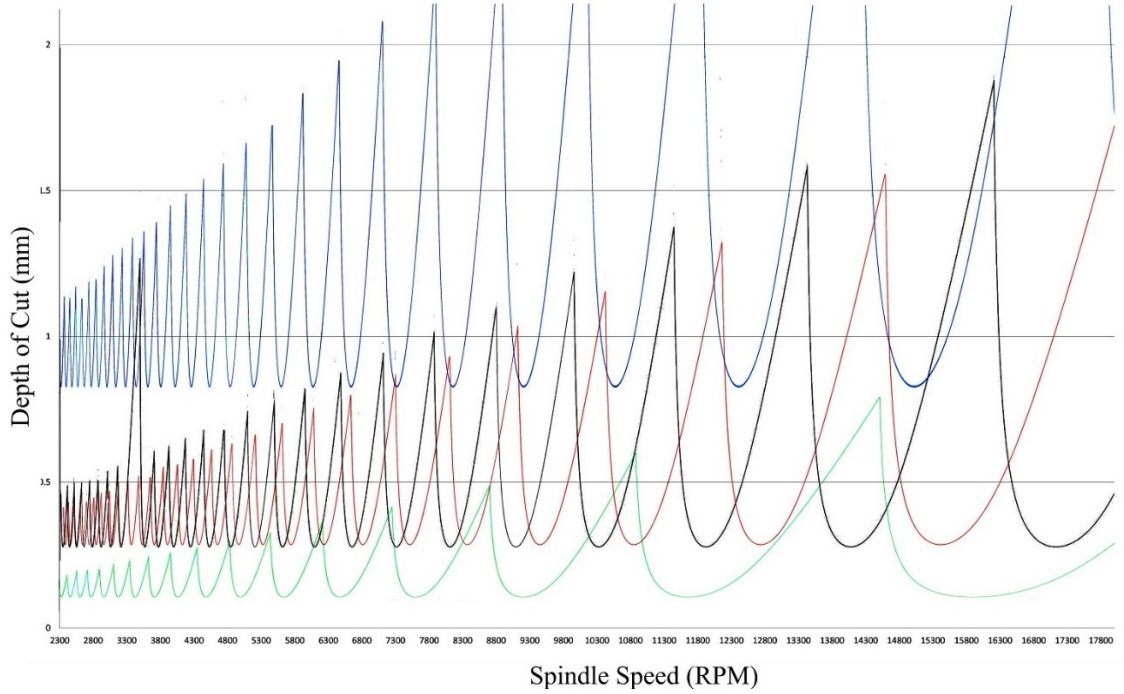

Figure 8-20: Stability Lobe Diagram of Multistage Assembly

8.11 Performance and Interactions – Gripper Subsystem

The dynamic response of the gripper system was investigated, due to vibrations being transmitted from the spindle rotation and cutting process, while the gripper is in a retracted state. The purpose of the investigation was to establish if the dual-purpose end-effector's feasibility is diminished by unwanted vibrations. The vibration response of the gripper unit was measured by placing one accelerometer on each gripper finger.

8.11.1 Vibration Response – Rotating Spindle

Machining is a highly dynamic operation. The machine tool motor and spindle rotate in excess of 10 000 RPM. Process vibration is inevitable at these speeds. The RREE is a coupled system consisting of three subsystems. It is imperative to understand the extent of these process vibrations on the gripper system. For this reason, a vibration test is conducted to run the MT spindle through its operating speed range.

8.11.1.1 Aim and Objectives

The aim of the testing was to investigate the dynamic effect of the rotating machine tool on gripper response. The objective of the test was to measure the vibration response of each gripper finger while the machine tool is rotating at different speeds.

8.11.1.2 Experimental Setup and Apparatus

1. Laptop Computer with National Instruments Signal Express Software (2017).
2. National Instruments Data Acquisition Device (cDAQ-9171 CompactDAQ).

3. National Instruments Sound and Vibration module (NI-9234 C Series).
4. Uniaxial Accelerometer (Bruel & Kjaer 4507B) and IEPE Lead Connecting Cables.
5. Test Frame.

8.11.1.3 Method

1. Turn off the machine tool spindle and disconnect it from the mains power supply.
2. Mount the accelerometer to the middle of the distal phalanx of each gripper finger, directed to the y-axis reference.
3. Configure NI Signal Express for data acquisition. Refer to Appendix E.1 for setup instructions. Figure 8-21 presents a portion of the block diagram created for data acquisition in the LabVIEW environment. Refer to Figure E 12-64 in Appendix E.14 for the complete block diagram;
4. Run the machine tool spindle at 2556 RPM using the laser tachometer to set speed.
5. Trigger signal measurement thirty seconds after the spindle is turned on.
6. Repeat steps four and five for spindle speeds of 3733 RPM, 4132 RPM, 4853 RPM, 5526 RPM, 6490 RPM, 7308 RPM, 8079 RPM, 8890 RPM, 9663 RPM, 10318 RPM, 11559 RPM, 12455 RPM, 13741 RPM and 14722 RPM respectively.

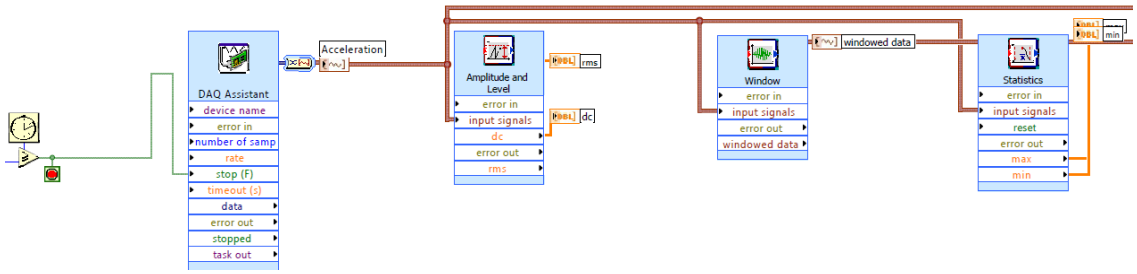

Figure 8-21: Portion of LabVIEW Block Diagram

8.11.1.4 Results

The machine-tool spindle was run at various speeds with no cutting engagement, and the average vibration response of each gripper finger's distal phalange was measured. The average acceleration – time response is shown in Figure 8-22. Random vibration responses of Fingers 1,2 and 3 are represented by the light blue, light green and light orange curves presented in Figure 8-22. The black curve represents the average random acceleration of all three gripper finger, which is approximated as the random vibration of the gripper system. Appendix E.1 contains the data points.

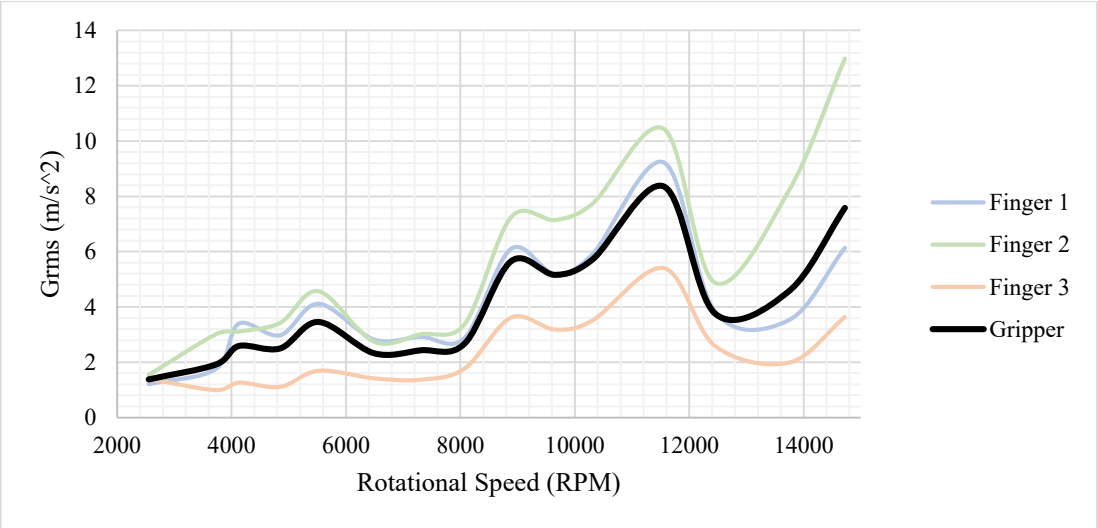

Figure 8-22: Graph of RMS Acceleration versus Rotational Speed of Spindle

8.11.2 Vibration Response – Linear Cut

The milling operation involves material removal at elevated rotational speeds. Process vibrations are induced from the feed mechanism, machine tool spindle, and cutting operation. These three principal sources of vibration have a compound effect on the end-effector structure. Therefore, it is vital to understand the extent of these compounded vibrations on the gripper system. For this reason, a vibration test is conducted to perform multiple linear cuts in Aluminium 6061.

8.11.2.1 Aim and Objectives

The aim of the experiment was to investigate the dynamic effect of machining operation on the gripper response. The objective was to measure the vibration of each gripper finger while the machine tool is engaged in a straight cut of Aluminium.

8.11.2.2 Experimental Setup and Apparatus

The majority of the apparatus used for this experiment is similar to that used in Section 8.11.1.2. Figure 8-23 presents the critical components of the experimental setup and apparatus used. Additional items are (1) Feed Axis Linear Actuator (2) Vice Fixture (3) Twenty-Two Aluminium 6061 Test Specimens.

Figure 8-23: Experimental Setup

8.11.2.3 Method

1. Turn off the machine tool spindle and disconnect it from the mains power supply.
2. Mount the accelerometer to the middle of the distal phalanx of each gripper finger, directed to the y-axis reference.
3. Configure NI Signal Express for data acquisition. Refer to Appendix E.1 for setup instructions.
4. Move linear actuator to reverse position.
5. Load aluminium sample in the fixture and secure.
6. Run the machine tool spindle at 8133 RPM using the laser tachometer to set speed.
7. Move linear actuator to forward position with feed rate of 0.73 mm/sec and 0.42 mm depth of cut.
8. Trigger signal measurement at the midpoint of cut in DAQ software.
9. Repeat steps four-eight for spindle speeds of 9057 RPM, 10766 RPM and 12530 RPM respectively.

8.11.2.4 Results

The acceleration – time response for Fingers 1, 2 and 3 are represented in Figure 8-24. The acceleration response was measured at each fingertip of each gripper finger. Random vibration responses of Fingers 1,2 and 3 are represented by the light blue, light green and light orange curves presented in Figure 8-24. The black curve represents the average random acceleration of all three gripper finger, which is approximated as the random vibration of the gripper system. Appendix E.2 contains the data points.

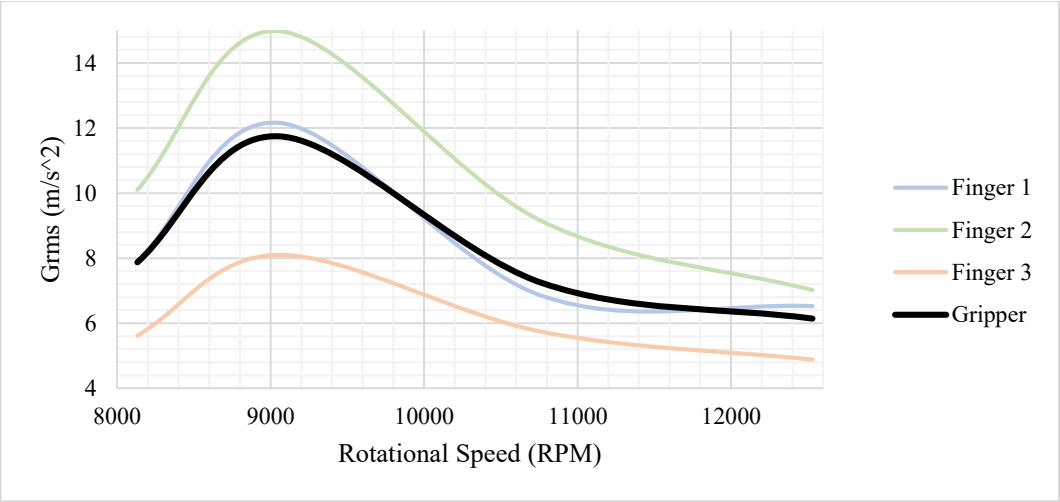

Figure 8-24: Graph of RMS Acceleration versus Rotational Speed of Spindle

8.11.3 Vibration Response – Reconfiguration

The gripper housing is rigidly coupled to the linearly actuated platform. This platform moves between two positions which provide the two modes of reconfiguration.

8.11.3.1 Aim and Objectives

The aim of the experiment was to investigate the dynamic effect of the reconfiguration operation on gripper response. Objectives were to measure the vibration of each gripper finger while the reconfiguration mechanism was actuated between grasp and machine modes. The average vibration of the gripper system was approximated as the average vibration result of finger vibrations.

8.11.3.2 Apparatus

The experimental setup and apparatus used for this experiment are the same as that in Section 8.11.1.2.

8.11.3.3 Method

1. Turn off the machine tool spindle and disconnect it from the mains power supply.
2. Mount the accelerometer to the middle of the distal phalanx of each gripper finger, directed to the y-axis reference.
3. Configure NI Signal Express for data acquisition. Refer to Appendix E.1 for setup instructions.
4. Run the linear actuator vertically upward to a maximum position at a speed of 1.77 mm/sec.
5. Trigger signal measurement two seconds after the stepper is engaged.
6. Run the linear actuator vertically downward to a maximum position at a speed of 1.77 mm/sec.
7. Trigger signal measurement two seconds after the stepper motor is engaged.
8. Repeat steps four – seven at linear speeds of 3.73 mm/sec and 5.57 mm/sec respectively.

8.11.4 Results

Figure 8-25 plots the average acceleration of each finger and the gripper against the speed of the linear actuator. Random vibration responses of Fingers 1,2 and 3 are represented by the light blue, light green and light orange curves presented in Figure 8-25. The black curve represents the average random acceleration of all three gripper finger, which is approximated as the random vibration of the gripper system. Appendix E.3 contains the data points.

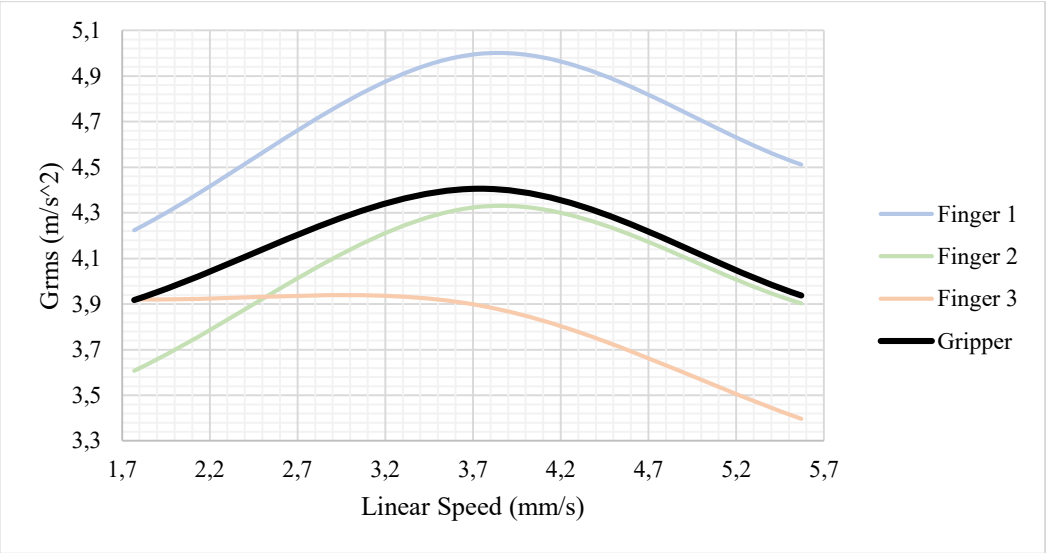

Figure 8-25: RMS Acceleration versus Linear Speed

A maximum average acceleration was observed on the first gripper finger; this is due to the close proximity of the finger to the stepper motor. A minimum average acceleration was observed at the third gripper finger; the distance between this finger and the stepper motor was the least of the three fingers.

8.12 Chapter Summary

Experiments were conducted to determine the operational characteristics of the RREE. The first test phase revealed individual performance metrics for each of the three subsystems. Spindle runout testing of the MT was investigated in Section 8.2. The grippers finger and hand force were investigated in Sections 8.3 and 8.4, respectively. The accuracy and repeatability of the gripper system were determined in Section 8.5. Slippage and geometric adaptability of the gripper system were obtained in Sections 8.6 and 8.7, respectively. Process cycle time was determined based on the duration between reconfiguration modes in Section 8.8. The accuracy and repeatability of the linear actuator were determined in Section 8.9. The second phase investigated the extent of interaction between subsystems. Performance and interactions of the spindle and gripper subsystems were tested in Sections 8.10 and 8.11, respectively. The integration of these subsystems altered the critical characteristics of the RREE structure. Stability of the RREE was determined in Section 8.10.2, and the dynamic response of the gripper system was investigated in Section 8.11. The following chapter provides a review of the research aim and objectives. RREE architecture is justified based on the current industry demand. A reflective analysis of the mechanical design is followed by a discussion of the computational analyses and experimental findings. Performance benchmarking of the RREE is conducted, followed by a discussion of implications, limitations and improvements.

Chapter 9 Discussion

9.1 Introduction

This chapter discusses the significance and implications of the findings concerning the research and development of the reconfigurable robotic end-effector. A summative assessment of the research and establishment of the state of the art in robotic end-effectors and design methods for reconfigurability is presented. Furthermore, the mechanical design of the RREE is justified based on the functional requirements and specifications. The performance of the RREE is summarised based on the output of its subsystems. The results of calculation, simulation and experimentation on these subsystems are discussed. Errors therein are noted, and the implications of these errors are explored. Essential performance and operational metrics are identified. The performance of the developed RREE prototype is benchmarked against six competitors. The implications of this research are discussed in relation to the performance of the RREE. The limitations of the RREE are noted; these limitations exist due to factors such as cost, manufacturability and technological constraints. Finally, improvements to the end-effector are discussed based on the shortcomings of the research.

9.2 Research Overview and Justification of RREE

Consumers demands are evolving, based on the availability of larger product varieties. The life cycle of produced goods is decreasing as a result of this. The market is in need of a compact two-in-one solution to machining and part handling. An end-effector that is able to retrofit to most serial robots and parallel robots will offer a higher level of flexibility in manufacturing.

This research has developed a cost-effective, compact reconfigurable end-effector that is able to perform both end-milling and part handling operations. The engineering design process and mechatronics design philosophy presented in Section 1.6 were used to fulfil this research.

Robotic gripping end-effectors have multiple forms which are based on application. Traditional industrial grippers, reviewed in Section 2.3, provide high repeatability and accuracy but are limited to task-specific applications. These grippers are not well-suited for dynamic manufacturing as the structure of such grippers is not adaptable or reconfigurable. Recently, soft robots have sparked interest in the gripping industry. Many researchers are studying the implications of this technology and its use in soft robotic grippers [44, 45, 49-51]. Soft grippers contrast industrial grippers as they are highly compliant, reconfigurable and more cost-effective. Based on the research conducted in Section 2.4, soft grippers are challenging to model, control, manufacture and are limited to low gripping force applications. The conceptual gripper design presented in Section 3.5.2 combined elements of mechanical grippers and soft rubber. The main advantages of this collaborative solution are two-fold. The gripper concept is tendon-driven, which allows for the independent actuation and control of individual gripper fingers. The flexible joint offers compliance and shape adaptability due to the elastic material property of rubber.

Robotic machining is a developing technology; as such, the number of readily available products are minimal. Researchers are predominantly developing milling and drilling machining robotic systems, as the architectures of serial and parallel robots are best suited for these processes [11, 169, 170].

There are limited attempts to merge both cutting and gripping into a single end-effector. Currently, dedicated end-effectors are used based on a specific type of application. Much research is being conducted on reconfigurable robotic grippers [48, 65-67]. These end-effectors offer reconfigurability of grasp, but not of process. This research focused on the development of a novel end-effector design, capable of reconfiguration between milling and gripping processes.

In addition to the overall reconfigurable design methodology presented in Section 3.3.1, the development of the RREE's subsystems required detailed design methodologies. Three such methodologies were utilised in this research, for the design of the MT, GU and RM subsystems.

The design methodology presented in Section 4.2.2 for the MT subsystem was adapted from Maeda's Expert Spindle Design [88]. The method proposed by Maeda [88] could not be utilised entirely due to the proprietary software required; this software was inaccessible during the time of this research. Nevertheless, elements of the method were applied to this study. The mechanical design of the MT was presented in Section 4.2; the MT met design specifications and reconfigurability requirements. The spindle was designed to machine woods, plastics and non-ferrous metals such as aluminium. The compact, brushless motor is coupled to the spindle via a belt-pulley drive system. While the GT2 belt-pulley system is theoretically functional, it is not the best power transmission mechanism for this design. The methodology did not take into account the vibrational effect of these belts at high speeds (above 12000 RPM). The method is well suited in bearing, tool-holder and motor selection through the calculation of bearing stiffness and cutting requirements such as tangential cutting force. The design of the spindle shaft and housing met the reconfigurability requirements of the RREE. The electronic system of the MT is controlled by potentiometer through the Arduino microcontroller. The method resulted in the successful design and implementation of the RREE MT.

The design methodology presented in Section 4.3.2 for the GU subsystem is original and applicable to the development of reconfigurable robotic grippers. The methodology required extensive use of SolidWorks CAD software; in addition, many gripper finger prototypes were used to produce the final design. The methodology accurately determined the torque requirement to grasp a specified load. This was used to select an electric motor. The requirements of reconfigurability have a significant impact on the design of mechanical and electronic systems. Due to the compact, modular gripper design, the transmission system is cable actuated. The methodology utilised the DH method and MATLAB to develop the kinematic model of the mechanism and simulate the planar workspace. Simplifications to the model resulted in an inaccurate workspace. The servomotors were position controlled by potentiometers through the Arduino microcontroller, and each gripper finger was actuated independently. Nonetheless, the developed methodology resulted in a capable, low-cost, flexible robotic gripper which is compatible with reconfigurable end-effectors.

The remaining subsystem design methodology was presented in Section 4.4.2, the RM's linear actuator provided system reconfiguration. The methodology is original, in that, the condition of reconfigurability dictated the design of the linear actuator. Scalability in reconfigurable design is maintained in the proposed method. However, the use of multiple platforms resulted in a bulky mechanical design that limits the dynamic ability of the end-effector.

The combination of research and design methodologies presented in this study has resulted in the successful implementation of the RREE.

9.3 Performance Summary

9.3.1 Machine Tool Subsystem

9.3.1.1 Force Prediction

The static structural FEA conducted in Section 5.3 determined the maximum von-Mises stress and deformation induced by the cutting forces calculated in Section 5.2. The numerical simulation yielded maximum forces of – 87.0245 N, 164.397 N and 4 N for feed, normal and axial respectively. The normal component of cutting force is less than 200 N; this correlates well with other studies given similar cutting conditions and workpiece material [90]. The axial component of cutting force is minimal due to the 2 mm depth of cut; this increases with the depth of cut and cutter diameter. The start and exit immersion angle range of 85° - 100° was used due to recurring periodic forces. Fundamentally, the maximum values of these force components were required for the Spindle Shaft structural simulation.

9.3.1.2 Static and Dynamic Simulations

Structural simulations are a useful tool which provides insights on poorly designed areas of a component. However, the correct loads, materials and constraints must be applied to produce a valid solution result. Checks to validate the simulation model were therefore necessary. Mesh metrics such as Jacobian and aspect ratio were within the acceptable range of aspect ratio less than 50 and Jacobian between 0 and 1. [122]. The CTETRA10 three-dimensional mesh element was assessed for quality and consistency in Section 5.3.4. Local mesh controls were applied to specific areas to improve accuracy and mitigate localised errors caused by small features. A mesh convergence study was conducted in Section 5.3.5, to validate the CTETRA10 element used for analyses conducted in Sections 5.3, 5.4, 5.5, 5.8 and 5.9. Figure 5-7 in Section 5.3.5 presented the Mesh Convergence Plot for the selected mesh element; the study confirmed Von-Mises stress convergence as the element size was reduced from 5 – 1 mm. The model geometry was constrained correctly in the necessary directions and locations to prevent rigid body motion; as a result, no solution errors occurred in the simulation. The simulation result of Von-Mises stress produced a safety factor of 2.11, which ensured that the structure does not fail under usage. The simulation model was simplified to improve computation speed and accuracy; in doing this, the tool geometry was simplified as the flutes were removed. The cutter flutes add structural rigidity to the endmill, and the simulation model negates this property. Nonetheless, the maximum deflection of the designed spindle shaft is 0.388 mm and occurs at the collet holder mounting-end of the shaft, as indicated in Figure 5-11. This resultant deformation was sub-millimetre and did not cause severe inconsistencies for its intended usage.

Machine failure as a result of large spindle deformation caused by self-excited vibration is uncommon. Modal analysis of the Spindle Shaft was conducted in Section 5.4, and the natural frequencies of the shaft were determined. The limitations and implications of the selected mesh element were previously discussed. The shaft was restrained at the bearing mount locations with non-translational constraints. Free vibration response of the structure resulted in multiple mode-coupling. This simulation does not include bearing stiffness and damping effects; therefore, the result is not an accurate representation of the dynamic

behaviour of the Spindle Shaft when used in the Machine Tool. Nonetheless, the dynamic behaviour of the Shaft was determined for the ideal case of free rotational degrees-of-freedom and fixed translational degrees-of-freedom.

Additionally, the dynamic characteristics of the MT Spindle structure were investigated in Section 5.5. Modal analysis was conducted in Siemens NX 11 simulation environment; the selected mesh element has been justified previously. Modal coupling effects of the robotic manipulator was not considered in the simulation as the RREE is intended to be used on multiple robots. The model was constrained by fixed constraints located at the bolted joint connection holes on the Robot Mount. The association between components are necessary to obtain a realistic solution, as the model consists of thirteen components. The surface-to-surface glueing simulation object-type was used to constrain all bodies together.

The dynamic response of the Spindle Shaft was determined from the coupled model by utilising the isolation feature for assemblies in the NX post-processor. Referring to Table 5-6 in conjunction with Figures 5-19 to 5-23, the subassembly and spindle shaft both experienced critical deformation at the second natural frequency of 542.3 Hz. Therefore, this is the critical mode from FEA analysis.

Based on the results from the investigative analysis on critical speed which was conducted in Section 5.6, the first natural frequency which induced large deformation in the structure occurred at 540.7 Hz. The critical speed at this frequency is 32442 RPM; this is significantly larger than the operational speed of the spindle shaft. The shaft structure resonates critically at a frequency of 2045 Hz, which occurs at a rotational speed of 122700 RPM. The required cutting speed for Aluminium 6061 is 12127.61 RPM. Therefore, according to the simulated results - the spindle shaft and RREE MT are designed well within dynamic limitations.

9.3.1.3 Experimental Modal Analysis of RREE

Experimental Modal Testing produces the Frequency Response Function of a structural system. Impulse Testing is a widely-used method of Experimental Modal Analysis [80, 151, 152, 155, 158, 171]. Section 7.9 presented the EMA of the RREE structure; the modal parameters were determined from the FRF plots in Figures 7-8 and 7-9. The RREE was mounted to the Test Frame which was developed for vibration testing of the RREE. A rigid coupling was created at the mounting point of the RREE, which permitted free oscillation at the tooltip.

A frequency range of 3200 Hz was used based on the recommended window configuration of 9000 samples at 18000 Hz. The highest peak on the Magnitude FRF plot coincided with the lowest peak on the Imaginary FRF plot; this point represents the critical frequency of the structure. Critical excitation occurred at 2694.4 Hz, the critical amplitude at this frequency was extracted from the Imaginary FRF plot (presented in Figure 7-11). The Half-Power method was used to approximate the damping ratio and experimental stiffness [161]. These modal parameters were required for the SLD prediction [157]. While a relatively simple technique to implement, it is difficult to obtain consistent results. Therefore, thirty tests were completed initially – the conceded result was an average of five identical measurements. Two assumptions were made for the EMA in this research. These are time invariance and linearity. The structure of the RREE did not change with time; it was controlled as measurements were taken. According to McConnell [172], Hanning windows are applicable to random time-domain excitation and response signals, due to the non-periodic nature of these

measurements. As such, the Hanning window filtered both measured signals to reduce leakage errors in EMA conducted in this research. Avitable [173] concurred that the Hanning window is commonly used in random excitation to prevent leakage. Schoukens et al [174] investigated the non-parametric data-driven modelling of linear systems. They used the Hanning window to estimate the frequency response and impulse response. The Hanning window is widely accepted and used for many types of signal measurements including non-continuous time-domain excitation.

External factors such as noise and vibration from the testing environment, usually distort measured data. In an attempt to mitigate these errors, all machines and air conditioners were not operated during the testing procedure. The bolted-joint coupling between the RREE Robot Mount and Test Frame introduced additional modal characteristics in the system. Nevertheless, research conducted by [83] determined that stiffness and damping at the Spindle–Holder interface mainly affects the first two modes of vibration. Since the chatter frequency does not occur at these modes, the RREE–Test Frame coupling did not influence the result of stability analysis. Furthermore, Erturk [83] determined that bearing stiffness affects the first two rigid-body modes of an MT. No occurrence of these rigid body modes was observed.

9.3.1.4 Stability Analysis of RREE

Stability Lobe Diagrams are used in milling operations to predict stable cutting parameters. Section 7.10 presented the predicted SLD for the MT RREE assembly. The SLD had many small lobes at low spindle speeds, more significant depth of cut occurred at higher rotational speeds. The lobes increased in size (height and width) as rotational speed was increased. The first lobe produced peak depth of cut of 0.46 mm; this occurred at a rotational speed of approximately 2700 RPM. The last lobe displayed a maximum depth of cut of 1.72 mm at a rotational speed of 16200 RPM. An abnormality was observed in the ninth lobe, as the lobe peaked out of the normal range. This could be attributed to the low damping ratio of the structure and its dynamic response. The maximum stable depth of cut at the required spindle speed of 12127.61 RPM was approximately 0.27 mm. In the range of 12700 – 13700 RPM and 14700 – 16700 RPM, more considerable stable depths of cut were attainable. From Figure 7-12, it was observed that at lower spindle speeds – lobe lines are dense as compared to higher speeds, where they are more spread out (horizontally). Furthermore, at lower spindle speeds, the maximum depth of cut is much less than at higher spindle speeds. The resultant SLD is indicative of the SLD's developed by other researchers, as presented in Section 7.8.

9.3.1.5 Stability Validation of RREE

The verification of the predicted SLD from Section 7.10 was presented in Section 7.11. Researchers utilised linear slot milling of samples at different speeds and depth of cut to verify the stability lobe diagram [158, 175, 176]. Visual inspection of machined surface quality and measurement of acceleration was used to determine chatter occurrence. Spindle speeds close to the required rotational speed of 12127.61 RPM were challenging to attain. However, test point seventeen yielded a stable cut – free of chatter, as presented by the smooth machined surface in Figure 7-16 (b). The stable cut was performed at a rotational speed of 12800 RPM, a feed rate of 0.73 mm/sec and a 0.22 mm depth of cut. In contrast, the worst cut occurred at the eighth test point, which resulted in the most substantial average acceleration. The sample was presented in Figure 7-16 (a); the spindle speed was measured at approximately 17000 RPM. The depth of cut was set below 0.5 mm and moderate feed rate was used. Nonetheless, the experimental validation resulted in the

linkage of SLD theory and experimental testing. The generated Stability Lobe Diagram has been validated based on experimental testing. The results confirmed that the SLD is an effective method of predicting stable and unstable cutting conditions.

9.3.1.6 Machine Tool Spindle Runout

Inaccuracies in the alignment of the shaft have a direct impact on the eccentricity of the machine tool. Therefore, MT spindle runout of the prototype was investigated in Section 8.2. The resolution of the DTI proved to be a limitation to the investigation. A DTI with a higher resolution was unavailable. Maximum runout of 0.01 mm was produced at five angular points; these were represented by the peaks in Figure 8-2. This correlates with the recommended runout of the ER11 collet that is used in the tool holder system [177]. Martin et al. [178] researched the effect of spindle runout on positional accuracy. The method used in this experiment is analogous to the method that was mentioned in Martins research. Insperger et al. [179] determined the effect of runout on the chatter frequencies of milling. They concluded that the stability region of the milling cutter does not change much due to runout. Therefore, the value of runout is permitted, considering the low manufacturing cost of the mill spindle. The Spindle Shaft and Housing were machined on a manual Lathe and low-cost angular contact ball bearings were used. Nevertheless, the runout was minimal for the purpose of this research and did not significantly affect the outcomes thereof.

9.3.1.7 Dynamics of Multistage End-Effector

Experimental modal analysis was conducted in Section 8.10.1 to determine the modal parameters of each assembly. Impulse Test produced FRF's of four different assembly states of the RREE. The critical frequency decreased, and the damping ratio increased, with decreasing mass. The critical excitation at higher frequencies corresponds to higher critical speeds. This is in accordance to the Rayleigh-Ritz method of critical speed for rotating shafts [180]. The fully assembled end-effector had the highest critical frequency; the corresponding critical speed was approximately 162 000 RPM. Critical speeds of the Spindle Shaft at each mode frequency were determined experimentally in Section 8.10.1. This validated the designed Spindle Shaft. The rotational speed of the spindle should not exceed these critical values as modal frequencies will occur. Large deformations and unstable structural characteristics occur at these natural frequencies. This speed is well above the operating range of the machine tool developed in this research. The results showed that the critical frequency and operating speed of the end-effector were highest when the gripper and reconfiguration subsystems were attached. The damping ratio of each subassembly indicated that the system is underdamped. The integration of all subsystems was observed to have a significant effect on the chatter onset frequency. Forced vibrations caused by an imbalance of the bearings was not observed in this study. This was validated by the submillimetre spindle runout of 0.01 mm.

9.3.1.8 Stability Analysis of Multistage End-Effector

A comparative study was conducted to determine the stability of the machine-tool spindle with and without the gripper and reconfiguration systems. Stability lobe diagrams were generated for each of the four assemblies; this was investigated in Section 8.10.2. Comparisons were drawn based on the following criteria: limiting depth of cut and horizontal distance between successive "troughs" and "crests". Higher limiting depths of cut are characteristic of high material removal rates; therefore, it is advantageous to attain a substantial value. The distance between successive lobe troughs or lobe crests is indicative of the

contained area of the lobe. Larger lobe areas correspond to more significant regions of stable cutting conditions. The limiting depth of cut for case d was the least of the four configurations. The most considerable depth of cut was attained by assembly case c, as was illustrated in Figure 8-17 (c). This is attributed to the stiffness of the tool assembly, as presented in Table 8-6. It is evident that the limiting depth of cut is approximately equivalent for cases a and b, that is, the fully assembled system and, gripper sub-system removed. The stable region of case a was more significant than that of case b, that is, the fully assembled system and, gripper subsystem removed. The results indicated that cutting stability is influenced by the reconfigurable dual-function design. Nevertheless, stable cutting was achieved. The machine tool system proved to exceed the theoretical rotational speed of 15000 RPM. The manufactured spindle yielded minimal runout when coupled with 2 mm end mill. The critical mode was determined, and parameters extracted. Stability of the machine tool was computed and verified using the modal parameters for the critical mode.

9.3.2 Gripper Subsystem

9.3.2.1 Workspace Computation

Gripper workspace was approximated in Section 4.3.13 by treating all three joints as revolute. The rubber joint was treated as revolute to simplify the analysis. Therefore, the computed workspace is not an ideal representation of the actual working region of the gripper. The rubber joint creates additional degrees of freedom as it permits rotation about the central axis of the distal phalanx. The numerical simulation did not account for this degree of rotation. Referring to the workspace requirements defined in Section 3.7, a minimum grasp volume of 0.001 cubic meters was specified. The workspace simulation approximates a range of 0.00071 – 0.00701 cubic metres. Therefore, the calculated working envelope of RREE gripper satisfied the minimum specified value.

9.3.2.2 Non-Linear Structural FEA

The purpose of this simulation was to determine the deformation characteristics of the rubber joint and its effect on the gripper. Rubber materials are flexible and prone to deformation under small loading conditions. The Mooney Rivlin material model was used to approximate the strain behaviour of rubber material. A rubber joint is an elastic object; as such, the applied force which produces deformation creates stored elastic potential energy in the rubber. The rubber springs back to its relative initial position when the applied force stops acting on it. Total distributed load of 4.488 N was applied to the contact surface of the distal phalanx. Fixed translational boundary constraint was applied to the middle phalanx, in the location of the revolute joint between the proximal and middle phalanges. The boundary condition applied ensured that there were no penetration sets between the solid bodies. The curvature-based solid mesh was checked for accuracy in Section 5.7.5. The resultant maximum displacement was 41.4 mm in the direction of the force vector. The result was expected as the maximum range of motion of the distal phalanx when the rest of the finger is fixed is 43 mm. Maximum Von-Mises stress of 3.26 MPa occurred at the joint located in the middle phalanx as indicated by the red region in Figure 5-28. Von-Mises failure criterion for UTS yielded a safety factor of 18.1 for the PLA middle phalanx. An immense strain occurred on the bottom side of the rubber joint, closer to the exterior surface of the geometry. Multiple checks were conducted to confirm the suitability of the simulation model, as presented in Section 5.7.5. The calculated theoretical

gripping force for 1 kg payload per finger was calculated in Section 4.3.6. This 4.488 N force did not induce critical stresses in the rubber to induce elastic limits.

9.3.2.3 Grasp and Hand Force

In Section 8.3, grasp testing of the RREE determined the maximum force output of each gripper finger. This force was applied by the end-tip of the distal phalanges of the gripper on a calibrated electronic balance. The end-effector servomotors were used at maximum torque output. Figure 8-4 illustrated the relationship between the approach angle and output load generated by the gripper finger. The results indicated that the force was a maximum at a 0° approach angle. As the approach angle increased, the finger force decreased. The force normalised at an approach angle of approximately 78°. The cable drive mechanism transmits rotational torque from the servomotor output shaft to the proximal phalanx of each finger. Large approach angles decrease the tension force produced by the servomotor in the cable. The gripper produces more significant grasp force for smaller approach angles. Objects that require less angular travel of the gripper finger have a more significant grasp force exerted on them. Consequently, lower grasp forces are available to objects with a smaller volume.

The grasping force of the gripper system was determined in Section 8.4. Due to the design of the gripper, a specially designed test apparatus was required to measure the grasp force of three fingers simultaneously. The average value of each extension was used to determine spring force for different grasp diameters. Hooke's law was used to determine spring force. Extension spring with spring constant 176.44 N/m was used in the force test apparatus. This spring force is equivalent to the force exerted by the gripper finger on the force measurement device. The simultaneous grasp force of each finger was determined. The addition of these three forces yields the grasp force of the gripper system at different grasp diameters. The minimum force of the gripper system was 19.23 N at a grasp diameter of 344 mm, and the maximum force of the gripper was 23.90 N at a grasp diameter of 384 mm.

Experimentation has shown that the RREE is capable of achieving grasp force in the range of 19 – 23 N for grasp diameters 144 – 384 mm, respectively. This measured force was inputted in Equation 4.16, which was previously used in Section 4.3.6. The resultant maximum payload is approximately 1.71 kg; this exceeded the target specification of the payload as defined in Section 3.7.

9.3.2.4 Accuracy and Repeatability of Gripper

The accuracy and repeatability of the gripper were determined by experimentation, as presented in Section 8.5. Based on the results of accuracy and repeatability presented in Appendix E.8 and Figure 8-8, the highest finger accuracy measurement was attained by gripper finger two at a 244 mm grasp diameter. While the most repeatable finger grasp was produced by the first gripper finger in a 384 mm diameter hold. It is difficult to draw conclusions based on these results; therefore, the average accuracy and repeatability for each grasp diameter were calculated. On average, the most accurate grasp occurred at a 344 mm grasp diameter, while the most repeatable grasp was produced at the 244 mm grasp diameter. The accuracy of the gripper decreased as grasp diameter is increased. However, there was no distinct trend between the grasp diameter and repeatability. The measurement of accuracy and repeatability at a grasp diameter of 344 mm disrupted trends in both accuracy and repeatability.

9.3.2.5 Slippage of Gripper

Slippage in robot grippers provides a realistic evaluation of the maximum static loading and failure therein; this was investigated in Section 8.6. Both test specimens required enclosed grasp mode for prehension. The first specimen was cubic with a smaller volume than the second test specimen. Observing Figure 8-9 (a), three points of contact restrain the object. Initially, the cube was held firmly at its top and bottom faces. As the load increased, the distance between the top surface of the cube and the gripper palm increased. The total load of the specimen was supported by the tips of each distal phalanx. The cubic geometry required three points of contact based on the architecture of the gripper. Grasp failure occurred when one of the fingers failed to maintain contact with the object. The second test specimen, which was presented in Figure 8-9 (b) failed due to the same reason as the first test specimen. However, the contact surface between the system of gripper fingers and the spool holder was higher than that of the cube. Based on the results presented by the experiment, the gripper system is better suited to grasp cylindrical objects of approximately twice the mass of cubic objects. Albeit, the cylindrical object has similar size and orientation to the spool holder.

9.3.2.6 Shape Adaptability of Gripper

The gripper mechanism was selected due to simplification of control and shape adaptability characteristics. Geometric adaptability of the gripper was investigated in Section 8.7; seven different shapes were used to test this characteristic. Objects which maintained surface contact with multiple finger linkages and the gripper palm produced firm grasps compared to objects that did not. Based on the results presented in Table 8-2 and Figures 8-11 to 8-15, the RREE gripper system is highly adaptable to multiple geometries. This was possible due to the gripper architecture and soft rubber joint present in each robot finger. This in conjunction with the underactuated design of the gripper, attributes to the ease-of-control as compared to fully actuated grippers.

9.3.2.7 Gripper Response – Rotating Machine Tool

The RREE is composed of three subsystems; each induces excitation to the structure of the end-effector. As such, the extent of excitation was studied to determine if the dual-purpose end-effector's feasibility is diminished by unwanted vibrations. The machine tool motor and spindle rotate in excess of 10 000 RPM; process vibration is inevitable at these speeds. For this reason, a vibration test was conducted to run the disengaged MT spindle through its operating speed range. Process vibrations were monitored through data acquisition system presented in Section 8.11.1.

In the event of a disengaged spindle, random acceleration increased with spindle speed, this was expected. The maximum average acceleration experienced by the fingers occurred at 11559 RPM. Spectral analysis was conducted to detect frequencies and amplitudes at various spindle speeds. The highest detected frequency occurred at 2556 RPM; the average value of this frequency was 530.77 Hz. This frequency is less than the critical frequency of the structure, which is 2694.4 Hz, as presented in Table 8-6 of Section 8.10.1. Therefore, unstable behaviour was not noticed. The largest detected amplitude was found at 14722 RPM, and phase occurred at a rotational speed of 4853 RPM. Noise and vibration levels were tolerable; the primary source of noise originated from the MT belt drive.

9.3.2.8 Gripper Response – Linear Milling

Vertical milling induces forced periodic vibrations between the cutting tool and workpiece. The dynamic effect of this machining process on the gripper is investigated in Section 8.11.2. The end milling process produced more significant accelerations at lower spindle speeds. The maximum average acceleration experienced by each of the fingers occurred at 9057 RPM. Spectral analysis was conducted to determine the corresponding frequencies and amplitude at each spindle speed. The highest detected frequency occurred at 12530 RPM; the average value of this frequency was 485.107 Hz. This frequency is less than the critical frequency of the structure, which is 2694.4 Hz, as presented in Table 8-6 of Section 8.10.1. Therefore, unstable behaviour was not noticed. The largest detected amplitude and phase also occurred at a rotational speed of 9057 RPM.

The vibration characteristics of the disengaged tool (investigated in Section 8.11.1) and engaged tool contrast. In the first case, when the tool is disengaged, the machine tool maintains a fixed-free boundary condition. This is best described as a vertical cantilever beam, fixed at the top and free at the bottom. In the second case, when the tool is engaged in the workpiece – the MT has a transient fixed-fixed boundary condition. This is due to the lateral support gained from the combined loading that occurs at the tool-tip. The milling forces prevent free oscillation of the machine tool.

9.3.2.9 Gripper Response – Reconfiguration

Machine reconfiguration is provided by the developed linear actuator mechanism. The actuator moves the gripper platform through the length of the lead screw, as presented in Section 4.4.7. The dynamic effect of this linear motion process on the gripper was investigated in Section 8.11.3. Based on the results presented in Figure 8-25, the gripper system experienced a maximum random process acceleration at a linear speed of 3.73 mm/sec. This is attributed to the excitation produced by the energised stepper motor; these vibrations propagate throughout the linear actuator subsystem. A frequency of 495.65 Hz was detected at the peak linear speed. This frequency is less than the critical frequency of the structure, which is 2694.4 Hz, as presented in Table 8-6 of Section 8.10.1. Therefore, unstable behaviour was not noticed. The rubber belt used in the drive system buffers part of the vibrations produced by the NEMA 17 stepper motor. The magnitude of such vibrations are minimal and do not pose a problem for the safe and reliable operation of the mechanism. Furthermore, the average vibration decreased as the linear speed increased. The gripper does not operate during reconfiguration; therefore, the induced vibrations do not impact the grasping process.

9.3.3 Reconfigurable Mechanism

9.3.3.1 Structural FEA of Platforms

Static structural FEA was undertaken to verify the design of the main platform and gripper platform. These Aluminium plates perform integral functions in the reconfiguration. Sections 5.8 and 5.9 investigated the stress and deformation response due to combined loading on the main and gripper plates, respectively. The limitations of the CTETRA10 mesh element was previously discussed in Section 9.3.1. Both components were over-designed for their function as UTS safety factors above 300 were achieved.

9.3.3.2 Cycle Time, Accuracy and Repeatability

The reconfiguration system utilises a linear mechanism to reconfigure the device between grasping and machining modes; the effectiveness of this mechanism was tested in Section 8.8. A cycle time under 2 seconds was achieved by the RREE. The specification for reconfiguration time was defined in Section 3.7 as 60 seconds. The RREE attained a reconfiguration time of a fraction of this specification. The efficiency of the reconfiguration mechanism is testament to the linear actuator design. The mechanism provided fast, effective positioning of the gripper system. In an effort to determine the positional accuracy and repeatability of the actuator, experimental testing for accuracy and repeatability were investigated in Section 8.9. Based on the results presented in Table 8-5, the best actuator accuracy measurement was attained at a linear speed of 14.72 mm/sec. While the most repeatable actuator measurement was produced at a linear speed of 32.12 mm/sec.

9.4 Benchmark of RREE

9.4.1 Definition of Benchmark Metrics

The National Institute of Standards and Technology have defined finger strength and grasp strength as two performance metrics for robotic grippers [181]. These metrics are briefly defined in terms of benchmarking criteria. The performance metrics and general metrics are described in Tables 9-1 and 9-2, respectively.

Table 9-1: Performance Metrics

End Effector	Metric Type	Description	Metric Variable	Metric Unit
Gripping System	Finger strength	A kinetic measure of the maximum force a robotic finger can exert on an object [181]	Force	N
	Grasp strength	A kinetic measure of the maximum force a robotic hand can impose on an object [181]	Force	N
	Payload (Max) Encompassing Grasp	Maximum mass that can be attached or supported by the robotic hand [181]	Mass	g
	Grasp Range (Min-Max)	Minimum and maximum object volume that can be grasped	Volume	mm^3
	Repeatability	Positional deviation from the average of displacement	Length	mm
Milling System	Spindle Speed (Range)	Minimum and maximum governed rotational speed of the spindle	Rotational Speed	RPM
	Spindle Torque (Maximum Speed)	The torque generated by the machine tool at the maximum governed rotational speed	Torque	Nm
	Spindle Runout	Runout is a rotation inaccuracy which occurs when the tool is no longer aligned with the central axis	Length	mm

Table 9-2: General Metrics

Metric Type	Description	Metric Variable	Metric Unit
Product Size	Dimensional volume of the product	Volume	mm^3
Product Mass	Dimensional mass of the product	Mass	g
Cycle time	Minimum time required to change between functions	Time	s
Product Cost	Cost in currency of the product	Money	ZAR

9.4.2 Benchmark of Metrics

Table 9-3 presents the benchmark of metrics. Comparable end-effectors were reviewed in Section 2.9.

Table 9-3: Benchmark of Metrics

Metric Type	Metric Variable	Metric Unit	Prototype	Competitor					
				Dremel	Kress	iSA	Yale	RobotiQ	DHR
Finger Strength (Max)	Force	N	7				4.11	20	22
Grasp Strength (Max)	Force	N	21				13.33	60	65
Payload (Max) Encompassing Grasp	Mass	g	2235				2000	10000	2000
Grasp Range (Min – Max)	Volume	mm^3	$0.71x10^6$ – $7.01x10^6$				$0.56x10^6$ – $0.81x10^6$	$1.43x10^6$ – $7.70x10^6$	$3.66x10^6$ – $4.68x10^6$
Repeatability	Length	mm	2.88				1	0.05	0.05
Spindle Speed (Range)	Rotational Speed	RPM	2000 – 15000	10000 – 33000	5000 – 25000	5000 – 30000			
Spindle Torque	Torque	Nm	0.6	0.5	0.35	0.28			
Spindle Runout	Length	mm	0.01	0.01	0.01	0.01			
Product Size	Volume	mm^3	$2.36 x10^6$	$0.43 x10^6$	$1.26x10^6$	$1.77x10^6$	$3.18x10^6$	$15.40x10^7$	$9.82x10^6$
Product Mass	Mass	g	4946	550	1700	2800	752	2300	1680
Cycle Time	Time	s	1.35						
Product Cost	Money	ZAR	18302,76	1299	4050	8000	7500	265828	150000

The maximum strength of the RREE gripper was significantly less than that of dedicated industrial grippers that. However, the prototype gripper outperformed dedicated reconfigurable grippers in the research and development state such as the Yale Model O. The payload rating of the RREE gripper exceeded both industrial and prototype grippers of similar size. The specified payload of the gripper is 9.91 N; however, the maximum achieved payload was 21.92 N. Therefore, the target specification was met in abundance. The RREE has a broader grasp range than the Yale Model O gripper but is able to grasp larger objects than the DHR gripper. The repeatability of the prototype gripper is significantly less than the other grippers. This is mainly attributed to the rubber joint used in the underactuated gripper. The specified repeatability was minimised. The gripper system met all target specifications presented in Section 3.7. However, based on the performance benchmark, industry-leading grippers such as the RobotiQ 3-Finger Adaptive outperform the developed gripper. It is noted that these competing grippers are dedicated gripping end-effectors; they cannot perform any other function.

The RREE MT spindle was unable to meet rotational speeds as high as dedicated machine tools such as Kress 1050-FME1. However, the developed MT met the target specification of 15000 RPM. The torque developed by the MT spindle motor exceeded that of the competition. Spindle runout is on-par with dedicated machine tool spindles. It is noted that the competing MT's are dedicated machining devices; attachment mechanisms must be developed to use them as end-effectors.

The RREE has a smaller footprint than the grippers but a larger footprint than the machine tools. The mass of the RREE is notably higher than the others. None of the competitors is able to change between manufacturing processes, therefore do not possess a cycle time. The cost of the RREE is significantly less than RobotiQ and DHR grippers but is higher than the Yale gripper and machine tools. The RREE offers

additional functionality compared to these competitors. Trade-offs such as repeatability, grasp strength and rotational speed are necessary to attain such a system.

9.5 Implications of Developed Reconfigurable Robotic End-Effector

The results of calculation, computation and experimentation presented in this research agree with previous studies. Section 9.3 of this chapter discussed the result of computation and experimentation with reference to similar results attained by other researchers. In stating this, some of the results obtained from this research have added to existing research.

The Mechanistic Cutting Force model developed by Altintas [165] was used to predict the components of milling forces produced in the machining process. The maximum combined loading of these force components was used to validate the spindle shaft. Static structural FEA was used to compute the displacement and Von-Mises stress produced by these predicted cutting forces. This resulted in the successful design of the RREE MT, which did not fail under experimental testing. The combination of these two methods to validate the spindle shaft design of machine tools was not previously noted in the review of the literature. The method is applicable to machine tool designers, and it is an efficient and effective method to verify spindle shaft design.

The calculation of Critical Speed of rotating shafts is a fundamental principle of solid mechanics [182]. In this research, natural frequencies of the developed MT spindle were computed by FEA Modal Analysis and determined experimentally by EMA. These natural frequencies were used to calculate the critical speeds of the designed MT spindle. This resulted in the prediction of the maximum rotational speed of the MT. The combination of these three methods to predict the maximum speed of machine tools was not previously noted in the review of the literature. The method is applicable to machine tool designers, and it is an efficient and effective method to predict stable operational speeds of rotating shafts.

The structural dynamics of the developed RREE was determined by EMA [151]. The method used in this research employed Impulse Hammer Testing at the tooltip of the MT. The research utilised an efficient, reliable method of computing the FRF from the measured input and output signals. The frequency-domain Frequency Response feature in National Instruments Signal Express software was used to generate these functions. Modal parameter extraction techniques were used to determine the natural frequencies, stiffness and damping of the structure. This software process was not previously noted in the review of the literature. The method is applicable to robot designers, and it is an efficient and reliable method to determine the modal characteristics of end-effectors.

Chatter prediction is conducted by utilisation of the Stability Lobe Diagram. Stability model developed by Altintas and Budak [156] was used to solve the stability equations, and the plotting method proposed by Yue [157] was used to graph the lobe-lines. In this research, the solution of the SLD was achieved using readily available consumer software. Typically, specialised software such as CutPro is used to generate these diagrams. This method of graphing the stability lobe diagram for chatter prediction in milling, using end-effectors was not previously noted in the review of the literature. The method is applicable to machinists, researchers and engineering students; it is a low-cost method to produce SLDs.

Validation of the predicted Stability Diagram was achieved by experimental milling of workpiece samples. The surface quality of the machined surface and average acceleration induced were used to validate the predicted stability diagram. This verification method for SLDs in milling, using an end-effector was not previously noted in the review of the literature. The method is applicable to robot designers and machine designers, it is a low-cost and effective method to verify SLDs.

The working volume of the gripper was approximated using the kinematic model of the underactuated gripper finger. MATLAB was used to compute the two-dimensional workspace of the gripper finger. The volumetric range of the gripper was calculated by combining the resultant finger workspace and gripper assembly in SolidWorks modelling environment. The combination of these two methods to validate the working volume of the gripping EEs was not previously noted in the review of the literature. The method is applicable to robot designers and students, and it provides an efficient and approximate solution of the three-dimensional workspace of three-finger robotic grippers.

Non-linear FEA was used to investigate the deformation characteristics of the rubber joint on the gripper finger. The effect of the soft-joint element on gripper compliance was a result of this analysis. This method of investigating the effect of soft-joints on deformation in underactuated grippers was not previously noted in the review of the literature. The method is applicable to robot designers, and it is an efficient and effective method to model the behaviour of soft-joints in robot grippers.

This research has produced four novel findings, all of which have not been previously studied. As such, these findings are original and have implications for the development of similar systems. The novel architecture and mechanical design of RREE presented in this research add value to the research and development of dual-function end-effectors. This study proved that such systems are an effective alternative to dedicated machining and gripping EEs. Performance and interactions between the machining and gripping subsystems of the end-effector were investigated. This resulted in a new approach to understanding the effect of reconfiguration in end-effectors. The method utilised EMA to determine the FRF's of four stages of assembly, components of subsystems were removed at each stage. Additionally, the modal parameters of the determined FRF's were used to predict the SLD of each assembly stage. This determined the effect of reconfigurability on milling stability and chatter prediction. Finally, the dynamic effect of reconfigurable subsystems on the mechanical structure of the gripper was investigated. This finding was used to validate the structural integrity of the gripper design.

The result of conceptualisation and design of RREEs pose a challenge to current approaches. Based on the survey of literature [48, 49, 65-70], reconfigurable robotic end-effectors are typically task-specific. They provide reconfigurability for a single process as is the case of the RobotiQ gripper. There are little to no attempts to use reconfigurability as a mechanism to change between manufacturing processes. One such attempt was presented by Rahman et al. [57], the robot was designed for gripping and cutting crops. The research proposed a design with no indication of its performance or evidence of prototyping.

The accuracy and repeatability of soft robotic grippers are debatable. Based on the results of experimental testing in Section 8.5, the hyperelasticity of rubber elements poses a severe challenge for positional accuracy and repeatability. The rubber joint used in the gripper system of the RREE adds compliance and

adaptability to the gripper. However, the gripper performed poorly in positional testing for accuracy and repeatability.

In summary, this research has produced four practical implications which are applicable to similar studies.

1. Design methodology for reconfigurable robotic end-effectors;
2. The low-cost technique which utilises Microsoft Excel to plot Stability Lobe Diagrams;
3. Multistage Experimental Modal Testing of end-effector provide insight into the effect of subsystems on structural dynamics;
4. The utilisation of 3D printing in the prototyping and development of robotic grippers.

9.6 Limitations and Improvements

The aim of this research was met through the fulfilment of the objectives presented in Section 1.4. However, as is present in all research, limitations to research objectives were noticed. These limitations did not adversely affect the aim of the study, as all research objectives have been satisfied.

Access to some research journals and literature databases may have limited some aspects of the research. The review of the literature presented in Chapter 2 and Sections 7.2 – 7.8 presented the findings of many recent studies. The mechanical design of the RREE was not significantly impacted by this limitation.

The error between the simulated and experimental modal characteristics of the RREE could not be calculated due to the nature of the testing conducted. While the modal analysis presented in Section 5.5 determined the mode shapes and natural frequencies, the EMA presented in Sections 7.9 and 8.10.1 did not determine the mode shapes of the structure. The EMA produced the natural frequencies and damping characteristics of the structure. Both natural frequencies and mode shapes are required to estimate the error between the results. Furthermore, modal correlation between the test and FEA data was no performed in this study. This would have permitted comparison and evaluation of the correlation between the EMA and FEA. As mentioned previously, the MAC provides a measure of consistency between one modal and another reference modal vector. The omission of such criterion prevented any meaningful comparison between the test and FEA data [162].

The result of stress analysis can be improved by further optimisation to determine the optimal values to which the subsystem of the RREE model could be designed and manufactured. The weaknesses of the structural design could be improved by employing design iterations with the aid of FEA. The weak areas are readily identifiable in FEA as they incur the highest stress concentrations. A few instances of design refinement would result in a stronger, more efficient design.

Additionally, the gripper subsystem was modelled as homogenous solid structures. The practical implication of infill density and layer composition was not considered in the stress analysis. Enhanced contact sets for the modelling of bearing stiffness and damping characteristics would bridge the gap between the experimental and simulated modal response. Bearing race deflection is an elastic deformation between the balls and the bearing raceways due to external loads. Utilisation of the Hertz contact model provided an estimation of the stiffness and damping characteristics of the bearings but did not account for the nonlinear perturbations induced in the raceways.

The construction of the RREE prototype has a direct influence on structural dynamics. The Spindle Shaft and Spindle Housing were machined on manual CNC Lathe. Due to the minimal size of these components, difficulties in machining arose. It was not possible to include small features such as fillets and abutments on the Spindle Shaft. Based on this, the modal parameters of the RREE and Machine Tool may change. Nonetheless, the outcome of this research was not significantly affected by this limitation.

The Machine Tool of the RREE utilised the belt-pulley system to transmit power from the spindle drive motor to the spindle shaft. Based on the experiments presented in Sections 7.11 and 8.11, the belt produced significant vibrations at rotational speeds above 15000 RPM. This has a direct influence on the dynamic characteristics of the end-effector structure. Nevertheless, the outcome of this research was not adversely affected by this limitation.

Lastly, it was not possible to test the performance of the RREE with parallel kinematic manipulators. The Fanuc-M10IA serial robot did not support milling processes due to its lack of stiffness. Therefore, the Test Frame was designed and constructed for this purpose. Additionally, the linear actuator of a Gantry CNC robot was used to fixture the workpiece. The feed required for slot milling in Section 7.11 was produced by this linear actuator. A PKM would have extended the range of end milling operations for testing and validation. Nonetheless, the outcome of this research was not significantly affected by this limitation as the RREE demonstrated end milling of Aluminium 6061, HDPE plastic and pine wood.

Improvements to the research and development of reconfigurable robotic end-effector for machining and part handling are presented.

The motors selected for the gripper and machine tool performed well in testing in accordance with the design and experimentation. Although motors with higher torque output would be necessary for grasping heavier objects and machining ferrous metals, higher torque loads may also increase holding forces and loading control.

Cutting force coefficients should be determined experimentally. Due to the lack of dynamometer equipment, these variables were referenced from similar studies [32], [25], [33] and [34]. These variables have a direct impact on the predicted Stability Lobe Diagrams.

The coupling of the end-effector to the Test Frame during dynamic testing is not ideal. The mounting of the end-effector has a direct influence on the measured tool-tip FRF's as determined by Experimental Modal Testing. Accurate results require high rigidity fixed mount to attain a fixed boundary condition requirement as described by Srinivas et al. [25].

Alternative materials should be considered for the Main Platform and Gripper Platform of the RM. Plastics such as HDPE and Delrin have good structural rigidity and strength properties. The use of plastic material decreases the mass of the Platforms while offering the required strength to support the combined loading.

A cooling system must be developed and integrated with the RREE. The servomotors used in the gripper system of the RREE increased in temperature when used continually. This was observed in Section 8.3 as the gripper was tested at maximum motor torque output. This will increase the effectiveness of the gripper for lengthy grasps.

Automatic tooling will increase the productivity of the RREE MT. The current ER11 tool holder does not facilitate automatic tool changing.

9.7 Chapter Summary

This chapter discussed the significance and implications of the findings concerning the research and development of the reconfigurable robotic end-effector. A summative review of the state of the art in robotic end-effectors and design methods for reconfigurability were presented. The performance of the RREE was summarised based on the output of its subsystems. The performance of the developed RREE prototype was benchmarked against six competitors. The implications of this research were discussed in relation to the performance of the RREE. The limitations of the RREE were noted, and improvements to the end-effector were discussed based on shortcomings of the research.

The remaining Chapter concludes the study. An evaluation of the extent to which the objectives meet the aim is followed by research contributions. A statement of future development is followed by a conclusion summary.

Chapter 10 Conclusion

10.1 Introduction

This chapter concludes the findings of the research outcomes in line with the aims and objectives of the research problem. The research contributions are discussed, which is followed by recommendations for future work.

10.2 Evaluation of Research Aim and Objectives

The aim of this research was to develop a reconfigurable robotic end-effector that is capable of both machining and part handling applications. This, in conjunction with evolving market demands, require manufacturers to adapt their manufacturing systems for low-volume, high-variety processes. Such processes require multiple tools to manufacture products. Two fundamental functions are gripping and milling.

The aim of this research was satisfied in full. This was accomplished by evaluating the research objectives defined in Section 1.4. A summary of each objective, the extent to which it has been met, and the section in the dissertation where it has been fulfilled is provided.

Part of the first objective was to research and establish the state of the art in robotic end-effectors. A review of technological advancements in the field of grasping and machining robotic end-effectors was presented in Chapter 2 of this dissertation. Common gripping end-effectors, industrial grippers and soft robotic grippers were reviewed. An in-depth study of robotic grippers revealed the advantages of soft robotics in grasping. Sixteen references to robotic machining are contained in this dissertation, four of which are contained in Section 2.6, while the remaining twelve are found in Section 1.3. Based on these works, the first research objective was established.

Another part of the first objective was to research and establish the state of the art in design methods for reconfigurability. Sections 2.7 and 2.8 investigated design methods for reconfigurability and reconfigurable robotic grippers, while four requirements for reconfigurability in machine design were discussed in Section 3.3.1. In summary, design methods for reconfigurable systems are prevalent in literature. However, design methods for reconfigurability on machine-level are not as conventional. Design methods of eight reconfigurable robotic grippers provided insights into the implications of such systems. The second object was met.

The second objective of this study was to research and develop the complete mechanical design blueprints for the complete fabrication of the reconfigurable robotic end-effector. The mechanical design of the RREE was presented in Chapters 3 and 4, while Appendix K contains the engineering drawings for replication. Chapter 6 involved the manufacturing and integration of subsystems. Chapter 3 defined specifications and conceptualised the reconfigurable architecture of the mechanical system. The gripping and machining subsystems produced the RREE concept, which was presented in Figure 3-8. Chapter 4 detailed the design methodologies, engineering system design and mechanical assemblies of the machine tool, gripper and reconfiguration subsystems. Therefore, full mechanical design blueprints for the fabrication of the RREE were presented in this research and the second objective was satisfied.

The third objective was to research and predict the performance of the end-effector using tools such as FEA and modal analysis. Numerical simulation was conducted in MATLAB to determine the workspace of the developed gripper system; this was done in Section 4.3.13 and Appendix D.6. Mechanistic force model was used to predict the tool-tip cutting forces produced by the vertical milling of wrought aluminium. Section 5.2 and Appendix D.5 presented the model and results of the simulation. FEA structural analysis was conducted in Sections 5.3, 5.7, 5.8 and 5.9 to predict the performance of designed components under loading conditions. Modal analyses in Sections 5.4 and 5.5 respectively, were used to determine the mode shapes and natural frequencies of the designed spindle shaft and MT assembly. This computational method determined the maximum deformation and Von-Mises stress induced at each mode for these two structures. The critical speed of rotating shafts was calculated in Section 5.6; this was used to predict the maximum safe speed range of the spindle. Mill stability models were researched in Section 7.8 to predict stable milling parameters. The third objective was accomplished.

Modelling the characteristics of a physical system has limitations. To understand these limitations, the fourth objective was to research, construct, assemble and test the performance of the end-effector in real-world machining applications. A full-scale prototype of the RREE was developed for this purpose. Chapter 6 covers the manufacturing, assembly, electronic control and systems integration of the RREE prototype, which was coupled with the Fanuc M10IA serial manipulator. The performance of the end-effector was rigorously tested in Sections 7.9 – 7.11 and Chapter 8. Spindle runout, grasp force, accuracy, repeatability, adaptability, cycle time, experimental modal analysis, stability prediction and validation, and vibration response testing were conducted. The RREE demonstrated competence in slot milling aluminium 6061, pinewood and HDPE plastics. As a result of this, the fourth research objective was achieved. This research revealed that obtaining optimal and feasible characteristics in terms of cost and manufacturability, size and weight, actuation mechanisms, robustness against machining forces, and susceptibility to mechanical vibrations are possible in a robotic machining end-effector. Developing a stability model for a reconfigurable machine tool can be readily performed using the EMA method.

Lastly, the performance of the developed RREE was compared to existing cutting technologies to determine its effectiveness. The fifth objective was to benchmark the performance of the end-effector against existing cutting technologies through data analysis and interpretation. Section 9.6 presented a benchmark of essential performance and overall design metrics of the system. The performance of six competing products was compared to the developed RREE. The development of the RREE and proof of operability realise the potential of reconfigurable end-effectors for machining and part-handling. Throughout the testing and evaluation of the machine, the performance of the prototype was impressive. Further improvement and refinement of the design could result in a “market ready” product. The device performed both machining and grasping operations as it was designed to.

10.3 Research Contribution

This research proved that reconfigurable robotic end-effectors provide an alternative to dedicated manufacturing systems. Additionally, the study motivated that reconfiguration mechanisms form a pivotal role in the functionality of reconfigurable machines. The research challenges defined in Section 1.5 have been overcome. The developed end-effector demonstrated that obtaining feasible and optimal

characteristics in terms of the size and weight, cost and manufacturability, actuation mechanisms, robustness against machining forces, and susceptibility to mechanical vibrations are possible.

A prototype was designed, constructed, and tested to validate the feasibility and practicality of such an end-effector. The end-effector is a combination of machining, gripping and reconfiguration subsystems.

The literature has focused on machining stability and part-handling as two separate fields of study. In this research, the extent of each subsystem's influence on the other was established.

The effect of the machine-tool on gripper system was investigated. End-milling operation of aluminium 6061 was conducted at various speeds to determine the average vibration response of the gripper. The average vibration of the gripper decreased after 9057 RPM with increasing spindle speed. The results showed that noise and vibrations caused by the metal cutting operation have no significant effect on the gripper subsystem.

A comparative study was conducted to determine the stability of the machine-tool spindle with and without the gripper and reconfiguration sub-systems. The results showed that the critical frequency and operating speed of the end-effector were highest when the gripper and reconfiguration subsystems are attached. The damping ratio of each subassembly stage indicated that the system is underdamped. The integration of all subsystems was observed to have a significant effect on the chatter onset frequency.

Stability lobe diagrams were generated for each assembly. The stability lobe diagrams provided useful information regarding the selection of chatter-free cutting conditions. The findings showed that the end-effector produced more significant stable regions with the gripper subsystem attached. Therefore, the stability of the end-effector is increased with the gripper subsystem.

The verification of the predicted Stability Diagram was achieved by experimental milling of workpiece samples. The findings demonstrated that the end-effector produced good surface quality milling and decreased vibrations when points under the lobe-lines were selected. Furthermore, the findings showed poor surface quality and increased vibrations when points above the lobe-line were selected. Therefore, the predicted Stability Lobe Diagram was proven to be accurate in the prediction of chattering in vertical milling operations.

3D printed underactuated robotic grippers are a low-cost, less accurate alternative to industrial grippers. Underactuated grippers are simple to design, manufacture and control. The results showed that objects which required minimum angular travel of the gripper finger have an increased grasp force.

The results of benchmarking proved that none of the competitors is able to change between manufacturing processes, and therefore, do not possess a cycle time. The cost of the RREE is significantly less than industrial three-finger grippers. Trade-offs such as repeatability, grasp strength and rotational speed are acceptable for this study as the RREE prototype is able to perform both machining and part handling.

Reconfigurable end-effectors have the potential to change the small to medium scale manufacturing industry. The development of reconfigurable end-effectors for multiple functions is beneficial to the manufacturing industry. These machines have the ability to reduce setup costs, robot downtime and increase productivity.

The presented findings suggest that the robot is able to operate successfully. To date, the literature has focused on machining stability and part-handling as two separate entities; however, this study offers an amalgamation of both areas of manufacturing.

It would be beneficial to pursue further research on RREE's in order to make automation accessible to developing manufacturers.

10.4 Future Work

Future studies should investigate the implications of dual-purpose robotic end-effectors on manipulator stability. Machining processes generate cutting forces; this is true for milling, drilling, turning and grinding. In future studies, any combination of machining function for dual-purpose end-effector should consider the dynamic limitations of the manipulator with which the end-effector is compatible.

Further investigation on the limitations of additional reconfigurable mechanisms should be conducted. This research has successfully implemented one such reconfiguration mechanism; the exploration of multiple methods will enhance the ability of robotic end-effectors. Multiple function end-effectors could be a result of this, an end-effector which can perform milling, grinding and gripping would have many implications to current manufacturing technologies.

Further research should investigate a unified methodological approach to the design of reconfigurable robotic end-effectors. The design methodology presented in this research, while useful, divided the end-effector design into multiple subsystems. This is evident in the systematic approach to the mechanical and electronic design of the end-effector. The reconfigurable design methodology utilised in this research required the identification of system structure and the relationships among them. This resulted in the subsystem approach to design.

Further research is needed to better understand the implications of flexible joints in underactuated robotic grippers. Investigation on the consistency of deformation characteristics of rubber joints is required. The findings presented in this research concur that rubber joints improve the flexibility and adaptability of underactuated grippers. However, the results also showed that the utilisation of flexible joints decreases the positional accuracy and repeatability of underactuated grippers.

To better understand the implications of the reconfigurable robotic end-effector for milling and gripping, further studies should be conducted to determine the performance of the RREE when attached to parallel robots. In this research, the Fanuc M10IA SKM was used to test the grasping performance of the RREE. The SKM did not possess the required stiffness for machining applications. Nevertheless, the RREE MT demonstrated vertical milling of aluminium, wood and plastic when attached to a fixed Frame. PKMs are known to be stiffer and more robust than SKMs.

Future research should be performed in the integration of acceleration and sound sensors with real-time vibration and sound analysing software. The aim of this signal monitoring system would be to detect the onset of chatter parameters based on the computed stability model. The system should adjust speeds and depths of cut to stable regions.

10.5 Chapter Summary

The aims and objectives stated in Section 1.4 were fulfilled by the research outcomes discussed throughout the dissertation. The research contributions were noted, and the advantages of their applications were summarised. Looking ahead, recommendations for further research in end-effector development derived from Section 9.6 was presented.

It can be concluded that the reconfigurable robotic end-effector concept provides a promising platform for robotic machining and part handling systems.

The device can be implemented with improvements in efficiency, flexibility, rigidity, and automation in comparison to dedicated end-effectors.

Thus, the aim and objectives were met, from which the research question presented in Section 1.3 can be answered as yes: a reconfigurable robotic end-effector can facilitate both part handling and machining operations.

Chapter 11 References

1. Padayachee, J., *Development of a Modular Reconfigurable Machine for Reconfigurable Manufacturing Systems*, in *School of Mechanical Engineering*. 2010, University of KwaZulu-Natal: Durban.
2. J., R.T.C.H.H.T.R.V.F.M.R.B., *An Investigation into the Use of Industrial Robots for Machining Soft and Low Density Materials with HSM Technique.* Journal of the Brazilian Society of Mechanical Sciences and Engineering, 2011. **33**(3): p. 343-350.
3. Chryssolouris, J.P.C.D.P.S.G. *Machining with Robots: A critical review*. in *Digital Enterprise Technology*. 2011. Athens, Greece.
4. Robotics, I.F.o., *IFR forecast: 1.7 million new robots to transform the world´s factories by 2020*. 2017, ifr.org: Frankfurt.
5. Hanson, K., *Plug and Play Profitability*, KUKA-robot-gripper, Editor. 2016, shopmetaltech.com: shopmetaltech.com.
6. Reddy, C.E., J. Padayachee, and G. Bright. *A RECONFIGURABLE ROBOTIC END EFFECTOR FOR MACHINING AND PART HANDLING–MACHINE TOOL SIMULATION*. in *29th Annual Conference of SAIIE*. 2018.
7. U. Schneider, J.R.D.P., M. Drust, A. Verl. *Position Control of an Industrial Robot Using an Optical Measurement System for Machining Purposes*. in *11th International Conference on Manufacturing Research (ICMR2013)*. 2013. Cranfield University, UK.
8. U. Schneider, J.R.D.P., M. Drust, A. Verl. *Combining holistic programming with kinematic parameter optimisation for robot machining*. in *45th International Symposium on Robotics (ISR 2014)*. 2014. Munich, German.
9. F. Domroes, M.R., B. Kuhlenktter. *Towards Autonomous Robot Machining*. in *45th International Symposium on Robotics (ISR 2014)*. 2014. Munich, Germany.
10. Alexandr Klimchik, D.B., Anatol Pashkevich, Sebastien Briot and Benôit Furet. *Compensation of Tool Deflection in Robotic-based Milling*. in *9th International Conference on Informatics in Control, Automation and Robotics (ICINCO-2012)*. 2012. Rome, Italy: SCITEPRESS.
11. Radu-Eugen Breaz, O.B., Anca Lucia Chicea and Sever Gabriel Racz, *Using Serial Industrial Robots In CNC Milling Processes*. 2015, University of Sibiu, Engineering Faculty: ResearchGate.
12. Lin, Y., H. Zhao, and H. Ding, *Posture optimization methodology of 6R industrial robots for machining using performance evaluation indexes.* Robotics and Computer-Integrated Manufacturing, 2017. **48**: p. 59-72.
13. Uhlmann, E., S. Reinkober, and T. Hollerbach, *Energy efficient usage of industrial robots for machining processes.* Procedia CIRP, 2016. **48**: p. 206-211.
14. Makinde, O., et al., *A bio-inspired approach for the design of a multifunctional robotic end-effector customized for automated maintenance of a reconfigurable vibrating screen.* Robotics and biomimetics, 2017. **4**(1): p. 4.
15. Pini, F. and F. Leali, *Human-robot collaborative reconfigurable platform for surface finishing processes.* Procedia Manufacturing, 2019. **38**: p. 76-83.
16. Canali, C., et al., *Theoretical and kinematic solution of high reconfigurable grasping for industrial manufacturing.* Procedia manufacturing, 2017. **11**: p. 265-274.
17. Avram, O. and A. Valente, *Trajectory Planning for Reconfigurable Industrial Robots Designed to Operate in a High Precision Manufacturing Industry.* Procedia CIRP, 2016. **57**: p. 461-466.
18. Liu, Y., et al. *Dimension Synthesis of a Spatial Parallel Kinematic Manipulator Based on S-shaped Test Specimen*. in *MATEC Web of Conferences*. 2017. EDP Sciences.

19. Patel, Y. and P. George, *Parallel manipulators applications—a survey.* Modern Mechanical Engineering, 2012. **2**(03): p. 57.
20. sciencebuddies.org, *The Engineering Design Process*, T.E.D. Process, Editor. 2019, sciencebuddies.org: sciencebuddies.org.
21. Vashisth, P.S.A.K.M., *Design of a Robotic Arm with Gripper & End Effector for Spot Welding.* Universal Journal of Mechanical Engineering, 2013. **1**(3): p. 92-97.
22. Groover, M.P., *Automation, Production Systems, and Computer-integrated Manufacturing*. 2 ed. 2002, Upper Saddle River, NJ: Prentice Hall.
23. Malik, A.K.A.G.M.A., *Robotic Grasping and Fine Manipulation Using Soft Fingertip*, in *Advances in Mechatronics*, P.H. Martinez-Alfaro, Editor. 2011, InTech. p. 300.
24. Owen-Hill, A., *How Many Fingers Do You Really Need for a Robot?*, in *How Many Fingers Do You Really Need for a Robot?* 2015, Robotiq: blog.robotiq.com.
25. Monkman, G.J., *Robot Grippers for Use With Fibrous Materials.* The International Journal of Robotics Research, 1995. **14**(2): p. 144-151.
26. Intech, *Taxonomy of robot grippers*, image3_w.jpg, Editor., Intech.
27. Alonso, M., A. Izaguirre, and M. Graña. *Current research trends in robot grasping and bin picking*. in *The 13th International Conference on Soft Computing Models in Industrial and Environmental Applications*. 2018. Springer.
28. bastiansolutions, *end-of-arm-tooling*, img_6720-(2).jpg, Editor. 2017.
29. P.D.Kulkarni, N.A.L.Y.P.B., *Study of End Effectors – A Review.* International Journal of Trend in Research and Development, 2015. **2**(5): p. 365-368.
30. Mohammed, K., *Design of a gripper tool for robotic picking and placing*. 2010, Uppsala University: Uppsala, Sweden.
31. Sentnilraja, V., *A Course Material on Robotics*. 2015, Sasurie College of Engineering Vijayamangalam, India. p. 133.
32. Monkman, R.S.W.T.L.G. *Study on the Holding Characterestics of a Magnetic Gripper*. in *COMSOL* 2011. Boston, United States of America: IEEE.
33. Schunk, *Schunk Electromagnetic gripper*, 12463-8136681.jpg, Editor. 2010.
34. Escriva, A.A.I., *Design of a Smart Gripper for Industrial Applications*, in *Department of Mechanical Engineering and Industrial Systems*. 2016, Tampere University of technology: Tampere, Finland. p. 74.
35. onrobot.com *VG10 - FLEXIBLE, ADJUSTABLE ELECTRICAL VACUUM GRIPPER*. 2019.
36. schunk.com *Product Information Magnetic gripper EGM B-L*. 2019.
37. schunk.com *Product Information Gripper for small components MPG 16*. 2019.
38. onrobot.com *Gecko Gripper User Manual*. 2019.
39. Shintake, J., et al., *Soft robotic grippers.* Advanced Materials, 2018. **30**(29): p. 1707035.
40. Huat, L.J., *Customizable soft pneumatic gripper devices*, in *Department of Mechanical Engineering* 2015, National University of Singapore: Singapore.
41. Majidi, C., *Soft Robotics: A Perspective—Current Trends and Prospects for the Future.* Soft Robotics, 2013. **1**(1).
42. Wang, L., *Shape adaptation through soft-matter extended phenotype enhances robots' functionality*. 2014, ETH Zurich.
43. Wang, L., *Shape Adaption through Soft-Matter Extended Phenotype Enhances Robots' Functionality*, in *Bio-Inspired Robotics Lab*. 2014, ETH Zurich: Zurich.

44. Dillenbourg, A.S.A.B.A.J.I.P., *Roombots–modular robots for adaptive furniture*, Roombots-modular_robots_for_adaptive_furniture.pdf, Editor. 2010, ResearchGate.
45. Festo, *Festo Bionic Handling Assistant* 0128-bha-2140x940px.jpg, Editor. 2012, Festo.
46. Lefeber, F.D.D., *Pneumatic Artificial Muscles: actuators for robotics and automation.* European Journal of Mechanical and Environmental Engineering 2002. **47**(1).
47. Lefeber, D., *PAM operation at constant load*, Figure-1-PAM-operation-at-constant-load.png, Editor. 2002.
48. Ziesmer, J.A., *Reconfigurable End Effector Allowing For In-Hand Manipulation Without Finger Gaiting Or Regrasping*, in *Faculty of the Graduate School*. 2009, Marquette University: Milwaukee, Wisconsin, USA.
49. Rezia Molfino, R.P.R.a.M.Z., *A LOW-COST RECONFIGURABLE GRIPPER FOR ASSEMBLY AND DISASSEMBLY TASKS IN WHITE INDUSTRY*, in *Department of Mechanics and Machine Design* 2006, University of Genova: Genova, Italy.
50. Bianca S. Homberg, R.K.K., Mehmet R. Dogar, and Daniela Rus, *Haptic Identification of Objects using a Modular Soft Robotic Gripper*, in *2015 IEEE/RSJ International Conference on Intelligent Robots and Systems (IROS)*. 2015, IEEE: Congress Center Hamburg, Germany.
51. Amend, J.R., et al., *A positive pressure universal gripper based on the jamming of granular material.* IEEE Transactions on Robotics, 2012. **28**(2): p. 341-350.
52. GlobalSpec, I. *Grippers Information*. 2018 [cited 2018 18 January 2018]; Available from: http://www.globalspec.com/learnmore/manufacturing_process_equipment/manufacturing_equipment_components/robots_robotic_accessories/grippers.
53. Bouchard, S., *Pneumatic robotic grippers vs electric grippers*. 2014, Robotiq: Quebec City, Canada.
54. N.Grossi, L.S., A.Scippa, G.Campatelli. *Chatter stability prediction in milling using speed-varying cutting force coefficients*. in *6th CIRP International Conference on High Performance Cutting, HPC2014*. 2014. University of California, Berkeley, USA: Elsevier B.V.
55. Sunilsing Rajput, D.S.D., *Prediction & Control of Chatter in Milling Machine Spindle-Tool Unit - A Review.* International Journal of Innovative Research in Science, Engineering and Technology, 2014. **3**(4): p. 47-52.
56. Dijk, N.v., *Active chatter control in high-speed milling processes*. 2011, Technische Universiteit Eindhoven: Eindhoven.
57. Md. Hafizur Rahman, M.H.-A.-N., Md. Mahabubur Rahman, *Design and Simulation of a Robot-Farmer for Gripping and Cutting Crops*, in *International Conference on Mechanical, Industrial and Energy Engineering 2014*. 2014: Khulna, Bangladesh.
58. Koren, Y., *General RMS characteristics. Comparison with dedicated and flexible systems*, in *Reconfigurable manufacturing systems and transformable factories*. 2006, Springer. p. 27-45.
59. Moodie, J.P.S.C.L., *Definition and Classification of Manufacturing Flexibility Types and Measures.* European Journal of Operational Research, 1998. **10**(4): p. 325-349.
60. Aboufazeli, N., *Reconfigurable Machine Tools Design Methodologies and Measuring Reconfigurability for Design Evaluation*, in *School of Industrial Engineering and Management Production Engineering and Management Department*. 2011, The Royal Institute of Technology: Sweden.
61. J. T. Black, R.A.K., *DeGarmo's Materials and Processes in Manufacturing*. 12 ed. 2017: John Wiley & Sons. 4.

62. Cardin, M.-A., *Enabling Flexibility in Engineering Systems: A Taxonomy of Procedures and a Design Framework* 2011, Department of Industrial and Systems Engineering, National University of Singapore Singapore.
63. Lee, G.H., *Reconfigurability consideration design of components and manufacturing systems.* The International Journal of Advanced Manufacturing Technology, 1997. **13**(5): p. 376-386.
64. M.G Mehrabi, A.G.U., Y Koren, P Heytler, *Trends and perspectives in flexible and reconfigurable manufacturing systems* Journal of intelligent manufacturing, 2002. **13**: p. 135-146.
65. Martin Riedel, M.N., Mathias Hüsing, Burkhard Corves *An adjustable gripper as a reconfigurable robot with a parallel structure*. in *Second InternationalWorkshop on Fundamental Issues and Future Research Directions for Parallel Mechanisms and Manipulators* 2008. Montpellier, France.
66. Tao Zhang, G.S., Ken Goldberg, *Compensatory Grasping with the Parallel Jaw Gripper.* 4th Workshop on Algorithmic Foundations of Robotics, 1999.
67. Anand Kumar Mishra, E.D.D., Ali Sadeghi, Alessio Mondini and Barbara Mazzolai, *SIMBA: Tendon-Driven Modular Continuum Arm with Soft Reconfigurable Gripper.* Frontiers in Robotics and AI 2017. **4**(4).
68. Jason Spiliotopoulos, G.M., Sotiris Makris, *A Reconfigurable Gripper for Dexterous Manipulation in Flexible Assembly.* MDPI Robotics, 2018. **3**(4).
69. Yeung, B.H.B., *Development of a 6 DOF Reconfigurable Gripper for Flexible Fixtureless Assembly* in *Graduate Department of Mechanicd and Industnd Engineering* 2000, University of Toronto Toronto, Canada.
70. Wei Gao, K.H., Jasjeet S. Seehra, Karthik Ramani, and Raymond J. Cipra, *HexaMorph: A Reconfigurable and Foldable Hexapod Robot Inspired by Origami*, in *IEEE/RSJ International Conference on Intelligent Robots and Systems*. 2014, IEEE: Chicago, IL, USA.
71. Yates, D.R., C. Vaessen, and M. Roupret, *From Leonardo to da Vinci: the history of robot-assisted surgery in urology.* BJU international, 2011. **108**(11): p. 1708-1713.
72. Shen, H., et al. *Development and Analysis of Robotic Arms for Humanoid Melo*. in *ASME International Mechanical Engineering Congress and Exposition*. 2018. American Society of Mechanical Engineers.
73. Challoo, R., et al. *Intelligent control of a Stanford JPL hand attached to a 4 DOF robot arm*. in *Proceedings of IEEE International Conference on Systems, Man and Cybernetics*. 1994. IEEE.
74. Keating, S.J., *Renaissance robotics: novel applications of multipurpose robotic arms spanning design fabrication, utility, and art*. 2012, Massachusetts Institute of Technology.
75. Pollen, A., *Adaptiv CNC*. 2017.
76. AG, i.G., *spindle motors and accessories* 2019, solectro.se: solectro.se.
77. STEPCRAFT, *STEPCRAFT2 CNC router with kress*, in *jpeg*, S.C.r.w. kress, Editor. 2015, stoneycnc.co.uk: stoneycnc.co.uk.
78. Backus, S.B. and A.M. Dollar, *An adaptive three-fingered prismatic gripper with passive rotational joints.* IEEE Robotics and Automation Letters, 2016. **1**(2): p. 668-675.
79. Suárez-Ruiz, F., et al. *Grasp mapping between a 3-finger haptic device and a robotic hand*. in *International Conference on Human Haptic Sensing and Touch Enabled Computer Applications*. 2014. Springer.

80. Matsubara, A., et al., *Non-contact measurement of dynamic stiffness of rotating spindle.* Procedia Cirp, 2014. **14**: p. 484-487.
81. Yale, *Openhand*, t1, Editor. 2015, www.eng.yale.edu: www.eng.yale.edu.
82. ROBOTIQ, *ROBOTIQ 3 Finger Adaptive Gripper* R.F.A. Gripper, Editor. 2018, www.thinkbotsolutions.com: www.thinkbotsolutions.com.
83. Ertürk, A., *Dynamic modeling of spindle-tool assemblies in machining centers*. 2006, PhD thesis.
84. Kevin Tai, A.-R.E.-S., Mohammadali Shahriari , Mohammad Biglarbegian and Shohel Mahmud, *State of the Art Robotic Grippers and Applications.* MDPI Robotics, 2016: p. 1 - 20.
85. Farid, A.M. and D.C. McFarlane, *A design structure matrix based method for reconfigurability measurement of distributed manufacturing systems.* International Journal of Intelligent Control and Systems, 2007. **1**(1): p. 118-129.
86. Farid, A.M., *Measures of reconfigurability and its key characteristics in intelligent manufacturing systems.* Journal of Intelligent Manufacturing, 2017. **28**(2): p. 353-369.
87. Oliver, D.W., T.P. Kelliher, and J.G. Keegan Jr, *Engineering Complex Systems*. 1997: McGraw-Hill Companies.
88. Maeda, O., Y. Cao, and Y. Altintas, *Expert spindle design system*. Vol. 45. 2005. 537-548.
89. Chen, W., et al., *Mechanical adaptability analysis of underactuated mechanisms.* Robotics and Computer-Integrated Manufacturing, 2018. **49**: p. 436-447.
90. Songmene, V., et al., *Machining and machinability of aluminum alloys.* Alum. Alloys Theory Appl, 2011.
91. Najiha, M., M. Rahman, and K. Kadirgama, *MACHINING PERFORMANCE OF ALUMINUM ALLOY 6061-T6 ON SURFACE FINISH USING MINIMUM QUANTITY LUBRICATION.* International Journal of Automotive & Mechanical Engineering, 2015. **11**.
92. Thiele Jr, E.W., et al., *Comparative Machinability of Brasses, Steels and Aluminum Alloys: CDA's Universal Machinability Index.* SAE transactions, 1990: p. 362-371.
93. Benjaminsen, T.K., *Rapid Prototyping CNC*. 2015.
94. Balaji, V., *High-Throughput Manufacturing of Portable Plastic Pneumatic Logic Circuits for Integrated Microfluidic Control*. 2017.
95. Alfadhli, B., et al., *Multi-Process CNC Build Preliminary Proposal.* Northern Arizona University, 2018.
96. Suraidah, S., et al. *End milling finite element method for cutting force prediction and material removal analysis*. in *IOP Conference Series: Materials Science and Engineering*. 2020. IOP Publishing.
97. zoro.com. *Cleveland #C76050 Specifications*. 2019 [cited 2019 20 October]; Available from: https://www.zoro.com/cleveland-square-end-mill-200mm-milling-dia-c76050/i/G2981373/#specifications.
98. Tool, R.M., *tech-chart-speeds-end-mill*, tech-chart-speeds-end-mill, Editor. 2015, richardsmicrotool.com: richardsmicrotool.com.
99. NTM. *PROPDRIVE v2 3548 1100KV Brushless Outrunner Motor*. 2019 [cited 2018 20 July 2018]; Available from: https://hobbyking.com/en_us/propdrive-v2-3548a-1100kv-brushless-outrunner-motor.html?___store=en_us.
100. Hanson, K., *Advantages of the ER Collet System*, in *Rotary toolholders*. 2013: Nextgen Tooling.
101. SDP, *Minimum Pulley Diameters*, M.P. Diameters, Editor. 2018: sdp-si.com.

102. SDP. *Recommended Usage*. 2018; Available from: https://www.sdp-si.com/D265/HTML/D265T042.html.

103. Popoli, W. *High Speed Spindle Design and Construction*. Engineering Research Center for Net Shape Manufacturing, 1998.

104. GlobalSpec, I., *Bearing preload: What is it and why is it important?* 2019, IEEE: insights.globalspec.com.

105. NSK. *NSK 7201 BW single row angular contact ball bearing*. 2016 [cited 2018; Available from: https://i.ebayimg.com/images/g/fjMAAOSwn4pbj1Lr/s-l1600.jpg.

106. NSK. *NSK 3201 double row angular contact ball bearing*. 2016 [cited 2018; Available from: https://www.bearing-king.co.uk/bearing/3201b-2ztn-nsk-double-row-angular-contact-ball-bearing-12x32x159mm/16347.

107. Wang, J., et al., *Modeling and Modal Analysis of Tool Holder-Spindle Assembly on CNC Milling Machine Using FEA*. Applied Mechanics and Materials Vol. 157-158. 2012, Switzerland: Trans Tech Publications. 220-226.

108. Zhu, X., *Tutorial on Hertz Contact Stress*, U.o. Arizona, Editor. 2012, College of Optical Sciences OPTI 421/521: INTRODUCTORY OPTOMECHANICAL ENGINEERING. p. 1-8.

109. NSK, *Super Precision Bearings*, N.M.a. Control, Editor. 2015, NSK.com: NSK.com. p. 30.

110. Bélanger-Barrette, M., *Flexibility vs Performance*, F.v. Performance, Editor. 2014, robotiq: https://blog.robotiq.com/bid/70628/What-does-Flexibility-in-Automated-Manufacturing-Means.

111. gallaghercorp, *Coefficient of Friction*, C.o. Friction, Editor. 2019, gallaghercorp: gallaghercorp.com.

112. FEETECH. *FEETECH FR0115M Product Datasheet*. 2019; Available from: https://www.mantech.co.za/Datasheets/Products/FR0115M.pdf.

113. Bottema, O., *On Grubler's formulae for mechanisms.* Applied Scientific Research, 1951. **2**(1): p. 162-164.

114. thethreadexchange.com. *WAXED THREAD GUIDE*. 2005 [cited 2019 16 November 2019]; Available from: https://www.thethreadexchange.com/miva/merchant.mvc?Screen=CTGY&Category_Code=waxed-thread-information.

115. SMOOTH-ON, *ECOFLEX SERIES TB*, in *122018-JR*, E.S. TB, Editor. 2018, smooth-on.com: smooth-on.com.

116. NEMA. *NEMA 17 STEPPER MOTOR HWPSMT609*. 2019 [cited 2018 20 July 2018]; Available from: https://www.diyelectronics.co.za/store/stepper-motors/43-nema-17-stepper-motor-17a-4-kg-cm.html.

117. Budak, E., Y. Altintas, and E. Armarego, *Prediction of milling force coefficients from orthogonal cutting data.* 1996.

118. Liu, D., et al., *Finite Element Analysis of High-Speed Motorized Spindle Based on ANSYS.* The Open Mechanical Engineering Journal, 2011. **5**: p. 1-10.

119. AZOM. *AISI 5140 Alloy Steel (UNS G51400)*. 2012 [cited 2018 19 September]; Available from: https://www.azom.com/article.aspx?ArticleID=6719.

120. AZOM. *Tungsten Carbide - An Overview*. 2002 [cited 2018 18 September]; Available from: https://www.azom.com/article.aspx?ArticleID=1203.

121. Unlu, M.Z., et al. *Iterative deformable FEM model for nonrigid PET/MRI breast image coregistration*. in *Medical Imaging 2006: Image Processing*. 2006. International Society for Optics and Photonics.

122. ENGINEERING, H.R.S. *CURVATURE BASED MESH ADVANTAGES IN SOLIDWORKS SIMULATION*. 2013 [cited 2019 8 November]; Available from: https://hawkridgesys.com/blog/curvature-based-mesh-advantages.
123. Patil, H. and P. Jeyakarthikeyan. *Mesh convergence study and estimation of discretization error of hub in clutch disc with integration of ANSYS*. in *IOP Conference Series: Materials Science and Engineering*. 2018. IOP Publishing.
124. NAFEMS. *The Importance of Mesh Convergence - Part 1*. 2019 [cited 2019 12 November]; Available from: https://www.nafems.org/join/directory/knowledge-base/the-importance-of-mesh-convergence-part-1/.
125. Fougeron, N., et al. *Subject specific hexahedral Finite Element mesh generation of the pelvis from bi-Planar X-ray images*. 2017.
126. Perumal, L., *A New Triangular Mesh Generation Technique.* International Journal of Machine Learning and Computing, 2019. **9**(5).
127. Ltd, A.M., *Aluminium Alloy 6082 - T6 Extrusions*, A.M. Ltd, Editor. 2019, Aalco Metals Ltd: Unit 6 Parkway Industrial Estate, Wednesbury WS10 7WP.
128. Farah, S., D.G. Anderson, and R. Langer, *Physical and mechanical properties of PLA, and their functions in widespread applications—A comprehensive review.* Advanced drug delivery reviews, 2016. **107**: p. 367-392.
129. SolidWorks, *Butyl Durometer 60 Mooney Rivlin Stress-Strain Curve*, S.-S. Curve, Editor. 2019, matereality.com: my.matereality.com.
130. Deng, Y., et al., *The impact of manufacturing parameters on submicron particle emissions from a desktop 3D printer in the perspective of emission reduction.* Building and Environment, 2016. **104**: p. 311-319.
131. HAREENDRAN, T.K. *HDD BLDC Motor*. 2019 [cited 2019 19 November]; Available from: https://www.electroschematics.com/hdd-bldc-motor/.
132. howtomechatronics.com, *How-does-an-ESC-Work-Electronic-Speed-Controller*, How-does-an-ESC-Work-Electronic-Speed-Controller-768x365.png, Editor. 2019, howtomechatronics.com: howtomechatronics.com.
133. futurelab3d. *How Brushless Motor and ESC Work*. 2019 [cited 2019 6 August]; Available from: How Brushless Motor and ESC Work.
134. Hobbywing. *Skywalker 2-6S 80A UBEC Brushless ESC* 2018 [cited 2019 20 November]; Available from: https://www.hobbywingdirect.com/products/skywalker-esc-80a-ubec?variant=3471339140.
135. howtomechatronics.com, *Arduino-BLDC-Motor-Control-Circuit-Diagram-Schematic*, Arduino-BLDC-Motor-Control-Circuit-Diagram-Schematic-768x419.png, Editor. 2019, howtomechatronics.com: howtomechatronics.com.
136. jameco. *How Do Servo Motors Work?* 2018 [cited 2019 19 July 2019]; Available from: https://www.jameco.com/jameco/workshop/howitworks/how-servo-motors-work.html.
137. keyestudio, *TB6560*, KS0318-1.png, Editor. 2018, wiki.keyestudio.com: wiki.keyestudio.com.
138. Arduino, *TB6560 Arduino Connection* tb6560-arduino.jpg, Editor. 2018, 2.bp.blogspot.com: 2.bp.blogspot.com.
139. Sharma, I.R. *Latest Trends in Machining*. 2001.
140. Groover, M.P., *Fundamental of Modern Manufacturing: Materials, Processes, and Systems*. 4 ed, ed. M. McDonald. 2010, United States of America: JOHN WILEY & SONS, INC. 1025.
141. Sheikh-Ahmad, J.Y., *Machining of Polymer Composites*. 2009, Springer Science + Business Media.

142. Smith, G.T., *Cutting Tool Technology*. 2008, London: Springer-Verlag. 606.
143. University, T., *Milling Geometry 245*. 2008, Tooling U. p. 23.
144. Velocity, T., *Endmill Terminology*, em_terminology_01.gif, Editor.
145. K F Ehmann, S.G.K., R E DeVor, I Lazoglu, *Machining process modelling: A review.* Journal of Manufacturing Science and Engineering, 1997. **119**: p. 655-663.
146. Bachrathy, D., *Cutting dynamics and surface quality*, in *Department of Applied Mechanics*. 2013, Budapest University of Technology and Economics.
147. Hwang, G.M.Z.T.W., *Analysis of the Cutting Dynamics in Microscale*. 1990, University of Maryland: Harvard p. 25.
148. Jui P. Hung, Y.L.L., Tzuo L. Luo and Hsi H. Hsiao *Prediction of the Dynamic Characteristics of a Milling Machine Using the Integrated Model of Machine Frame and Spindle Unit.* International Journal of Mechanical and Mechatronics Engineering, 2012. **6**(7): p. 1234-1240.
149. Sutherland and J. William, *A dynamic model of the cutting force system in the end milling process*. 2018.
150. Instruments, N. *Modal Parameter Extraction LabVIEW VIs*. 2015 [cited 2018 5 September 2018]; Available from: http://www.ni.com/example/31121/en/#toc1.
151. Doina, M. *Modal analysis applied to milling machines*. in *Mathematical Applications in Science and Mechanics*. 2013. Dubrovnik, Croatia: WSEAS Press.
152. Jakeer Hussain Shiak, S.J., *DYNAMIC MODELLING AND MACHINING STABILITY IN A NEW MILL-SPINDLE DESIGN FOR DRILLING MACHINE.* ELK Asia Pacific Journals – Special Issue, 2015.
153. Instruments, C., *Impact hammer modal testing*.
154. Cvijetin Mlađenović, M. and A.Ž. Zeljković, *DEFINITION OF MACHINING SYSTEMS STABILITY LOBE DIAGRAM USING ANALYTICAL MODELS.* Journal of Production Engineering, 2015. **18**(1): p. 47-50.
155. Gaber, O. and S.M. Hashemi, *Effects of Machine Tool Spindle Decay on the Stability Lobe Diagram: An Analytical-Experimental Study.* Shock and Vibration, 2016. **2016**: p. 9.
156. E. Budak, Y.A., *Analytical Prediction of Stability Lobes in Milling.* Annals of the CIRP, 1995. **44**(1): p. 357-362.
157. Yue, J., *Creating a Stability Lobe Diagram*. 2006. 301-50.
158. Palpandian P, P.R.V., Satish Babu S, *Stability Lobe Diagram for High Speed Machining Processes:Comparison of Experimental and Analytical Methods – A Review.* International Journal of Innovative Research in Science, Engineering and Technology, 2013. **2**(3): p. 747-752.
159. Abbas, A.E., et al., *Application of decision analysis to milling profit maximisation: An introduction*. Vol. 35. 2009. 1-2.
160. Babu, V.P.a.N.R. *Influence of Milling Cutter Dynamics on Stability Lobe Diagrams*. in *International Conference on Precision, Meso, Micro and Nano Engineering*. 2017. Chennai, India: COPEN 10.
161. Casiano, M., *Extracting damping ratio from dynamic data and numerical solutions.* 2016.
162. Rotondella, V., et al., *Dynamic modal correlation of an automotive rear subframe, with particular reference to the modelling of welded joints.* Advances in Acoustics and Vibration, 2017. **2017**.
163. Merritt, H.E., *Theory of self-excited machine-tool chatter: Contribution to machine-tool chatter research—1.* Journal of engineering for industry, 1965. **87**(4): p. 447-454.

164. Tlusty, J., *The stability of the machine tool against self-excited vibration in machining.* Proc. Int. Res. in Production Engineering, Pittsburgh, ASME, 1963. **465**.

165. Altintas, Y., *Manufacturing automation: metal cutting mechanics, machine tool vibrations, and CNC design*. 2000, The Pitt Building, Trumpington Street, Cambridge, United Kingdom: Cambridge University Press.

166. Rubeo, M.A. and T.L. Schmitz, *Mechanistic force model coefficients: A comparison of linear regression and nonlinear optimization.* Precision Engineering, 2016. **45**: p. 311-321.

167. Aidan, R., J. Padayachee, and G. Bright. *Research and development of a 5-axis hybrid kinematic CNC machine*. in *2017 24th International Conference on Mechatronics and Machine Vision in Practice (M2VIP)*. 2017. IEEE.

168. Kumičáková, D., V. Tlach, and M. Císar, *Testing the performance characteristics of manipulating industrial robots.* 2016.

169. Maciej Petko, G.K. *Mechatronic Design of a Parallel Manipulator for Milling*. in *International Conference on Advanced Intelligent Mechatronics*. 2005. Monterey, California, USA: IEEE.

170. Liang Jie, J.S.-H. *The Study of Design Method for Robotic Drill End Effector*. in *13th Global Congress on Manufacturing and Management, GCMM 2016*. 2016. China: Elsevier Ltd.

171. Brüggemann, T., D. Biermann, and A. Zabel, *Development of an automatic modal pendulum for the measurement of frequency responses for the calculation of stability charts.* Procedia CIRP, 2015. **33**: p. 587-592.

172. McConnell, K.G. and P.S. Varoto. *The Effects of Windowing on FRF Estimations for Closely Spaced Peaks and Valleys*. in *PROCEEDINGS-SPIE THE INTERNATIONAL SOCIETY FOR OPTICAL ENGINEERING*. 1995. SPIE INTERNATIONAL SOCIETY FOR OPTICAL.

173. Avitabile, P., *Experimental modal analysis.* Sound and vibration, 2001. **35**(1): p. 20-31.

174. Schoukens, J., K. Godfrey, and M. Schoukens, *Nonparametric data-driven modeling of linear systems: Estimating the frequency response and impulse response function.* IEEE Control Systems Magazine, 2018. **38**(4): p. 49-88.

175. Powałka, B., M. Chodźko, and K. Jemielniak, *Stability analysis in milling based on operational modal data.* Journal of Machine Engineering, 2011. **11**.

176. Brecher, C., P. Chavan, and A. Epple, *Efficient determination of stability lobe diagrams by in-process varying of spindle speed and cutting depth.* Advances in Manufacturing, 2018. **6**(3): p. 272-279.

177. shop-apt.co.uk. *ER11 Collet 3.5mm - 3mm Clamping Range High Precision Series*. 2019 [cited 2019 19 September]; Available from: https://www.shop-apt.co.uk/er-collets-high-precision-0010mm-runout/er11-collet-35mm-3mm-clamping-range-high-precision-series.html.

178. Martin, D.L., R.O. Wilcox, and L. Precision. *Spindle Runout Effects on Positional Accuracy*. in *Symposium on Small Hole Technology*. 1990.

179. Insperger, T., et al. *The effect of runout on the chatter frequencies of milling processes*. in *Proceedings of the 9th CIRP International Workshop on Modeling of Machining Operations, Bled, Slovenia*. 2006. Citeseer.

180. Akpobi, J., C.J.J.o.A.S. Ovuworie, and E. Management, *Computer–Aided Design of the Critical Speed of Shafts.* 2008. **12**(4).

181. Belanger-Barrette, M., *Robot Gripper Metrics Studied at NIST*. 2015, Robotiq: robotiq.com.

182. Zulu, A., *THEORETICAL DETERMINATION OF THE CRITICAL SPEEDS OF SHAFTS UNDER AXIAL BUCKLING LOADS.*

183. steminbreitbach, *Elatech drive calculation*, steminbreitbach, Editor. 2018, steminbreitbach.com: steminbreitbach.com. p. 158-180.

184. Shigley, J.E., *Shigley's mechanical engineering design*. 8th ed. 2011: Tata McGraw-Hill Education.

185. break_it_fix_it. *Controlling 3 Servo Motors With 3 Potentiometers and an Arduino*. 2019 [cited 2019 21 April]; Available from: https://www.instructables.com/id/Controlling-3-servo-motors-with-3-potentiometers-a/.

186. lobodol. *ESC-calibration.ino*. 2018 [cited 2019 15 January]; Available from: https://github.com/lobodol/ESC-calibration/blob/master/ESC-calibration.ino.

187. Dejan. *Arduino Brushless Motor Control Tutorial | ESC | BLDC*. Arduino Tutorials 2019 [cited 2019 16 May]; Available from: https://howtomechatronics.com/tutorials/arduino/arduino-brushless-motor-control-tutorial-esc-bldc/.

188. NTM, *NTM Propdrive 3548 Characteristic Curve*, N.P.C. Curve, Editor. 2019.

189. Technology, L. *NEMA 17 Stepper Motor Characteristic Curve*. 2019.

190. Arduino, *TB6560 Technical Specifications*, stepper-motor-driver-stepper-motor-driver-board-single-axis-controller-10-speed.jpg, Editor. 2017, upload.ecvv.com: upload.ecvv.com.

Chapter 12 Appendices

Appendix A Quality Function Deployment – House of Quality

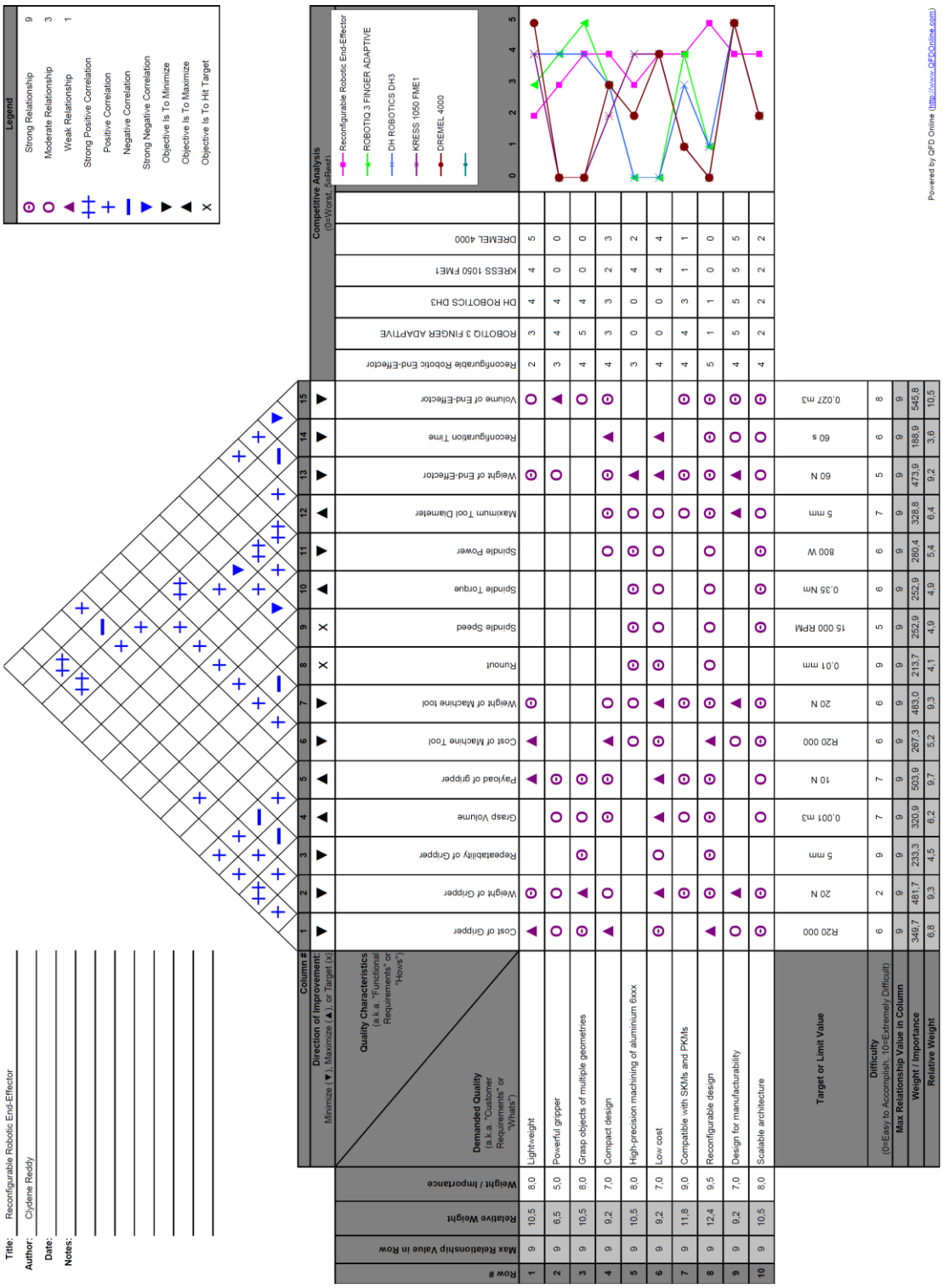

Figure A 12-1: QFD HoQ

Appendix B Mechanical Calculation Data

B.1 Spindle Calculations

The recommended surface cutting speed for end milling wrought aluminium alloy is 76.2 m/min. The recommended tooth feed rate for end milling wrought aluminium alloy with 2 flutes, 2 mm diameter carbide tool is 0.0254 mm/tooth [98]. These parameters, in conjunction with Equations B.1 and B.2, are used to compute the required spindle speed, feed rate, depth of cut and width of cut. The variables used in the Equations are presented in Table B 12-1.

$$n = \frac{1000.v_c}{\pi.D} \tag{B.1}$$

$$v_f = n.z.f_z \tag{B.2}$$

Table B 12-1: Workpiece Calculation Variables

Variable	Symbol	Unit
Rotational Cutting Speed	N	rpm
Cutting Speed	v_c	m/min
Tool Diameter	D	mm
Number of Teeth	z	
Tooth Feed	f_z	mm/tooth
Feed Rate	v_f	mm/min

Using the data for these parameters and the above Equations, a rotational cutting speed of 12127.61 RPM and a feed rate of 616.08 mm/min was calculated. The width of cut is 2 mm for an end milling process. The depth of cut is set at 2 mm.

The maximum rotational speed of the belt is determined by the following Equation. Table B 12-2 defines variables and units for Equation B.3.

$$n = \frac{v_s \times 60}{\pi \times d_m} \tag{B.3}$$

Table B 12-2: Maximum Rotational Speed Calculation Variables

Variable	Symbol	Unit
Surface Speed	v_s	m/s
Pitch Diameter	d_m	m

The pitch diameter of the motor pulley is 12.7 mm. The resultant maximum rotational speed of the belt is 29029.86 RPM. The calculated rotational cutting speed is 12127.61 RPM, the GT2 belt is ideally suited for the application.

To select belt combination, design considerations of the spindle and brushless motor were considered. The approximate distance between the centres of the spindle shaft and the spindle drive motor is defined in Section 3.7. Given this length of 120 mm, the approximate belt length is determined using Equations B.4 and B.5 below. The specification of the selected tool holder and spindle motor require pulleys of inner diameter 8 mm and 5 mm respectively. GT2 pulleys with these inner diameters and 20 teeth are available and cost-efficient. Both pulleys have the same number of teeth; this was selected due to the ideal speed and torque output of the NTM BLDC motor. Therefore, the power transmission ratio is 1:1. Figure B 12-2 and Table B 12-3 present the variables and assumptions used in the calculation.

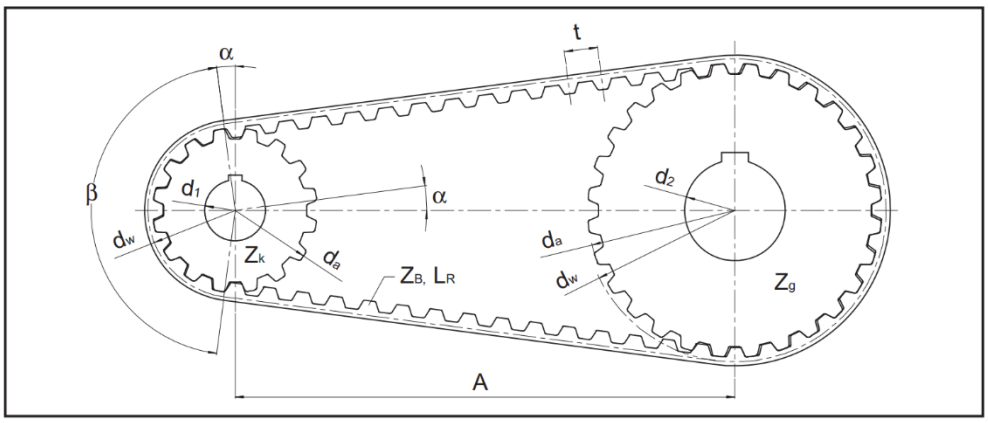

Figure B 12-2: Timing Belt – Pulley Calculation diagram [183]

$$L_R = 2 \times A \times \sin\left(\frac{\beta}{2}\right) + \frac{t}{2} \times (z_g + z_k + (1 - \frac{\beta}{180}) \times (z_g - z_k) \quad \text{(B.4)}$$

$$L_R = 2 \times A + \pi \times d_w \quad \text{(B.5)}$$

Table B 12-3: Belt Length Calculation Variables

Variable	Symbol	Unit
Center Distance	A	mm
Wrap angle	β	degrees
Pitch	t	mm
Number of teeth of the large pulley	z_g	
Number of teeth of the small pulley	z_k	
Belt Length	L_R	mm
Pulley pitch diameter	d_w	mm

The pitch diameter of the motor pulley is 12.7 mm. Using the centre distance of 120 mm, the calculated belt length is 279.90 mm. Due to the unavailability of a belt with this specific length, a 280 mm belt was selected. Belt tensioning mechanism is incorporated to adjust pretension of the belt and pulley assembly. Tolerance for allowable tensioning and adjustment of the belt-pulley is incorporated in the designed mount.

The spindle shaft will be supported by two angular contact ball bearings. The bearings require mounting specifications and tolerances as indicated by the manufacturer. These parameters were used in the dimensioning of the spindle shaft. The manufacturers recommended fillet and abutment specifications are presented in Figure B 12-3 and Table B 12-4.

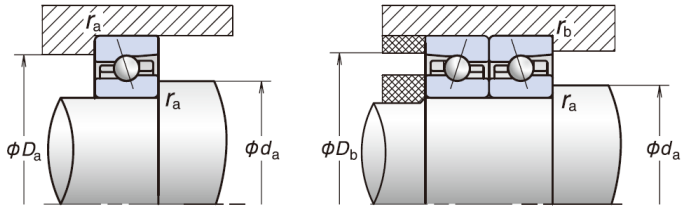

Figure B 12-3: Recommended Abutment and Fillet Dimensions [109]

Table B 12-4: Recommended Abutment and Fillet Dimensions [109]

d_a (Min)	D_a (Max)	r_a (Max)	D_b (Max)	r_b (Max)
17 mm	27 mm	0.6 mm	29.5 mm	0.3 mm

B.2 Gripper Calculations

Servomotors vary in size, output torque, cost, efficiency, controllability, speed, current and voltage. Specification of the gripper requires the motor to be lightweight, compact, simple to control and cost-effective. There are many compact, low-cost servo motors available. The output torque required for gripping specification of 1 kg must be determined to select appropriate servomotor. Equation B.6 below is used to determine the minimal gripping force. The gripping force is the sum of all individual finger force.

$$F_g > \frac{m(g + a_r)}{u}(SF) \tag{B.6}$$

Table B 12-5: Gripping Force Calculation

F_g	Gripping Force (N)	13.464
m	Mass of Part (kg)	1
g	Gravitational Acceleration ($m.s^{-2}$)	9.81
a_r	Robot Acceleration ($m.s^{-2}$)	5
u	Coefficient of Static Friction	2.2
SF	Safety Factor	2

Distal phalanx will have friction coating for increased grasp ability. The glove material is polyurethane with a static coefficient friction factor of 2.2. A safety factor of 2 is used to account for inefficiencies in the gripper system. Total gripping force of 13.464 N is required for 1 kg payload. Since there are three fingers, grasp force per finger is 4.488 N. Torque can be estimated using the lever arm of gripper finger and required grasp force of one finger. Torque is calculated using Equation B.7.

$$T = r_a F_a \sin\theta_a \tag{B.7}$$

Table B 12-6: Torque Estimation Calculation

T	Torque (Nm)	0.706
r_a	Radius from the axis of rotation (m)	0.15724
F_a	Applied Force (N)	4.488
θ_a	The angle between the Lever Arm and Axis of Rotation (°)	90

B.3 Linear Actuator Calculations

The power screw calculations were performed on the threaded rod of the linear actuator as is documented below. Equation B.8 is used to calculate the torque required to raise the load.

$$T_R = \frac{Wd_m}{2}\left[\frac{f\pi d_m + L(\cos\alpha_n)}{\pi d_m \cos\alpha_n - fL}\right] + \frac{Wf_c d_c}{2} \quad (B.8)$$

The linear actuator does not possess a collar, and this can be seen in Appendix K.25. The collar terms variables are therefore not considered. The pitch diameter was used instead of the mean diameter. The formula was obtained from Shingley [184].

$$d_m = d_p = d - 0.649519p$$

$$d_p = 8 - 0.649519(2) = 6.70 \text{ mm}$$

$$T_R = \frac{Wd_m}{2}\left[\frac{f\pi d_m + L(\cos\alpha_n)}{\pi d_m \cos\alpha_n - fL}\right] + \frac{Wf_c d_c}{2}$$

W = 15.53

dm = 6.70

2αn = 29

f = 0.15 for brass nut

Lead = 8 mm

The Force, W, was obtained from adding weights of gripper subassembly and gripper platform in Appendix E. The friction value, f, was approximated to be 0.15, and the thread angle was 29° [184].

$$15.53 + 9.81 = \frac{2 \times T_R}{6.70 \times 10^{-3}\left[\frac{0.15\pi(6.70 \times 10^{-3}) + 8 \times 10^{-3}\left(\cos\frac{29}{2}\right)}{\pi(6.70 \times 10^{-3})\left(\cos\frac{29}{2}\right) - 0.15(8 \times 10^{-3})}\right]}$$

$$T = 0.048 \text{ Nm}$$

Taking into account other forms of friction from two linear guides, 20% of friction is accounted for.

$$T = 0.048 \times 1.2 = 0.058 \text{ Nm}$$

The efficiency of the linear actuators, η, was calculated as follows:

$$\eta = \frac{WLead}{2\pi M_t} = \frac{25.34 \times 8 \times 10^{-3}}{2\pi \times 0.058} = 0.5571 = 55.71\%$$

Given required torque of 0.12 Nm, corresponding speed is determined from Appendix C.2 as 1500 rpm. Linear speed is given by equation. The lead of the screw is 8 mm.

$$v = NL = 1500 \times 8 \times 10^{-3} = 12 \text{ m.min}^{-1} = 200 \text{ mm.s}^{-1}$$

Travel time for the length of the lead screw is given by equation. Length of the lead screw is 74 mm.

$$\Delta t = \frac{\Delta x}{v} = \frac{74}{200} = 0.37 \text{ s}$$

The number of steps stepper must take to travel 74 mm is calculated. NEMA 17 motor possesses a resolution of 1.8° per step.

$$S = \frac{\Delta x \times 360}{R \times L} = \frac{74 \times 360}{1.8 \times 8} = 1850 \text{ steps}$$

Given the required time of 0.37 s and steps of 1850, the delay in seconds is calculated by means of an equation.

$$\text{delay} = \frac{\Delta t}{S} = \frac{0.37}{1850} = 200 \text{ microseconds}$$

Appendix C FEA Simulation Results

C.1 Standard Mesh Quality Settings

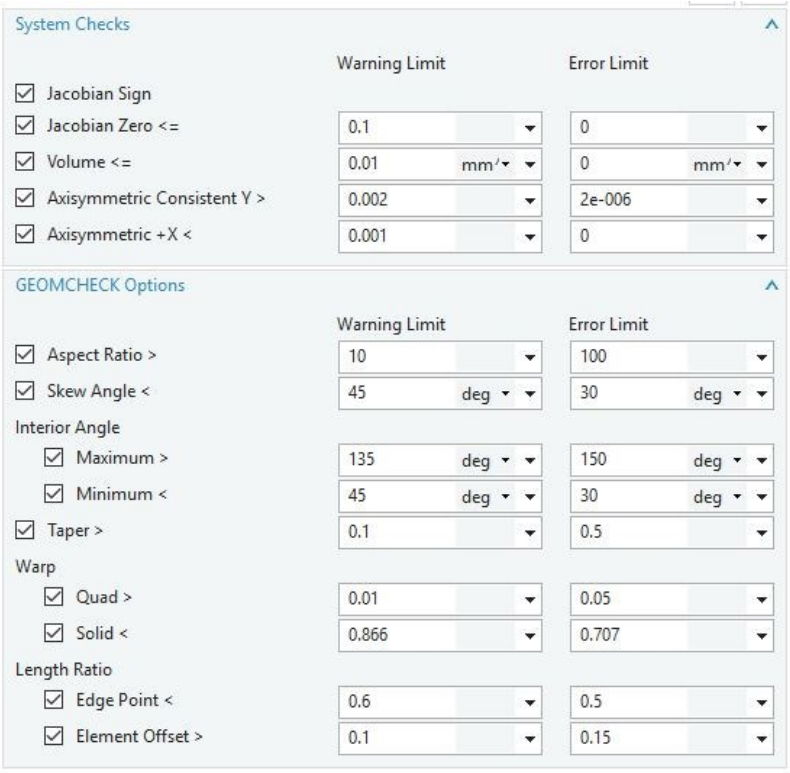

Figure C 12-4: NX Nastran Mesh Quality Settings

C.2 Spindle Shaft Modal Simulation Results

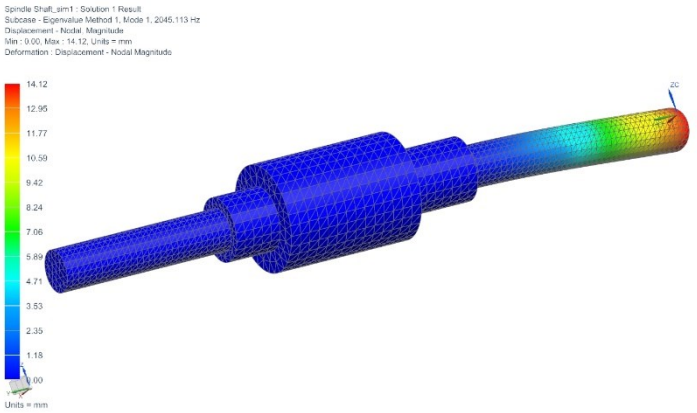

Figure C 12-5: Spindle Shaft First Mode Displacement Plot

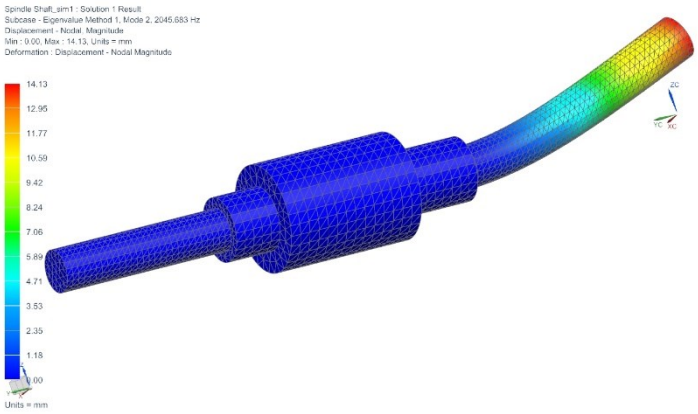

Figure C 12-6: Spindle Shaft Second Mode Displacement Plot

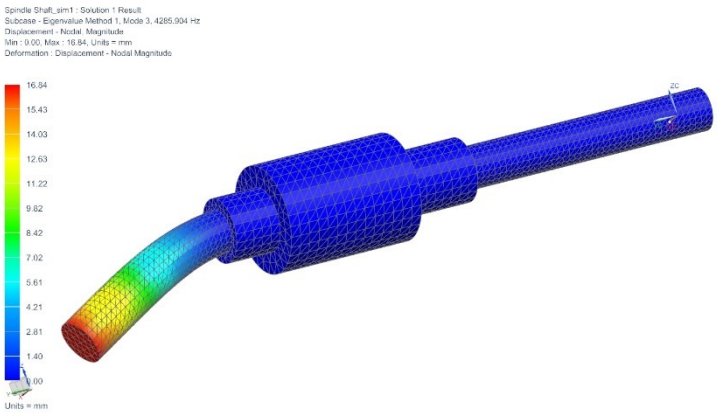

Figure C 12-7: Spindle Shaft Third Mode Displacement Plot

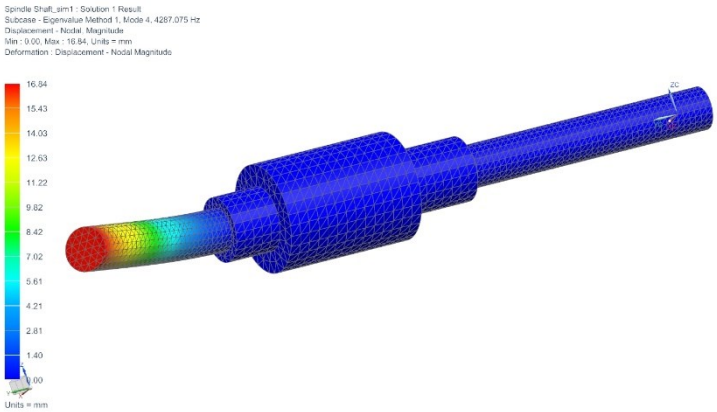

Figure C 12-8: Spindle Shaft Fourth Mode Displacement Plot

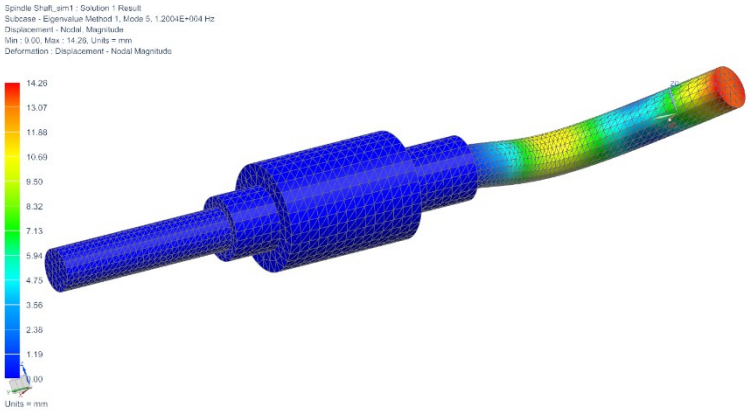

Figure C 12-9: Spindle Shaft Fifth Mode Displacement Plot

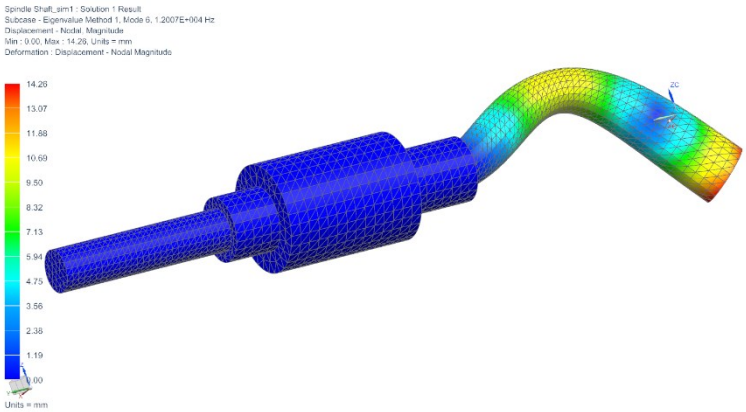

Figure C 12-10: Spindle Shaft Sixth Mode Displacement Plot

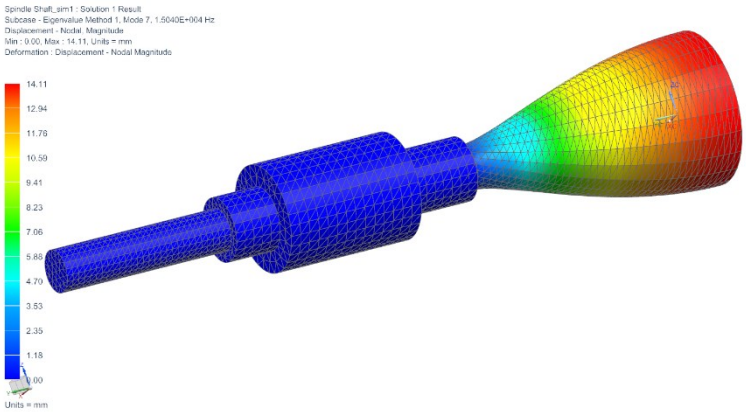

Figure C 12-11: Spindle Shaft Seventh Mode Displacement Plot

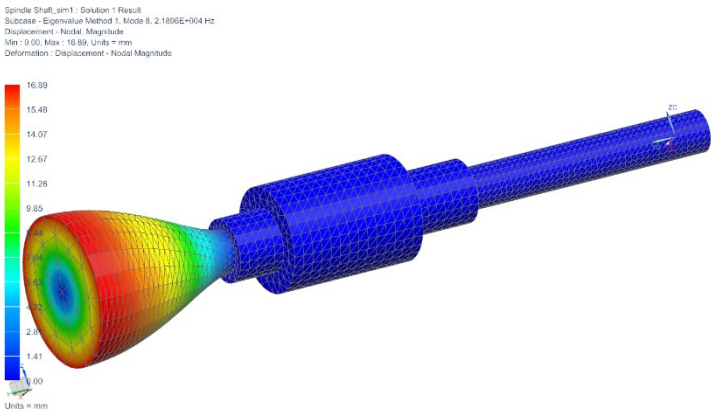

Figure C 12-12: Spindle Shaft Eighth Mode Displacement Plot

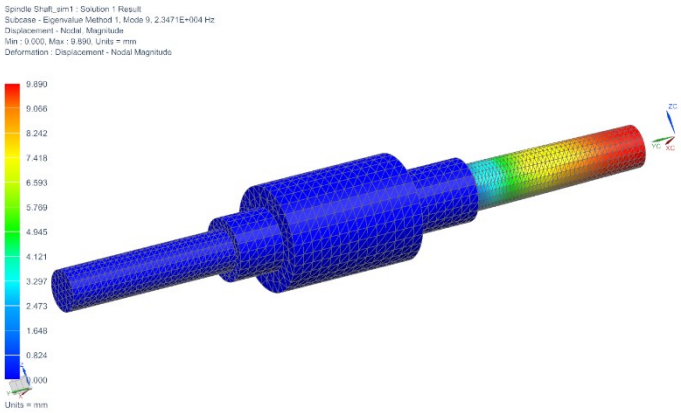

Figure C 12-13: Spindle Shaft Ninth Mode Displacement Plot

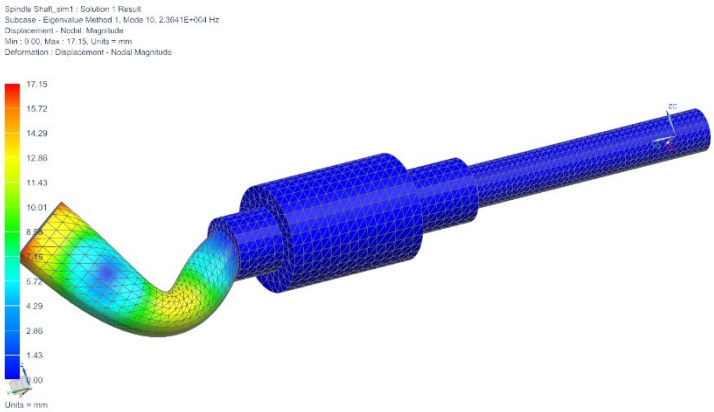

Figure C 12-14: Spindle Shaft Tenth Mode Displacement Plot

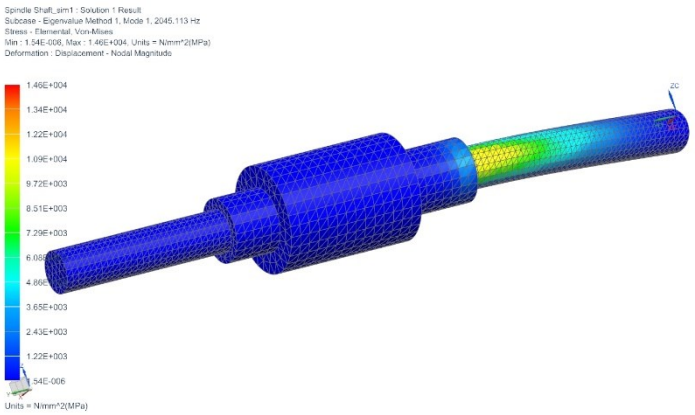

Figure C 12-15: Spindle Shaft First Mode Von-Mises Stress Plot

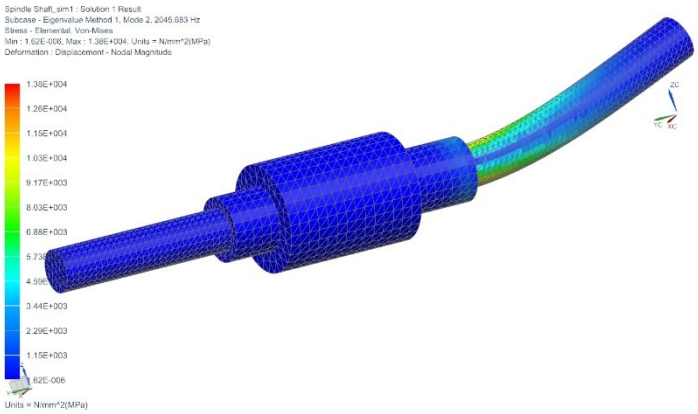

Figure C 12-16: Spindle Shaft Second Mode Von-Mises Stress Plot

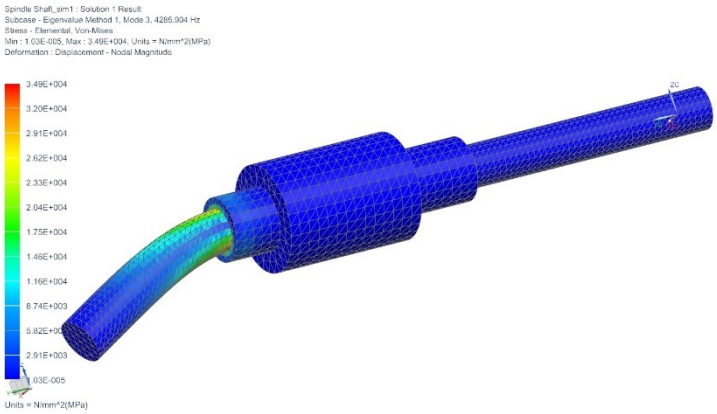

Figure C 12-17: Spindle Shaft Third Mode Von-Mises Stress Plot

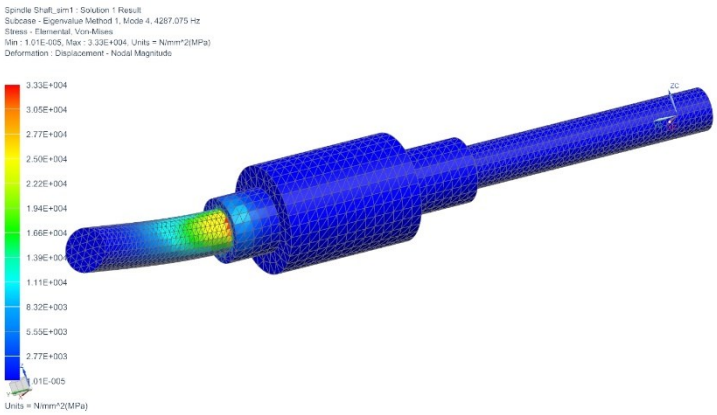

Figure C 12-18: Spindle Shaft Fourth Mode Von-Mises Stress Plot

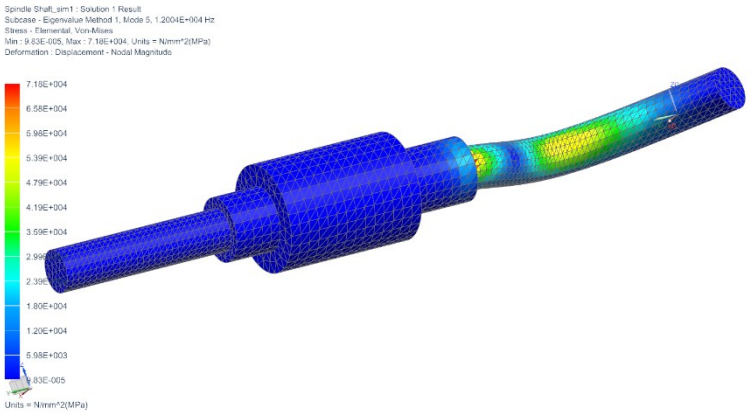

Figure C 12-19: Spindle Shaft Fifth Mode Von-Mises Stress Plot

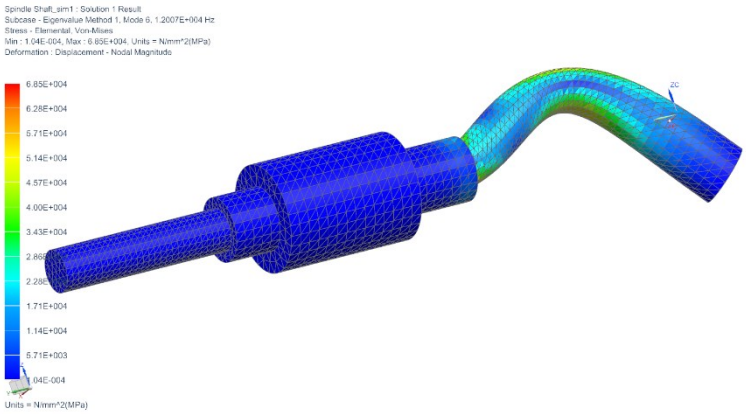

Figure C 12-20: Spindle Shaft Sixth Mode Von-Mises Stress Plot

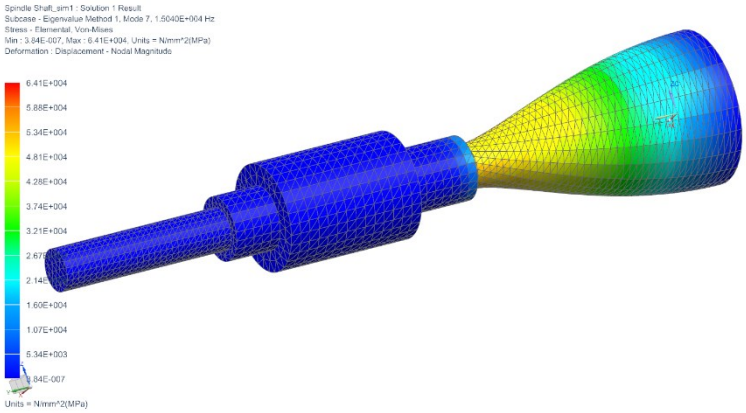

Figure C 12-21: Spindle Shaft Seventh Mode Von-Mises Stress Plot

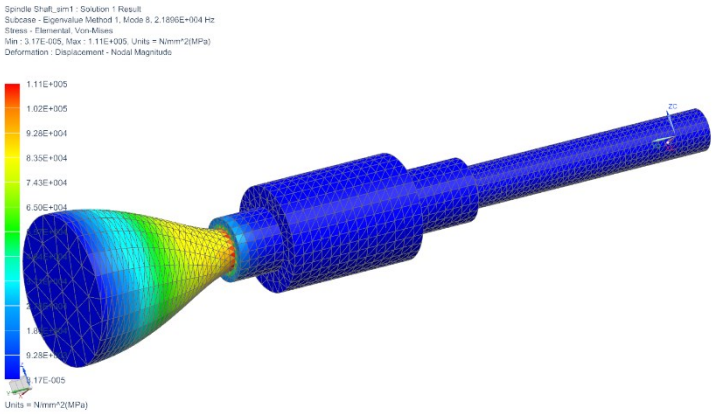

Figure C 12-22: Spindle Shaft Eighth Mode Von-Mises Stress Plot

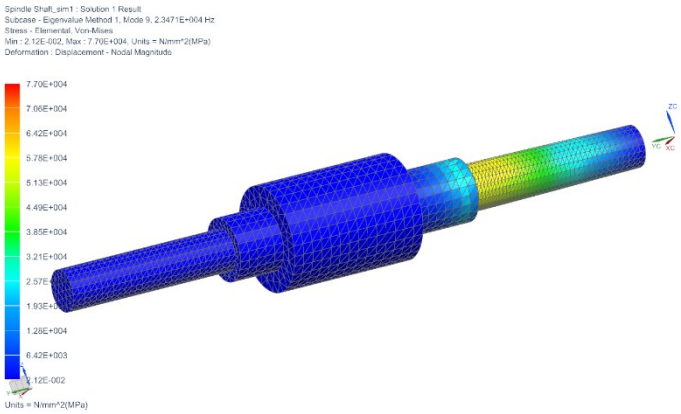

Figure C 12-23: Spindle Shaft Ninth Mode Von-Mises Stress Plot

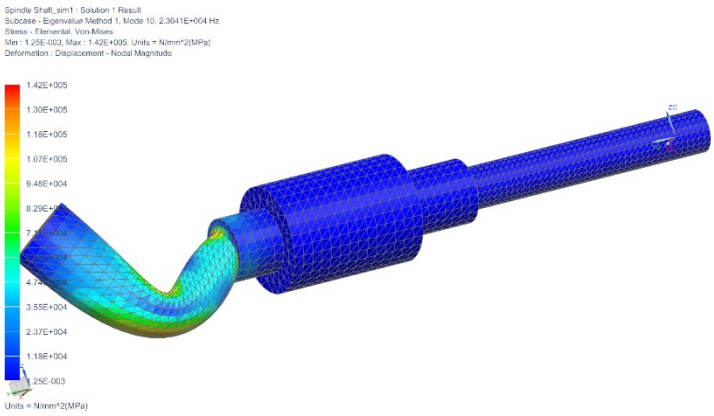

Figure C 12-24: Spindle Shaft Tenth Mode Von-Mises Stress Plot

C.3 MT Modal Simulation Results

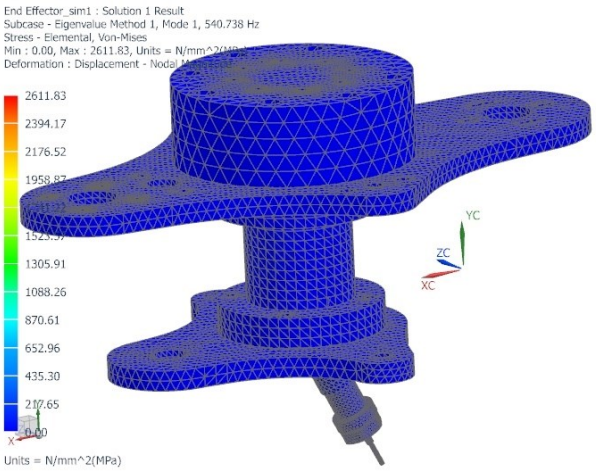

Figure C 12-25: Machine Tool First Mode Von-Mises Stress Plot

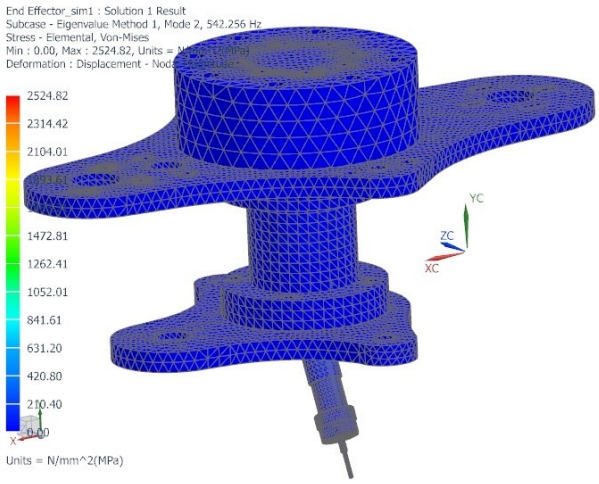

Figure C 12-26: Machine Tool Second Mode Von-Mises Stress Plot

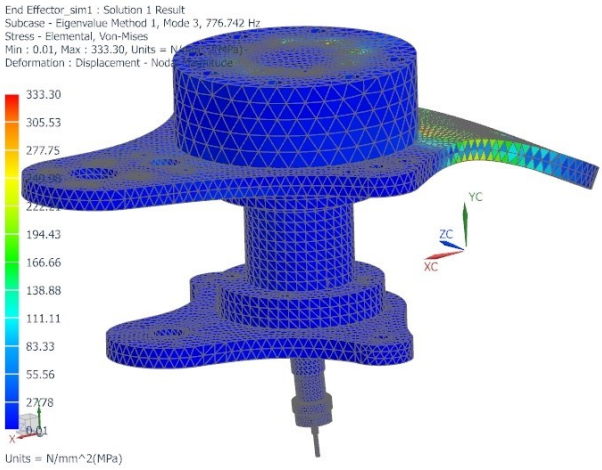

Figure C 12-27: Machine Tool Third Mode Von-Mises Stress Plot

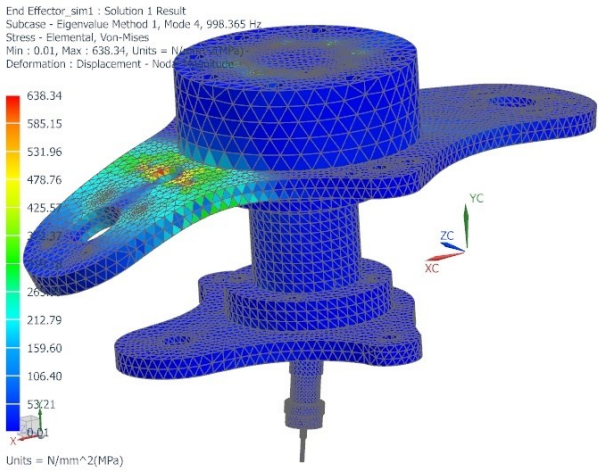

Figure C 12-28: Machine Tool Fourth Mode Von-Mises Stress Plot

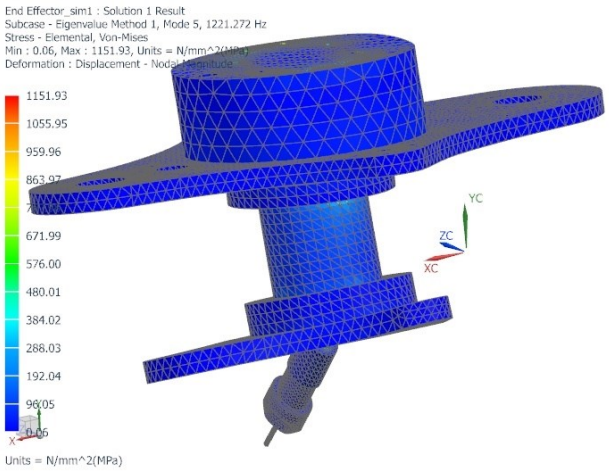

Figure C 12-29: Machine Tool Fifth Mode Von-Mises Stress Plot

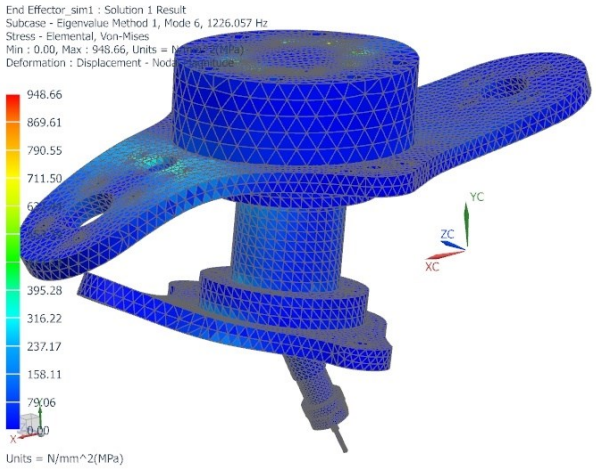

Figure C 12-30: Machine Tool Sixth Mode Von-Mises Stress Plot

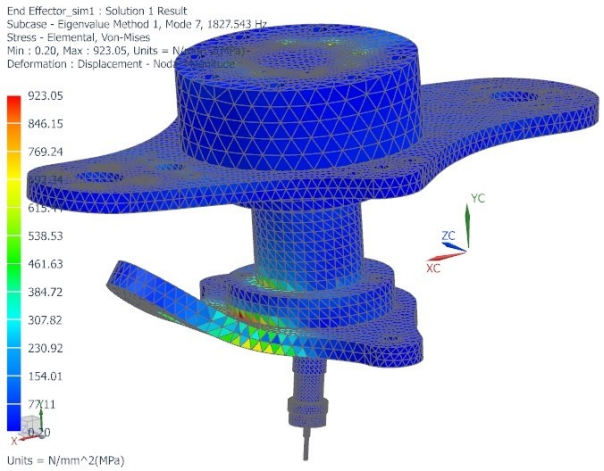

Figure C 12-31: Machine Tool Seventh Mode Von-Mises Stress Plot

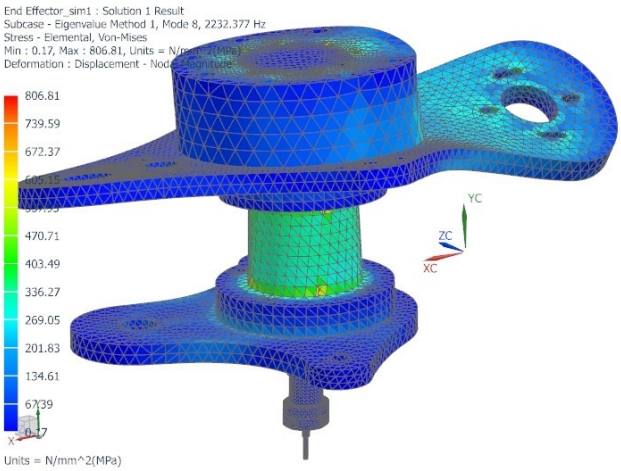

Figure C 12-32: Machine Tool Eighth Mode Von-Mises Stress Plot

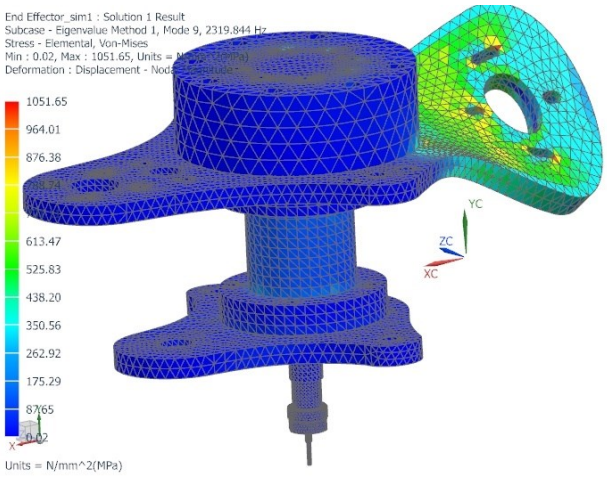

Figure C 12-33: Machine Tool Ninth Mode Von-Mises Stress Plot

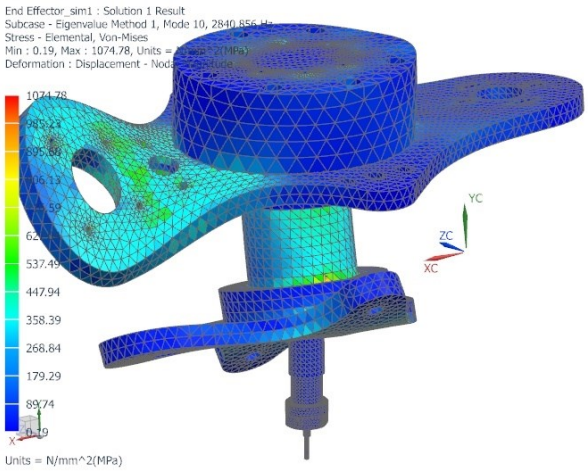

Figure C 12-34: Machine Tool Tenth Mode Von-Mises Stress Plot

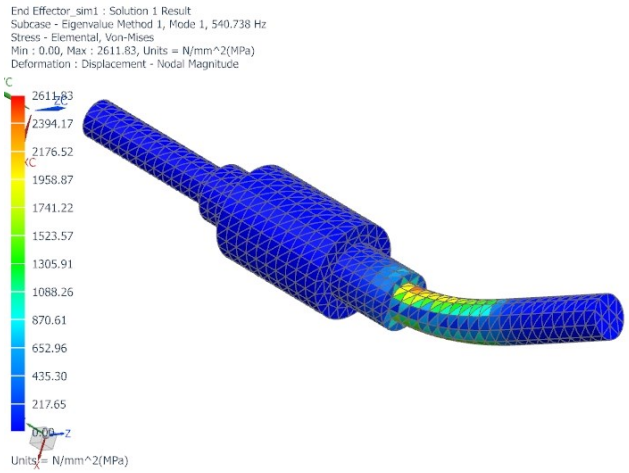

Figure C 12-35: MT Spindle Shaft First Mode Von-Mises Stress Plot

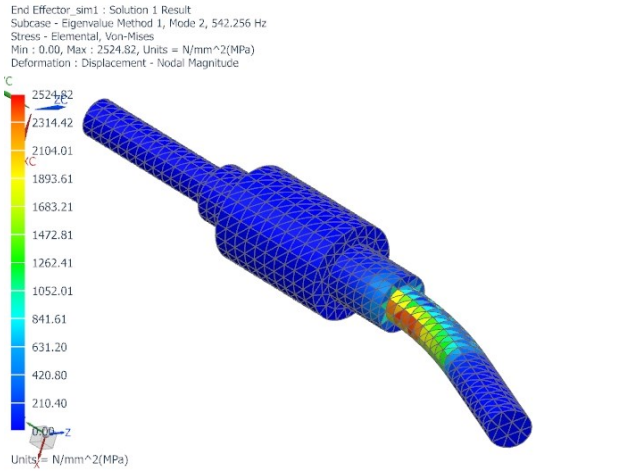

Figure C 12-36: MT Spindle Shaft Second Mode Von-Mises Stress Plot

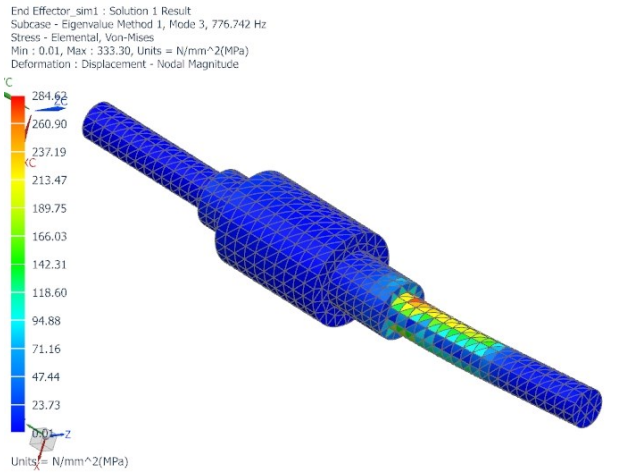

Figure C 12-37: MT Spindle Shaft Third Mode Von-Mises Stress Plot

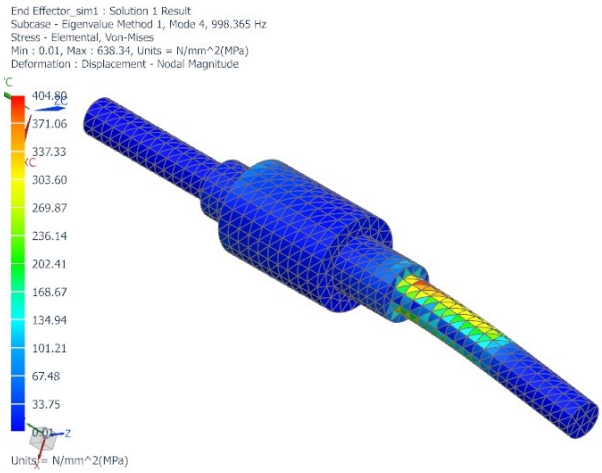

Figure C 12-38: MT Spindle Shaft Fourth Mode Von-Mises Stress Plot

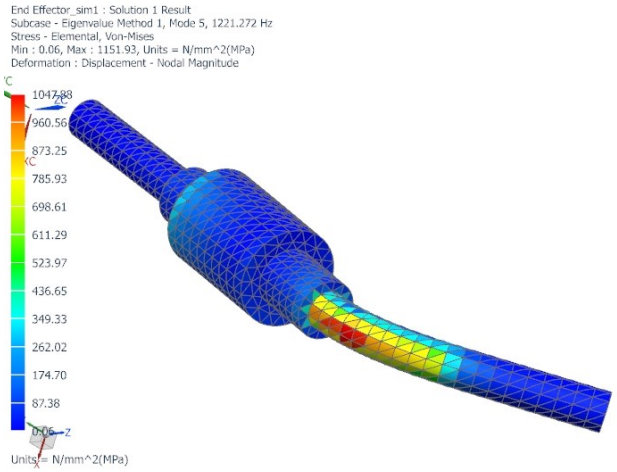

Figure C 12-39: MT Spindle Shaft Fifth Mode Von-Mises Stress Plot

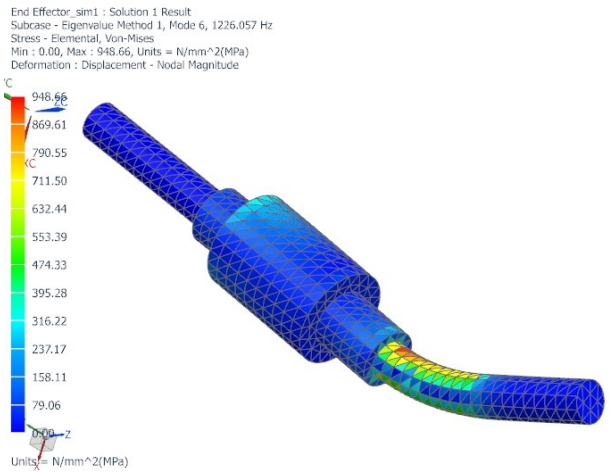

Figure C 12-40: MT Spindle Shaft Sixth Mode Von-Mises Stress Plot

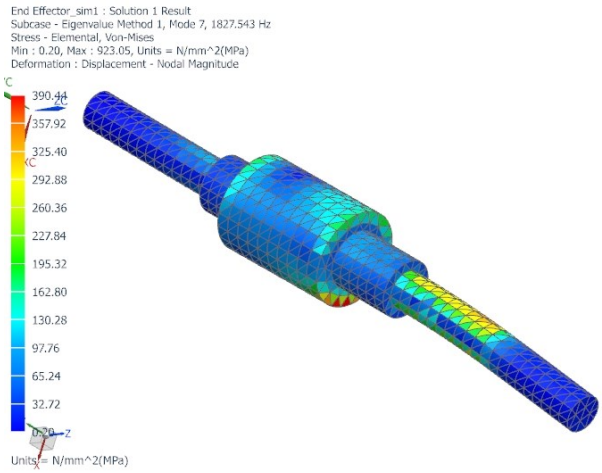

Figure C 12-41: MT Spindle Shaft Seventh Mode Von-Mises Stress Plot

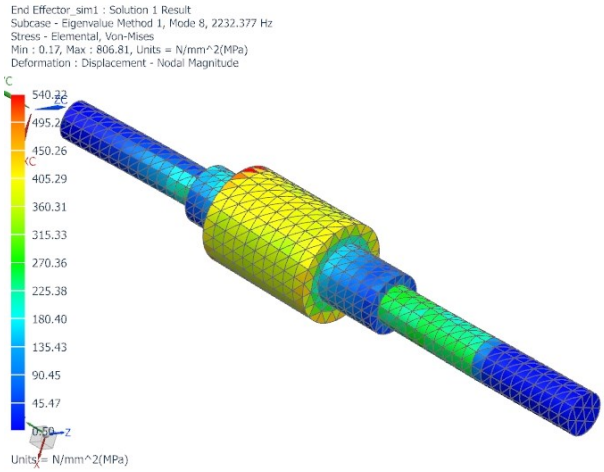

Figure C 12-42: MT Spindle Shaft Eighth Mode Von-Mises Stress Plot

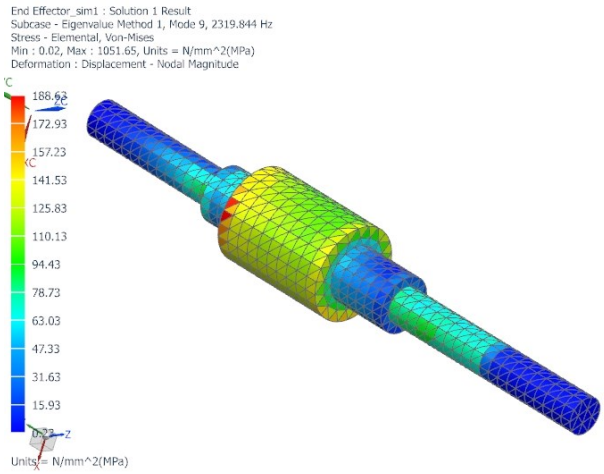

Figure C 12-43: MT Spindle Shaft Ninth Mode Von-Mises Stress Plot

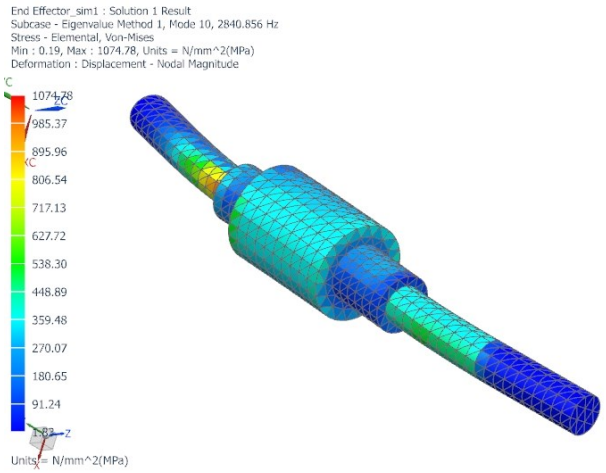

Figure C 12-44: MT Spindle Shaft Tenth Mode Von-Mises Stress Plot

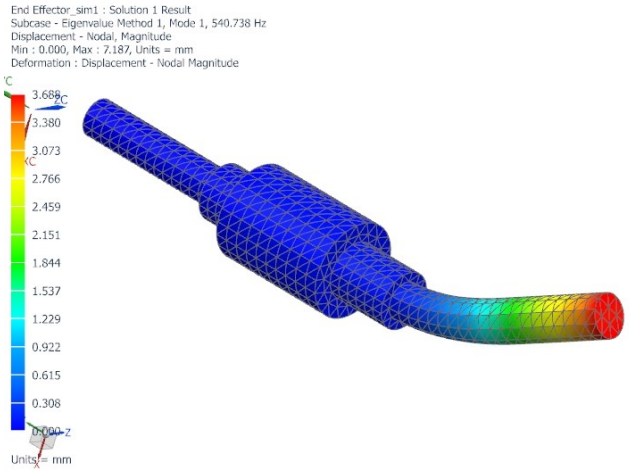

Figure C 12-45: MT Spindle Shaft First Mode Displacement Plot

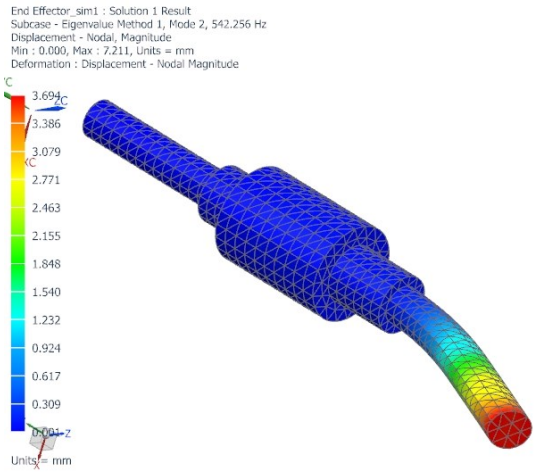

Figure C 12-46: MT Spindle Shaft Second Mode Displacement Plot

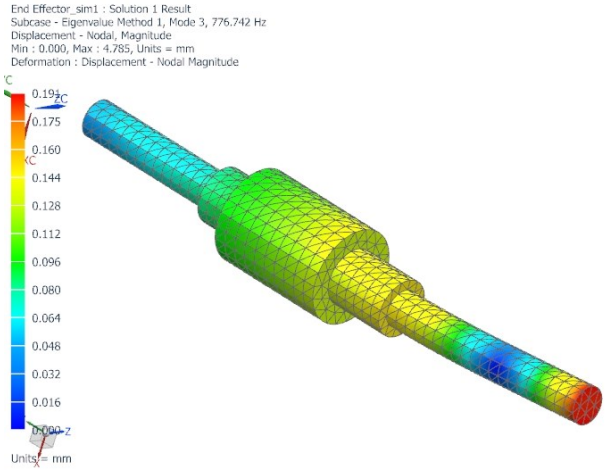

Figure C 12-47: MT Spindle Shaft Third Mode Displacement Plot

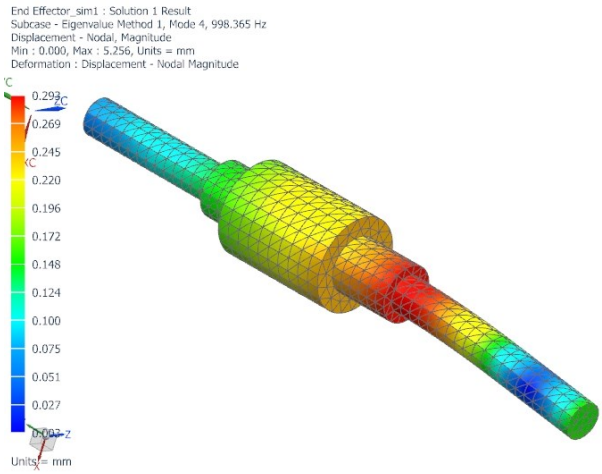

Figure C 12-48: MT Spindle Shaft Fourth Mode Displacement Plot

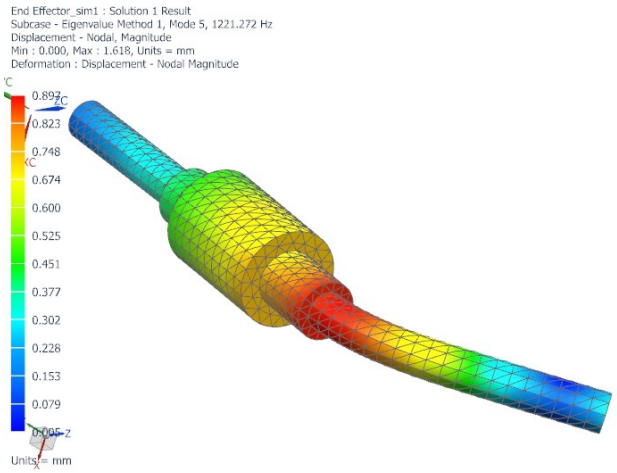

Figure C 12-49: MT Spindle Shaft Fifth Mode Displacement Plot

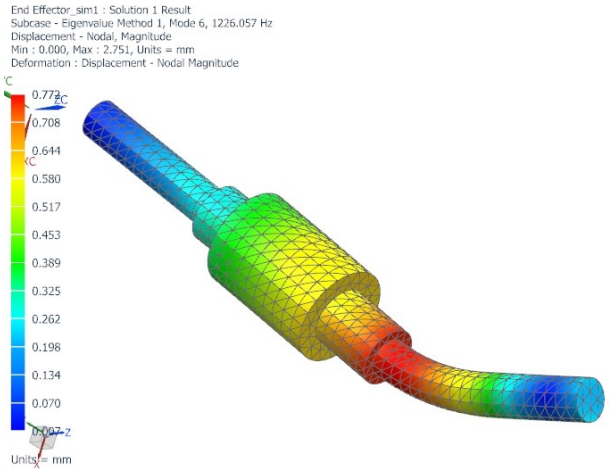

Figure C 12-50: MT Spindle Shaft Sixth Mode Displacement Plot

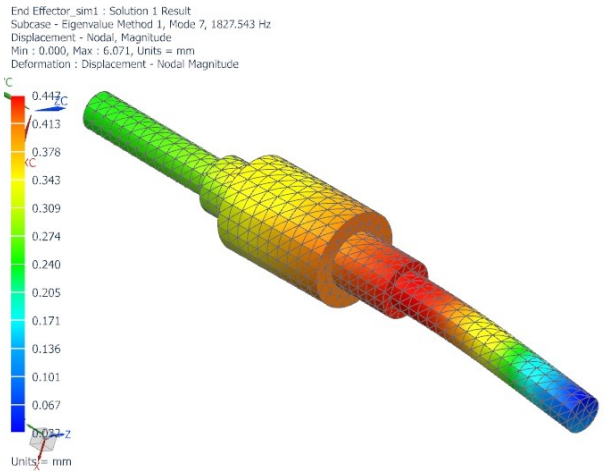

Figure C 12-51: MT Spindle Shaft Seventh Mode Displacement Plot

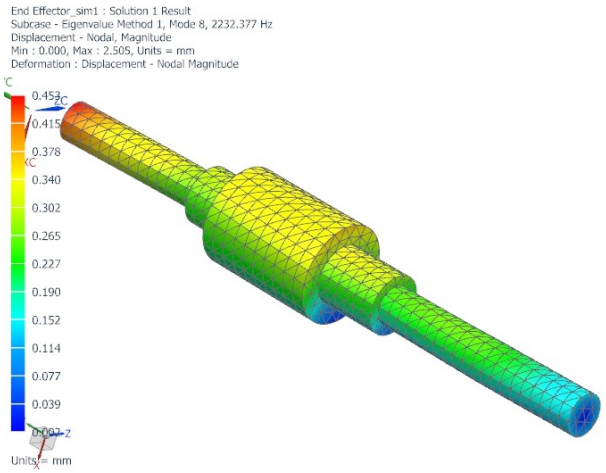

Figure C 12-52: MT Spindle Shaft Eighth Mode Displacement Plot

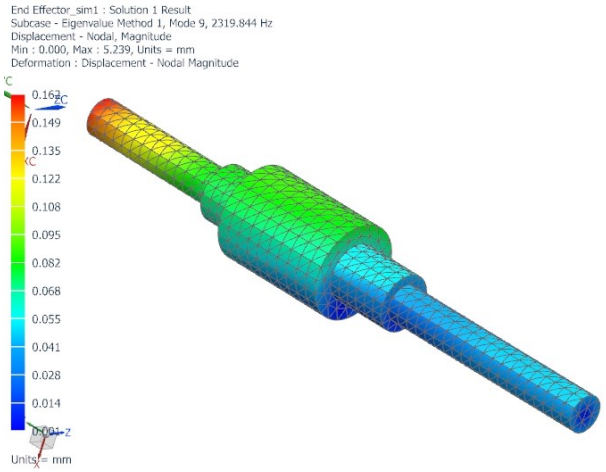

Figure C 12-53: MT Spindle Shaft Ninth Mode Displacement Plot

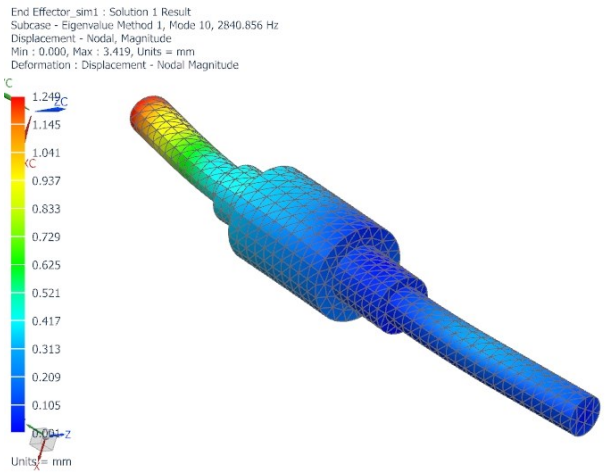

Figure C 12-54: MT Spindle Shaft Tenth Mode Displacement Plot

Appendix D Numerical Simulation Code and Results

D.1 Tangential Cutting Force Solution

Table D 12-7: Tangential Cutting Force Numerical Solution

V	D (mm)	Ktc	Kte	Theta	a (mm)	sin(theta)	c (mm/rev	h (phij)	Ftj (phij)	Tc (N.m)	Pt (Watts)
1,27	0,002	805	6	0	2	0	0,1	0	12	0,012	15,24000419
1,27	0,002	805	6	1	2	0,017452	0,1	0,001745	14,80984	0,01481	18,80849872
1,27	0,002	805	6	2	2	0,034899	0,1	0,00349	17,61882	0,017619	22,37590625
1,27	0,002	805	6	3	2	0,052336	0,1	0,005234	20,42609	0,020426	25,94114011
1,27	0,002	805	6	4	2	0,069756	0,1	0,006976	23,23079	0,023231	29,5031143
1,27	0,002	805	6	5	2	0,087156	0,1	0,008716	26,03207	0,026032	33,06074381
1,27	0,002	805	6	6	2	0,104528	0,1	0,010453	28,82908	0,028829	36,61294496
1,27	0,002	805	6	7	2	0,121869	0,1	0,012187	31,62096	0,031621	40,15863569
1,27	0,002	805	6	8	2	0,139173	0,1	0,013917	34,40687	0,034407	43,69673597
1,27	0,002	805	6	9	2	0,156434	0,1	0,015643	37,18595	0,037186	47,22616806
1,27	0,002	805	6	10	2	0,173648	0,1	0,017365	39,95736	0,039957	50,74585685
1,27	0,002	805	6	11	2	0,190809	0,1	0,019081	42,72025	0,04272	54,25473021
1,27	0,002	805	6	12	2	0,207912	0,1	0,020791	45,47378	0,045474	57,75171931
1,27	0,002	805	6	13	2	0,224951	0,1	0,022495	48,21712	0,048217	61,23575893
1,27	0,002	805	6	14	2	0,241922	0,1	0,024192	50,94943	0,050949	64,70578779
1,27	0,002	805	6	15	2	0,258819	0,1	0,025882	53,66987	0,05367	68,1607489
1,27	0,002	805	6	16	2	0,275637	0,1	0,027564	56,37761	0,056378	71,59958984
1,27	0,002	805	6	17	2	0,292372	0,1	0,029237	59,07184	0,059072	75,0212631
1,27	0,002	805	6	18	2	0,309017	0,1	0,030902	61,75174	0,061752	78,42472642
1,27	0,002	805	6	19	2	0,325568	0,1	0,032557	64,41647	0,064416	81,80894305
1,27	0,002	805	6	20	2	0,34202	0,1	0,034202	67,06524	0,067065	85,17288214
1,27	0,002	805	6	21	2	0,358368	0,1	0,035837	69,69724	0,069697	88,51551899
1,27	0,002	805	6	22	2	0,374607	0,1	0,037461	72,31166	0,072312	91,83583542
1,27	0,002	805	6	23	2	0,390731	0,1	0,039073	74,90771	0,074908	95,13282001
1,27	0,002	805	6	24	2	0,406737	0,1	0,040674	77,4846	0,077485	98,40546848
1,27	0,002	805	6	25	2	0,422618	0,1	0,042262	80,04154	0,080042	101,6527839
1,27	0,002	805	6	26	2	0,438371	0,1	0,043837	82,57775	0,082578	104,8737772
1,27	0,002	805	6	27	2	0,45399	0,1	0,045399	85,09247	0,085092	108,0674672
1,27	0,002	805	6	28	2	0,469472	0,1	0,046947	87,58492	0,087585	111,232881
1,27	0,002	805	6	29	2	0,48481	0,1	0,048481	90,05435	0,090054	114,3690545
1,27	0,002	805	6	30	2	0,5	0,1	0,05	92,5	0,0925	117,4750323
1,27	0,002	805	6	31	2	0,515038	0,1	0,051504	94,92113	0,094921	120,5498683
1,27	0,002	805	6	32	2	0,529919	0,1	0,052992	97,317	0,097317	123,592626
1,27	0,002	805	6	33	2	0,544639	0,1	0,054464	99,68688	0,099687	126,6023783
1,27	0,002	805	6	34	2	0,559193	0,1	0,055919	102,0301	0,10203	129,5782086
1,27	0,002	805	6	35	2	0,573576	0,1	0,057358	104,3458	0,104346	132,5192104
1,27	0,002	805	6	36	2	0,587785	0,1	0,058779	106,6334	0,106633	135,4244878
1,27	0,002	805	6	37	2	0,601815	0,1	0,060182	108,8922	0,108892	138,2931558
1,27	0,002	805	6	38	2	0,615661	0,1	0,061566	111,1215	0,111121	141,1243407
1,27	0,002	805	6	39	2	0,62932	0,1	0,062932	113,3206	0,113321	143,91718
1,27	0,002	805	6	40	2	0,642788	0,1	0,064279	115,4888	0,115489	146,6708229
1,27	0,002	805	6	41	2	0,656059	0,1	0,065606	117,6255	0,117626	149,3844308
1,27	0,002	805	6	42	2	0,669131	0,1	0,066913	119,73	0,11973	152,0571769
1,27	0,002	805	6	43	2	0,681998	0,1	0,0682	121,8017	0,121802	154,6882472
1,27	0,002	805	6	44	2	0,694658	0,1	0,069466	123,84	0,12384	157,2768403
1,27	0,002	805	6	45	2	0,707107	0,1	0,070711	125,8442	0,125844	159,8221675
1,27	0,002	805	6	46	2	0,71934	0,1	0,071934	127,8137	0,127814	162,3234536
1,27	0,002	805	6	47	2	0,731354	0,1	0,073135	129,7479	0,129748	164,7799367
1,27	0,002	805	6	48	2	0,743145	0,1	0,074314	131,6463	0,131646	167,1908685

1,27	0,002	805	6	49	2	0,75471	0,1	0,075471	133,5082	0,133508	169,5555145
1,27	0,002	805	6	50	2	0,766044	0,1	0,076604	135,3332	0,135333	171,8731546
1,27	0,002	805	6	51	2	0,777146	0,1	0,077715	137,1205	0,13712	174,1430826
1,27	0,002	805	6	52	2	0,788011	0,1	0,078801	138,8697	0,13887	176,3646073
1,27	0,002	805	6	53	2	0,798636	0,1	0,079864	140,5803	0,14058	178,5370519
1,27	0,002	805	6	54	2	0,809017	0,1	0,080902	142,2517	0,142252	180,6597545
1,27	0,002	805	6	55	2	0,819152	0,1	0,081915	143,8835	0,143883	182,7320688
1,27	0,002	805	6	56	2	0,829038	0,1	0,082904	145,475	0,145475	184,7533633
1,27	0,002	805	6	57	2	0,838671	0,1	0,083867	147,026	0,147026	186,7230224
1,27	0,002	805	6	58	2	0,848048	0,1	0,084805	148,5357	0,148536	188,6404461
1,27	0,002	805	6	59	2	0,857167	0,1	0,085717	150,0039	0,150004	190,5050504
1,27	0,002	805	6	60	2	0,866025	0,1	0,086603	151,4301	0,15143	192,3162672
1,27	0,002	805	6	61	2	0,87462	0,1	0,087462	152,8138	0,152814	194,0735449
1,27	0,002	805	6	62	2	0,882948	0,1	0,088295	154,1546	0,154155	195,7763482
1,27	0,002	805	6	63	2	0,891007	0,1	0,089101	155,4521	0,155452	197,4241583
1,27	0,002	805	6	64	2	0,898794	0,1	0,089879	156,7058	0,156706	199,0164734
1,27	0,002	805	6	65	2	0,906308	0,1	0,090631	157,9156	0,157916	200,5528084
1,27	0,002	805	6	66	2	0,913545	0,1	0,091355	159,0808	0,159081	202,0326953
1,27	0,002	805	6	67	2	0,920505	0,1	0,09205	160,2013	0,160201	203,4556834
1,27	0,002	805	6	68	2	0,927184	0,1	0,092718	161,2766	0,161277	204,8213391
1,27	0,002	805	6	69	2	0,93358	0,1	0,093358	162,3064	0,162306	206,1292465
1,27	0,002	805	6	70	2	0,939693	0,1	0,093969	163,2905	0,163291	207,3790072
1,27	0,002	805	6	71	2	0,945519	0,1	0,094552	164,2285	0,164228	208,5702405
1,27	0,002	805	6	72	2	0,951057	0,1	0,095106	165,1201	0,16512	209,7025836
1,27	0,002	805	6	73	2	0,956305	0,1	0,09563	165,9651	0,165965	210,7756914
1,27	0,002	805	6	74	2	0,961262	0,1	0,096126	166,7631	0,166763	211,7892372
1,27	0,002	805	6	75	2	0,965926	0,1	0,096593	167,5141	0,167514	212,7429122
1,27	0,002	805	6	76	2	0,970296	0,1	0,09703	168,2176	0,168218	213,6364259
1,27	0,002	805	6	77	2	0,97437	0,1	0,097437	168,8736	0,168874	214,4695061
1,27	0,002	805	6	78	2	0,978148	0,1	0,097815	169,4818	0,169482	215,2418991
1,27	0,002	805	6	79	2	0,981627	0,1	0,098163	170,042	0,170042	215,9533696
1,27	0,002	805	6	80	2	0,984808	0,1	0,098481	170,554	0,170554	216,6037008
1,27	0,002	805	6	81	2	0,987688	0,1	0,098769	171,0178	0,171018	217,1926948
1,27	0,002	805	6	82	2	0,990268	0,1	0,099027	171,4332	0,171433	217,7201719
1,27	0,002	805	6	83	2	0,992546	0,1	0,099255	171,7999	0,1718	218,1859717
1,27	0,002	805	6	84	2	0,994522	0,1	0,099452	172,118	0,172118	218,5899521
1,27	0,002	805	6	85	2	0,996195	0,1	0,099619	172,3873	0,172387	218,9319901
1,27	0,002	805	6	86	2	0,997564	0,1	0,099756	172,6078	0,172608	219,2119817
1,27	0,002	805	6	87	2	0,99863	0,1	0,099863	172,7794	0,172779	219,4298413
1,27	0,002	805	6	88	2	0,999391	0,1	0,099939	172,9019	0,172902	219,5855028
1,27	0,002	805	6	89	2	0,999848	0,1	0,099985	172,9755	0,172975	219,6789187
1,27	0,002	805	6	90	2	1	0,1	0,1	173	0,173	219,7100604
1,27	0,002	805	6	91	2	0,999848	0,1	0,099985	172,9755	0,172975	219,6789187
1,27	0,002	805	6	92	2	0,999391	0,1	0,099939	172,9019	0,172902	219,5855028
1,27	0,002	805	6	93	2	0,99863	0,1	0,099863	172,7794	0,172779	219,4298413
1,27	0,002	805	6	94	2	0,997564	0,1	0,099756	172,6078	0,172608	219,2119817
1,27	0,002	805	6	95	2	0,996195	0,1	0,099619	172,3873	0,172387	218,9319901
1,27	0,002	805	6	96	2	0,994522	0,1	0,099452	172,118	0,172118	218,5899521
1,27	0,002	805	6	97	2	0,992546	0,1	0,099255	171,7999	0,1718	218,1859717
1,27	0,002	805	6	98	2	0,990268	0,1	0,099027	171,4332	0,171433	217,7201719

1,27	0,002	805	6	99	2	0,987688	0,1	0,098769	171,0178	0,171018	217,1926948
1,27	0,002	805	6	100	2	0,984808	0,1	0,098481	170,554	0,170554	216,6037008
1,27	0,002	805	6	101	2	0,981627	0,1	0,098163	170,042	0,170042	215,9533696
1,27	0,002	805	6	102	2	0,978148	0,1	0,097815	169,4818	0,169482	215,2418991
1,27	0,002	805	6	103	2	0,97437	0,1	0,097437	168,8736	0,168874	214,4695061
1,27	0,002	805	6	104	2	0,970296	0,1	0,09703	168,2176	0,168218	213,6364259
1,27	0,002	805	6	105	2	0,965926	0,1	0,096593	167,5141	0,167514	212,7429122
1,27	0,002	805	6	106	2	0,961262	0,1	0,096126	166,7631	0,166763	211,7892372
1,27	0,002	805	6	107	2	0,956305	0,1	0,09563	165,9651	0,165965	210,7756914
1,27	0,002	805	6	108	2	0,951057	0,1	0,095106	165,1201	0,16512	209,7025836
1,27	0,002	805	6	109	2	0,945519	0,1	0,094552	164,2285	0,164228	208,5702405
1,27	0,002	805	6	110	2	0,939693	0,1	0,093969	163,2905	0,163291	207,3790072
1,27	0,002	805	6	111	2	0,93358	0,1	0,093358	162,3064	0,162306	206,1292465
1,27	0,002	805	6	112	2	0,927184	0,1	0,092718	161,2766	0,161277	204,8213391
1,27	0,002	805	6	113	2	0,920505	0,1	0,09205	160,2013	0,160201	203,4556834
1,27	0,002	805	6	114	2	0,913545	0,1	0,091355	159,0808	0,159081	202,0326953
1,27	0,002	805	6	115	2	0,906308	0,1	0,090631	157,9156	0,157916	200,5528084
1,27	0,002	805	6	116	2	0,898794	0,1	0,089879	156,7058	0,156706	199,0164734
1,27	0,002	805	6	117	2	0,891007	0,1	0,089101	155,4521	0,155452	197,4241583
1,27	0,002	805	6	118	2	0,882948	0,1	0,088295	154,1546	0,154155	195,7763482
1,27	0,002	805	6	119	2	0,87462	0,1	0,087462	152,8138	0,152814	194,0735449
1,27	0,002	805	6	120	2	0,866025	0,1	0,086603	151,4301	0,15143	192,3162672
1,27	0,002	805	6	121	2	0,857167	0,1	0,085717	150,0039	0,150004	190,5050504
1,27	0,002	805	6	122	2	0,848048	0,1	0,084805	148,5357	0,148536	188,6404461
1,27	0,002	805	6	123	2	0,838671	0,1	0,083867	147,026	0,147026	186,7230224
1,27	0,002	805	6	124	2	0,829038	0,1	0,082904	145,475	0,145475	184,7533633
1,27	0,002	805	6	125	2	0,819152	0,1	0,081915	143,8835	0,143883	182,7320688
1,27	0,002	805	6	126	2	0,809017	0,1	0,080902	142,2517	0,142252	180,6597545
1,27	0,002	805	6	127	2	0,798636	0,1	0,079864	140,5803	0,14058	178,5370519
1,27	0,002	805	6	128	2	0,788011	0,1	0,078801	138,8697	0,13887	176,3646073
1,27	0,002	805	6	129	2	0,777146	0,1	0,077715	137,1205	0,13712	174,1430826
1,27	0,002	805	6	130	2	0,766044	0,1	0,076604	135,3332	0,135333	171,8731546
1,27	0,002	805	6	131	2	0,75471	0,1	0,075471	133,5082	0,133508	169,5555145
1,27	0,002	805	6	132	2	0,743145	0,1	0,074314	131,6463	0,131646	167,1908685
1,27	0,002	805	6	133	2	0,731354	0,1	0,073135	129,7479	0,129748	164,7799367
1,27	0,002	805	6	134	2	0,71934	0,1	0,071934	127,8137	0,127814	162,3234536
1,27	0,002	805	6	135	2	0,707107	0,1	0,070711	125,8442	0,125844	159,8221675
1,27	0,002	805	6	136	2	0,694658	0,1	0,069466	123,84	0,12384	157,2768403
1,27	0,002	805	6	137	2	0,681998	0,1	0,0682	121,8017	0,121802	154,6882472
1,27	0,002	805	6	138	2	0,669131	0,1	0,066913	119,73	0,11973	152,0571769
1,27	0,002	805	6	139	2	0,656059	0,1	0,065606	117,6255	0,117626	149,3844308
1,27	0,002	805	6	140	2	0,642788	0,1	0,064279	115,4888	0,115489	146,6708229
1,27	0,002	805	6	141	2	0,62932	0,1	0,062932	113,3206	0,113321	143,91718
1,27	0,002	805	6	142	2	0,615661	0,1	0,061566	111,1215	0,111121	141,1243407
1,27	0,002	805	6	143	2	0,601815	0,1	0,060182	108,8922	0,108892	138,2931558
1,27	0,002	805	6	144	2	0,587785	0,1	0,058779	106,6334	0,106633	135,4244878
1,27	0,002	805	6	145	2	0,573576	0,1	0,057358	104,3458	0,104346	132,5192104
1,27	0,002	805	6	146	2	0,559193	0,1	0,055919	102,0301	0,10203	129,5782086
1,27	0,002	805	6	147	2	0,544639	0,1	0,054464	99,68688	0,099687	126,6023783
1,27	0,002	805	6	148	2	0,529919	0,1	0,052992	97,317	0,097317	123,592626

1,27	0,002	805	6	149	2	0,515038	0,1	0,051504	94,92113	0,094921	120,5498683
1,27	0,002	805	6	150	2	0,5	0,1	0,05	92,5	0,0925	117,4750323
1,27	0,002	805	6	151	2	0,48481	0,1	0,048481	90,05435	0,090054	114,3690545
1,27	0,002	805	6	152	2	0,469472	0,1	0,046947	87,58492	0,087585	111,232881
1,27	0,002	805	6	153	2	0,45399	0,1	0,045399	85,09247	0,085092	108,0674672
1,27	0,002	805	6	154	2	0,438371	0,1	0,043837	82,57775	0,082578	104,8737772
1,27	0,002	805	6	155	2	0,422618	0,1	0,042262	80,04154	0,080042	101,6527839
1,27	0,002	805	6	156	2	0,406737	0,1	0,040674	77,4846	0,077485	98,40546848
1,27	0,002	805	6	157	2	0,390731	0,1	0,039073	74,90771	0,074908	95,13282001
1,27	0,002	805	6	158	2	0,374607	0,1	0,037461	72,31166	0,072312	91,83583542
1,27	0,002	805	6	159	2	0,358368	0,1	0,035837	69,69724	0,069697	88,51551899
1,27	0,002	805	6	160	2	0,34202	0,1	0,034202	67,06524	0,067065	85,17288214
1,27	0,002	805	6	161	2	0,325568	0,1	0,032557	64,41647	0,064416	81,80894305
1,27	0,002	805	6	162	2	0,309017	0,1	0,030902	61,75174	0,061752	78,42472642
1,27	0,002	805	6	163	2	0,292372	0,1	0,029237	59,07184	0,059072	75,0212631
1,27	0,002	805	6	164	2	0,275637	0,1	0,027564	56,37761	0,056378	71,59958984
1,27	0,002	805	6	165	2	0,258819	0,1	0,025882	53,66987	0,05367	68,1607489
1,27	0,002	805	6	166	2	0,241922	0,1	0,024192	50,94943	0,050949	64,70578779
1,27	0,002	805	6	167	2	0,224951	0,1	0,022495	48,21712	0,048217	61,23575893
1,27	0,002	805	6	168	2	0,207912	0,1	0,020791	45,47378	0,045474	57,75171931
1,27	0,002	805	6	169	2	0,190809	0,1	0,019081	42,72025	0,04272	54,25473021
1,27	0,002	805	6	170	2	0,173648	0,1	0,017365	39,95736	0,039957	50,74585685
1,27	0,002	805	6	171	2	0,156434	0,1	0,015643	37,18595	0,037186	47,22616806
1,27	0,002	805	6	172	2	0,139173	0,1	0,013917	34,40687	0,034407	43,69673597
1,27	0,002	805	6	173	2	0,121869	0,1	0,012187	31,62096	0,031621	40,15863569
1,27	0,002	805	6	174	2	0,104528	0,1	0,010453	28,82908	0,028829	36,61294496
1,27	0,002	805	6	175	2	0,087156	0,1	0,008716	26,03207	0,026032	33,06074381
1,27	0,002	805	6	176	2	0,069756	0,1	0,006976	23,23079	0,023231	29,5031143
1,27	0,002	805	6	177	2	0,052336	0,1	0,005234	20,42609	0,020426	25,94114011
1,27	0,002	805	6	178	2	0,034899	0,1	0,00349	17,61882	0,017619	22,37590625
1,27	0,002	805	6	179	2	0,017452	0,1	0,001745	14,80984	0,01481	18,80849872
1,27	0,002	805	6	180	2	1,23E-16	0,1	1,23E-17	12	0,012	15,24000419
									V	1,27	
									Max F	173	
									Tmaxc	0,173	
									Pmaxt	219,7101	

D.2 MATLAB Code: X Component of Cutting Force

```
%initialise constants

ktc=805;

krc=418;

kac=227;

kte=6;

kre=6;

kae=1;

phist=85;

phiex=100;

N=2;

beta=30;

a=2;
```

```
c=0.1;
d=2;
i=0; %incremental degree step
j=0; %incremental tooth step
%define function
syms x
kappa=2*tan(beta)/d;
phijx=phi+j*pi-kappa*x;
hjofphi=c*sin(phijx);
dfxjphijx=-(ktc*hjofphi+kte)*cos(phijx)-(krc*hjofphi+kre)*sin(phijx);
for phi = phist+i
int(dfxjphijx,0,a)
double(ans)
end
```

D.3 MATLAB Code: Y Component of Cutting Force

```
%initialise constants
ktc=805;
krc=418;
kac=227;
kte=6;
kre=6;
kae=1;
phist=85;
phiex=100;
N=2;
beta=30;
a=2;
c=0.1;
d=2;
i=0; %incremental degree step
j=0; %incremental tooth step
%define function
```

```
syms x
kappa=2*tan(beta)/d;
phijx=phi+j*pi-kappa*x;
hjofphi=c*sin(phijx);
dfxjphijx=(ktc*hjofphi+kte)*sin(phijx)-(krc*hjofphi+kre)*cos(phijx);
for phi = phist+i
int(dfxjphijx,0,a)
double(ans)
end
```

D.4 MATLAB Code: Z Component of Cutting Force

```
%initialise constants
ktc=805;
krc=418;
kac=227;
kte=6;
kre=6;
kae=1;
phist=85;
phiex=100;
N=2;
beta=30;
a=2;
c=0.1;
d=2;
i=0; %incremental degree step
j=0; %incremental tooth step
%define function
syms x
kappa=2*tan(beta)/d;
phijx=phi+j*pi-kappa*x;
hjofphi=c*sin(phijx);
dfaphix=kac*hjofphi+kae;
```

```
for phi = phist+i
int(dfaphix,0,a)
double(ans)
end
```

D.5 Numerical Result of x, y and z Cutting Force Components

Table D 12-8: Numerical Result of x, y and z Cutting Force Components

	i	j=0	j=1	Fx	j=0	j=1	Fy	j=0	j=1	Fz
0	85	-41.7185	-42.2893	-84.0078	78.9505	78.6488	157.5993	1.7455	2.2545	4
1	86	-42.9801	-43.5424	-86.5225	81.2344	81.5517	162.7861	1.1681	2.8319	4
2	87	-40.3615	-40.3983	-80.7598	81.1348	81.7794	162.9142	1.3555	2.6445	4
3	88	-41.7819	-41.2594	-83.0413	78.6208	79	157.6208	2.1355	1.8645	4
4	89	-43.7533	-43.1519	-86.9052	81.0665	80.8318	161.8983	2.7909	1.2091	4
5	90	-40.7676	-40.6402	-81.4078	82.1323	81.4993	163.6316	2.7192	1.2808	4
6	91	-40.8278	-41.2916	-82.1194	79.1803	78.7311	157.9114	1.9862	2.0138	4
7	92	-43.198	-43.8265	-87.0245	80.3957	80.5433	160.939	1.266	2.734	4
8	93	-41.0074	-41.2229	-82.2303	81.7654	82.374	164.1394	1.2206	2.7794	4
9	94	-40.8556	-40.4598	-81.3154	78.969	79.4791	158.4481	1.8918	2.1082	4
10	95	-43.7571	-43.114	-86.8711	80.021	79.9636	159.9846	2.6625	1.3375	4
11	96	-41.7306	-41.4314	-83.162	82.4846	81.9124	164.397	2.8241	1.1759	4
12	97	-40.1868	-40.5066	-80.6934	79.8745	79.3136	159.1881	2.228	1.772	4
13	98	-42.9062	-43.5509	-86.4571	79.5725	79.5385	159.111	1.4233	2.5777	4.001
14	99	-41.8759	-42.2528	-84.1287	81.9299	82.4541	164.384	1.1477	2.8523	4
15	100	-40.2702	-40.0327	-80.3029	79.736	80.3364	160.0724	1.6567	2.3433	4

D.6 Gripper Finger Workspace – 3R Approximation MATLAB Code

```
l1 = 5.8;
l2 = 4.8;
l3 = 5.45;
theta1 = 0:0.01:1.5708;
theta2 = 0:0.01:0.785398;
theta3 = 0:0.01:0.802851;
[THETA1,THETA2,THETA3] = meshgrid(theta1,theta2,theta3); % generate a grid of theta1 and theta2 values
X = l1 * cos(THETA1) + l2 * cos(THETA1 + THETA2) + l3*cos(THETA1 + THETA2 + THETA3);
Y = l1 * sin(THETA1) + l2 * sin(THETA1 + THETA2) + l3*sin(THETA1 + THETA2 + THETA3);
data1 = [X(:) Y(:) THETA1(:)];
data2 = [X(:) Y(:) THETA2(:)];
```

```
plot(X(:),Y(:),'r.');
axis equal;
xlabel('X (cm)','fontsize',20)
ylabel('Y (cm)','fontsize',20)
title('X-Y coordinates for 3 link finger','fontsize',20)
```

Appendix E Experimental Results

E.1 Vibration Response: Rotating Spindle

Table E 12-9: Vibration Response Rotating Spindle

Speed (RPM)	Finger	GRMS	GMAX	GMIN	Frequency (Hz)	Amplitude (g/N)	Phase (Degree)
2556	1	1,20704	3,72198	-3,31654	574,982	0,89793	115,467
	2	1,54494	4,71504	-4,395	574,916	1,26074	3,01537
	3	1,3938	4,09424	-3,59287	442,413	1,30548	-64,2336
3733	1	1,76377	4,67761	-4,18671	78,3921	2,00948	-164,187
	2	3,01642	7,687	-7,14884	627,019	3,82574	64,6919
	3	0,987213	3,10933	-3,04275	626,978	0,860951	-2,09486
4132	1	3,39718	8,77312	-8,79391	86,8608	4,28378	-26,7553
	2	3,11406	6,02727	-7,33117	86,8079	3,46848	-34,3878
	3	1,26141	4,48047	-3,2507	173,55	1,19185	157,528
4853	1	2,97587	9,10513	-6,5388	100,305	2,57838	208,155
	2	3,42582	8,07362	-7,9029	100,281	4,23842	201,961
	3	1,10576	3,15857	-3,08712	100,301	1,15401	15,1756
5526	1	4,11621	10,8102	-9,78309	116,08	4,73367	-202,631
	2	4,56913	11,8432	-11,1673	116,08	5,27409	-32,2285
	3	1,69073	4,75833	-6,03444	464,47	1,24323	51,2543
6490	1	2,82483	8,91985	-7,59136	134,718	3,11666	13,5075
	2	2,75032	7,44216	-8,1987	134,723	2,76314	180,731
	3	1,41548	4,18322	-4,66096	107,699	1,16257	-36,6924
7308	1	2,9195	8,01118	-7,13366	155,129	2,42508	159,444
	2	3,01649	10,0603	-9,1744	124,087	2,81513	2,63013
	3	1,36527	4,11368	-5,00603	186,242	0,702753	84,8157
8079	1	2,88833	9,39322	-9,64371	135,666	1,82065	17,7923
	2	3,38515	10,3199	9,88571	169,616	2,21389	124,588
	3	1,77224	5,05484	-5,6202	339,188	1,41339	166,068
8890	1	6,10304	16,987	-14,4592	558,003	5,31539	-60,3879
	2	7,24755	15,8883	-16,034	186,006	9,01017	188,312
	3	3,61796	8,04486	-8,52519	186,019	4,26891	-8,61478
9663	1	5,15839	16,397	-13,5086	488,988	4,66289	96,9297
	2	7,14471	20,9112	-17,5193	488,923	5,37896	-66,534
	3	3,18126	11,4433	-7,7773	203,733	3,38508	-104,874
10318	1	5,9218	18,8157	-16,1443	514,545	4,37777	4,87862

	2	7,74518	21,3836	-20,6936	171,631	7,61645	-130,794
	3	3,52009	10,4863	-10,1945	171,637	3,04935	17,6112
11559	1	9,22372	23,0938	-23,8452	189,579	7,41344	-169,775
	2	10,4359	28,6649	-22,3907	189,579	11,83342	-169,258
	3	5,40763	16,8976	-12,8177	189,586	5,77234	6,87602
12455	1	3,8165	12,9404	-10,597	263,879	2,23213	-166,787
	2	4,87411	15,8149	-12,182	263,877	4,84383	-216,835
	3	2,58521	8,15889	-8,35235	263,963	2,12752	-92,4822
13741	1	3,52152	11,0549	-10,6728	583,406	2,66059	49,3299
	2	8,19637	18,818	-19,551	291,738	9,79262	-13,8488
	3	1,98292	5,45458	-6,12533	291,681	1,83905	70,868
14722	1	6,13762	15,0304	-15,7005	308,639	7,14257	110,33
	2	12,9759	32,1287	-22,8672	308,687	16,9982	-144,857
	3	3,63352	7,84289	-12,9498	308,616	3,13727	105,09

Configuration of NI SignalExpress for Gripper Vibration Response

Mount the accelerometer to the middle of the end phalange of each gripper finger, directed to the y-axis reference.

5. Connect the accelerometer to the DAQ module using the IEPE lead.
6. Turn on the DAQ and connect it via USB to the computer.
7. Open SignalExpress software and configure the accelerometer.
8. Calibrate accelerometer with calibrator.
9. Select frequency spectrum analysis and use Hanning window with force 50.0% and exponent 10.0%.
10. Select frequency response testing and magnitude and phase response and use Hanning window with force 50.0% and exponent 10.0%.

E.2 Vibration Response: Linear Cut

Table E 12-10: Vibration Response Linear Cut

Speed (RPM)	Finger	G_{RMS}	G_{MAX}	G_{MIN}	Frequency (Hz)	Amplitude (g/N)	Phase (Degrees)
8133	1	7,89731	21,8873	-19,7561	471,069	10,1898	133,17
	2	10,1027	32,5835	-25,8474	470,902	13,2264	95,9288
	3	5,61553	17,0386	-15,9051	470,988	6,5334	147,623
9057	1	12,1609	27,2795	-29,654	484,652	16,5765	165,578
	2	14,9742	37,4504	-36,8621	484,399	19,3498	151,24
	3	8,09723	19,614	-23,9875	484,689	9,81102	191,82
10766	1	6,84704	20,8351	-24,324	446,841	4,66332	102,521
	2	9,1423	31,5244	-26,6472	178,797	9,53022	-77,7319
	3	5,73447	17,4907	-14,4489	178,796	5,36719	114,122
12530	1	6,52742	23,4487	-25,3175	485,136	3,99773	142,62
	2	7,02278	30,9159	-28,9506	485,069	4,89264	131,873
	3	4,87898	17,8757	-17,5064	485,116	3,44551	143,909

E.3 Vibration Response: Linear Actuator

Table E 12-11: Vibration Response Reconfiguration Mechanism

Speed	Finger	G_{RMS}	G_{MAX}	G_{MIN}	Frequency (Hz)	Amplitude (g/N)	Phase (Degrees)
1,77 mm/s	1	4,2233	10,4674	-15,1044	15,7695	4,2514	-179,664
	2	3,60776	11,7215	-9,18502	988,255	2,74031	151,76
	3	3,92028	9,18799	-9,88232	247,065	4,25627	-16,1268
3,73 mm/s	1	4,99772	10,7062	-11,4978	495,585	6,59667	-76,2853
	2	4,32651	9,86299	-9,08567	495,647	5,69896	-37,3591
	3	3,89446	10,9354	-9,35065	495,675	4,729	-56,5263
5,57 mm/s	1	4,51179	11,9088	-11,2931	495,686	5,75997	218,833
	2	3,90325	10,3948	-10,1072	495,576	4,73472	-82,5072
	3	3,39624	10,3596	-8,37536	495,592	3,95743	-105,115

E.4 Stability Lobe Diagram A

*Refer to attached CD for the complete simulation data

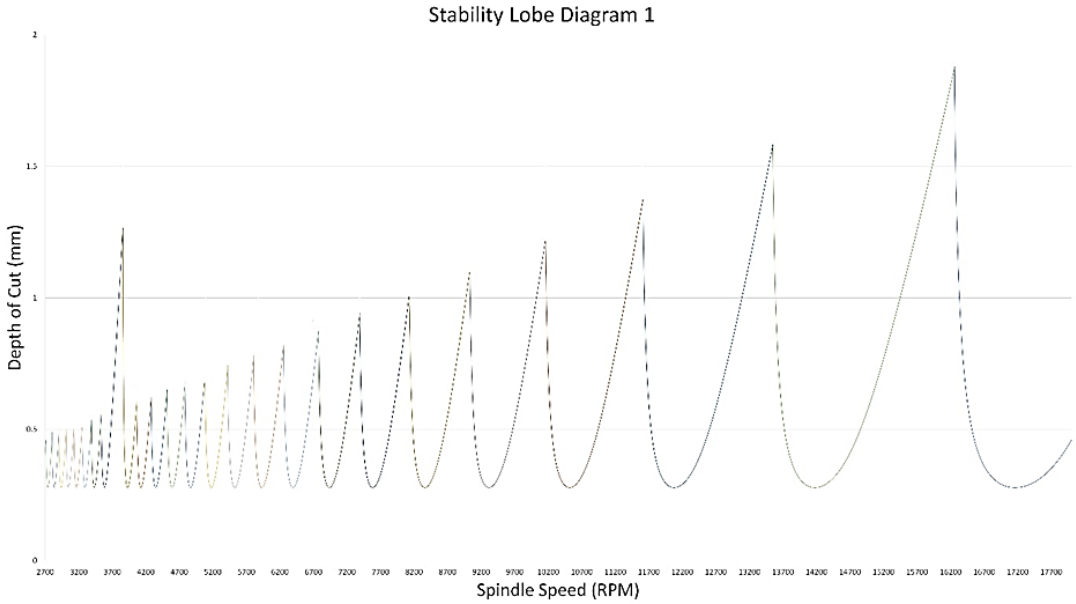

Figure E 12-55: SLD Plot Case A

j	fj	rj	bj	Nj	0	1	2	3	4	5	6	7	8	9	10	11	12	13	14	15	16	17	18	19	20	21	22	23	24	25	26	27	28	29	30
1	2695.4	1.000371	3.2413537	81973.11	40706.88	27076.34	20284.24	16216.36																		3677.811									2609.593
2	2696.4	1.000742	1.6303904	83141.41	41000.64	27209.39	20360.72	16266.42	13543.07	11600.84	10145.81													3856.969	3681.436									2611.699
3	2697.4	1.001113	1.0973223	84333.64	41296.3	27342.71	20437.19	16316.41	13578.55	11627.48	10166.66	9081.931	8125.069	7383.7										3860.866	3685.049									2613.798
4	2698.4	1.001485	0.8337297	85346.31	41592.88	27475.87	20513.42	16366.19	13613.86	11653.98	10187.39	9048.663	8138.91	7395.379	6776.327	6252.909	5804.553	5416.192						3864.741	3688.641									2615.887
5	2699.4	1.001856	0.6779286	86775.76	41889.41	27608.44	20589.17	16415.6	13648.88	11680.27	10207.94	9065.251	8152.633	7406.958	6786.258	6261.543	5812.147	5422.938	5082.584	4782.43	4515.75	4277.241	4062.663	3868.585	3692.205									2617.961
6	2700.4	1.002227	0.5760243	88018.21	42184.95	27740.03	20664.22	16464.51	13683.53	11706.26	10228.27	9081.655	8166.203	7418.409	6796.08	6270.084	5819.66	5429.613	5088.565	4787.83	4520.658	4281.728	4066.786	3872.392	3695.735	3534.493	3386.733				2901.534			2620.018
7	2701.4	1.002598	0.5049192	89263.9	42478.6	27870.26	20738.36	16512.79	13717.72	11731.9	10248.32	9097.837	8179.59	7429.708	6805.773	6278.514	5827.077	5436.203	5094.472	4793.164	4525.506	4286.161	4070.86	3876.155	3699.225	3537.742	3389.768	3253.675	3128.089	3011.837	2903.916	2803.462		2622.054
8	2702.4	1.002969	0.4530643	90527.07	42769.53	27998.77	20811.41	16560.33	13751.38	11757.14	10268.06	9113.765	8192.769	7440.832	6815.319	6286.817	5834.384	5442.697	5100.294	4798.422	4530.287	4290.533	4074.88	3879.868	3702.669	3540.949	3392.765	3256.485	3130.73	3014.327	2906.269	2805.691	2711.841	2624.067
9	2703.4	1.00334	0.4140437	91786.12	43056.97	28125.28	20883.21	16607.02	13784.42	11781.92	10287.44	9129.409	8205.716	7451.764	6824.701	6294.981	5841.569	5449.086	5105.022	4803.597	4534.994	4294.838	4078.839	3883.526	3706.063	3544.111	3395.72	3259.255	3133.336	3016.784	2908.592	2807.891	2713.93	2626.054
10	2704.4	1.003711	0.3840077	93043.58	43340.24	28249.52	20953.63	16652.78	13816.81	11806.21	10306.43	9144.747	8218.413	7462.487	6833.907	6302.994	5848.625	5455.36	5111.65	4808.683	4539.62	4299.072	4082.734	3887.126	3708.404	3547.223	3398.029	3261.984	3135.902	3019.205	2910.881	2810.06	2715.99	2628.014
11	2705.4	1.004083	0.3605065	94296.21	43618.76	28371.25	21022.54	16697.55	13848.49	11829.97	10325.02	9159.759	8230.845	7472.99	6842.927	6310.847	5855.543	5461.514	5117.172	4813.675	4544.163	4303.231	4086.56	3890.663	3712.688	3550.283	3401.491	3264.669	3138.429	3021.588	2913.134	2812.197	2718.019	2629.946
12	2706.4	1.004454	0.3419071	95541.03	43892.01	28490.29	21089.86	16741.26	13879.42	11853.17	10343.18	9174.431	8242.999	7483.263	6851.754	6318.536	5862.317	5467.544	5122.584	4818.57	4548.619	4307.311	4090.316	3894.136	3715.913	3553.289	3404.303	3267.308	3140.912	3023.932	2915.352	2814.299	2720.017	2631.847
13	2707.4	1.004825	0.3270787	96775.32	44159.57	28606.51	21155.51	16783.89	13909.58	11875.8	10360.89	9188.753	8254.869	7493.299	6860.381	6326.054	5868.945	5473.445	5127.883	4823.364	4552.985	4311.31	4093.999	3897.543	3719.078	3556.241	3407.065	3269.901	3143.353	3026.236	2917.532	2816.367	2721.982	2633.719
14	2708.4	1.005196	0.3152137	97996.63	44421.11	28719.78	21219.44	16825.39	13938.96	11897.85	10378.16	9202.718	8266.448	7503.095	6868.806	6333.399	5875.424	5479.215	5133.068	4828.057	4557.361	4315.228	4097.608	3900.883	3722.182	3559.137	3409.776	3272.446	3145.75	3028.499	2919.674	2818.399	2723.914	2635.559
15	2709.4	1.005567	0.3057199	99202.83	44676.36	28830.03	21281.62	16865.75	13967.54	11919.32	10394.98	9216.324	8277.736	7512.65	6877.027	6340.57	5881.752	5484.855	5138.137	4832.648	4561.445	4319.065	4101.143	3904.156	3725.225	3561.977	3412.435	3274.945	3148.104	3030.722	2921.779	2820.397	2725.814	2637.369
16	2710.4	1.005938	0.2981531	100392.1	44925.13	28937.23	21342.04	16904.98	13995.31	11940.19	10411.34	9229.57	8288.732	7521.963	6885.045	6347.568	5887.931	5490.365	5143.092	4837.137	4565.539	4322.82	4104.605	3907.363	3728.208	3564.761	3415.044	3277.395	3150.414	3032.904	2923.846	2822.359	2727.68	2639.148
17	2711.4	1.006309	0.2921735	101562.7	45167.31	29041.34	21400.7	16943.06	14022.3	11960.47	10427.25	9242.46	8299.438	7531.036	6892.862	6354.395	5893.962	5495.745	5147.993	4841.525	4569.543	4326.494	4107.994	3910.503	3731.13	3567.46	3417.601	3279.8	3152.68	3035.047	2925.876	2824.286	2729.515	2640.897
18	2712.4	1.006681	0.2875172	102713.5	45402.84	29142.37	21457.6	16980.01	14048.49	11980.17	10442.72	9254.997	8309.86	7539.874	6900.48	6361.052	5899.847	5500.999	5152.663	4845.815	4573.459	4330.089	4111.312	3913.579	3733.993	3570.165	3420.109	3282.158	3154.905	3037.15	2927.869	2826.18	2731.317	2642.615
19	2713.4	1.007052	0.2839753	103843.4	45631.68	29240.36	21512.77	17015.85	14073.91	11999.31	10457.75	9267.19	8320.002	7548.481	6907.904	6367.544	5905.589	5506.128	5157.283	4850.007	4577.288	4333.607	4114.559	3916.591	3736.798	3572.787	3422.569	3284.472	3157.087	3039.215	2929.827	2828.04	2733.088	2644.305
20	2714.4	1.007423	0.2813812	104951.4	45853.89	29335.33	21566.24	17050.6	14098.58	12017.88	10472.35	9279.046	8329.871	7556.862	6915.139	6373.875	5911.192	5511.136	5161.797	4854.106	4581.033	4337.049	4117.739	3919.541	3739.547	3575.358	3424.981	3286.742	3159.23	3041.242	2931.75	2829.868	2734.829	2645.966
21	2715.4	1.007794	0.2795997	106037.1	46069.52	29427.35	21618.05	17084.29	14122.5	12035.92	10486.54	9290.575	8339.475	7565.024	6922.19	6380.049	5916.66	5516.026	5166.207	4858.112	4584.697	4340.417	4120.852	3922.431	3742.241	3577.879	3427.347	3288.97	3161.333	3043.233	2933.639	2831.664	2736.541	2647.6
22	2716.4	1.008165	0.2785203	107099.8	46278.67	29516.49	21668.23	17116.94	14145.71	12053.43	10500.33	9301.787	8348.822	7572.974	6929.063	6386.071	5921.997	5520.872	5170.518	4862.031	4588.282	4343.715	4123.902	3925.264	3744.882	3580.351	3429.668	3291.157	3163.399	3045.189	2935.496	2833.43	2738.724	2649.207
23	2717.4	1.008536	0.2780518	108139.4	46481.47	29602.81	21716.84	17148.59	14168.23	12070.43	10513.73	9312.692	8357.922	7580.72	6935.764	6391.947	5927.209	5525.469	5174.732	4865.864	4591.79	4346.945	4126.89	3928.04	3747.473	3582.777	3431.947	3293.305	3165.428	3047.112	2937.321	2835.167	2739.88	2650.789
24	2718.4	1.008907	0.2781179	109155.7	46678.06	29686.4	21763.94	17179.27	14190.07	12086.94	10526.76	9323.301	8366.782	7588.268	6942.3	6397.682	5932.299	5530.03	5178.853	4869.614	4595.225	4350.109	4129.818	3930.763	3750.014	3585.158	3434.185	3295.414	3167.423	3049.002	2939.116	2836.876	2741.509	2652.346
25	2719.4	1.009279	0.2786549	110148.7	46868.6	29767.35	21809.36	17209.02	14211.27	12102.98	10539.42	9333.627	8375.413	7595.627	6948.676	6403.282	5937.272	5534.49	5182.885	5873.286	4598.59	4353.21	4132.69	3933.434	3752.509	3587.496	3436.384	3297.488	3169.383	3050.86	2940.882	2838.558	2743.114	2653.88
26	2720.4	1.00965	0.2796087	111118.4	47053.26	29845.75	21853.76	17237.87	14231.85	12118.57	10551.74	9343.68	8383.824	7602.804	6954.9	6408.752	5942.134	5538.852	5186.832	4876.883	4601.888	4356.25	4135.507	3936.056	3754.959	3589.793	3438.545	3299.526	3171.312	3052.689	2942.621	2840.213	2744.694	2655.391
27	2721.4	1.010021	0.2809331	112065.1	47232.23	29921.68	21896.6	17265.86	14251.84	12133.72	10563.73	9353.472	8392.024	7609.808	6960.979	6414.098	5946.889	5543.122	5190.697	4880.407	4605.121	4359.233	4138.272	3938.631	3757.365	3592.05	3440.669	3301.532	3173.21	3054.49	2944.333	2841.845	2746.251	2656.88
28	2722.4	1.010392	0.2825887	112989	47405.68	29995.24	21938.14	17293.02	14271.26	12148.45	10575.4	9363.015	8400.022	7616.645	6966.917	6419.326	5951.541	5547.302	5194.484	4883.862	4608.293	4362.161	4140.988	3941.16	3759.731	3594.27	3442.759	3303.505	3175.078	3056.263	2946.019	2843.452	2747.787	2658.349
29	2723.4	1.010763	0.2845415	113880.4	47573.8	30066.53	21978.42	17319.38	14290.13	12162.79	10586.76	9372.318	8407.827	7623.323	6972.723	6424.44	5956.096	5551.398	5198.197	4887.251	4611.406	4365.035	4143.655	3943.647	3762.057	3596.454	3444.816	3305.448	3176.918	3058.01	2947.682	2845.037	2749.301	2659.798
30	2724.4	1.011134	0.286762	114769.8	47736.79	30135.63	22017.5	17344.99	14308.48	12176.75	10597.84	9381.393	8415.448	7629.849	6978.401	6429.445	5960.558	5555.413	5201.838	4890.577	4614.463	4367.86	4146.278	3946.092	3764.346	3598.604	3446.842	3307.362	3178.732	3059.733	2949.321	2846.601	2750.795	2661.228
31	2725.4	1.011505	0.2892245	115627.5	47894.83	30202.63	22055.42	17369.87	14326.33	12190.34	10608.64	9390.251	8422.894	7636.23	6983.958	6434.348	5964.931	5559.35	5205.412	4893.843	4617.466	4370.636	4148.857	3948.498	3766.599	3600.722	3448.838	3309.249	3180.52	3061.431	2950.939	2848.144	2752.27	2662.64
32	2726.4	1.011876	0.2919064	116464.1	48048.11	30267.62	22092.25	17394.06	14343.7	12203.58	10619.17	9398.901	8430.172	7642.474	6989.399	6439.152	5969.22	5563.214	5208.921	4897.052	4620.418	4373.367	4151.395	3950.867	3768.818	3602.808	3450.805	3311.11	3182.284	3063.108	2952.535	2849.668	2753.727	2664.035
33	2727.4	1.012248	0.2947881	117280	48196.82	30330.69	22128.03	17417.59	14360.62	12216.5	10629.46	9407.354	8437.29	7648.586	6994.73	6443.883	5973.427	5567.007	5212.368	4900.206	4623.322	4376.055	4153.894	3953.2	3771.005	3604.864	3452.745	3312.945	3184.025	3064.763	2954.112	2851.173	2755.166	2665.415
34	2728.4	1.012619	0.2978521	118075.7	48341.13	30391.91	22162.79	17440.49	14377.11	12229.1	10639.5	9415.617	8444.256	7654.572	6999.956	6448.484	5977.558	5570.734	5215.757	4903.309	4626.18	4378.701	4156.355	3955.499	3773.161	3606.893	3454.66	3314.756	3185.744	3066.397	2955.67	2852.66	2756.589	2666.778
35	2729.4	1.01299	0.3010083	118851.7	48481.22	30451.37	22196.6	17462.79	14393.18	12241.4	10649.32	9423.701	8451.077	7660.44	7005.082	6453.02	5981.616	5574.397	5219.09	4906.362	4628.993	4381.307	4158.781	3957.766	3775.288	3608.894	3456.549	3316.545	3187.441	3068.012	2957.209	2854.131	2757.996	2668.127
36	2730.4	1.013361	0.304467	119608.5	48617.25	30509.15	22239.5	17484.5	14408.86	12253.41	10658.92	9431.614	8457.76	7666.195	7010.112	6457.475	5985.604	5578	5222.37	4909.369	4631.765	4383.876	4161.173	3960.003	3777.387	3610.871	3458.416	3318.313	3189.119	3069.609	2958.732	2855.586	2759.389	2669.462
37	2731.4	1.013732	0.3079992	120346.8	48749.4	30565.31	22261.51	17505.67	14424.17	12265.15	10668.31	9439.363	8464.311	7671.838	7015.052	6461.853	5989.526	5581.545	5225.599	4912.33	4634.497	4386.41	4163.533	3962.21	3779.459	3612.822	3460.26	3320.06	3190.778	3071.188	2960.238	2857.025	2760.767	2670.784
38	2732.4	1.014103	0.3116468	121067	48877.82	30619.93	22292.69	17526.32	14439.11	12276.62	10677.5	9446.957	8470.737	7677.38	7019.906	6466.158	5993.385	5585.035	5228.78	4915.249	4637.191	4388.909	4165.862	3964.39	3781.506	3614.751	3462.082	3321.787	3192.419	3072.75	2961.729	2858.45	2762.132	2672.093
39	2733.4	1.014474	0.3154218	121769.6	49002.67	30673.08	22323.07	17546.47	14453.72	12287.85	10686.5	9454.403	8477.044	7682.824	7024.677	6470.393	5997.183	5588.473	5231.915	4918.127	4639.849	4391.376	4168.162	3966.543	3783.529	3616.658	3463.885	3323.496	3194.043	3074.297	2963.205	2859.861	2763.483	2673.39
40	2734.4	1.014846	0.3193081	122455.3	49124.09	30724.82	22352.69	17566.14	14468	12298.85	10695.32	9461.708	8483.237	7688.174	7029.37	6474.561	6000.925	5591.861	5235.007	4920.967	4642.473	4393.812	4170.434	3968.671	3785.529	3618.544	3465.668	3325.187	3195.65	3075.828	2964.666	2861.259	2764.823	2674.675
41	2735.4	1.015217	0.3232977	123124.4	49242.22	30775.21	22381.58	17585.35	14481.96	12309.61	10703.98	9468.878	8489.322	7693.435	7033.988	6478.666	6004.611	5595.201	5238.057	4923.77	4645.064	4396.219	4172.68	3970.775	3787.507	3620.409	3467.433	3326.861	3197.242	3077.345	2966.115	2862.645	2766.151	2675.95
42	2736.4	1.015588	0.3273833	123777.5	49357.21	30824.31	22409.78	17604.14	14495.63	12320.17	10712.47	9475.92	8495.303	7698.611	7038.535	6482.71	6008.246	5598.497	5241.067	4926.538	4647.623	4398.597	4174.901	3972.856	3789.464	3622.256	3469.181	3328.519	3198.819	3078.848	2967.55	2864.019	2767.467	2677.214
43	2737.4	1.01693	0.3351585	124415.2	49469.17	30872.19	22463.31	17622.5	14509.02	12330.51	10720.8	9482.84	8501.186	7703.706	7043.014	6486.697	6011.831	5601.749	5244.04	4929.273	4650.153	4400.949	4177.097	3974.915	3791.401	3624.085	3470.912	3330.162	3200.382	3080.338	2968.974	2865.381	2768.774	2678.468
44	2738.4	1.01633	0.3358172	125037.8	49578.24	30918.88	22464.21	17640.48	14522.14	12340.66	10728.98	9489.643	8506.974	7708.723	7047.429	6490.629	6015.369	5604.96	5246.976	4931.975	4652.654	4403.276	4179.271	3976.954	3793.32	3625.897	3472.627	3331.79	3201.931	3081.815	2970.385	2866.732	2770.07	2679.713
45	2739.4	1.016701	0.3401541	125645.9	49684.53	30964.45	22490.5	17658.07	14535	12350.62	10737.02	9496.334	8512.674	7713.667	7051.782	6494.508	6018.862	5608.132	5248.879	4934.648	4655.129	4405.579	4181.423	3978.972	3795.221	3627.692	3474.327	3333.404	3203.468	3083.281	2971.786	2868.074	2771.356	2680.949
46	2740.4	1.017072	0.3445642	126240	49788.16	31008.93	22516.21	17675.3	14547.61	12360.41	10744.93	9502.92	8518.287	7718.541	7056.075	6498.337	6022.312	5611.267	5252.748	4937.291	4657.578	4407.858	4183.554	3980.972	3797.104	3629.471	3476.013	3335.005	3204.992	3084.735	2973.176	2869.405	2772.633	2682.176
47	2741.4	1.017444	0.3490429	126820.4	49889.23	31052.39	22541.37	17692.19	14559.99	12370.02	10752.71	9509.404	8523.819	7723.347	7060.313	6502.119	6025.721	5614.366	5255.586	4939.907	4660.002	4410.115	4185.665	3982.954	3798.971	3631.235	3477.685	3336.594	3206.504	3086.178	2974.556	2870.727	2773.902	2683.395
48	2742.4	1.017815	0.3535861	127387.7	49987.86	31094.85	22566	17708.75	14572.15	12379.47	10760.36	9515.791	8529.273	7728.088	7064.497	6505.855	6029.09	5617.431	5258.395	4942.496	4662.402	4412.352	4187.757	3984.919	3800.823	3632.985	3479.344	3338.17	3208.006	3087.611	2975.927	2872.04	2775.162	2684.606
49	2743.4	1.018186	0.3581319	128288.3	50084.13	31136.37	22590.11	17724.99	14584.08	12388.77	10767.9	9522.085	8534.652	7732.77	7068.63	6509.548	6032.423	5620.464	5261.175	4945.06	4664.78	4414.568	4189.831	3986.867	3802.659	3634.722	3480.99	3339.735	3209.496	3089.035	2977.288	2873.345	2776.414	2685.81
50	2744.4	1.018557	0.3628511	129484.4	50178.15	31176.99	22613.75	17740.93	14595.82	12397.92	10775.32	9528.291	8539.961	7737.393	7072.713	6513.198	6035.719	5623.466	5263.927	4947.6	4667.137	4416.765	4191.888	3988.8	3804.481	3636.045	3482.624	3341.288	3210.977	3090.448	2978.641	2874.641	2777.658	2687.006

Figure E 12-56: SLD Numerical Solution Sample Data Points Case A

E.5 Stability Lobe Diagram B

*Refer to attached CD for the complete simulation data

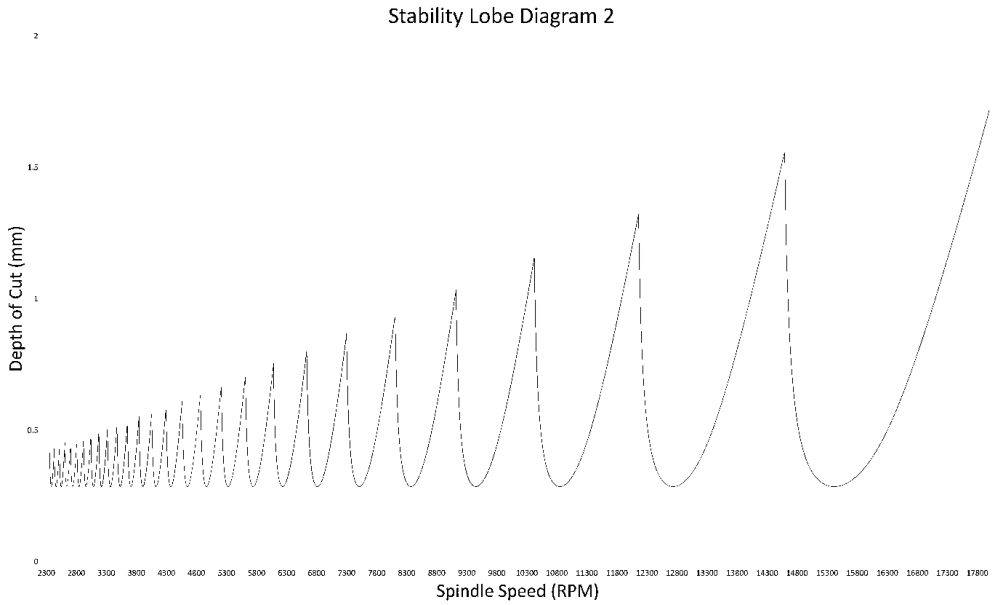

Figure E 12-57: SLD Plot Case B

j	fj	rj	bj	Nj	0	1	2	3	4	5	6	7	8	9	10	11	12	13	14	15	16	17	18	19	20	21	22	23	24	25	26	27	28	29	30
1	2415.93	1.000414	3.7772382	73352.78	36456.36	24255.73																													
2	2416.93	1.000828	1.8977434	74276.87	36690.86	24362.71	18235.55	14570.98	12132.81																										
3	2417.93	1.001242	1.2747828	75218.19	36926.87	24469.95	18297.48	14611.71	12161.88	10415.58	9107.805																								
4	2418.93	1.001656	0.9659573	76174.67	37163.78	24577.2	18359.3	14652.33	12190.85	10437.44	9124.995	8105.744	7291.313																						
5	2419.93	1.00207	0.7827872	77144.1	37400.99	24684.19	18420.87	14692.75	12219.67	10459.18	9142.082	8119.6	7302.827	6635.357	6079.682	5609.884																			
6	2420.93	1.002485	0.6624459	78124.22	37637.93	24790.67	18482.04	14732.88	12248.27	10480.75	9159.034	8133.346	7314.248	6645.037	6088.018	5617.161	5213.908	4864.676	4559.291																
7	2421.93	1.002899	0.5780077	79112.71	37874.02	24896.4	18542.7	14772.64	12276.59	10502.11	9175.819	8146.957	7325.559	6654.623	6096.275	5624.369	5220.273	4870.351	4564.394	4294.606	4054.93	3840.592													
8	2422.93	1.003313	0.5160288	80107.28	38108.73	25001.15	18602.71	14811.95	12304.59	10523.22	9192.41	8160.411	7336.741	6664.101	6104.44	5631.498	5226.57	4875.967	4569.445	4299.181	4059.103	3844.419	3651.304	3476.662											
9	2423.93	1.003727	0.4608728	81105.64	38341.54	25104.72	18661.97	14850.75	12332.21	10544.05	9208.781	8173.689	7347.779	6673.459	6112.503	5638.54	5232.79	4881.516	4574.436	4303.705	4063.228	3848.204	3654.793	3479.894	3320.97	3175.928	3043.025	2920.798	2805.683						
10	2424.93	1.004141	0.432409	82105.59	38572	25206.92	18720.37	14888.96	12359.42	10564.57	9224.909	8186.773	7358.658	6682.685	6120.455	5645.486	5238.928	4886.992	4579.364	4308.171	4067.303	3851.943	3658.242	3483.089	3323.942	3178.704	3045.626	2923.243	2810.315	2705.788	2606.696	2516.488	2432.315	2353.59
11	2425.93	1.004555	0.4034629	831.05	38799.68	25307.59	18777.84	14926.55	12386.18	10584.75	9240.776	8199.648	7369.366	6691.769	6128.286	5652.33	5244.976	4892.39	4584.223	4312.577	4071.324	3855.633	3661.646	3486.244	3326.878	3181.445	3048.195	2925.658	2812.593	2707.941	2610.798	2520.383	2436.02	2357.123
12	2426.93	1.004969	0.3802304	84101.86	39024.21	25406.58	18834.28	14963.47	12412.46	10604.57	9256.366	8212.303	7379.894	6700.703	6135.991	5659.065	5250.932	4897.707	4589.01	4316.919	4075.287	3859.271	3665.004	3489.356	3329.775	3184.152	3050.733	2928.044	2814.842	2710.068	2612.813	2522.297	2437.843	2358.86
13	2427.93	1.005383	0.3613936	85094.3	39245.26	25503.76	18889.66	14999.67	12438.24	10624.02	9271.666	8224.726	7390.234	6709.481	6143.565	5665.688	5256.789	4902.939	4593.722	4321.194	4079.191	3862.857	3668.313	3492.425	3332.632	3188.822	3053.236	2930.399	2817.063	2712.168	2614.804	2524.189	2439.643	2360.577
14	2428.93	1.005797	0.346011	86080.56	39462.54	25599.05	18943.91	15035.13	12463.49	10643.08	9286.666	8236.911	7400.38	6718.098	6151.002	5672.195	5262.547	4908.083	4598.357	4325.401	4083.034	3866.387	3671.573	3495.449	3335.448	3189.455	3055.705	2932.722	2819.255	2714.241	2616.77	2526.056	2441.421	2362.274
15	2429.93	1.006211	0.3333922	87059.06	39675.81	25692.35	18997	15069.84	12488.21	10661.74	9301.359	8248.852	7410.328	6726.55	6158.302	5678.584	5268.202	4913.139	4602.914	4329.538	4086.815	3869.862	3674.782	3498.427	3338.223	3192.049	3058.139	2935.013	2821.417	2716.286	2618.709	2527.9	2443.177	2363.949
16	2430.93	1.006625	0.3230194	88028.35	39884.89	25783.61	19048.89	15103.76	12512.38	10679.99	9315.741	8260.547	7420.075	6734.836	6165.461	5684.853	5273.755	4918.104	4607.391	4333.605	4090.533	3873.28	3677.941	3501.358	3340.955	3194.605	3060.538	2937.27	2823.548	2718.304	2620.623	2529.719	2444.91	2365.603
17	2431.93	1.00704	0.3144966	88987.16	40088.62	25872.79	19099.58	15136.9	12536	10697.84	9329.81	8271.993	7429.62	6742.955	6172.479	5691.002	5279.203	4922.978	4611.789	4337.602	4094.188	3876.642	3681.048	3504.244	3343.645	3197.122	3062.901	2939.496	2825.649	2720.293	2622.51	2531.514	2446.62	2367.236
18	2432.93	1.007454	0.3075159	89934.35	40289.89	25959.85	19149.04	15169.25	12559.07	10715.29	9343.565	8283.19	7438.963	6750.907	6179.357	5697.031	5284.548	4927.763	4616.107	4341.528	4097.781	3879.948	3684.105	3507.083	3346.293	3199.6	3065.229	2941.688	2827.72	2722.254	2624.372	2533.284	2448.308	2368.847
19	2433.93	1.007868	0.3018941	90868.93	40485.61	26044.78	19197.29	15200.81	12581.59	10732.32	9357.008	8294.141	7448.107	6758.694	6186.096	5702.941	5289.791	4932.458	4620.947	4345.385	4101.311	3883.197	3687.111	3509.877	3348.899	3202.041	3067.521	2943.849	2829.762	2724.187	2626.208	2535.031	2449.973	2370.438
20	2434.93	1.008282	0.2972567	91790.08	40676.75	26127.59	19244.33	15231.59	12603.56	10748.95	9370.143	8304.848	7457.052	6766.317	6192.696	5708.734	5294.932	4937.065	4624.51	4348.173	4104.78	3886.392	3690.068	3512.625	3351.465	3204.443	3069.779	2945.977	2831.773	2726.094	2628.018	2536.754	2451.616	2372.007
21	2435.93	1.008696	0.2936263	92697.09	40863.27	26208.28	19290.16	15261.6	12624.99	10765.19	9382.974	8315.314	7465.803	6773.778	6199.162	5714.411	5299.974	4941.585	4628.596	4352.893	4108.188	3889.532	3692.976	3515.329	3353.989	3206.809	3072.004	2948.074	2833.756	2727.973	2629.803	2538.454	2453.237	2373.557
22	2436.93	1.00911	0.2908034	93588.38	41045.2	26286.88	19334.8	15290.84	12645.9	10781.04	9395.506	8325.544	7474.362	6781.082	6205.495	5719.976	5304.918	4946.02	4632.607	4356.547	4111.538	3892.62	3695.836	3517.99	3356.475	3209.139	3074.195	2950.141	2835.711	2729.826	2631.564	2540.131	2454.838	2375.086
23	2437.93	1.009524	0.2887135	94466.49	41222.55	26363.4	19378.28	15319.34	12666.28	10796.5	9407.747	8335.544	7482.735	6788.231	6211.698	5725.43	5309.767	4950.373	4636.546	4360.137	4114.83	3895.656	3698.649	3520.609	3358.922	3211.434	3076.353	2952.178	2837.638	2731.654	2633.302	2541.786	2456.417	2376.596
24	2438.93	1.009938	0.2872359	95328.06	41395.38	26437.9	19420.61	15347.1	12686.16	10811.6	9419.703	8345.319	7490.926	6795.23	6217.775	5730.776	5314.523	4954.644	4640.414	4363.664	4118.066	3898.641	3701.417	3523.186	3361.331	3213.694	3078.48	2954.185	2839.538	2733.456	2635.016	2543.419	2457.976	2378.088
25	2439.93	1.010352	0.2863088	96173.83	41563.74	26510.41	19461.83	15374.16	12705.54	10826.33	9431.382	8354.876	7498.94	6802.083	6223.729	5736.018	5319.19	4958.838	4644.213	4367.13	4121.248	3901.578	3704.141	3525.724	3363.704	3215.921	3080.577	2956.165	2841.412	2735.235	2636.707	2545.031	2459.516	2379.561
26	2440.93	1.010766	0.2858632	97003.64	41727.71	26580.98	19501.97	15400.52	12724.45	10840.71	9442.793	8364.22	7506.782	6808.795	6229.565	5741.159	5323.769	4962.955	4647.945	4370.537	4124.377	3904.468	3706.822	3528.223	3366.042	3218.116	3082.644	2958.118	2843.261	2736.99	2638.378	2546.623	2461.037	2381.016
27	2441.93	1.01118	0.2858514	97817.39	41887.39	26640.65	19541.04	15426.21	12742.89	10854.75	9453.943	8373.36	7514.459	6815.37	6235.285	5746.202	5328.264	4966.999	4651.613	4373.887	4127.456	3907.312	3709.463	3530.684	3368.346	3220.28	3084.683	2960.044	2845.086	2738.723	2640.027	2548.196	2462.539	2382.454
28	2442.93	1.011595	0.2862254	98615.06	42042.85	26716.48	19579.09	15451.24	12760.88	10868.46	9464.843	8382.302	7521.976	6821.812	6240.895	5751.151	5332.677	4970.972	4655.218	4377.181	4130.485	3910.112	3712.063	3533.11	3370.617	3222.413	3086.694	2961.944	2846.887	2740.434	2641.655	2549.75	2464.024	2383.876
29	2443.93	1.012009	0.2859454	99396.67	42194.21	26781.53	19616.15	15475.65	12778.43	10881.85	9475.499	8391.052	7529.338	6828.127	6246.398	5756.008	5337.013	4974.877	4658.764	4380.423	4133.467	3912.87	3714.625	3535.501	3372.856	3224.518	3088.678	2963.821	2848.666	2742.124	2643.265	2551.286	2465.492	2385.282
30	2444.93	1.012423	0.2879771	100162.3	42341.58	26844.84	19652.25	15499.45	12795.57	10894.94	9483.922	8399.618	7536.551	6834.319	6251.797	5760.778	5341.272	4978.717	4662.252	4383.614	4136.403	3915.586	3717.151	3537.858	3375.065	3226.595	3090.637	2965.674	2850.423	2743.794	2644.855	2552.804	2466.944	2386.672
31	2445.93	1.012837	0.2892905	100912.2	42485.05	26906.48	19687.42	15522.66	12812.3	10907.73	9496.119	8408.006	7543.621	6840.393	6257.098	5765.464	5345.459	4982.493	4665.684	4386.755	4139.296	3918.264	3719.641	3540.183	3377.245	3228.646	3092.572	2967.504	2852.159	2745.445	2646.428	2554.305	2468.38	2388.048
32	2446.93	1.013251	0.2908595	101646.4	42624.76	26966.49	19721.7	15545.31	12828.64	10920.24	9506.1	8416.224	7550.552	6846.354	6262.303	5770.068	5349.576	4986.708	4669.064	4389.85	4142.146	3920.904	3722.097	3542.478	3379.397	3230.67	3094.483	2969.312	2853.875	2747.077	2647.984	2555.791	2469.901	2389.41
33	2447.93	1.013665	0.2926609	102385.1	42760.8	27024.95	19755.12	15567.41	12844.61	10932.47	9515.872	8424.278	7557.352	6852.205	6267.417	5774.595	5353.627	4988.865	4672.391	4392.899	4144.956	3923.507	3724.52	3544.743	3381.522	3232.67	3096.371	2971.1	2855.571	2748.691	2649.522	2557.26	2471.208	2390.758
34	2448.93	1.014079	0.2946746	103068.6	42893.31	27081.89	19787.7	15588.99	12860.21	10944.44	9525.444	8432.175	7564.024	6857.951	6272.442	5779.047	5357.613	4993.466	4675.67	4395.905	4147.728	3926.076	3726.912	3546.98	3383.621	3234.647	3098.237	2972.868	2857.249	2750.288	2651.045	2558.715	2472.601	2392.093
35	2449.93	1.014493	0.2968824	103757.2	43022.38	27137.37	19819.49	15610.07	12875.47	10956.16	9534.824	8439.92	7570.575	6863.597	6277.384	5783.427	5361.537	4997.014	4678.902	4398.869	4150.462	3928.612	3729.274	3548.189	3385.695	3236.6	3100.083	2974.616	2858.91	2751.868	2652.553	2560.156	2473.98	2393.416
36	2450.93	1.014907	0.2992884	104431.1	43148.13	27191.46	19850.51	15630.66	12890.4	10967.63	9544.02	8447.521	7577.008	6869.147	6282.245	5787.739	5365.402	5000.51	4682.089	4401.793	4153.161	3931.115	3731.608	3551.372	3387.745	3238.532	3101.909	2976.346	2860.554	2753.453	2654.046	2561.594	2475.347	2394.727
37	2451.93	1.015321	0.3018183	105090.6	43270.69	27244.2	19880.8	15650.79	12905.01	10978.88	9553.039	8454.982	7583.33	6874.604	6287.028	5791.985	5369.21	5003.957	4685.232	4404.679	4155.826	3933.589	3733.913	3553.531	3389.773	3240.444	3103.716	2978.059	2862.181	2754.983	2655.525	2562.998	2476.701	2396.027
38	2452.93	1.015735	0.3045193	105736	43390.15	27295.63	19910.37	15670.47	12919.32	10989.9	9561.889	8462.31	7589.543	6879.972	6291.737	5796.167	5372.965	5007.356	4688.334	4407.528	4158.458	3936.032	3736.193	3555.665	3391.779	3242.335	3105.504	2979.755	2863.793	2756.518	2656.991	2564.399	2478.044	2397.316
39	2453.93	1.01615	0.30736	106367.7	43506.62	27345.82	19939.26	15689.73	12933.33	11000.7	9570.576	8469.511	7595.654	6885.256	6296.375	5800.289	5376.667	5010.711	4691.396	4410.342	4161.059	3938.448	3738.447	3557.777	3393.764	3244.207	3107.275	2981.434	2865.39	2758.04	2658.443	2565.789	2479.376	2398.594
40	2454.93	1.016564	0.3103301	106985.9	43620.22	27394.81	19967.5	15708.57	12947.06	11011.31	9579.107	8476.588	7601.666	6890.458	6300.945	5804.354	5380.319	5014.022	4694.421	4413.122	4163.63	3940.837	3740.677	3559.866	3395.729	3246.061	3109.029	2983.099	2866.972	2759.548	2659.884	2567.167	2480.697	2399.862
41	2455.93	1.016978	0.3134203	107590.9	43731.03	27442.64	19995.11	15727.02	12960.52	11021.71	9587.489	8483.549	7607.584	6895.583	6305.45	5808.363	5383.924	5017.291	4697.409	4415.87	4166.172	3942.201	3742.883	3561.935	3397.675	3247.898	3110.768	2984.788	2868.541	2761.044	2661.313	2568.535	2482.008	2401.121
42	2456.93	1.017392	0.3166221	108183.2	43839.17	27489.36	20022.11	15745.09	12973.72	11031.93	9595.727	8490.397	7613.41	6900.633	6309.892	5812.318	5387.483	5020.521	4700.362	4418.588	4168.686	3945.539	3745.068	3563.983	3399.603	3249.718	3112.491	2986.383	2870.097	2762.528	2662.73	2569.892	2483.309	2402.37
43	2457.93	1.017806	0.3199328	108762.9	43944.73	27535.01	20048.54	15762.8	12986.67	11041.96	9603.829	8497.138	7619.15	6905.611	6314.274	5816.223	5390.998	5023.713	4703.281	4421.276	4171.175	3947.854	3747.231	3566.013	3401.513	3251.521	3114.199	2988.005	2871.641	2764	2664.137	2571.239	2484.601	2403.611
44	2458.93	1.01822	0.3233309	109330.5	44047.8	27579.63	20074.41	15780.16	12999.38	11051.83	9611.799	8503.775	7624.807	6910.521	6318.599	5820.079	5394.471	5026.668	4706.169	4423.935	4173.638	3950.147	3749.374	3568.023	3403.407	3253.31	3115.893	2989.614	2873.172	2765.461	2665.533	2572.576	2485.883	2404.843
45	2459.93	1.018634	0.3268245	109886.2	44148.47	27623.27	20099.74	15797.19	13011.87	11061.53	9619.642	8510.313	7630.384	6915.365	6322.869	5823.889	5397.904	5029.988	4709.026	4426.568	4176.077	3952.418	3751.497	3570.017	3405.284	3255.083	3117.573	2991.21	2874.692	2766.911	2666.92	2573.904	2487.157	2406.067
46	2460.93	1.019048	0.3304031	110430.4	44246.83	27665.96	20124.56	15813.89	13024.13	11071.06	9627.365	8516.756	7635.884	6920.146	6327.086	5827.653	5401.298	5033.075	4711.854	4429.174	4178.493	3954.668	3753.602	3571.993	3407.146	3256.843	3119.241	2992.795	2876.201	2768.351	2668.297	2575.223	2488.423	2407.284
47	2461.93	1.019462	0.3340614	110963.4	44342.96	27707.73	20148.89	15830.29	13036.19	11080.45	9634.972	8523.109	7641.311	6924.867	6331.253	5831.375	5404.656	5036.13	4714.653	4431.756	4180.887	3956.898	3755.689	3573.953	3408.993	3258.589	3120.896	2994.368	2877.699	2769.781	2669.665	2576.534	2489.881	2408.493
48	2462.93	1.019876	0.3377946	111485.5	44436.95	27748.63	20172.75	15845.39	13048.04	11089.69	9642.468	8529.374	7646.668	6929.53	6335.371	5835.095	5407.978	5039.154	4717.426	4434.314	4183.259	3959.109	3757.759	3575.897	3410.826	3260.322	3122.54	2995.93	2879.188	2771.202	2671.024	2577.836	2490.932	2409.695
49	2463.93	1.02029	0.3415981	111996.9	44528.87	27788.69	20196.15	15862.21	13059.7	11098.78	9649.857	8535.555	7651.957	6934.137	6339.443	5838.697	5411.267	5042.149	4720.173	4436.849	4185.612	3961.302	3759.812	3577.827	3412.646	3262.043	3124.172	2997.482	2880.666	2772.614	2672.375	2579.131	2492.175	2410.89
50	2464.93	1.020705	0.345468	112498.1	44618.8	27827.94	20219.12	15877.76	13071.18	11107.75	9657.144	8541.656	7657.182	6938.692	6343.47	5842.3	5414.523	5045.115	4722.895	4439.362	4187.944	3963.478	3761.849	3579.742	3414.452	3263.752	3125.793	2999.023	2882.136	2774.018	2673.718	2580.419	2493.411	2412.079

Figure E 12-58: SLD Numerical Solution Sample Data Points Case B

E.6 Stability Lobe Diagram C

*Refer to attached CD for the complete simulation data

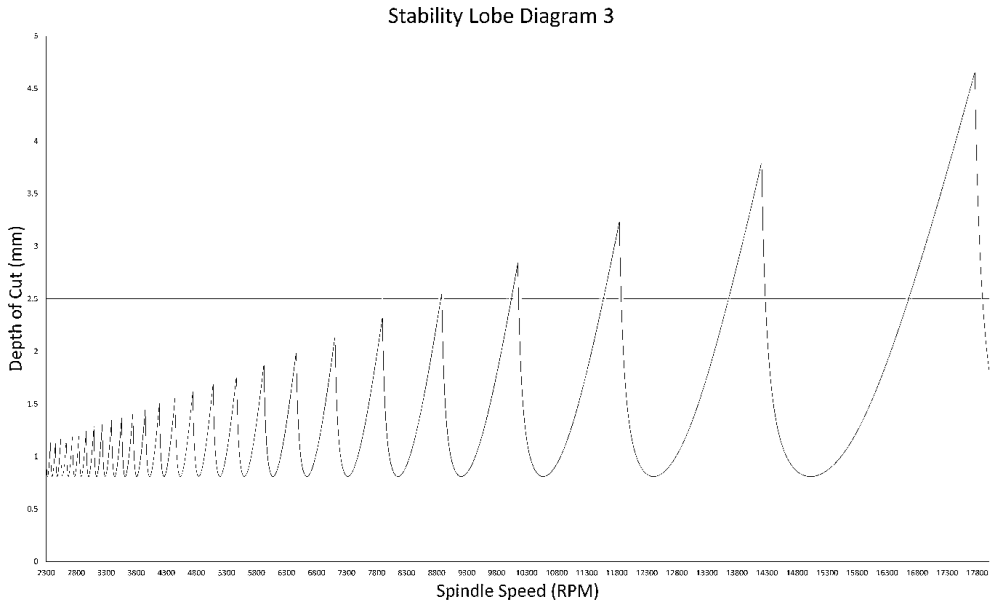

Figure E 12-59: SLD Plot Case C

j	fj	rj	bj	Nj	0	1	2	3	4	5	6	7	8	9	10	11	12	13	14	15	16	17	18	19	20	21	22	23	24	25	26	27	28	29	30
1	2349.8	1.000426	12.377647	71226.48	35429.17																														2274.755
2	2350.8	1.000851	6.2121482	72003.08	35627.93	23670.08	17722.01																												2276.476
3	2351.8	1.001277	4.1656016	72792.6	35827.91	23761.58	17775.16	14198.13	11819.58																										2278.196
4	2352.8	1.001703	3.1487972	73593.77	36028.73	23853.17	17828.28	14233.22	11844.74	10142.69																									2279.911
5	2353.8	1.002129	2.5438929	74405.23	36230.03	23944.69	17881.28	14268.2	11869.8	10161.68	8883.33	7890.673																							2281.621
6	2354.8	1.002554	2.1449414	75225.61	36431.43	24035.97	17934.07	14303.02	11894.74	10180.58	8898.243	7902.813	7107.689	6457.938	5917.031	5459.733																			2283.325
7	2355.8	1.00298	1.8636756	76053.47	36632.56	24126.85	17986.56	14337.63	11919.52	10199.35	8913.056	7914.871	7117.746	6466.49	5924.421	5466.203	5073.777	4733.923																	2285.02
8	2356.8	1.003406	1.655976	76887.39	36833.08	24217.19	18038.67	14371.96	11944.09	10217.96	8927.748	7926.832	7127.722	6474.975	5931.753	5472.624	5079.464	4739.008	4441.324																2286.706
9	2357.8	1.003832	1.4973129	77725.92	37032.66	24306.85	18090.33	14405.98	11968.44	10236.4	8942.302	7938.681	7137.607	6483.384	5939.021	5478.99	5085.103	4744.05	4445.871	4182.958	3949.404	3740.552	3552.679											2288.382
10	2358.8	1.004257	1.3729799	78567.65	37230.96	24395.69	18141.47	14439.64	11992.52	10254.65	8956.702	7950.407	7147.391	6491.707	5946.217	5485.294	5090.688	4749.046	4450.377	4187.051	3953.147	3743.993	3555.859	3385.728	3231.133										2290.047
11	2359.8	1.004683	1.1736157	79411.18	37427.7	24483.6	18192.02	14472.9	12016.32	10272.67	8970.933	7961.998	7157.064	6499.939	5953.335	5491.531	5096.215	4753.991	4454.838	4191.105	3956.854	3747.402	3559.01	3388.653	3233.86	3092.591	2963.148								2291.699
12	2360.8	1.005109	1.1292794	80255.17	37622.61	24570.46	18241.92	14505.73	12039.81	10290.47	8984.984	7973.444	7166.618	6508.072	5960.369	5497.697	5101.68	4758.883	4459.252	4195.117	3960.523	3750.777	3562.13	3391.55	3236.561	3095.118	2965.521	2846.339	2736.368				2370.084	2293.339
13	2361.8	1.005535	1.1267506	81098.32	37815.42	24656.19	18291.13	14538.09	12062.97	10308.02	8998.841	7984.737	7176.048	6516.101	5967.316	5503.787	5107.08	4763.717	4463.615	4199.084	3964.153	3754.117	3565.218	3394.418	3239.235	3097.621	2967.871	2848.553	2738.459	2636.557	2541.968	2453.93	2371.787	2294.964
14	2362.8	1.00596	1.071843	81959.4	38005.91	24740.68	18339.6	14569.96	12085.77	11325.3	9012.498	7995.868	7185.346	6524.021	5974.17	5509.799	5112.413	4768.492	4467.926	4203.004	3967.741	3757.419	3568.272	3397.255	3241.882	3100.099	2970.198	2850.745	2740.529	2638.518	2543.829	2455.701	2373.474	2296.576
15	2363.8	1.006386	1.0259936	82777.25	38193.88	24823.88	18387.3	14601.32	12108.22	10342.32	9025.945	8006.834	7194.508	6531.828	5980.93	5515.73	5117.674	4773.205	4472.183	4206.877	3971.286	3760.682	3571.291	3400.061	3244.499	3102.55	2972.5	2852.915	2742.579	2640.46	2545.673	2457.455	2375.146	2298.173
16	2364.8	1.006812	0.907505	83610.79	38379.16	24905.71	18434.18	14632.15	12130.28	10359.05	9039.176	8017.627	7203.531	6539.52	5987.592	5521.577	5122.864	4777.855	4476.385	4210.701	3974.787	3763.906	3574.275	3402.834	3247.087	3104.974	2974.778	2855.061	2744.608	2642.382	2547.498	2459.192	2376.803	2299.755
17	2365.8	1.007238	0.9550791	84439	38561.6	24986.13	18480.23	14662.43	12151.97	10375.5	9052.188	8028.246	7212.412	6547.093	5994.154	5527.339	5127.981	4782.442	4480.53	4214.474	3978.244	3767.09	3577.222	3405.575	3249.646	3107.37	2977.03	2857.185	2746.615	2644.284	2549.304	2460.911	2378.443	2301.322
18	2366.8	1.007663	0.9277064	85260.98	38741.06	25065.09	18525.44	14692.15	12173.26	10391.66	9064.976	8038.688	7221.149	6554.548	6000.616	5533.016	5133.023	4786.964	4484.619	4218.197	3981.655	3770.234	3580.133	3408.282	3252.173	3109.739	2979.257	2859.285	2748.6	2646.166	2551.092	2462.613	2380.066	2302.873
19	2367.8	1.008089	0.90459	86075.88	38917.44	25142.57	18569.77	14721.31	12194.16	10407.53	9077.539	8048.952	7229.741	6561.882	6006.977	5538.606	5137.991	4791.42	4488.65	4221.869	3985.022	3773.337	3583.007	3410.956	3254.671	3112.08	2981.459	2861.361	2750.564	2648.028	2552.861	2464.298	2381.673	2304.41
20	2368.8	1.008515	0.8850921	86882.94	39090.65	25218.53	18613.24	14749.91	12214.66	10423.11	9089.876	8059.036	7238.187	6569.095	6013.237	5544.11	5142.884	4795.812	4492.624	4225.491	3988.342	3776.399	3585.844	3413.596	3257.138	3114.393	2983.635	2863.414	2752.506	2649.869	2554.612	2465.965	2383.264	2305.93
21	2369.8	1.008941	0.8686967	87681.49	39260.64	25292.97	18655.82	14777.93	12234.76	10438.39	9101.988	8068.941	7246.488	6576.189	6019.395	5549.527	5147.703	4800.139	4496.541	4229.062	3991.618	3779.42	3588.645	3416.204	3259.575	3116.679	2985.785	2865.443	2754.426	2651.691	2556.343	2467.615	2384.839	2307.436
22	2370.8	1.009366	0.8548815	88470.93	39427.36	25365.87	18697.53	14805.39	12254.47	10453.38	9113.875	8078.669	7254.645	6583.163	6025.453	5554.859	5152.448	4804.402	4500.401	4232.983	3994.989	3782.402	3591.409	3418.778	3261.981	3118.937	2987.911	2867.449	2756.325	2653.492	2558.056	2469.247	2386.397	2308.927
23	2371.8	1.009792	0.8435975	89250.76	39590.77	25437.24	18738.36	14832.29	12273.78	10468.08	9125.54	8088.221	7262.66	6590.019	6031.412	5560.106	5157.12	4808.6	4504.205	4236.054	3998.036	3785.344	3594.138	3421.32	3264.359	3121.168	2990.011	2869.433	2758.202	2655.274	2559.751	2470.862	2387.94	2310.402
24	2372.8	1.010218	0.8342541	90020.51	39750.87	25507.09	18778.33	14858.62	12292.7	10482.49	9136.986	8097.6	7270.534	6596.759	6037.273	5565.27	5161.72	4812.737	4507.955	4239.476	4001.18	3788.246	3596.831	3423.83	3266.707	3123.372	2992.087	2871.393	2760.059	2657.036	2561.428	2472.461	2389.466	2311.863
25	2373.8	1.010644	0.826707	90779.81	39907.66	25575.43	18817.43	14884.41	12311.24	10496.62	9148.215	8106.807	7278.269	6603.385	6043.038	5570.352	5166.249	4816.811	4511.65	4242.851	4004.28	3791.111	3599.49	3426.308	3269.026	3125.55	2994.139	2873.332	2761.895	2658.78	2563.087	2474.042	2391.078	2313.309
26	2374.8	1.011069	0.8207496	91528.35	40061.14	25642.26	18855.69	14909.65	12329.4	10510.47	9159.232	8115.847	7285.868	6609.898	6048.709	5575.354	5170.709	4820.826	4515.292	4246.178	4007.339	3793.937	3602.115	3428.756	3271.317	3127.702	2996.167	2875.248	2763.711	2660.504	2564.728	2475.608	2392.474	2314.742
27	2375.8	1.011495	0.8162059	92265.87	40211.34	25707.62	18893.12	14934.36	12347.2	10524.05	9170.04	8124.722	7293.334	6616.301	6054.287	5580.277	5175.101	4824.781	4518.882	4249.46	4010.356	3796.727	3604.706	3431.173	3273.581	3129.83	2998.172	2877.144	2765.507	2662.211	2566.353	2477.158	2393.955	2316.16
28	2376.8	1.01921	0.812925	92992.17	40358.3	25771.53	18929.72	14958.54	12364.62	10537.37	9180.645	8133.436	7300.67	6622.596	6059.775	5585.123	5179.427	4828.678	4522.422	4252.696	4013.334	3799.481	3607.265	3433.562	3275.818	3131.932	3000.155	2879.018	2767.285	2663.9	2567.961	2478.693	2395.422	2317.565
29	2377.8	1.012347	0.8107769	93707.1	40502.05	25834	18965.53	14982.22	12381.7	10550.42	9191.052	8141.994	7307.88	6628.787	6065.175	5588.894	5183.688	4832.519	4525.912	4255.889	4016.273	3802.2	3609.793	3435.921	3278.029	3134.011	3002.116	2880.873	2769.043	2665.571	2569.553	2480.213	2396.876	2318.957
30	2378.8	1.012772	0.8096948	94410.56	40642.64	25895.08	19000.56	15005.39	12398.43	10563.23	9201.265	8150.399	7314.966	6634.876	6070.489	5594.592	5187.887	4836.306	4529.354	4259.04	4019.173	3804.885	3612.29	3438.253	3280.215	3136.067	3004.055	2882.708	2770.784	2667.226	2571.13	2481.718	2398.315	2320.336
31	2379.8	1.013198	0.8094425	95102.49	40780.12	25954.79	19034.82	15028.08	12414.82	10575.78	9211.29	8158.656	7321.931	6640.866	6075.72	5599.219	5192.024	4840.04	4532.749	4262.149	4022.037	3807.537	3614.757	3440.558	3282.376	3138.1	3005.974	2884.524	2772.507	2668.864	2572.691	2483.209	2399.741	2321.703
32	2380.8	1.013624	0.8100721	95782.85	40914.56	26013.16	19068.33	15050.3	12430.89	10588.1	9221.132	8166.769	7328.781	6646.76	6080.871	5603.778	5196.103	4843.722	4536.099	4265.218	4024.865	3810.156	3617.195	3442.836	3284.513	3140.112	3007.873	2886.321	2774.212	2670.487	2574.238	2484.686	2401.155	2323.058
33	2381.8	1.01405	0.8114622	96451.67	41046.01	26070.23	19101.12	15072.05	12446.64	10600.18	9230.797	8174.741	7335.517	6652.56	6085.943	5608.27	5200.124	4847.354	4539.406	4268.248	4027.659	3812.745	3619.605	3445.089	3286.628	3142.102	3009.752	2888.101	2775.901	2672.094	2575.77	2486.15	2402.556	2324.401
34	2382.8	1.014475	0.8135461	97108.98	41174.54	26126.03	19133.21	15093.36	12462.08	10612.04	9240.289	8182.579	7342.143	6658.27	6090.939	5612.698	5204.089	4850.937	4542.67	4271.241	4030.419	3815.304	3621.988	3447.318	3288.719	3144.072	3011.612	2889.863	2777.575	2673.686	2577.289	2487.601	2403.945	2325.733
35	2383.8	1.014901	0.8162648	97754.84	41300.22	26180.6	19164.61	15114.24	12477.22	10623.68	9249.615	8190.284	7348.664	6663.893	6095.862	5617.063	5208.001	4854.474	4545.892	4274.197	4033.147	3817.834	3624.345	3449.523	3290.789	3146.022	3013.455	2891.608	2779.232	2675.264	2578.794	2489.04	2405.322	2327.054
36	2384.8	1.015327	0.8195659	98388.34	41423.11	26233.96	19195.35	15134.69	12492.07	10635.11	9258.78	8197.863	7355.082	6669.431	6100.714	5621.368	5211.86	4857.966	4549.075	4277.118	4035.843	3820.335	3626.677	3451.704	3292.838	3147.953	3015.28	2893.338	2780.875	2676.828	2580.287	2490.466	2406.689	2328.364
37	2385.8	1.015753	0.8234026	99012.6	41543.29	26286.16	19225.45	15154.74	12506.65	10646.33	9267.789	8205.32	7361.401	6674.887	6105.497	5625.614	5215.67	4861.414	4552.22	4280.005	4038.509	3822.81	3628.984	3453.864	3294.867	3149.865	3017.088	2895.051	2782.504	2678.379	2581.767	2491.881	2408.044	2329.665
38	2386.8	1.016178	0.8277331	99624.73	41660.82	26337.23	19254.92	15174.4	12520.95	10657.36	9276.647	8212.657	7367.624	6680.265	6110.215	5629.804	5219.431	4864.82	4555.328	4282.859	4041.146	3825.258	3631.267	3456.002	3296.877	3151.76	3018.879	2896.75	2784.118	2679.917	2583.235	2493.285	2409.389	2330.955
39	2387.8	1.016604	0.8325197	100225.9	41775.78	26387.2	19283.79	15193.67	12534.99	10668.19	9285.36	8219.88	7373.754	6685.566	6114.868	5633.934	5223.145	4868.185	4558.4	4285.682	4043.754	3827.681	3633.528	3458.12	3298.867	3153.637	3020.655	2898.434	2785.719	2681.442	2584.691	2494.678	2410.724	2332.236
40	2388.8	1.01703	0.8377288	100816.2	41888.24	26456.11	19312.08	15212.58	12548.77	10678.85	9293.932	8226.993	7379.796	6690.793	6119.46	5638.023	5226.814	4871.51	4561.437	4288.474	4046.336	3830.08	3635.766	3460.217	3300.84	3155.498	3022.415	2900.104	2787.307	2682.956	2586.136	2496.061	2412.049	2333.508
41	2389.8	1.017456	0.8433297	101395.9	41998.28	26483.98	19339.8	15231.13	12562.31	10689.32	9302.368	8233.998	7385.751	6695.949	6123.992	5642.056	5230.439	4874.798	4564.441	4291.237	4048.891	3832.455	3637.984	3462.296	3302.795	3157.343	3024.161	2901.761	2788.883	2684.458	2587.571	2497.434	2413.365	2334.772
42	2390.8	1.017881	0.849295	101965.1	42105.95	26530.87	19366.98	15249.34	12575.62	10699.62	9310.673	8240.901	7391.623	6701.037	6128.466	5646.04	5234.023	4878.05	4567.414	4293.972	4051.421	3834.807	3640.181	3464.356	3304.733	3159.172	3025.893	2903.404	2790.446	2685.948	2588.995	2498.797	2414.672	2336.027
43	2391.8	1.018307	0.8555995	102524	42211.33	26576.78	19393.63	15267.21	12588.7	10709.75	9318.852	8247.704	7397.415	6706.059	6132.886	5649.977	5237.566	4881.266	4570.355	4296.679	4053.927	3837.138	3642.358	3466.398	3306.655	3160.987	3027.611	2905.035	2791.998	2687.428	2590.409	2500.15	2415.97	2337.273
44	2392.8	1.018733	0.8622204	103072.8	42314.49	26621.77	19419.77	15284.77	12601.55	10719.73	9326.909	8254.412	7403.129	6711.018	6137.252	5653.868	5241.07	4884.448	4573.266	4299.36	4056.409	3839.447	3644.516	3468.423	3308.561	3162.787	3029.316	2906.654	2793.539	2688.898	2591.813	2501.495	2417.259	2338.512
45	2393.8	1.019159	0.8691372	103611.6	42415.49	26665.85	19445.41	15302.01	12614.2	10729.55	9334.849	8261.027	7408.769	6715.915	6141.567	5657.716	5244.536	4887.598	4576.149	4302.015	4058.889	3841.737	3646.657	3470.431	3310.452	3164.573	3031.008	2908.261	2795.069	2690.357	2593.208	2502.831	2418.541	2339.744
46	2394.8	1.019584	0.8763308	104140.7	42514.41	26709.06	19470.58	15318.96	12626.64	10739.22	9342.676	8267.554	7414.338	6720.753	6145.832	5661.522	5247.966	4890.716	4579.004	4304.646	4061.306	3844.007	3648.779	3472.423	3312.329	3166.346	3032.688	2909.857	2796.588	2691.807	2594.595	2504.159	2419.815	2340.968
47	2395.8	1.02001	0.8837839	104660.3	42611.3	26751.42	19495.29	15335.62	12638.89	10748.74	9350.393	8273.994	7419.837	6725.534	6150.049	5665.287	5251.362	4893.804	4581.833	4307.253	4063.723	3846.258	3650.885	3474.4	3314.192	3168.107	3034.356	2911.442	2798.098	2693.246	2595.972	2505.479	2421.081	2342.185
48	2396.8	1.020436	0.8914807	105170.6	42706.22	26792.97	19519.56	15352	12650.94	10758.13	9358.005	8280.352	7425.269	6730.259	6154.221	5669.013	5254.723	4896.862	4584.636	4309.838	4066.12	3848.49	3652.974	3476.362	3316.041	3169.855	3036.014	2913.017	2799.598	2694.68	2597.342	2506.791	2422.34	2343.395
49	2397.8	1.020862	0.8994055	105671.8	42799.24	26833.73	19543.4	15368.11	12662.81	10767.39	9365.515	8286.63	7430.637	6734.933	6158.348	5672.702	5258.053	4899.892	4587.414	4312.401	4068.497	3850.706	3655.047	3478.31	3317.877	3171.591	3037.66	2914.581	2801.089	2696.103	2598.703	2508.095	2423.593	2344.599
50	2398.8	1.021287	0.907548	106164	42890.42	26873.73	19566.83	15383.97	12674.5	10776.51	9372.928	8292.831	7435.944	6739.555	6162.432	5676.354	5261.35	4902.896	4590.168	4314.943	4070.855	3852.905	3657.106	3480.245	3319.701	3173.316	3039.295	2916.137	2802.57	2697.518	2600.057	2509.393	2424.838	2345.796

Figure E 12-60: SLD Numerical Solution Sample Data Points Case C

E.7 Stability Lobe Diagram D

*Refer to attached CD for the complete simulation data

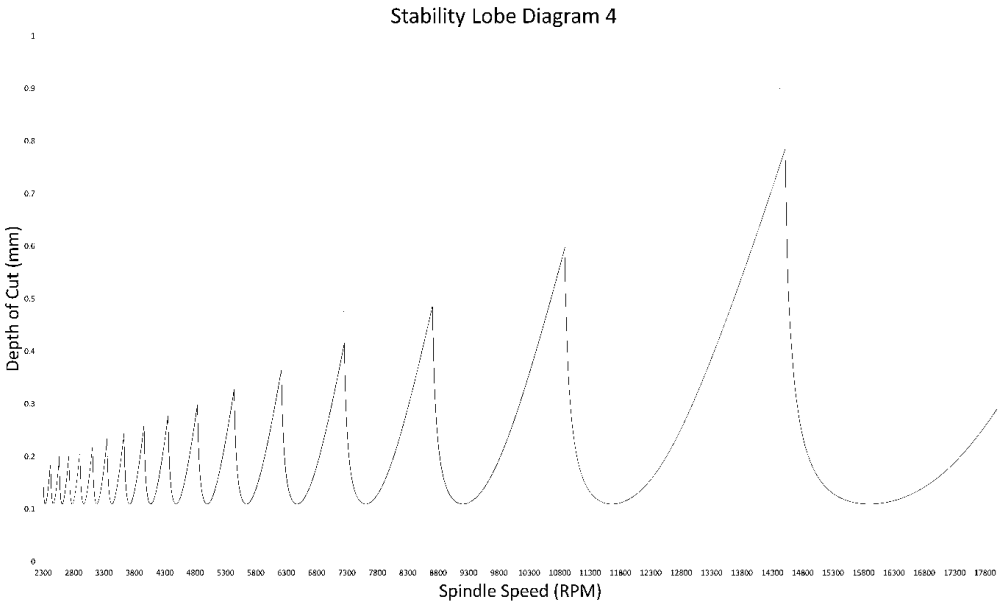

Figure E 12-61: SLD Plot Case D

j	fj	rj	bj	Nj	0	1	2	3	4	5	6	7	8	9	10	11	12	13	14	15	16	17	18	19	20	21	22	23	24	25	26	27	28	29	30
1	1438.87	1.000695	1.0992534	43853.96	21753.66	14464.33																			2057.065	1963.495	1878.008	1799.764	1727.728	1661.237	1599.674	1542.511	1489.292	1439.623	1393.16
2	1439.87	1.001391	0.5542007	44591.09	21941.26	14550.43	10884.15	8693.614	7237.084																2050.026	1966.255	1880.649	1802.187	1730.009	1663.39	1601.711	1544.443	1491.129	1441.373	1394.83
3	1440.87	1.002086	0.3742977	45344.74	22130.04	14636.66	10934.25	8726.768	7260.892	6216.651	5435.005	4827.964													2062.376	1969.004	1883.221	1804.601	1732.281	1665.535	1603.742	1546.37	1492.961	1443.118	1396.495
4	1441.87	1.002782	0.2856835	46111.97	22319.2	14722.64	10984.1	8759.724	7284.543	6234.604	5449.198	4839.536	4352.567	3954.639											2065.907	1971.737	1885.778	1807.001	1734.541	1667.669	1605.761	1548.285	1494.782	1444.853	1398.151
5	1442.87	1.003477	0.233586	46888.69	22507.95	14808.04	11033.51	8792.363	7307.956	6252.373	5463.245	4850.99	4362.134	3962.786	3630.426	3349.501	3108.931								2068.814	1974.447	1888.334	1809.381	1736.783	1669.786	1607.765	1550.187	1496.59	1446.576	1399.796
6	1443.87	1.004173	0.1997477	47674.78	22695.52	14892.55	11082.33	8824.578	7331.057	6269.904	5477.106	4862.299	4371.577	3970.83	3637.387	3355.607	3114.345	2905.449	2722.815	2561.788					2071.691	1977.13	1890.825	1811.739	1739.004	1671.883	1609.751	1552.071	1498.382	1448.284	1401.427
7	1444.87	1.004868	0.176344	48464.16	22881.24	14975.88	11130.38	8856.273	7353.783	6287.151	5490.744	4873.417	4380.874	3978.752	3644.246	3361.623	3119.682	2910.229	2727.131	2565.709	2422.328	2294.125	2178.81	2074.532	1979.781	1893.306	1814.07	1741.199	1673.957	1611.715	1553.936	1500.156	1449.974	1403.041
8	1445.87	1.005564	0.1594627	49254.83	23064.46	15057.77	11177.54	8887.367	7376.077	6304.073	5504.13	4884.34	4390.006	3986.537	3650.988	3367.541	3124.934	2914.934	2731.381	2569.576	2425.869	2297.384	2181.825	2077.335	1982.396	1895.755	1816.37	1743.367	1676.005	1613.655	1555.778	1501.909	1451.645	1404.637
9	1446.87	1.006259	0.1469302	50043.98	23244.65	15138.01	11223.71	8917.793	7397.894	6320.639	5517.239	4895.043	4398.958	3994.172	3657.604	3373.35	3130.091	2919.557	2735.559	2573.379	2429.352	2300.592	2184.795	2080.096	1984.972	1898.108	1818.639	1745.505	1678.026	1615.57	1557.596	1503.639	1453.296	1406.214
10	1447.87	1.006955	0.1374425	50823.01	23421.33	15216.43	11268.78	8947.497	7419.2	6336.824	5530.053	4905.51	4407.719	4001.648	3664.086	3379.044	3135.15	2924.093	2739.661	2577.114	2432.774	2303.746	2187.715	2082.811	1987.508	1900.545	1820.872	1747.611	1680.017	1617.458	1559.39	1505.346	1454.924	1407.77
11	1448.87	1.00765	0.1301697	51607.56	23594.12	15292.89	11312.69	8976.439	7439.968	6352.61	5542.56	4915.732	4416.28	4008.958	3670.428	3384.619	3140.105	2928.54	2743.683	2580.779	2436.134	2306.843	2190.584	2085.481	1990.002	1902.882	1823.071	1749.665	1681.979	1619.317	1561.157	1507.029	1456.529	1409.304
12	1449.87	1.008346	0.1245585	52377.53	23762.72	15367.29	11355.4	9004.594	7460.182	6367.984	5554.749	4925.703	4424.637	4016.099	3676.627	3390.072	3144.955	2932.895	2747.625	2584.372	2439.43	2309.883	2193.401	2088.103	1992.452	1905.181	1825.233	1751.725	1683.909	1621.148	1562.897	1508.687	1458.112	1410.817
13	1450.87	1.009041	0.1202258	53137.11	23926.9	15439.56	11396.87	9031.945	7479.832	6382.942	5566.618	4935.42	4432.787	4023.099	3682.683	3395.403	3149.699	2937.157	2751.485	2587.893	2442.662	2312.865	2196.166	2090.678	1994.86	1907.439	1827.359	1753.732	1685.808	1622.95	1564.611	1510.32	1459.67	1412.308
14	1451.87	1.009737	0.1168882	53884.77	24086.51	15509.67	11437.09	9058.487	7498.916	6397.482	5578.166	4944.882	4440.73	4029.868	3688.594	3400.61	3154.338	2941.326	2755.264	2591.342	2445.829	2315.789	2198.879	2093.206	1997.224	1909.658	1829.449	1755.705	1687.677	1624.723	1566.297	1511.928	1461.206	1413.777
15	1452.87	1.010432	0.114375	54619.22	24241.44	15577.59	11476.07	9084.224	7517.438	6411.607	5589.395	4954.092	4448.469	4036.498	3694.364	3405.696	3158.871	2945.405	2758.963	2594.72	2448.933	2318.656	2201.541	2095.687	1999.546	1911.839	1831.503	1757.646	1689.515	1626.468	1567.958	1513.511	1462.719	1415.225
16	1453.87	1.011128	0.1125656	55339.43	24391.66	15643.35	11513.81	9109.164	7535.405	6425.324	5600.312	4963.055	4456.008	4042.962	3699.993	3410.664	3163.302	2949.394	2762.584	2598.028	2451.974	2321.468	2204.152	2098.123	2001.826	1913.981	1833.522	1759.554	1691.323	1628.186	1569.593	1515.071	1464.209	1416.652
17	1454.87	1.011823	0.1111751	56044.6	24537.18	15706.96	11550.33	9133.325	7552.83	6438.642	5610.922	4971.776	4463.351	4049.264	3705.487	3415.515	3167.633	2953.296	2766.127	2601.269	2454.955	2324.225	2206.714	2100.514	2004.066	1916.086	1835.507	1761.431	1693.102	1629.877	1571.203	1516.607	1465.678	1418.058
18	1455.87	1.012519	0.110294	56734.13	24678.02	15768.47	11585.67	9156.726	7569.727	6451.572	5621.237	4980.263	4470.504	4055.409	3710.85	3420.255	3171.867	2957.114	2769.597	2604.444	2457.878	2326.93	2209.229	2102.862	2006.267	1918.156	1837.459	1763.278	1694.853	1631.541	1572.789	1518.121	1467.126	1419.445
19	1456.87	1.013214	0.1097915	57407.61	24814.27	15827.92	11619.85	9179.39	7586.114	6464.128	5631.265	4988.524	4477.474	4061.403	3716.085	3424.886	3176.009	2960.851	2772.996	2607.556	2460.745	2329.584	2211.698	2105.169	2008.43	1920.191	1839.379	1765.095	1696.578	1633.181	1574.352	1519.613	1468.553	1420.813
20	1457.87	1.013909	0.1096112	58064.78	24946.02	15885.38	11652.92	9201.344	7602.009	6476.324	5641.017	4996.567	4484.269	4067.253	3721.199	3429.414	3180.06	2964.51	2776.326	2610.607	2463.557	2332.19	2214.124	2107.436	2010.557	1922.193	1841.27	1766.885	1698.276	1634.797	1575.892	1521.085	1469.961	1422.163
21	1458.87	1.014605	0.1097072	58705.53	25073.4	15940.92	11684.92	9222.616	7617.432	6488.174	5650.306	5004.403	4490.895	4072.963	3726.195	3433.842	3184.027	2968.095	2779.591	2613.601	2466.318	2334.75	2216.508	2109.665	2012.649	1924.164	1843.131	1768.647	1699.95	1636.39	1577.411	1522.536	1471.351	1423.495
22	1459.87	1.0153	0.1100423	59329.86	25196.53	15994.6	11715.89	9243.233	7632.403	6499.693	5659.742	5012.039	4497.36	4078.54	3731.081	3438.176	3187.911	2971.608	2782.793	2616.539	2469.03	2337.265	2218.852	2111.858	2014.709	1926.104	1844.965	1770.385	1701.601	1637.961	1578.91	1523.969	1472.723	1424.811
23	1460.87	1.015996	0.1105854	59937.87	25315.56	16046.51	11745.87	9263.226	7646.943	6510.897	5668.738	5019.486	4503.672	4083.992	3735.861	3442.419	3191.718	2975.055	2785.936	2619.425	2471.695	2339.739	2221.158	2114.017	2016.737	1928.016	1846.772	1772.098	1703.229	1639.512	1580.39	1525.384	1474.078	1426.111
24	1461.87	1.016691	0.1113107	60529.74	25430.64	16096.71	11774.91	9282.622	7661.072	6521.801	5677.595	5026.753	4509.839	4089.323	3740.54	3446.577	3195.452	2978.436	2789.023	2622.261	2474.316	2342.173	2223.429	2116.144	2018.736	1929.901	1848.554	1773.788	1704.835	1641.042	1581.851	1526.782	1475.417	1427.397
25	1462.87	1.017387	0.1121967	61105.74	25541.91	16145.28	11803.05	9301.451	7674.811	6532.42	5686.054	5033.849	4515.867	4094.54	3745.123	3450.654	3199.115	2981.757	2792.056	2625.049	2476.894	2344.568	2225.665	2118.239	2020.706	1931.76	1850.313	1775.457	1706.422	1642.555	1583.295	1528.163	1476.742	1428.668
26	1463.87	1.018082	0.1132249	61666.14	25649.55	16192.3	11830.34	9319.741	7688.179	6542.768	5694.398	5040.783	4521.765	4099.65	3749.616	3454.653	3202.712	2985.021	2795.039	2627.793	2479.432	2346.929	2227.869	2120.305	2022.65	1933.594	1852.05	1777.105	1707.99	1644.049	1584.723	1529.53	1478.051	1429.926
27	1464.87	1.018778	0.1143799	62211.32	25753.69	16237.84	11856.81	9337.518	7701.195	6552.86	5702.546	5047.562	4527.538	4104.657	3754.023	3458.58	3206.247	2988.23	2797.974	2630.495	2481.933	2349.255	2230.042	2122.344	2024.569	1935.406	1853.765	1778.733	1709.539	1645.527	1586.135	1530.882	1479.348	1431.171
28	1465.87	1.019473	0.1156481	62741.63	25854.49	16281.97	11882.52	9354.81	7713.877	6562.708	5710.509	5054.197	4533.194	4109.567	3758.349	3462.438	3209.722	2991.387	2800.864	2633.156	2484.398	2351.549	2232.186	2124.356	2026.464	1937.196	1855.461	1780.343	1711.072	1646.988	1587.533	1532.22	1480.632	1432.404
29	1466.87	1.020169	0.1170182	63257.48	25952.1	16324.76	11907.49	9371.641	7726.243	6572.326	5718.296	5060.693	4538.739	4114.386	3762.599	3466.23	3213.14	2994.495	2803.71	2635.78	2486.829	2353.813	2234.304	2126.344	2028.336	1938.965	1857.137	1781.936	1712.588	1648.436	1588.916	1533.545	1481.903	1433.626
30	1467.87	1.020864	0.11848	63759.29	26046.67	16366.27	11931.76	9388.036	7738.309	6581.726	5725.918	5067.06	4544.179	4119.118	3766.776	3469.961	3216.506	2997.557	2806.516	2638.368	2489.229	2356.048	2236.395	2128.308	2030.187	1940.715	1858.796	1783.512	1714.09	1649.869	1590.287	1534.858	1483.163	1434.837
31	1468.87	1.02156	0.1200249	64247.48	26138.33	16405.57	11955.38	9404.017	7750.092	6590.919	5733.383	5073.303	4549.519	4123.769	3770.884	3473.634	3219.822	3000.576	2809.284	2640.921	2491.598	2358.257	2238.462	2130.25	2032.018	1942.446	1860.437	1785.073	1715.577	1651.288	1591.645	1536.16	1484.413	1436.038
32	1469.87	1.022255	0.1216453	64712.5	26227.22	16445.73	11978.37	9419.606	7761.607	6599.918	5740.7	5079.429	4554.766	4128.342	3774.928	3477.251	3223.09	3003.553	2812.016	2643.443	2493.938	2360.439	2240.506	2132.171	2033.83	1944.16	1862.063	1786.619	1717.05	1652.696	1592.992	1537.451	1485.652	1437.23
33	1470.87	1.022951	0.1233345	65184.76	26313.48	16483.79	12000.77	9434.825	7772.869	6608.732	5747.877	5085.445	4559.923	4132.842	3778.91	3480.817	3226.314	3006.492	2814.714	2645.935	2496.252	2362.598	2242.529	2134.073	2035.624	1945.838	1863.674	1788.151	1718.511	1654.092	1594.327	1538.731	1486.882	1438.413
34	1471.87	1.023646	0.1250866	65634.7	26397.22	16520.82	12022.61	9449.692	7783.889	6617.371	5754.921	5091.358	4564.997	4137.273	3782.834	3484.333	3229.495	3009.394	2817.38	2648.398	2498.541	2364.734	2244.531	2135.956	2037.401	1947.54	1865.271	1789.67	1719.96	1655.476	1595.652	1540.002	1488.102	1439.587
35	1472.87	1.024342	0.1268963	66072.75	26478.57	16556.86	12043.91	9464.227	7794.882	6625.845	5761.839	5097.171	4569.991	4141.638	3786.704	3487.803	3232.637	3012.261	2820.015	2650.835	2500.805	2366.848	2246.513	2137.822	2039.162	1949.208	1866.854	1791.177	1721.397	1656.849	1596.968	1541.264	1489.315	1440.753
36	1473.87	1.025037	0.1287589	66499.33	26557.64	16591.96	12064.72	9478.446	7805.26	6634.163	5768.659	5102.892	4574.91	4145.942	3790.522	3491.229	3235.74	3015.095	2822.621	2653.246	2503.047	2368.943	2248.477	2139.671	2040.909	1950.861	1868.425	1792.672	1722.823	1658.213	1598.274	1542.517	1490.519	1441.912
37	1474.87	1.025733	0.1306705	66914.85	26634.54	16626.18	12085.04	9492.366	7815.634	6642.332	5775.326	5108.524	4579.759	4150.187	3794.291	3494.613	3238.808	3017.898	2825.2	2655.632	2505.267	2371.017	2250.424	2141.504	2042.64	1952.502	1869.983	1794.156	1724.239	1659.567	1599.571	1543.761	1491.715	1443.063
38	1475.87	1.026428	0.1326272	67319.71	26709.37	16659.56	12104.91	9506.003	7825.814	6650.361	5781.907	5114.073	4584.539	4154.377	3798.014	3497.958	3241.842	3020.672	2827.753	2657.996	2507.467	2373.074	2252.354	2143.322	2044.358	1954.13	1871.53	1795.63	1725.646	1660.912	1600.86	1544.998	1492.904	1444.208
39	1476.87	1.027123	0.1346257	67714.3	26782.23	16692.14	12124.34	9519.372	7835.811	6658.257	5788.386	5119.542	4589.256	4158.515	3801.692	3501.266	3244.844	3023.418	2830.281	2660.338	2509.648	2375.113	2254.269	2145.126	2046.064	1955.747	1873.067	1797.094	1727.043	1662.246	1602.141	1546.228	1494.086	1445.347
40	1477.87	1.027819	0.136663	68099	26853.22	16723.95	12143.37	9532.485	7845.634	6666.027	5794.771	5124.936	4593.913	4162.602	3805.33	3504.538	3247.815	3026.137	2832.787	2662.66	2511.81	2377.136	2256.169	2146.917	2047.757	1957.353	1874.593	1798.548	1728.432	1663.578	1603.414	1547.451	1495.262	1446.479
41	1478.87	1.028514	0.1387364	68474.17	26922.41	16755.05	12162.01	9545.357	7855.293	6673.677	5801.064	5130.26	4598.512	4166.643	3808.927	3507.777	3250.758	3028.832	2835.271	2664.963	2513.956	2379.144	2258.055	2148.695	2049.439	1958.948	1876.11	1799.993	1729.812	1664.899	1604.681	1548.667	1496.432	1447.605
42	1479.87	1.02921	0.1408434	68840.17	26989.9	16785.45	12180.28	9557.999	7864.794	6681.214	5807.271	5135.516	4603.057	4170.639	3812.488	3510.984	3253.673	3031.503	2837.733	2667.247	2516.085	2381.137	2259.928	2150.462	2051.11	1960.533	1877.617	1801.43	1731.185	1666.213	1605.941	1549.877	1497.596	1448.726
43	1480.87	1.029905	0.1423619	69197.34	27055.76	16815.2	12198.2	9570.423	7874.147	6688.643	5813.397	5140.708	4607.551	4174.593	3816.013	3514.161	3256.563	3034.151	2840.177	2669.514	2518.198	2383.116	2261.789	2152.217	2052.777	1962.108	1879.116	1802.859	1732.551	1667.52	1607.194	1551.081	1498.754	1449.842
44	1481.87	1.030601	0.1451499	69546.01	27120.06	16844.33	12215.79	9582.64	7883.359	6695.969	5819.446	5145.839	4611.996	4178.506	3819.504	3517.31	3259.428	3036.778	2842.601	2671.764	2520.297	2385.082	2263.637	2153.961	2054.421	1963.675	1880.607	1804.281	1734.909	1668.821	1608.442	1552.28	1499.907	1450.953
45	1482.87	1.031296	0.1473454	69886.49	27182.89	16872.86	12233.06	9594.66	7892.437	6703.199	5825.42	5150.912	4616.394	4182.381	3822.964	3520.431	3262.27	3039.385	2845.008	2673.998	2522.381	2387.035	2265.475	2155.695	2056.063	1965.233	1882.09	1805.695	1735.261	1670.115	1609.684	1553.473	1501.055	1452.06
46	1483.87	1.031992	0.1495668	70219.1	27244.3	16900.83	12250.02	9606.492	7901.387	6710.336	5831.325	5155.931	4620.748	4186.22	3826.393	3523.527	3265.09	3041.972	2847.398	2676.218	2524.453	2388.977	2267.301	2157.419	2057.695	1966.784	1883.565	1807.103	1736.606	1671.404	1610.92	1554.661	1502.199	1453.162
47	1484.87	1.032687	0.1518126	70544.11	27304.36	16928.25	12266.7	9618.146	7910.216	6717.385	5837.163	5160.897	4625.06	4190.025	3829.793	3526.598	3267.888	3044.541	2849.771	2678.423	2526.512	2390.907	2269.118	2159.134	2059.276	1968.246	1884.903	1808.504	1737.946	1672.687	1612.151	1555.844	1503.338	1454.26
48	1485.87	1.033383	0.1540814	70861.82	27363.14	16955.17	12283.11	9629.629	7918.929	6724.35	5842.937	5165.814	4629.332	4193.796	3833.166	3529.646	3270.667	3047.093	2852.13	2680.615	2528.558	2392.826	2270.924	2160.84	2060.936	1969.861	1886.495	1809.899	1739.28	1673.965	1613.378	1557.023	1504.472	1455.353
49	1486.87	1.034078	0.1563719	71172.49	27420.68	16981.59	12299.25	9640.951	7927.532	6731.236	5848.652	5170.683	4633.566	4197.537	3836.512	3532.672	3273.426	3049.629	2854.474	2682.794	2530.594	2394.736	2272.722	2162.538	2062.545	1971.388	1887.95	1811.288	1740.608	1675.237	1614.599	1558.197	1505.603	1456.443
50	1487.87	1.034774	0.1586828	71476.38	27477.04	17007.55	12315.15	9652.118	7936.03	6738.046	5854.308	5175.508	4637.764	4201.247	3839.834	3535.676	3276.167	3052.148	2856.804	2684.961	2532.618	2396.635	2274.51	2164.228	2064.146	1972.911	1889.4	1812.671	1741.991	1676.506	1615.816	1559.368	1506.73	1457.53

Figure E 12-62: SLD Numerical Solution Sample Data Points Case D

E.8 Repeatability and Accuracy of Gripper

Table E 12-12: Accuracy and Repeatability of Gripper Data Points 144 mm

144 mm Diameter	Finger 1		Finger 2		Finger 3	
	xc (mm)	38.37327	xc (mm)	39.66504	xc (mm)	36.45321
Iteration	x (mm)	li x	x (mm)	li x	x (mm)	li x
1	43.64	0.545	41.54	0.155	39.18	0.131
2	42.33	0.765	40.84	0.545	38.4	0.911
3	42.17	0.925	40.33	1.055	37.54	1.771
4	43.69	0.595	41.75	0.365	41.23	1.919
5	43.96	0.865	42.58	1.195	43.53	4.219
6	43.54	0.445	40.7	0.685	37.89	1.421
7	43.35	0.255	40.31	1.075	37.25	2.061
8	43.03	0.065	42.88	1.495	39.07	0.241
9	42.63	0.465	41.87	0.485	40.65	1.339
10	42.61	0.485	41.05	0.335	38.37	0.941
Mean	43.095		41.385		39.311	
Accuracy	4.721733		1.71996		2.8577867	
l bar	0.541		0.739		1.4954	
Std dev li	0.265003		0.439879		1.1598505	
Repeatability	1.336009		2.058636		4.9749515	

Table E 12-13: Accuracy and Repeatability of Gripper Data Points 244 mm

244 mm Diameter	Finger 1		Finger 2		Finger 3	
	xc (mm)	38.37327	xc (mm)	39.66504	xc (mm)	36.45321
Iteration	x (mm)	li x	x (mm)	li x	x (mm)	li x
1	40.08	1.174	39.03	0.299	44.88	0.32
2	41.1	0.154	38.28	0.451	45.51	0.95
3	42.16	0.906	39.53	0.799	44.59	0.03
4	42.75	1.496	39.04	0.309	45.75	1.19
5	41.55	0.296	39.19	0.459	44.48	0.08
6	40.31	0.944	38.79	0.059	44.26	0.3
7	42.6	1.346	38.2	0.531	44.83	0.27
8	40.07	1.184	39.47	0.739	44.64	0.08
9	41.21	0.044	37.82	0.911	44.03	0.53
10	40.71	0.544	37.96	0.771	42.63	1.93
Mean	41.254		38.731		44.56	
Accuracy	2.880733		0.93404		8.106787	
l bar	0.8088		0.5328		0.568	
Std dev li	0.517415		0.269677		0.612568	
Repeatability	2.361045		1.341831		2.405705	

Table E 12-14: Accuracy and Repeatability of Gripper Data Points 344 mm

344 mm Diameter	Finger 1		Finger 2		Finger 3	
	xc (mm)	38.37327	xc (mm)	39.66504	xc (mm)	36.45321
Iteration	x (mm)	li x	x (mm)	li x	x (mm)	li x
1	37.1	0.98	39.94	4.788	38.27	0.526
2	35.3	0.82	36.72	1.568	41.47	3.726
3	35.91	0.21	35.41	0.258	40.08	2.336
4	35.08	1.04	34.44	0.712	36.93	0.814
5	37.1	0.98	34.8	0.352	40.07	2.326
6	37.72	1.6	34.91	0.242	34.45	3.294
7	36.58	0.46	34.27	0.882	38.28	0.536
8	36.46	0.34	33.08	2.072	35.26	2.484
9	34.26	1.86	34.02	1.132	36.3	1.444
10	35.69	0.43	33.93	1.222	36.33	1.414
Mean	36.12		35.152		37.744	
Accuracy	2.253267		4.51304		1.290787	
l bar	0.872		1.3228		1.89	
Std dev li	0.542296		1.353488		1.123538	
Repeatability	2.498887		5.383263		5.260614	

Table E 12-15: Accuracy and Repeatability of Gripper Data Points 384 mm

384 mm Diameter	Finger 1		Finger 2		Finger 3	
	xc (mm)	38.37327	xc (mm)	39.66504	xc (mm)	36.45321333
Iteration	x (mm)	li x	x (mm)	li x	x (mm)	li x
1	42.05	0.674	43.93	0.164	47.23	1.399
2	42.34	0.384	46.05	1.956	49.6	0.971
3	42.46	0.264	44.09	0.004	50.01	1.381
4	42.13	0.594	43.11	0.984	49.99	1.361
5	43.24	0.516	44.95	0.856	49.06	0.431
6	42.69	0.034	44.42	0.326	48.04	0.589
7	43.67	0.946	42.53	1.564	46.29	2.339
8	42.97	0.246	43.62	0.474	46.53	2.099
9	42.67	0.054	43.53	0.564	49.95	1.321
10	43.02	0.296	44.71	0.616	49.59	0.961
Mean	42.724		44.094		48.629	
Accuracy	4.350733		4.42896		12.17579	
l bar	0.4008		0.7508		1.2852	
Std dev li	0.285041		0.613862		0.598155	
Repeatability	1.255922		2.592385		3.079664	

Table E 12-16: Results of Repeatability and Accuracy testing

144 mm diameter	Accuracy (mm)	Repeatability (mm)
Finger 1	4.72	1.34
Finger 2	1.72	2.06
Finger 3	2.86	4.97
Gripper	3.10	2.79

244 mm diameter	Accuracy (mm)	Repeatability (mm)
Finger 1	2.88	2.36
Finger 2	0.93	1.34
Finger 3	8.11	2.41
Gripper	3.97	2.04

344 mm diameter	Accuracy (mm)	Repeatability (mm)
Finger 1	2.25	2.50
Finger 2	4.51	5.38
Finger 3	1.29	5.26
Gripper	2.68	4.38

384 mm diameter	Accuracy (mm)	Repeatability (mm)
Finger 1	4.35	1.26
Finger 2	4.43	2.59
Finger 3	12.18	3.08
Gripper	6.99	2.31

E.9 Repeatability and Accuracy of Linear Actuator

Table E 12-17: Accuracy and Repeatability of Linear Actuator Data Points

Position 1	85.48 mm/sec		32.12 mm/sec		14.72 mm/sec	
	xc (mm)	2	xc (mm)	2	xc (mm)	2
Iteration	x (mm)	li x	x (mm)	li x	x (mm)	li x
1	2.17	0.124	2.34	0.034	2.3	0.091
2	2.3	0.006	2.32	0.014	2.31	0.101
3	2.3	0.006	2.32	0.014	2.23	0.021
4	2.31	0.016	2.28	0.026	2.15	0.059
5	2.33	0.036	2.32	0.014	2.08	0.129
6	2.32	0.026	2.28	0.026	2.16	0.049
7	2.32	0.026	2.3	0.006	2.15	0.059
8	2.28	0.014	2.3	0.006	2.25	0.041
9	2.31	0.016	2.3	0.006	2.21	0.001
10	2.3	0.006	2.3	0.006	2.25	0.041
Mean	2.294		2.306		2.209	
Accuracy	0.294		0.306		0.209	
l bar	0.0276		0.0152		0.0592	
Std dev li	0.035312		0.010163		0.03836	
Repeatability	0.133536		0.045689		0.174281	

E.10 Spindle Runout Data

Table E 12-18: Spindle Runout Data Points

2 mm endmill	Turn number	Angle (degrees)	Runout (mm)
	0	0	0
0.3 minutes for 1 revolution	1	18	-0,01
3.333 rpm	2	36	0
	3	54	0
	4	72	0,01
	5	90	0,01
	6	108	0
	7	126	0
	8	144	0
	9	162	-0,01
	10	180	-0,01
	11	198	-0,01
	12	216	0
	13	234	0
	14	252	0,01
	15	270	0,01
	16	288	0
	17	306	0
	18	324	0
	19	342	-0,01
	20	360	-0,01

E.11 Grasp Force – Finger Data

Table E 12-19: Grasp Force Test Finger Data Points

Finger	Position	Angle	Mass 1	Mass 2	Mass 3	Average Mass (g)	Average Force (N)
1	1	88	236.9	240.3	242.8	240	2.3544
1	2	45	320.5	327.6	340.1	329.4	3.231414
1	3	0	696.7	685.3	688.5	690.1666667	6.770535
2	1	88	260.5	245.3	260.7	255.5	2.506455
2	2	45	280.3	276.2	294.3	283.6	2.782116
2	3	0	724.3	705.3	710.6	713.4	6.998454
3	1	88	260.3	240.5	237.8	246.2	2.415222
3	2	45	311.2	300.5	298.2	303.3	2.975373
3	3	0	637.3	640.7	688.9	655.6333333	6.431763

E.12 Grasp Force – Hand Data

Table E 12-20: Grasp Force Test Hand Data Points

144 mm diameter	Average Extension (mm)	Spring Constant (N/m)	Force (N)
Finger 1	43.095	176.4388489	7.603632194
Finger 2	41.385	176.4388489	7.301921763
Finger 3	39.311	176.4388489	6.93598759
		Hand Force (N)	21.84154155

244 mm diameter	Average Extension (mm)	Spring Constant (N/m)	Force (N)
Finger 1	41.254	176.4388489	7.278808273
Finger 2	38.731	176.4388489	6.833653058
Finger 3	44.56	176.4388489	7.862115108
		Hand Force (N)	21.97457644

344 mm diameter	Average Extension (mm)	Spring Constant (N/m)	Force (N)
Finger 1	36.12	176.4388489	6.372971223
Finger 2	35.152	176.4388489	6.202178417
Finger 3	37.744	176.4388489	6.659507914
		Hand Force (N)	19.23465755

384 mm diameter	Average Extension (mm)	Spring Constant (N/m)	Force (N)
Finger 1	42.724	176.4388489	7.538173381
Finger 2	44.094	176.4388489	7.779894604
Finger 3	48.629	176.4388489	8.580044784
		Hand Force (N)	23.89811277

E.13 Geometric Adaptability Test Data

Table E 12-21: Geometric Adaptability Test Data

Test 1				Test 2			
Sphere	Iteration	Success	Fail	Rectangular Prism 1	Iteration	Success	Fail
	1	1	0		1	1	0
	2	1	0		2	0	1
	3	1	0		3	1	0
	4	1	0		4	1	0
	5	1	0		5	1	0
	6	1	0		6	1	0
	7	1	0		7	1	0
	8	1	0		8	1	0
	9	1	0		9	0	1
	10	1	0		10	1	0
Success Rate (%)	100%			Success Rate (%)	80%		
Failure Rate (%)	0%			Failure Rate (%)	20%		

Test 3				Test 4			
Rectangular Prism 2	Iteration	Success	Fail	Cube	Iteration	Success	Fail
	1	1	0		1	1	0
	2	1	0		2	1	0
	3	1	0		3	1	0
	4	1	0		4	1	0
	5	1	0		5	1	0
	6	1	0		6	1	0
	7	1	0		7	1	0
	8	1	0		8	1	0
	9	1	0		9	1	0
	10	1	0		10	1	0
Success Rate (%)	100%			Success Rate (%)	100%		
Failure Rate (%)	0%			Failure Rate (%)	0%		

Test 5				Test 6			
Cylinder 1	Iteration	Success	Fail	Cylinder 2	Iteration	Success	Fail
	1	1	0		1	1	0
	2	0	1		2	1	0
	3	1	0		3	1	0
	4	1	0		4	1	0
	5	1	0		5	1	0
	6	0	1		6	1	0
	7	1	0		7	1	0
	8	1	0		8	1	0
	9	1	0		9	1	0
	10	1	0		10	1	0
Success Rate (%)	80%			Success Rate (%)	100%		
Failure Rate (%)	20%			Failure Rate (%)	0%		

Test 7			
Spool 1	Iteration	Success	Fail
	1	1	0
	2	1	0
	3	1	0
	4	1	0
	5	1	0
	6	1	0
	7	1	0
	8	1	0
	9	1	0
	10	1	0
Success Rate (%)	100%		
Failure Rate (%)	0%		

Test 8			
Spool 2	Iteration	Success	Fail
	1	1	0
	2	1	0
	3	1	0
	4	1	0
	5	1	0
	6	1	0
	7	1	0
	8	0	1
	9	1	0
	10	1	0
Success Rate (%)	90%		
Failure Rate (%)	10%		

Test 9			
Square Pyramid 1	Iteration	Success	Fail
	1	1	0
	2	1	0
	3	1	0
	4	1	0
	5	1	0
	6	1	0
	7	1	0
	8	1	0
	9	1	0
	10	1	0
Success Rate (%)	100%		
Failure Rate (%)	0%		

Test 10			
Square Pyramid 2	Iteration	Success	Fail
	1	1	0
	2	1	0
	3	1	0
	4	1	0
	5	1	0
	6	1	0
	7	1	0
	8	1	0
	9	1	0
	10	1	0
Success Rate (%)	100%		
Failure Rate (%)	0%		

Test 11			
Triangular Prism 1	Iteration	Success	Fail
	1	1	0
	2	0	1
	3	1	0
	4	1	0
	5	1	0
	6	1	0
	7	1	0
	8	0	1
	9	0	1
	10	1	0
Success Rate (%)	70%		
Failure Rate (%)	30%		

Test 12			
Triangular Prism 2	Iteration	Success	Fail
	1	1	0
	2	1	0
	3	1	0
	4	1	0
	5	1	0
	6	1	0
	7	1	0
	8	1	0
	9	1	0
	10	1	0
Success Rate (%)	100%		
Failure Rate (%)	0%		

E.14 LabVIEW Block Diagrams

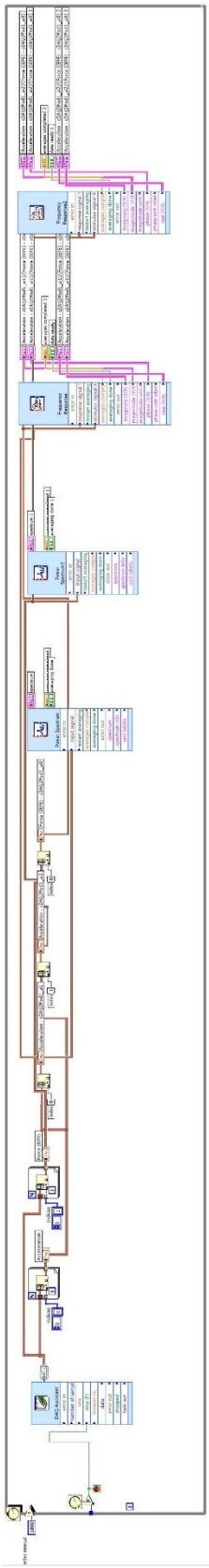

Figure E 12-63: EMA LabVIEW Block Diagram

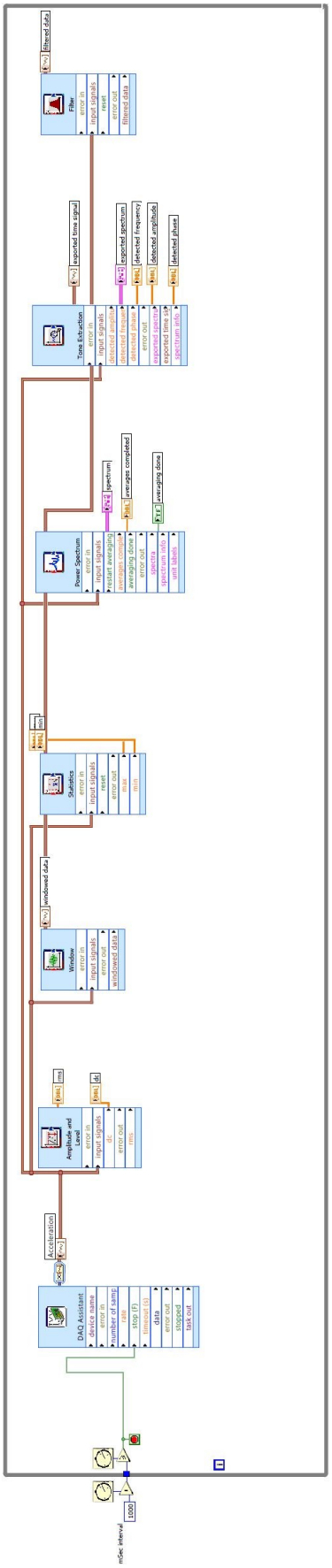

Figure E 12-64: Gripper Response LabVIEW Block Diagram

E.15 SLD Validation

Table E 12-22: Experimental Results

Data point	Spindle speed (RPM)	Feed rate (mm/sec)	Depth of Cut (mm)	RMS acceleration (m/s^2)
1	15000	0.73	0.20	109.232
2	15000	0.73	0.38	99.1965
3	17500	0.73	0.30	141.159
4	18000	0.73	0.30	141.44
5	14700	1.12	0.23	113.676
6	15500	1.12	0.40	116.37
7	17250	1.12	0.30	137.572
8	17000	1.12	0.40	142.364
9	15000	1.53	0.15	109.013
10	13600	1.53	0.40	126.858
11	18000	1.53	0.21	134.325
12	18500	1.53	0.35	128.105
13	14500	2.07	0.18	103.212
14	15000	2.07	0.45	119.507
15	18000	2.07	0.31	130.51
16	18000	2.07	0.24	128.035
17	12800	0.73	0.22	81.9777
18	13000	1.12	0.25	91.6355
19	13000	1.53	0.29	100.556
20	13500	2.07	0.48	102.186
21	13500	0.73	0.25	87.4996
22	12700	1.12	0.39	99.2269

Appendix F Arduino Control Code

F.1 Servo Control Code [185]

```
#include <Servo.h>

Servo myservo3;

Servo myservo5;

Servo myservo6;

intpotpin=0;
int potpin2 = 1;

int potpin3 = 2;

intval=0;
int val2 = 0;

int val3 = 0;

voidsetup()
{

myservo3.attach(9);
myservo5.attach(10);

myservo6.attach(11);

}

voidloop()
{

val=analogRead(potpin);
val = map(val, 3, 1023, 0, 176);

myservo3.write(val);

delay(25);

val2=analogRead(potpin2);
val2 = map(val2, 3, 1023, 0, 176);

myservo5.write(val2);

delay(25);

val3=analogRead(potpin3);
val3 = map(val3, 3, 1023, 0, 175);

myservo6.write(val3);

delay(25);

}
```

F.2 Stepper Control Code

```
const int stepPin = 5;
const int dirPin = 2;
const int enPin = 8;
void setup() {
  pinMode(stepPin,OUTPUT);
  pinMode(dirPin,OUTPUT);
  pinMode(enPin,OUTPUT);
  digitalWrite(enPin,LOW);
}
void loop() {
  digitalWrite(dirPin,LOW);
  for(int x = 0; x < 1850; x++) {
    digitalWrite(stepPin,HIGH);
    delayMicroseconds(200);
    digitalWrite(stepPin,LOW);
    delayMicroseconds(200);
  }
  delay(1000);
}
const int stepPin = 5;
const int dirPin = 2;
const int enPin = 8;
void setup() {
  pinMode(stepPin,OUTPUT);
  pinMode(dirPin,OUTPUT);
  pinMode(enPin,OUTPUT);
  digitalWrite(enPin,LOW);
}
void loop() {
  digitalWrite(dirPin,HIGH);
  for(int x = 0; x < 1850; x++){
```

```
    digitalWrite(stepPin,HIGH);
    delayMicroseconds(200);
    digitalWrite(stepPin,LOW);
    delayMicroseconds(200);
  }
  delay(1000);
}
```

F.3 BLDC Calibration Code [186]

```
#include <Servo.h>
#define MIN_PULSE_LENGTH 1000
#define MAX_PULSE_LENGTH 2000
Servo motA;
char data;
void setup() {
    Serial.begin(9600);
    motA.attach(4, MIN_PULSE_LENGTH, MAX_PULSE_LENGTH);
    displayInstructions();
}
void loop() {
    if (Serial.available()) {
        data = Serial.read();
        switch (data) {
            case 48 : Serial.println("Sending minimum throttle");
                    motA.writeMicroseconds(MIN_PULSE_LENGTH);
            break;
            case 49 : Serial.println("Sending maximum throttle");
                    motA.writeMicroseconds(MAX_PULSE_LENGTH);
            break;
            case 50 : Serial.print("Running test in 3");
                    delay(1000);
                    Serial.print(" 2");
                    delay(1000);
```

```
                Serial.println(" 1...");
                delay(1000);
                test();
            break;
        }
    }
}
void test()
{
    for (int i = MIN_PULSE_LENGTH; i <= MAX_PULSE_LENGTH; i += 5) {
        Serial.print("Pulse length = ");
        Serial.println(i);
        motA.writeMicroseconds(i);
        delay(200);
    }
    Serial.println("STOP");
    motA.writeMicroseconds(MIN_PULSE_LENGTH);
}
void displayInstructions()
{
    Serial.println("READY - PLEASE SEND INSTRUCTIONS AS FOLLOWING :");
    Serial.println("\t0 : Send min throttle");
    Serial.println("\t1 : Send max throttle");
    Serial.println("\t2 : Run test function\n");
}
```

F.4 BLDC Control Code [187]

```
#include <Servo.h>
Servo ESC;
int potValue;
void setup() {
ESC.attach(9,1000,2000);
}
```

```
void loop() {
potValue = analogRead(A0);
potValue = map(potValue, 0, 1023, 0, 180);
ESC.write(potValue);
```

Appendix G Motor Characteristic Curves

G.1 BLDC Motor Curves

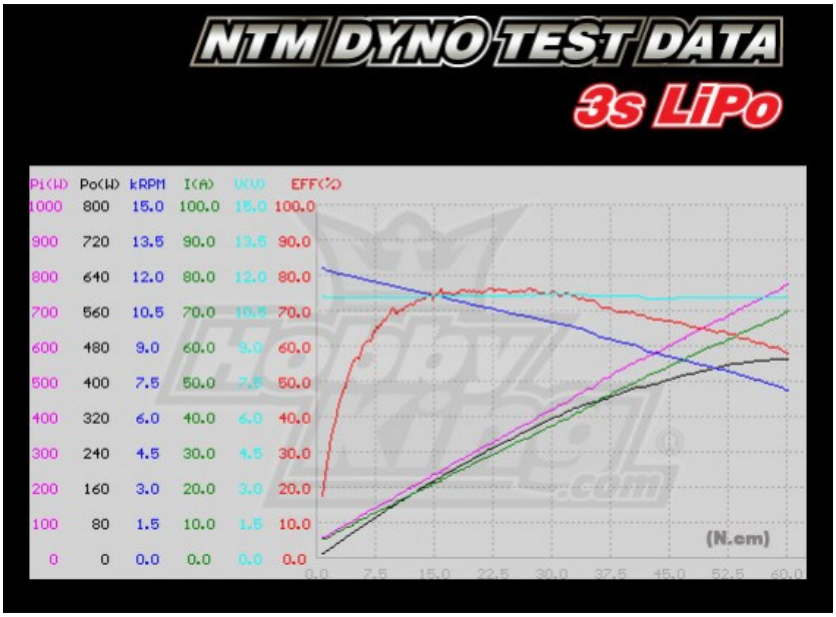

Figure G 12-65: NTM PROPDRIVE 1100KV Brushless Motor Test Data [188]

G.2 Stepper Motor Curve

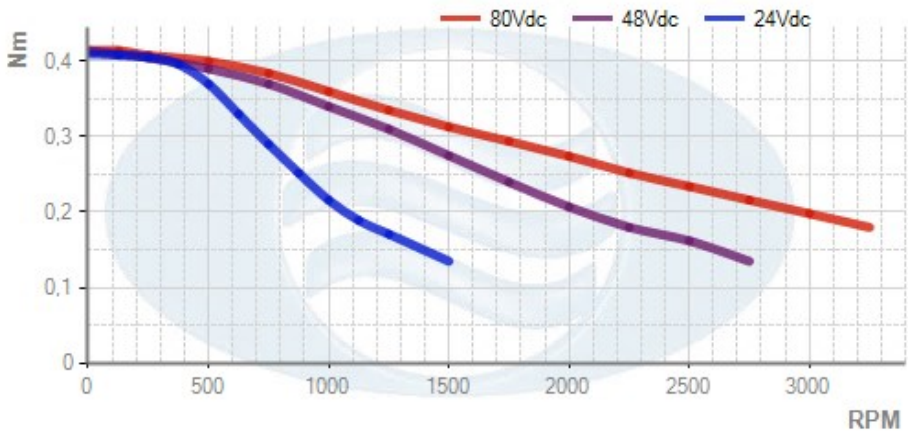

Figure G 12-66: NEMA 17 Stepper Motor Characteristic Curve [189]

Appendix H Stepper Driver Technical Data

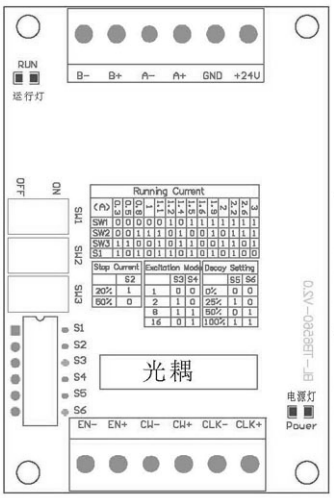

衰减设置（Decay Setting）		
	S5	S6
0%	OFF	OFF
25%	ON	OFF
50%	OFF	ON
100%	ON	ON

静止时半流（Stop Current）	
	S2
20%	ON
50%	OFF

细分设置（Excitation Mode）		
	S3	S4
整步	OFF	OFF
半步	ON	OFF
8细分	ON	ON
16细分	OFF	ON

工作电流设置（Running Current）														
(A)	0.3	0.5	0.8	1	1.1	1.2	1.4	1.5	1.6	1.9	2	2.2	2.6	3
SW1	OFF	OFF	OFF	OFF	OFF	ON	OFF	ON	ON	ON	ON	ON	ON	ON
SW2	OFF	OFF	ON	ON	ON	OFF	ON	OFF	OFF	ON	OFF	ON	ON	ON
SW3	ON	ON	OFF	OFF	ON	OFF	ON	ON	OFF	OFF	ON	ON	OFF	ON
S1	ON	OFF	ON	OFF	ON	ON	OFF	ON	OFF	ON	OFF	ON	OFF	OFF

Figure H 12-67: TB6560 Technical Specification [190]

Appendix I Mass Calculation

Gripper Subassembly						
Material	**Component**	**Mass (gram)**	**Mass (kg)**	**Weight (N)**	**Quantity**	**Total Weight (N)**
PLA	Finger 1/2 Mount	113	0.113	1.10853	2	2.21706
PLA	Finger 3 Mount	110	0.11	1.0791	1	1.0791
	FEETECH Servomotor	59	0.059	0.57879	3	1.73637
PLA	Servomotor Cover	10	0.01	0.0981	3	0.2943
PLA	Servo Pulley	6	0.006	0.05886	3	0.17658
PLA	Anchor Link	34	0.034	0.33354	3	1.00062
PLA	Mid Link	21	0.021	0.20601	3	0.61803
PLA	End Link	18	0.018	0.17658	3	0.52974
Butyl 60 Durometer	Rubber Joint	4.5	0.0045	0.044145	3	0.132435
PLA	Retraction Pulley	2	0.002	0.01962	3	0.05886
High Tensile Steel	Pin Long	1.63	0.00163	0.0159903	3	0.0479709
High Tensile Steel	Pin Short	0.34	0.00034	0.0033354	6	0.0200124
PLA	Palm	158	0.158	1.54998	1	1.54998
Polyurethane	Glove	80	0.08	0.7848	3	2.3544
PLA	Spring Mount	2	0.002	0.01962	3	0.05886
Spring Steel	Spring 1	0	0	0	10	0
Spring Steel	Spring 2	0	0	0	0	0
	Cable - Waxed Thread	0	0	0	0	0
High Tensile Steel	socket head cap screw_iso Configuration: ISO 4762 M3 x 6 - 6N	0.1	0.0001	0.000981	12	0.011772
High Tensile Steel	Pin Longer	2.72	0.00272	0.0266832	3	0.0800496
High Tensile Steel	M4 X 65mm Cap Head Screws (DIN 912) - A2	6	0.006	0.05886	6	0.35316
High Tensile Steel	socket head cap screw_iso Configuration: ISO 4762 M5 x 20 - 20S	0.59	0.00059	0.0057879	8	0.0463032
High Tensile Steel	hex nut style 1 gradeab_iso Configuration: ISO - 4032 - M5 - W - N	0.19	0.00019	0.0018639	8	0.0149112
					Subtotal	**12.3805143**

Reconfigurable Subassembly						
Material	**Component**	**Mass (gram)**	**Mass (kg)**	**Weight (N)**	**Quantity**	**Total Weight (N)**
Aluminium 6082	Mounting Platform	762.61	0.76261	7.4812041	1	7.4812041
Aluminium 6082	Mount	697.11	0.69711	6.8386491	1	6.8386491
Aluminium 6082	Sliding Platform	321.38	0.32138	3.1527378	1	3.1527378
Aluminium 6082	Spindle Platform	309.18	0.30918	3.0330558	1	3.0330558
Chrome Steel	Chromed Steel Linear Rod 8 104	40.25	0.04025	0.3948525	2	0.789705
Stainless Steel	Lead Screw 8 120	55.73	0.05573	0.5467113	1	0.5467113
High Tensile Steel	socket head cap screw_iso Configuration: ISO 4762 M5 x 50 - 22N	1.22	0.00122	0.0119682	7	0.0837774
High Tensile Steel	hex nut style 1 gradeab_iso Configuration: ISO - 4032 -M5 - D - N□ □	0.19	0.00019	0.0018639	7	0.0130473
High Tensile Steel	hexalobular socket cheese head_iso Configuration: ISO 14580 - #3 x 10 x 9 - 4.8-N	0.15	0.00015	0.0014715	4	0.005886
High Tensile Steel	hexalobular socket cheese head_iso Configuration: ISO 14580 - #6 x 25 x 23 - 4.8-N□	1.18	0.00118	0.0115758	4	0.0463032
High Tensile Steel	hex thin nut chamfered gradeab_iso Configuration: ISO - 4035 - M8 - N□	0.43	0.00043	0.0042183	4	0.0168732
High Tensile Steel	socket head cap screw_iso Configuration: ISO 4762 M5 x 50 - 22N	0.63	0.00063	0.0061803	4	0.0247212
High Tensile Steel	hex nut style 1 gradeab_iso Configuration: ISO - 4032 -M5 - D - N□ □	0.19	0.00019	0.0018639	4	0.0074556
High Tensile Steel	socket head cap screw_iso Configuration: ISO 4762 M3 x 16 - 16N	0.18	0.00018	0.0017658	4	0.0070632
High Tensile Steel	hex nut style 1 gradeab_iso Configuration: ISO - 4032 - M3 - D - N	0.05	0.00005	0.0004905	4	0.001962
	8MM FLANGE PILLOW BLOCK BEARING - KFL08	26	0.026	0.25506	2	0.51012
	LINEAR BALL BEARING - LM8UU - 8MM DIAMETER	20	0.02	0.1962	2	0.3924
	SHF8 LINEAR SHAFT SUPPORT	20	0.02	0.1962	2	0.3924
Brass	TR8X8 METRIC LEAD SCREW NUT	10	0.01	0.0981	1	0.0981
Aluminium 6061	GT2 PULLEY (5MM BORE / 20 TOOTH / 6MM BELT)	6	0.006	0.05886	1	0.05886
Aluminium 6061	GT2 PULLEY (8MM BORE / 20 TOOTH / 6MM BELT)	13	0.013	0.12753	1	0.12753
	NEMA 17	240	0.24	2.3544	1	2.3544
					Subtotal	**25.9829622**

Machine Tool Subassembly						
Material	**Component**	**Mass (gram)**	**Mass (kg)**	**Weight (N)**	**Quantity**	**Total Weight (N)**
4340 Steel	Spindle Shaft	121.31	0.12131	1.1900511	1	1.1900511
Aluminium 6082	Spindle Housing	466.38	0.46638	4.5751878	1	4.5751878
	Double Row Bearing NSK 3201	51	0.051	0.50031	1	0.50031
	Single Row Bearing NSK 7201 BW	40	0.04	0.3924	1	0.3924
40 CR Steel	ER11-A 8mm Collet Chuck Holder Motor Shaft Tool Holder Extension Rod CNC Tool	49.9	0.0499	0.489519	1	0.489519
Aluminium 6082	Single Row Bearing Preload Cover	33.62	0.03362	0.3298122	1	0.3298122
Aluminium 6082	Double Row Bearing Preload Cover	40.24	0.04024	0.3947544	1	0.3947544
	Belt	0	0	0	0	0
Spring Steel 65MN	ER11 Collet 3,175 mm	10	0.01	0.0981	1	0.0981
Tungsten Carbide	End mill Double Flute 2 mm	5	0.005	0.04905	1	0.04905
	NTM Propdrive 3548 1100KV BLDC Motor	185	0.185	1.81485	1	1.81485
High Tensile Steel	hex nut style 1 gradeab_iso Configuration: ISO - 4032 - M5 - D - N	0.19	0.00019	0.0018639	8	0.0149112
High Tensile Steel	socket head cap screw_iso Configuration: ISO 4762 M5 x 35 - 22S	0.87	0.00087	0.0085347	8	0.0682776
High Tensile Steel	socket head cap screw_iso Configuration: ISO 4762 M3 x 20 - 20N□	0.2	0.0002	0.001962	4	0.007848
High Tensile Steel	plain washer 10669 type nl_iso Configuration: ISO 10669-3-N	0.04	0.00004	0.0003924	4	0.0015696
High Tensile Steel	hex nut style 1 gradeab_iso Configuration: ISO - 4032 - M3 - W - N	0.05	0.00005	0.0004905	4	0.001962
Aluminium 6061	GT2 PULLEY (5MM BORE / 20 TOOTH / 6MM BELT)	6	0.006	0.05886	1	0.05886
Aluminium 6061	GT2 PULLEY (8MM BORE / 20 TOOTH / 6MM BELT)	13	0.013	0.12753	1	0.12753
High Tensile Steel	hex nut style 1 gradeab_iso Configuration: ISO - 4032 - M8 - D - N	0.74	0.00074	0.0072594	2	0.0145188
High Tensile Steel	socket head cap screw_iso Configuration: ISO 4762 M4 x 12 - 20N□	0.29	0.00029	0.0028449	8	0.0227592
					Subtotal	**10.1522709**
					Total Weight (N)	**48.5157474**
					Total Weight (kg)	**4.94554**

Figure I 12-68: Mass Calculation

Appendix J Cost Calculation

Gripper Subassembly				
Material	Component	Unit Price (ZAR)	Quantity	Total Cost (ZAR)
PLA	Finger 1/2 Mount	200	2	400
PLA	Finger 3 Mount	200	1	200
	FEETECH FR0115M Servomotor	305,92	3	917,76
PLA	Servomotor Cover	50	3	150
PLA	Servo Pulley	50	3	150
PLA	Anchor Link	150	3	450
PLA	Mid Link	150	3	450
PLA	End Link	120	3	360
Butyl 60 Durometer	Rubber Joint	50	3	150
PLA	Retraction Pulley	30	3	90
High Tensile Steel	Pin Long	5	3	15
High Tensile Steel	Pin Short	4	6	24
PLA	Palm	500	1	500
Polyurethane	Glove	1200	3	3600
PLA	Spring Mount	50	3	150
Spring Steel	Spring 1	15	1	15
Spring Steel	Spring 2	15	1	15
	Cable - Waxed Thread	50	1	50
High Tensile Steel	socket head cap screw ISO 4762 M3 x 6	2	12	24
High Tensile Steel	Pin Longer	1	3	3
High Tensile Steel	M4 X 65mm Cap Head Screws	3	6	18
High Tensile Steel	socket head cap screw ISO 4762 M5 x 20	4	8	32
High Tensile Steel	hex nut M5	3	8	24
	Meanwell RS-15-5 Power Supply	140	3	420
	Potentiometer Sparkfun	50	3	150
	Cables	200	1	200
	Arduino Uno	120	1	120
			Total Price (ZAR)	8677,76

Reconfigurable Subassembly				
Material	Component	Price Per Unit (ZAR)	Quantity	Total Cost (ZAR)
Aluminium 6082	Mounting Platform	500	1	500
Aluminium 6082	Mount	400	1	400
Aluminium 6082	Sliding Platform	300	1	300
Aluminium 6082	Spindle Platform	300	1	300
Chrome Steel	Chromed Steel Linear Rod 8 104	80	2	160
Stainless Steel	Lead Screw 8 120	150	1	150
High Tensile Steel	socket head cap screw ISO 4762 M5 x 50	5	7	35
High Tensile Steel	hex nut style M5 □ □	2	7	14
High Tensile Steel	hexalobular socket cheese head ISO 14580 - #3 x 10 x 9	2	4	8
High Tensile Steel	hexalobular socket cheese head ISO 14580 - #6 x 25 x 23□	5	4	20
High Tensile Steel	hex thin nut chamfered ISO - 4035 - M8 □	6	4	24
High Tensile Steel	socket head cap screw ISO 4762 M5 x 50	3	4	12
High Tensile Steel	hex nut ISO - 4032 -M5□	2	4	8
High Tensile Steel	socket head cap screw ISO 4762 M3 x 16	3	4	12
High Tensile Steel	hex nut style 1 gradeab_iso Configuration: ISO - 4032 - M3 - D - N	4	4	16
	8MM FLANGE PILLOW BLOCK BEARING - KFL08	130	2	260
	LINEAR BALL BEARING - LM8UU - 8MM DIAMETER	80	2	160
	SHF8 LINEAR SHAFT SUPPORT	45	2	90
Brass	TR8X8 METRIC LEAD SCREW NUT	150	1	150
Aluminium 6061	GT2 PULLEY (5MM BORE / 20 TOOTH / 6MM BELT)	40	1	40
Aluminium 6061	GT2 PULLEY (8MM BORE / 20 TOOTH / 6MM BELT)	40	1	40
	NEMA 17 4 KG CM		1	0
	TB6560 microstepping driver	190	1	190
	Meanwell SP-240-24 power supply	600	1	600
	Cables	100	1	100
	Connectors	100	1	100
	Arduino Uno	120	1	120
			Total Price (ZAR)	3809

Machine Tool Subassembly				
Material	Component	Price Per Unit (ZAR)	Quantity	
4340 Steel	Spindle Shaft	300	1	300
Aluminium 6082	Spindle Housing	250	1	250
	Double Row Bearing NSK 3201	500	1	500
	Single Row Bearing NSK 7201 BW	300	1	300
40 CR Steel	ER11-A 8mm Collet Chuck Holder	180	1	180
Aluminium 6082	Single Row Bearing Preload Cover	250	1	250
Aluminium 6082	Double Row Bearing Preload Cover	250	1	250
	Belt	55	0	0
Spring Steel 65MN	ER11 Collet 3,175 mm	60	1	60
Tungsten Carbide	End mill Double Flute 2 mm (Two Flute Cleveland 2 mm End Mill)	350	1	350
	NTM Propdrive 3548 1100KV BLDC Motor	600	1	600
High Tensile Steel	hex nut style 1 gradeab_iso Configuration: ISO - 4032 - M5 - D - N	2	8	16
High Tensile Steel	socket head cap screw_iso Configuration: ISO 4762 M5 x 35 - 22S	3	8	24
High Tensile Steel	socket head cap screw_iso Configuration: ISO 4762 M3 x 20 - 20N	3	4	12
High Tensile Steel	plain washer 10669 type nl_iso Configuration: ISO 10669-3-N	1	4	4
High Tensile Steel	hex nut style 1 gradeab_iso Configuration: ISO - 4032 - M3 - W - N	3	4	12
Aluminium 6061	GT2 PULLEY (5MM BORE / 20 TOOTH / 6MM BELT)	40	1	40
Aluminium 6061	GT2 PULLEY (8MM BORE / 20 TOOTH / 6MM BELT)	40	1	40
High Tensile Steel	hex nut style 1 gradeab_iso Configuration: ISO - 4032 - M8 - D - N	2	2	4
High Tensile Steel	socket head cap screw_iso Configuration: ISO 4762 M4 x 12 - 20N	3	8	24
	Hobbywing Skywalker 2-6S 80A UBEC	450	1	450
	Meanwell SE-600-24 Power Supply	1400	1	1400
	Arduino Uno	150	1	150
	Potentiometer Sparkfun	50	1	50
	Cables	200	1	200
	Connectors	100	1	100
	NTM Propdrive 3548 1100KV BLDC Motor MOUNT KIT	250	1	250
	Machining	0	1	0
			Total Price (ZAR)	5816
			Net Price (ZAR)	18302,76

Figure J 12-69: Cost Calculation

Appendix K Mechanical Drawings

K.1 Spindle Housing

*Don’t print beyond this page.

K.2 Spindle Shaft

K.3 Bottom Preload Clamp

K.4 Top Preload Clamp

K.5 Spindle Subassembly

K.6 Machine Tool Subassembly

K.7 Gripper Housing ½

K.8 Gripper Housing 3

K.9 Proximal Phalanx

K.10 Middle Phalanx

K.11 Distal Phalanx

K.12 Servo Pulley

K.13 Retraction Pulley

K.14 Top Spring Loader Bracket

K.15 Bottom Spring Loader Bracket

K.16 Gripper Palm

K.17 Servo Cover

K.18 Gripper ½ Subassembly

K.19 Gripper 3 Subassembly

K.20 Gripper Assembly

K.21 Robot Mount

K.22 Main Platform

K.23 Gripper Platform

K.24 Spindle Mount

K.25 Reconfiguration Mechanism Assembly

K.26 RREE Assembly

K.27 RREE Subsystem

K.28 Glove Mold

K.29 Grasp Force Test Unit

K.30 RREE Test Frame Assembly